University of Alberta

Electrodeposited Ni_3Al base intermetallic coatings and their resistance to high temperature degradation in hydrocarbon cracking environments

by

Haifeng Liu 

A thesis submitted to the Faculty of Graduate Studies and Research in partial fulfillment of the

requirements for the degree of *Doctor of Philosophy*

in

Materials Engineering

Department of *Chemical and Materials Engineering*

Edmonton, Alberta

Spring 2006

Your file Votre référence
ISBN: 0-494-14011-9
Our file Notre référence
ISBN: 0-494-14011-9

University of Alberta

Library Release Form

Name of Author: *Haifeng Liu*

Title of Thesis: *Electrodeposited Ni3Al base intermetallic coatings and their resistance to high temperature degradation in hydrocarbon cracking environments.*

Degree: *Doctor of Philosophy*

Year this Degree Granted: *2006*

Signature

Dedicated to My Wife, Qiang Zhang, and My Son, Bruce Xuan Liu.

Abstract

This research was aimed at developing novel Ni-Al base intermetallic coatings to protect commercial Fe-Ni-Cr tube alloys from severe corrosive degradation at high temperatures. These alloys are widely used in petrochemical, chemical, and energy conversion industries. The coating process and coating evaluation were the two main aspects of this investigation.

A two-step coating processing has been successfully developed to in situ apply pure and CeO_2-modified Ni_3Al intermetallic coatings onto Fe-Ni-Cr substrates. The process consists of the electrodeposition of Ni-Al and Ni-Al-CeO_2 composite coatings from a Watt's nickel bath containing Al and CeO_2 particles via a cost-effective electroplating technique and an annealing treatment of the as-plated coatings. It was found that the deposition of Al particles obeyed a Guglielmi model, and that REO particles interfered significantly with the deposition of Al particles.

The long-term resistance of pure and CeO_2-modified Ni_3Al coatings to cyclic oxidation, carburization, coke formation, and metal dusting was evaluated in flowing dry air, 2%CH_4-H_2, and CO-H_2-H_2O respectively. Due to the high porosity, pure and CeO_2-dispersed Ni_3Al coatings exhibited poor resistance to cyclic oxidation at 850 ℃. CeO_2 improved the spallation resistance of the Ni_3Al base coatings during cyclic oxidation at 1050 ℃. CeO_2-dispersed Ni_3Al coatings showed better carburization resistance, particularly at 1050 ℃. Ni_3Al-based coatings, Those CeO_2-dispersed were susceptible to coke formation and metal dusting at 650 ℃. Pre-oxidation improved the resistance of

Ni_3Al-based coatings to coke formation and metal dusting at 650 °C, but the effectiveness depended on the integrity of the induced alumina scale. Special attention was paid to several aspects of coating degradation. These aspects included microstructure changes, degradation mechanisms, coating/substrate interdiffusion, effect of corrosive atmosphere, and effect of CeO_2 on coating performance. Advanced analytic technologies—including SEM, EDS, EPMA, XRD, XPS, and AES—were adopted in this investigation.

Acknowledgement

I would first like to thank my advisor, Dr. Weixing Chen, whose profound knowledge, wise guidance and continuous encouragement made the completion of my doctoral research possible. I will not forget his patience in helping me revise my publications and this dissertation. It has been an honor to conduct research under his supervision. I also extend my thanks to the committee members—Dr. Prakash C. Patnaik, Dr. Jan A. Jung, Dr. Dongyang Li, Dr. Douglas G. Ivey, and Dr. Qi Liu—for carefully reviewing my dissertation and providing valuable suggestions.

I am grateful for the assistance from Ms. Tina Barker in scheduling and finishing my work on materials characterization using electron microscopy. Special thanks go to my group members—Mr. Evan Vokes, Mr. Lilu Zhou, Mr. Jinlong Zhao, Dr. You Wang, Dr. Chengbo Xiao, and Dr. Daxiong He—for their kind help during my research.

Finally, I would like to acknowledge financial support from the Natural Sciences and Engineering Research Council of Canada (NSERC) and Nova Chemicals Limited.

Table of Contents

Dedication i

Abstract ii

Acknowledgement iv

List of Tables x

List of Figures xii

List of Abbreviations xxii

1. Introduction and Literature Review 1

1.1 Introduction 2

1.1.1 High-Temperature Corrosion and Protection 2

1.1.2 Surface Coating Systems 2

1.2 Literature Review 5

1.2.1 Electrodeposition of Ni-Al-based Composite Coatings 5

1.2.2 Physical and Mechanical Properties of Ni_3Al 18

1.2.3 Oxidation of Ni_3Al 20

1.2.4 Carbonaceous Corrosions 34

1.3 Research Objectives 48

1.4 Bibliography 50

2. Electrodeposited Ni – Al Composite Coatings with High Al Content via Sediment Co-deposition 62

2.1 Introduction 63

2.2 Experimental 65

2.2.1 Sediment Co-deposition 65

2.2.2 Volume Fraction of Al Particles 66
2.2.3 Diffusion Treatment 67
2.3 Results and Discussion 67
2.3.1 Morphology of SCD Coatings 67
2.3.2 Effects of Processing Parameters 69
2.3.3 Co-deposition Mechanism 72
2.3.4 Diffusion Treatment 77
2.4 Concluding Remarks 80
2.5 Bibliography 81

3. Reactive Oxide-dispersed Ni_3Al Intermetallic Coatings by Sediment Co-deposition 84
3.1 Introduction 85
3.2 Experimental Procedures 86
3.2.1 Coating Process 86
3.2.2 Characterization 87
3.3 Results 88
3.3.1 Ni-Al Composite Coatings 88
3.3.2 Ni-Al-REO Composite Coatings 90
3.4 Discussion 100
3.4.1 Interfering Effect 100
3.4.2 Formation of REO-dispersed Ni_3Al 103
3.5 Concluding Remarks 105
3.6 Bibliography 106

4. **Cyclic Oxidation Behavior of Electrodeposited Ni_3Al-CeO_2-Based Coatings at 850 °C and 1050 °C** 109
4.1 Introduction 110
4.2 Experimental 111
4.2.1 Coating Process 111
4.2.2 Cyclic-oxidation Test 112

4.2.3 Characterization 113
4.3 Coating Microstructures 113
4.4 Oxidation at 850 °C 116
4.4.1 Oxidation kinetics 116
4.4.2 Morphologies of Oxide Scales 119
4.4.3 Cross-sectional Morphologies of Oxide Scales 121
4.4.4 Cross-sectional Microstructures of Coating Layer 125
4.4.5 Discussion 130
4.4.6 Conclusions 138
4.5 Oxidation at 1050 °C 139
4.5.1 Oxidation Kinetics 139
4.5.2 Morphologies of Oxide Scales 140
4.5.3 CeO_2 Particles in Coatings and Oxide Scales 151
4.5.4 Cross-sections of Oxidized Coatings 157
4.5.5 Discussion 159
4.5.6 Conclusions 164
4.6 Concluding Remarks 165
4.7 Bibliography 165

5. **On The Improvement of Cyclic-oxidation Resistance of Electrodeposited Ni-Al-Based Intermetallic Coatings at 850 °C** 171
5.1 Introduction 172
5.2 Experimental 173
5.2.1 Sample Preparation 173
5.2.2 Cyclic Oxidation 174
5.2.3 Characterization 174
5.3 Results 175
5.3.1 Coating Microstructures 175
5.3.2 Oxidation Kinetics 178
5.3.3 Cross-sections of Oxide Scales 180
5.4 Discussion 184

5.4.1 Special Annealing 184
5.4.2 Modified Ni-Al Coatings and Thin Films 185
5.5 Concluding Remarks 186
5.6 Bibliography 186

6. Carburization of Electrodeposited Ni_3Al-CeO_2-Based Coatings in 2%CH_4-H_2 Reducing Atmospheres 188
6.1 Introduction 189
6.2 Experimental Procedures 190
6.2.1 Sample Preparation 190
6.2.2 Cyclic-carburization Test 191
6.2.3 Materials Characterization 192
6.3 Results 192
6.3.1 Carburization Kinetics 192
6.3.2 Morphologies of The Uncoated Fe-Ni-Cr Alloy 194
6.3.3 Morphologies of The Pure Ni_3Al Coating 197
6.3.4 Morphologies of The CeO_2-dispersed Ni_3Al Coatings 204
6.4 Discussion 209
6.4.1 Carburization in 2%CH_4-H_2 209
6.4.2 Oxidation of Ni_3Al-Based Coatings in 2%CH_4-H_2 211
6.4.3 Coke Formation on Ni_3Al-Based Coatings 212
6.4.4 Effect of CeO_2 Particles 213
6.5 Concluding Remarks 214
6.6 Bibliography 218

7. Coke Formation and Metal Dusting of Electroplated Ni_3Al-CeO_2-Based Coatings in CO-H_2-H_2O 222
7.1 Introduction 223
7.2 Experimental Procedures 224
7.2.1 Sample Preparation 224
7.2.2 Metal-dusting Test 225

7.2.3 Materials Characterization 227
7.3 Results 227
7.3.1 Metal-dusting Kinetics 227
7.3.2 Coating Morphologies 230
7.4 Discussion 267
7.4.1 Un-pre-oxidized Coatings 267
7.4.2 Coatings with Pre-oxidation 275
7.5 Concluding Remarks 278
7.6 Bibliography 280

8. Concluding Remarks and Future Work 286
8.1 Concluding Remarks 287
8.1.1 The Coating Process 287
8.1.2 The Coating Evaluation 287
8.2 Future Work 289
8.2.1 Interfering Effect 289
8.2.2 Elimination of Pores 290
8.2.3 Elimination of Ni Particles During Pre-oxidation 290
8.3 Bibliography 290

List of Tables

Chapter 1. Introduction and Literature Review

Table 1-1. The equilibrium partial pressure of various metal oxides at 1200 °K (923 °C)[17].

Table 1-2. A comparison of various coating techniques.

Table 1-3. The dependence of the final phase structure in fully annealed Ni-Al composite coatings on the Al content.

Table 1-4. Typical physical and mechanical properties of pure Ni_3Al compound.

Table 1-5. The effect of alloying elements on the oxidation of Ni_3Al, adapted from [99].

Chapter 2. Electrodeposited Ni – Al Composite Coatings with High Al Content via Sediment Co-deposition

Table 2-1. Watt's type nickel bath and typical operating conditions.

Table 2-2. Conditions of diffusion treatment of Ni-Al particles composite coatings.

Table 2-3. The surface coverage at different particle concentration in bath.

Chapter 3. Reactive Oxide-dispersed Ni_3Al Intermetallic Coatings by Sediment Co-deposition

Table 3-1. The composition of plating bath and typical operating conditions.

Table 3-2. The phase information of annealed Ni-Al-REO Coatings.

Chapter 4. Cyclic Oxidation Behavior of Electrodeposited Ni_3Al-CeO2-Based Coatings at 850 °C and 1050 °C

Table 4-1. Characteristics of the five Ni-Al-CeO_2 coatings used in the investigation.

Table 4-2. The XRD results for oxidized coatings at 850 °C after the specified time.

Table 4-3. Some mechanical properties of oxides and the coating matrix.
Table 4-4. The XRD analysis of oxide products on oxidized coating samples.

Chapter 5. On The Improvement of Cyclic-oxidation Resistance of Electrodeposited Ni-Al-Based Intermetallic Coatings at 850 °C

Table 5-1. Ni_3Al base coatings used in the investigation.

Chapter 6. Carburization of Electrodeposited Ni_3Al-CeO2-Based Coatings in 2%CH_4-H_2 Reducing Atmospheres

Table 6-1. Ni_3Al base coatings used in the investigation.
Table 6-2. The XRD analysis of the carburization products at 850 °C.
Table 6-3. The XRD analysis of the carburization products at 1050 °C.
Table 6-4. The dissociation pressures of Cr_2O_3 and Al_2O_3.

Chapter 7. Coke Formation and Metal Dusting of Electroplated Ni_3Al-CeO2-Base Coatings in CO-H_2-H_2O

Table 7-1. Ni_3Al base coatings used in the investigation.
Table 7-2. The oxygen partial pressures in H_2-0.6%H_2O and the dissociation pressures of NiO, Cr_2O_3, and Al_2O_3 at 650 °C and 1100 °C.
Table 7-3. The XRD analysis of the coke formed on the testing samples after 500 hr exposure.

List of Figures

Chapter 1. Introduction and Literature Review

Figure 1-1. The relationship between particle content and current density.

Figure 1-2. The effect of particle loading in plating bath on the particle content in composite coatings.

Figure 1-3. The effect of the cathode position in plating bath on the particle content: (a) vertical; (b) horizontal.

Figure 1-4. The setups of two different electroplating techniques using horizontal cathode: (a) Sediment co-deposition; (b) Barrel plating [36].

Figure 1-5. The five-step mechanism of co-deposition by Celis [78].

Figure 1-6. The force balance on the particle attached to the cathode [83].

Figure 1-7. The unit cell of Ni_3Al crystal with an ordered $L1_2$ structure.

Figure 1-8. The standard free energy change of formation of oxides [98].

Figure 1-9. Typical oxidation mechanisms of metal and alloys.

Figure 1-10. The effects of temperature and Al content on the evolution of oxide scale on Ni-Al alloys: (a) phase diagram; (b) magnified Ni-rich portion [113]. (The shadow area in (a) and (b) represent the critical Al content to form protective Al_2O_3 scale.)

Figure 1-11. The oxidation stages of PM Ni_3Al for the low temperature range [103].

Figure 1-12. The oxidation stages of PM Ni_3Al for the high temperature range [103].

Figure 1-13. Arrhenius plot comparing data of parabolic rate constants k_p for oxidation of Ni_3Al alloys. PM: Power Metallurg, C: Cast, SC: Single crystal, CRA: Cast + Rolled +Annealed [103].

Figure 1-14. The comparison of long-term cyclic oxidation of alloy 800H and alloy 617 with the NiAl 11 alloy (Ni_3Al base alloy) [20].

Figure 1-15. The thermodynamic stability diagram at 1000 °C for the systems of Cr-O-C and Si-O-C [157].

Figure 1-16. Temperature dependence of cyclic carburization of different alloys in CH_4-H_2 (a_c=0.8) [20].

Figure 1-17. Schematic illustration of metal dusting in iron and low alloy steels: (a) surface reaction and carbon transfer; (b) formation of Fe_3C layer; (c) nucleation and growth of graphite into Fe_3C; (d) outward diffusion along graphite and segregation of Fe atom, which catalyzes the coke formation [7,174,178].

Figure 1-18. Schematic metal dusting mechanism chart for ferritic and austentic stainless steels [175].

Chapter 2. Electrodeposited Ni – Al Composite Coatings with High Al Content via Sediment Co-deposition

Figure 2-1 Schematic diagram of sediment co-deposition (SCD) setup.

Figure 2-2. Typical BSE micrographs of SCD Ni-Al composite coating (80 g/l, 10s/1200s): (a) low magnification; (b) high magnification.

Figure 2-3. The effect of current density on the Al content in composite coatings.

Figure 2-4. The effect of particle loading (or particle concentration) on the volume fraction of Al particles in composite coatings: (a) particle loading; (b) particle concentration.

Figure 2-5. The effect of the ratio of Off/On time on Al particle content in composite coatings.

Figure 2-6. The Al particle content in coatings vs the ratio of Off/On time with: (a) fixed On time, 1200s; (b) fixed Off time, 10s.

Figure 2-7. $\frac{C(1-\alpha)}{\alpha}$ vs C at different current density.

Figure 2-8. The morphologies of annealed Ni-Al composite coatings at different conditions: (a) 550 °C, 2 hr; (b) 550 °C, 2 hr +670 °C, 2 hr; (c) 550 °C, 2 hr +670 °C, 2 hr + 800 °C, 3 hr; (d) 800 °C, 3 hr.

Figure 2-9. The XRD patterns of annealed Ni-Al composite coatings under four different conditions of diffusion treatment.

Chapter 3. Reactive Oxide-dispersed Ni_3Al Intermetallic Coatings by Sediment Co-deposition

Figure 3-1. Typical BSE micrographs of Ni-Al binary composite coatings with the 80 g/l Al bath loading: (a) as-plated coating, (b) annealed coating.

Figure 3-2. The X-ray pattern of the annealed Ni-Al composite coating with the 80 g/l Al bath loading.

Figure 3-3. The effect of the REO bath loading on the volume fraction of Al particles in Ni-Al-REO composite coatings.

Figure 3-4. Morphology of Ni-Al-nano CeO_2 composite coatings with 1 g/l nano CeO_2: (a) as-plated, (b) annealed.

Figure 3-5. Morphology of Ni-Al-nano CeO_2 composite coatings with 20 g/l nano CeO_2 : (a) as-plated, (b) annealed.

Figure 3-6. The X-ray patterns of REO phases in the annealed Ni-Al-REO coatings. (a) $CeAlO_3$ phase in the annealed Ni-Al-nano CeO_2 coating with 20 g/l CeO_2. (b) CeO_2 phase in the annealed Ni-Al-5μm CeO_2 coating with 10 g/l CeO_2. (c) Y_2O_3 phase in the annealed Ni-Al-Y_2O_3 (<1μm) coating with 10 g/l Y_2O_3.

Figure 3-7. Typical pictures of Ni-Al-5μm CeO_2 composite coatings with 1 g/l CeO_2 particle loading: (a) as-plated, (b) annealed.

Figure 3-8. Typical pictures of Ni-Al-5μm CeO_2 composite coatings with 10 g/l CeO_2 particle loading: (a) as-plated, (b) annealed.

Figure 3-9. Ni-Al-Y_2O_3 (<1μm) coatings with 1 g/l Y_2O_3: (a) as-plated, (b) annealed.

Figure 3-10. Ni-Al-Y_2O_3 (<1μm) coatings with 10 g/l Y_2O_3: (a) as-plated, (b) annealed.

Figure 3-11. Ni -Y_2O_3 (<1μm) binary composite coatings with 40g/l Y_2O_3.

Chapter 4. Cyclic Oxidation Behavior of Electrodeposited Ni_3Al-CeO_2-Based Coatings at 850 °C and 1050 °C

Figure 4-1. The typical morphologies of annealed Ni-Al and Ni-Al-CeO_2 composite coatings: (a) the pure Ni_3Al coating (80+0); (b) the 80+5 (5 μm) coating.

Figure 4-2. The mass change of CeO_2-modified Ni_3Al coatings during cyclic oxidation at 850 °C: (a) up to 200 hr; (b) up to 1000 hr.

Figure 4-3. The change of oxidation rate component of Ni_3Al-based coatings during cyclic oxidation at 850 °C up to 1000 hr.

Figure 4-4. The surface morphologies of Ni_3Al-based coatings after cyclic oxidation at 850 °C: (a) 80+0 (pure Ni_3Al), 10 hr, 5000×; (b) 80+0 (pure Ni_3Al), 100 hr, 5000×; (c) 80+0 (pure Ni_3Al), 500 hr, 1500×; (d) 80+5 (9-15 nm), 500 hr, 1500×.

Figure 4-5. The cross-sectional images of coatings oxidized at 850 °C: (a) 80+0 (pure Ni_3Al), 100 hr; (b) 80+0 (pure Ni_3Al), 500 hr; (c) 80+5 (5 μm), 500 hr; (d) 80+5 (9-15 nm), 500 hr.

Figure 4-6. The cross-sectional images of coatings oxidized at 850 °C for 1000hr: (a) 80+0 (pure Ni_3Al); (b) 80+5 (5μm); (c) 80+1 (9-15nm); (d) 80+5 (9-15nm).

Figure 4-7. The cross section of the Ni_3Al-based coatings and Fe-Ni-Cr alloy substrate after cyclic oxidation for 500hr: (a) 80+0; (b) 80+5 (5μm).

Figure 4-8. Compositional profile in the pure Ni_3Al coating / Fe-Ni-Cr substrate system after cyclic oxidation at 850 °C.

Figure 4-9. The variation of pore density (vol%) with time and the position of oxidation zone in Ni_3Al based coatings during cyclic oxidation: (a) 80+0 (pure Ni_3Al); (b) 80+5 (5 μm); (c) 80+1 (9-15 nm) (d) 80+5 (9-15 nm).

Figure 4-10. Schematic illustration showing the formation of oxidized channels in porous Ni_3Al-based coatings during cyclic oxidation: (a) Initial stage of Oxidation; (b) Formation of interconnected oxidized channels.

Figure 4-11. Pore density (vol%) as a function of normalized distance to the coating/matrix interface in various Ni_3Al based coatings after cyclic oxidation at 850 °C for 500 hr.

Figure 4-12. The cyclic oxidation results of the pure and the CeO_2-dispersed Ni_3Al coatings after oxidation at 1050 °C for 500 hr.

Figure 4-13. The surface morphology of the pure Ni_3Al coating after oxidation at 1050 °C for 10 hr: (a) a low-magnification view; (b) a high-magnification view.

Figure 4-14. The surface morphology of the pure Ni_3Al coating after oxidation at 1050 °C for 500 hr: (a) a low-magnification view; (b) a high-magnification view.

Figure 4-15. The morphology of Al_2O_3 scale on the pure Ni_3Al coatings after oxidation at 1050 °C for 500 hr: (a) the polished cross section; (b) the fracture surface (low-magnification view); (c) the scale/coating interface; (d) the fractured oxide surface (high-magnification view).

Figure 4-16. The surface morphology of the 80+1 (9-15 nm) coating after oxidation at 1050 °C for 10 hr: (a) a low-magnification view; (b) a high-magnification view.

Figure 4-17. The surface morphology of the 80+1 (9-15 nm) coating after oxidation at 1050 °C for 500 hr: (a) a low-magnification view; (b) a high-magnification view.

Figure 4-18. The morphology of Al_2O_3 scale on the 80+1 (9-15nm) coatings after oxidation at 1050 °C for 500hr: (a) the polished cross section; (b) the fracture surface.

Figure 4-19. The morphology of Al_2O_3 scale on the 80+5 (5 μm) coatings after oxidation at 1050 °C for 500 hr: (a) the polished cross section; (b) the fracture surface.

Figure 4-20. The distribution of CeO_2 particles: (a) in the 80+5 (5 μm) coating (cross-sectional view); (b) in the 80+5 (9-15 nm) coating (plain view).

Figure 4-21. Nano CeO_2 particles in the 80+5 (9-15 nm) coating after oxidation at 1050 °C for 500 hr: (a) Secondary electron image; (b) AES spectrum.

Figure 4-22. The distribution of CeO_2 particles in the oxide scales on the 80+5 (5 μm) coating after oxidation at 1050 °C for 500 hr: (a) in the $NiAl_2O_4$ spinel scale; (b) in the α-Al_2O_3 scale; (c) the AES spectrums of area 1 and area 2 in Fig. 4-22 (b); (d) the AES spectrums of line scan along area 1 in Fig. 4-22 (b).

Figure 4-23. The cross-section morphologies of Ni_3Al base coatings after being cyclically oxidized at 1050 °C: (a) the pure Ni_3Al coating after 10 hr; (b) the pure Ni_3Al coating after 20 hr; (c) the pure Ni_3Al coating after 500 hr; (d) the 80+5 (5 μm) coating after 500 hr.

Figure 4-24. The composition profile of Al in the pure Ni_3Al coating, the 80+1 (5 μm) coating, and the 80+1 (9-15 nm) coating after being cyclically oxidized at 1050 °C for 500 hr.

Chapter 5. On The Improvement of Cyclic-oxidation Resistance of Electrodeposited Ni-Al-Base Intermetallic Coatings at 850 °C

Figure 5-1. The cross-sectional morphologies of pure Ni-Al coatings: (a) 80+0; (b) 80+0-LA.

Figure 5-2. The cross-sectional morphologies of Ni-Al-oxide particle coatings: (a) 80+1-nano; (b) 80+10-nano; (d) 80+5-Y_2O_3.

Figure 5-3. The cyclic-oxidation behaviors of various Ni-Al-based coatings at 850 °C for periods of up to 1000 hr: (a) slowly annealed (b) doped with reactive oxides; (c) with additional electroplated thin film.

Figure 5-4. The cross-sectional morphologies of the 80+0-LA coating after cyclic oxidation at 850 °C: (a) for 100 hr; (b) for 500 hr; (c) for 1000 hr; (d) the 80+0 coating for 1000 hr.

Figure 5-5. The cross-sectional morphologies of coatings after cyclic oxidation at 850 °C for 1000 hr: (a) the 80+10-nano coating; (b) the 80+5-Y_2O_3 coating.

Figure 5-6. The cross-sectional morphology of the 80+10-nano/80+0 coating after cyclic oxidation at 850 °C for 1000 hr.

Chapter 6. Carburization of Electrodeposited Ni_3Al-CeO_2-Based Coatings in 2%CH_4-H_2 Reducing Atmospheres

Figure 6-1. The cyclic-carburization results of the Fe-Ni-Cr alloy and the Ni-Al-based coatings for periods up to 500hr: (a) at 850 °C; (b) at 1050 °C.

Figure 6-2. The cross-sectional morphology of the uncoated Fe-Ni-Cr alloy after carburization for 500 hr: (a) at 850 °C; (b) at 1050 °C.

Figure 6-3. The surface morphology of the pure Ni_3Al coating after carburization at 850 °C for: (a) 10 hr; (b) 500 hr.

Figure 6-4. The cross-sectional morphology of the pure Ni_3Al coating after carburization at 850 °C for 500hr: (a) the coating section; (b) the coating/substrate; interface; (c) the Al_2O_3 scale.

Figure 6-5. The surface morphologies of the pure Ni_3Al coating after carburization at 1050 °C for: (a) 10 hr; (b) 100 hr.

Figure 6-6. The surface morphology of the pure Ni_3Al coating after carburization at 1050 °C for 500 hr: (a) the plain view; (b) EDS analysis of the phase by the indicated by the arrow in (a).

Figure 6-7. The cross section of the pure Ni_3Al coating after carburization at 1050 °C for 500 hr: (a) a low-magnification view; (b) the coating/substrate interface; (c) the severe oxidation zone.

Figure 6-8. The typical morphology of the 80+1 (5mm) coating after carburization at 850 °C for 500 hr: (a) the plain view; (b) the cross sectional view.

Figure 6-9. The surface morphology of the 80+1 (5mm) coating after carburization at 1050 °C for: (a) 10 hr; (b) 100 hr; (c) 500 hr.

Figure 6-10. The cross-section of the 80+1 (5mm) coating after carburization at 1050 °C for 500 hr: (a) a low-magnification view; (b) a high-magnification view.

Figure 6-11. A schematic summary of the cyclic carburization of electrodeposited Ni_3Al base coatings in $2\%CH_4$-H_2 at 850 °C for periods of up to 500 hr.

Figure 6-12. A schematic summary of the cyclic carburization of electrodeposited Ni_3Al base coatings in $2\%CH_4$-H_2 at 1050 °C for periods of up to 500 hr.

Chapter 7. Coke Formation and Metal Dusting of Electroplated Ni_3Al-CeO_2-Based Coatings in CO-H_2-H_2O

Figure 7-1. Cyclic metal dusting behaviors of the Fe-Ni-Cr alloys and Ni_3Al-based coatings at 650 °C for periods of up to 500 hr: (a) without pre-oxidation; (b) with pre-oxidation.

Figure 7-2. The pure Ni_3Al coating (80+0) after metal dusting for 50 hr: (a) the coating surface; (b) EDS analysis of the filaments cluster in (a); (b) EDS analysis of the coating matrix in (a).

Figure 7-3. The surface morphology of the pure Ni_3Al coating (80+0) after metal dusting for 200 hr: (a) at low magnification; (b) at high magnification.

Figure 7-4. The surface morphology of pure Ni_3Al coating (80+0) after metal dusting for 500 hr: (a) the coating surface before the removing of coke; (b) at high magnification; (c) pits on the coating surface after the removing of coke; (d) EDS analysis of the pit area in (c).

Figure 7-5. The cross section of the pure Ni_3Al coating after metal dusting: (a) for 200 hr; (b) for 500 hr; (c) a high-magnification view of the pits in (b); (d) EDS analysis of area 1 in (c); (e) EDS analysis of area 3 in (c).

Figure 7-6. The surface morphology of the 80+5 (5 μm) coating after metal dusting for 50hr: (a) a typical coking region; (b) EDS analysis of the area indicated in (b).

Figure 7-7. The surface morphology of the 80+5 (5 μm) coating after metal dusting for 500 hr: (a) a low-magnification view; (b) a high-magnification view.

Figure 7-8. The surface morphologies (after the removing of coke) of the two 5 μm CeO_2-dispersed Ni_3Al coatings after metal dusting for 500 hr: (a) the 80+5 (5 μm) coating; (b) the 80+1 (5 μm) coating.

Figure 7-9. The cross section of the 80+5 (5 μm) coating after metal dusting for 500 hr: (a) at low-magnification; (b) at high-magnification.

Figure 7-10. The surface morphology of the 80+5 (9-15 nm) coating after metal dusting: (a) a low-magnification view after 50 hr; (b) a high-magnification view after 50 hr; (c) a low-magnification view after 200 hr; (b) a high-magnification view after 200 hr.

Figure 7-11. The surface morphology of the 80+5 (5 μm) coating after metal dusting for 500 hr: (a) before the scraping of coke; (b) after the scraping of coke.

Figure 7-12. The cross section of the 80+5 (9-15 nm) coating after metal dusting for 200 hr: (a) a low-magnification view; (b) a high-magnification view.

Figure 7-13. The cross section of the 80+5 (9-15nm) coating after metal dusting for 500 hr: (a) a low-magnification view; (b) a high-magnification view.

Figure 7-14. Surface morphologies of Ni_3Al-based coatings after pre-oxidation in H_2-0.6%H_2O at 1100 °C for 24 hr: (a) pure Ni_3Al coating; (b) high-

magnification view of the spalled area in (a); (c) the 80+5 (5 μm) coating; (d) the 80+1 (5 μm) coating; (e) the 80+5 (9-15 nm) coating; (f) the 80+1 (9-15 nm) coating.

Figure 7-15. The XPS analysis of the surfaces of pure Ni_3Al coatings: (a) after pre-oxidation; (b) after metal dusting for 50 hr. (The strong peak of O 1s isn't fully showed in both the figures, and some minor impurities, such as Ca, Na, and Si, are not labeled in both figures.)

Figure 7-16. The cross-section view of the pure Ni_3Al coating after pre-oxidation at 1100 °C in H_2-0.6%H_2O for 24 hr: (a) the cross section of coating, (b) the oxide layer induced by the pretreatment.

Figure 7-17. The surface morphology of the pre-oxidized pure Ni_3Al coating after metal dusting for 50 hr: (a) the low-magnification view; (b) the high-magnification view showing the formation of catalytic coke.

Figure 7-18. The coke on the pre-oxidized pure Ni_3Al coating after metal dusting for 200 hr: (a) the low-magnification view; (b) the high-magnification view.

Figure 7-19. The surface morphology of the pre-oxidized pure Ni_3Al coating after metal dusting for 500 hr: (a) the massive coke on the coating surface; (b) the high-magnification view of the coke.

Figure 7-20. The surface morphology of the pre-oxidized pure Ni_3Al coating after metal dusting for 500 hr (after the scraping of coke): (a) the severe pitting on the coating surface; (b) the EDS analysis of the pitting area.

Figure 7-21. The cross section of the pre-oxidized pure Ni_3Al coating after metal dusting for 200 hr: (a) the low-magnification view; (b) the high-magnification view of a typical pit.

Figure 7-22. The cross section of the pre-oxidized pure Ni_3Al coating after metal dusting for 500 hr: (a) the low-magnification view; (b) the high-magnification view of a typical pit; (c) the pit/the coating matrix interface in (b); (d) the view of the area without pitting.

Figure 7-23. The surface morphologies of the pre-oxidized 5 μm CeO_2-dispersed Ni_3Al coatings after metal dusting for 500 hr: (a) the 80+5 (5 μm) coating; (b)

the 80+5 (5 μm) coating after the removing of coke; (c) the 80+1 (5 μm) coating; (d) the 80+1 (5 μm) coating after the coke deposits were scraped.

Figure 7-24. The cross section of the pre-oxidized 80+5 (5 μm) coating after metal dusting for 500 hr: (a) at low magnification; (b) at high magnification.

Figure 7-25. The surface morphology of the pre-oxidized 80+5 (9-15 nm) coating after metal dusting for 200hr: (a) at low magnification; (b) at high magnification.

Figure 7-26. The surface morphologies of pre-oxidized nano CeO_2-dispersed Ni_3Al coatings after metal dusting for 500 hr: (a) the 80+5 (9-15 nm) coating; (b) the 80+5 (9-15 nm) coating after the removing of coke; (c) the 80+1 (9-15 nm) coating; (d) the 80+1 (9-15 nm) coating after the removing of coke.

Figure 7-27. The cross section of the pre-oxidized 80+5 (9-15 nm) coating after metal dusting for 500 hr: (a) at low magnification; (b) at high magnification.

Figure 7-28. Backscattered Electron Micrographs showing the cross-sectional morphologies of the CeO_2-dispersed Ni_3Al coatings: (a) the 80+1 (5 μm) coating; (b) the 80+5 (5 μm) coating. (c) the 80+1 (9-15 nm) coating; (d) the 80+5 (9-15 nm) coating.

List of Abbreviations

Auger Electron Spectroscopy:	AES
Backscattered Electron:	BSE
Cetyltrimethyl Ammonium Hydrogen Sulfate:	CTAHS
Cetylpyridinium Chloride:	CPC
Chemical Vapor Deposition:	CVD
Conventional Electrodeposition:	CED
Electron Probe Microanalysis:	EPMA
Energy Dispersive Spectroscopy:	EDS
Internal-oxidation Zone:	IOZ
Physical Vapor Deposition:	PVD
Reactive Elements:	REs
Reactive Element Effect:	REE
Reactive Oxides:	REOs
Rotating Cylinder Electrode:	RCE
Rotating Disc Electrode:	RDE
Scanning Electron Microscope:	SEM
Secondary Electron:	SE
Sediment Co-deposition:	SCD
Self-propagating High-temperature Synthesis:	SHS
Sodium Dodecyl Sulphate:	SDS
Wavelength Dispersive Spectroscopy:	WDS
X-ray Diffraction:	XRD
X-ray Photoelectron Spectroscopy:	XPS

Chapter 1

Introduction and Literature Review

1.1 Introduction

1.1.1 High-temperature Corrosion and Protection

Fe-based or Ni-based chromia-forming tube alloys have been used widely in modern metallurgical, petrochemical, and energy conversion industries, where high temperature degradations such as oxidization, carburization, and metal dusting have become more challenging due to a demand for higher operating temperatures. The resultant oxidation and carburization cause either a direct waste of the metals or a severe deterioration of their properties [1-7]. A typical example of such high temperature degradation is the case of cracking tubes used in ethylene production furnaces. Unavoidable coke formation and carburization are the main causes of premature failure of Fe-Cr-Ni tubes. Due to these two factors, normal operation must be interrupted every 20-60 days, and a decoking process involving oxidizing atmospheres is used to remove the coke [2]. The ethylene industry was estimated to lose $2 billion in production annually due to this periodic interruption [8].

To control high-temperature corrosion, one may use alloys with more Ni and Cr [4, 9, 10] or alloys containing Al or Si [4, 7, 10]. An increase of Cr content facilitates the formation of Cr_2O_3 scale. However, Cr_2O_3 is unstable above 1050 °C [3, 5, 6, 11, 12]. Alloying with large amounts of Ni and Cr is also prohibited due to cost of materials. Addition of Al or Si can improve the oxidation and carburization resistance of the alloys by forming Al_2O_3 or SiO_2 scale beneath Cr_2O_3. Unfortunately, addition of more than 2wt% Al or Si reduces the ductility and weldability of alloys [10], yet a minimum of 4wt% of Al or Si is required to form a continuous external protective scale [1, 6, 13]. An alternative solution is to apply surface coatings on alloys. Surface coatings act as barriers to oxidation and carburization attacks, while base alloys retain excellent mechanical properties. Under the circumstances, the low-grade tube alloys can still be used. Surface coatings have attracted great attention, and have frequently proven to be effective in resisting the problems of oxidation, carburization, and other high-temperature corrosions [10, 14-16].

1.1.2 Surface Coating Systems

1.1.2.1 Coating Materials

Chromia, silica or alumina-forming alloys are suitable coating materials for high-temperature protection. Of these, alumina-forming alloys have received most attention. One advantage of Al_2O_3 scale is that it can be formed at extremely low oxygen partial pressure, 10^{-37} atm, as shown in Table 1 [17] (most petrochemical environments have a typical oxygen partial pressure ranging from 10^{-25} to 10^{-30} atm). Unlike Cr_2O_3, Al_2O_3 is thermodynamically stable up to its melting point, 2327 °K, without significant evaporation [17, 18].

Table 1-1. The equilibrium partial pressure of various metal oxides at 1200 °K (923 °C) [17].

Oxide	$\log p_{O_2} / p^0_{O_2}$
2/3 Al_2O_3	-37.6
2/3Cr_2O_3	-24.0
2NiO	-11.5
1/2Fe_3O_4	-15.9
2/3Fe_2O_3	-7.4

Of the many conventional coating systems, Al-Si, Al-Cr-Si, or Cr-Si metallic coatings formed by diffusion or chemical vapor deposition (CVD) and physical vapor deposition (PVD) have superior oxidation and carburization resistances [10, 14-16, 19]. The current trend is to develop Ni_3Al or NiAl intermetallics as the novel protective coatings. The limited research conducted has shown that these aluminides have superior resistance to oxidation and carburization [17, 20, 21]. The excellent oxidation and carburization performances of Al-Si and Al-Cr-Si coatings relates to the formation of Ni-Al intermetallic phases.

1.1.2.2 Coating Technology

Current methods of producing aluminide coatings include diffusion, physical vapor deposition (PVD), chemical vapor deposition (CVD), and thermal spray. Characteristics of these coating methods are summarized in Table 1-2. Diffusion (e.g.,

pack cementation) is a traditional coating process. Aluminizing a nickel or iron-based alloy is the simplest way to prepare Ni-Al or Fe-Al intermetallic coatings [22-24]. However, this process changes the surface composition and mechanical properties of the substrate. Consequently, diffusion aluminide coatings have inherent brittleness and poor thermal stability. PVD and CVD can apply dense layers with different compositions and properties on substrates without modifying the composition of those substrates. The main obstacle to PVD and CVD is the high cost caused by the use of expensive instruments and the complex processes involved. Thermal spray can deposit any material capable of melting without decomposing, and can produce exceptionally thick coatings. However, porosities of 2-20%, is common in thermal spray coatings. This, plus the undesirable oxide network and the poor bonding strength, limits their application [25].

Table 1-2. A comparison of various coating techniques.

	Temperature	Porosity	Bonding	Cost	Rate
Diffusion	E: <1100 °C S: <1100 °C	Low	Excellent	Medium	L or M
PVD	E: <1000 °C S: <200 °C	Free	Good	High	L or M
CVD	E: <1000 °C S: <200 °C	Free	Good	High	L or M
Thermal spray	E: 2000~30000°C S: 50~160 °C	High, 2~20vol%	Good	Medium	VH
Electro-deposition	E: <100 °C S: <100 °C	Free	Poor	Low	M or H

E: environment; S: substrate; M: medium; L: low; H: high; VH: very high.

The current trend is to use conventional electrodeposition (CED) to prepare nickel aluminide coatings. This is a two-step process consisting of (1) the electrodeposition of metal matrix (e.g., Ni) / metal particles (e.g., Al) composites, and (2) diffusion treatment to form alloy coatings containing Ni-Al intermetallic phases. The CED technique is low-cost compared to other coating techniques. Other advantages are that it can be conducted

at room temperature and on large surface areas. It is especially useful when coating metallic components that have complex shapes and variable dimensions.

This investigation focused on developing Ni_3Al-based high-temperature coatings, using the cost-effective electrodeposition technique, that are to be applied to commercial Fe-Ni-Cr tube alloys for preventing oxidation and carburization in typical ethylene production environments. In the next section, the literature pertinent to this investigation will be reviewed.

1.2 Literature Review

1.2.1 Electrodeposition of Ni-Al-Based Composite Coatings

1.2.1.1 Electrodeposited Composite Coatings

Electrodeposition is widely used to deposit Ni, Cr, Zn, and Cu onto various substrates for the purpose of decoration, wear resistance, and corrosion resistance. The basic principle underlying co-deposition of metal matrix / particle composites is similar to that of conventional electrodeposition. The main difference is that particles are added and suspended in plating solution by agitation. During deposition, particles first are transferred to the cathode surface under agitation. The interaction results in the entrapment of particles in the cathode surface. The electro-co-deposition is initially developed to produce metal matrix / ceramic particles composite coatings. A dispersion of hard ceramic particles, such as SiC, WC, TiO_2, Al_2O_3, SiO_2, and diamond, can strengthen metallic coatings through enhanced resistance to wear [26-29]. Solid lubricant particles such as PTFE and graphite are also employed to produce self-lubricated composite coatings [28, 30, 31].

Electrodeposition of metal matrix / metal particle composites (EMMC) was attempted as early as the 1960's [32]. In 1972, Bazzard et al. [32, 33] studied the feasibility of depositing Ni-Cr particle composite coatings from a nickel sulfamate bath, and reported that Ni-Cr alloys can be formed after annealing the composites at temperatures between 800 °C and 1050 °C. Cameron et al. [34, 35] electrodeposited Co-

Cr_3C_2 particle composites in 1979. Their results showed that a pre-heat treatment at 1000 °C in argon could form a Co-Cr alloy. Foster et al. [36], Honey et al. [37], and Saremi et al. [38] successfully applied Ni (or Co)-CrAlY particle composites onto gas turbines, forming MCrAlY-type high-temperature coatings. Systems such as Ni-Zr and Ni-Ti were also explored [39-41]. Recently, Zhang et al. [42] reported Ni-nano Cr particle composite films.

In recent years, Ni-Al particle systems have emerged as one of the most popular EMMCs. Izaki et al. [43] were the first to conducted the co-deposition of Ni-Al composites from a Watt's type nickel bath with 9μm Al particles suspended. Composites with 5~23mol% Al were obtained. After annealing treatment at 800 °C for 3 hr in vacuum, Ni-Al alloy films containing γ'-Ni_3Al intermetallic phases were formed. Susan et al. [44, 45] and Barmak et al. [46] reported Ni-Al composite coatings with as much as 20vol% of Al particles from a nickel sulphamate bath. The heat treatment at 825 °C for 3 hr in a vacuum yielded a two-phase, γ-Ni + γ'-Ni_3Al, alloy coating [45]. Recently, Napłoszek-Bilnik et al. [47, 48] produced Ni-Al and Ni-Al-Ti composites containing 4-44wt% Al particles. Ni-28wt% nano Al composite coatings were also obtained by Zhou et al. [49].

1.2.1.2 Formation of Ni-Al Intermetallic Coatings

Ni-Al alloy coatings result from a diffusion reaction between Al particles and a Ni matrix during annealing treatment [43, 45, 47]. The phase development depends strongly on annealing temperature and time. Susan [45] summarized that most Al particles in Ni-Al coatings remained unreacted at low annealing temperatures (400-450 °C) for a short time. If annealing time was increased, Al-rich intermetallic phases such as $NiAl_3$, Ni_2Al_3, and NiAl occurred. At temperatures of 500-530 °C, the NiAl phase dominated. Above 600 °C, the diffusion reaction became rapid. The final phase structure after full annealing, however, is controlled by the Al content in Ni-Al coatings [43]. Table 1-3 provides the dependence of the final phase structure on the Al content based on the equilibrium Ni-Al binary diagram at 300 °K [43, 50]. According to Table 1-3, to obtain alloy coatings containing intermetallic phases, the Al content must be no less than 10at% (14.5vol%).

Recent studies have shown that electrodeposited Ni-Al coatings with low Al content have satisfied long-term oxidation resistance at temperatures below 900 °C [43, 51, 52]. However, to achieve a high oxidation resistance above 900 °C, higher Al content is required to form single-phase γ'-Ni_3Al or β-NiAl intermetallic coatings. Consequently, deposition variables should be optimized to yield as many Al particles in the coating as possible.

Table 1-3. The dependence of the final phase structure in fully annealed Ni-Al composite coatings on the Al content.

Al content	≤10at% (14.5vol%)	10~22at% (14.5~30vol%)	22~28at% (30~37vol%)
Phase	γ-Ni	γ-Ni + γ'-Ni_3Al	γ'-Ni_3Al

1.2.1.3 Factors Affecting Particle Content

(a) Current Density

Current density—a critical parameter in electroplating—may have an influence on the deposition efficiency or the deposition of metal coating. The latter is generally proportional to the current density. The effect of current density on particle deposition, however, depends strongly on the nature of the particles in question [53, 54]. Three typical relationships between particle content and current density have been identified thus (Fig. 1-1).

The relationship designated Type 1 is commonly observed in Cu-Al_2O_3 [54-57], Cu-SiO_2 [58], Ni-Al_2O_3 [46, 59], Co-Ni-Al_2O_3 [60], and Zn-polystyrene [30]. The amount of co-deposited particles reaches a maximum value at low current densities, typically 10-20 mA/cm^2, and decreases with a further increase of current density. The Type 3 relationship has multiple peaks of particle incorporation with current density, manifested in Ni-SiC [54] and Co-Cr_3C_2 [53]. Type 2 describes a monotonic dependence of particle content on current density. This characteristic has been reported in conducting

particle systems such as Ni-Cr [32], Ni-CrAlY [36], Ni-Al [44, 46-48], Ni-Ti [47, 48] and Cr-graphite [61], and inert particle systems like Cu-P [62] and Ni-WC [63].

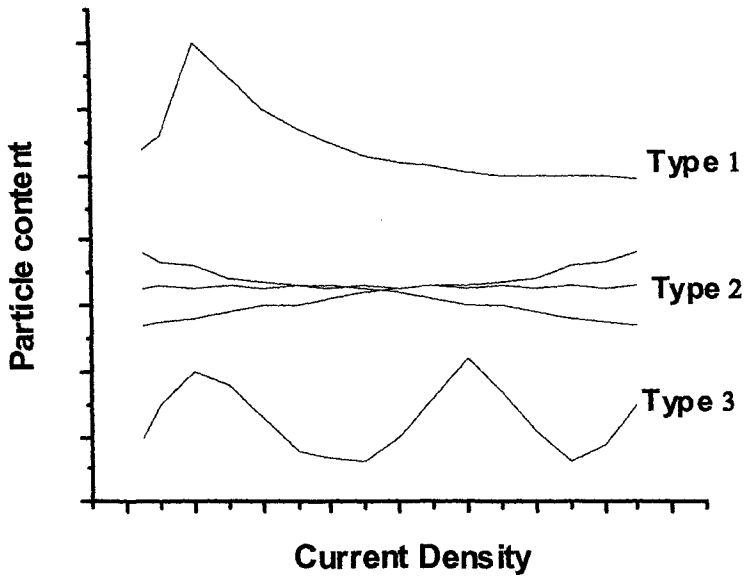

Figure 1-1. The relationship between particle content and current density.

However, the three typical relationships outlined above may not be general, for many results are inconsistent with the generalization shown in Fig. 1-1. For example, Müller [64] reported that the deposition of SiC particles in ZnNi-SiC system is consistent with the Type 1 relationship but not Type 2. A recent studies reported that Al particle content and Ti particle content in composites increased with current density [47], which differed from observations where the metal particle content was insensitive to current density [32, 36, 44, 46]. Despite its complexity, current density should be selected with a combined consideration of the deposition efficiency and the particle content. Current density too high or too low should be avoided.

(b) Particle Loading

Particle loading is the dominant factor affecting the particle content in the composite coatings. The relationship between the particle content and the particle loading resembles the well-know Langmuir isothermal adsorption curve [65]. According to Fig. 1-2, the particle content in the composite coatings rapidly increases with the particle

loading in the plating bath at the initial stage, but levels off with a further increase of the particle content. This behavior has been consistently observed in various particle systems, regardless of the particle nature [26, 29, 30, 34, 36, 44-47, 55, 60].

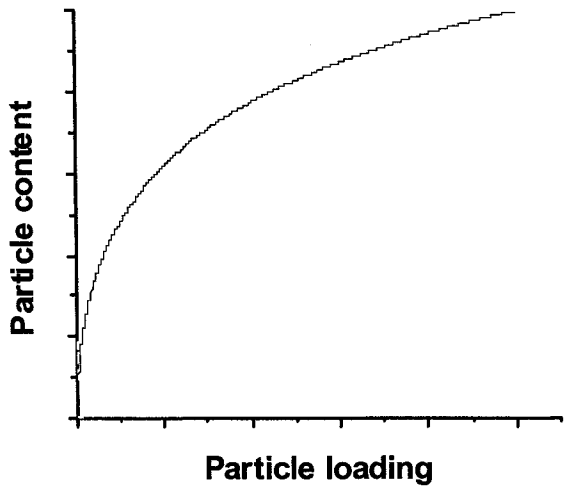

Figure 1-2. The effect of particle loading in plating bath on the particle content in composite coatings.

(c) Agitation

Many agitation methods have been proposed. These include plating pumping [55], air bubble pumping [34, 66], vibratory agitation [67], rotating disc electrode (RDE) [26], rotating cylinder electrode (RCE) [30, 57], magnetic agitation [26, 68], and mechanical stirring [44-46]. The functions of agitation are to suspend particles homogeneously in a plating bath, avoid the agglomeration of particles and transport particles to the cathode surface [69]. A number of researchers [26, 30, 60, 63, 70-73] found that the particle content would reach a maximum and decrease value as the agitation rate was raised continuously. Violent agitation eventually led to a decrease of particle content by sweeping particles away from the cathode surface. The optimum agitation rate will, however, depend on the individual agitation method and the resultant flow condition.

(d) Surfactant

Although oxides, carbides, graphite, metals, and polymers have been co-deposited, the particle content is very low (1-10vol%) [57] if the plating bath is free of surfactants. The carbides, the graphite, and the polymers are hydrophobic. The susceptibility to agglomeration and sediment in the plating bath significantly reduces the co-deposition of particles. Addition of surfactants can improve the stability of the suspension of particles in a bath, and thus the amount of co-deposited particles. It was reported that as high as 70vol% PTFE particles could be deposited in Ni-PTFE composites with an addition of cationic and nonionic surfactants [69]. Up to 50vol% of SiC and diamond particles were obtained with the aid of similar surfactants [69]. Metal particles and their oxides, however, are hydrophilic in an aqueous solution. The developed hydration force makes it difficult for particles to approach the electrodes. Cationic surfactants such as cetyltrimethyl ammonium hydrogen sulfate (CTAHS) and cetylpyridinium chloride (CPC), or anionic surfactants like sodium dodecyl sulphate (SDS), are always used to modify surfaces of these particles and to promote co-deposition. It has been reported that Al_2O_3 content in Ni-Al_2O_3 composite coatings deposited with surfactants can be 5 times higher than that without surfactants [69]. Surfactants can also act as wetting agents and provide particles with the same surface charge. A repulsive force among the charged particles is helpful to disperse particles in the bath, especially for nano particles [74]. Cationic surfactants can develop a positive surface charge on the particles, which are attracted by the negatively charged cathode.

However, surfactants should be used with caution. Excessive surfactants can reduce cathode efficiency, and lead to brittle and stressed deposits due to the trapping of residual surfactants in the composites [69, 75]. In practice, the amount of surfactants should be kept at a very low level, e.g., less than 0.5g/l.

(e) Cathode Position

As shown in Fig. 1-3 (a), for conventional electrodeposition (CED), the cathode is always positioned vertically. Shielding by previously-adsorbed particles, which may prevent other particles from entering the gap among adsorbed particles, is one disvantage of a vertical cathode. The particle content with the CED technique has an upper limit of

30vol% [36]. Susan [45] had reported that only 20vol% Al particle content could be achieved even with an Al particle loading of as high as 400 g/L.

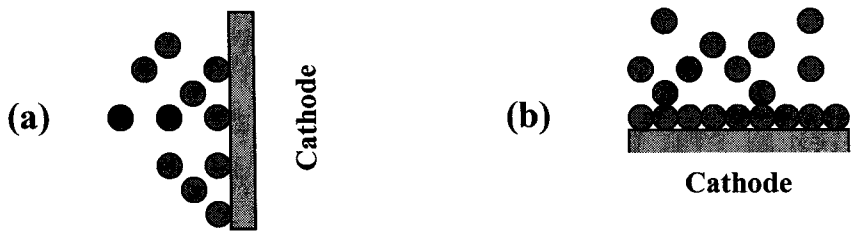

Figure 1-3. The effect of the cathode position in plating bath on the particle content: (a) vertical; (b) horizontal.

The optimal way to enhance the entrapment of particles is to employ a horizontal cathode, as shown in Fig. 1-3 (b). Particles can settle on the cathode surface more easily owing to the gravity. This can minimize the shielding effect and allow more particles to be incorporated. Based on this principle, two related processes—the sediment co-deposition (SCD) and the barrel plating—have been developed (Fig. 1-4 (a) and (b) respectively).

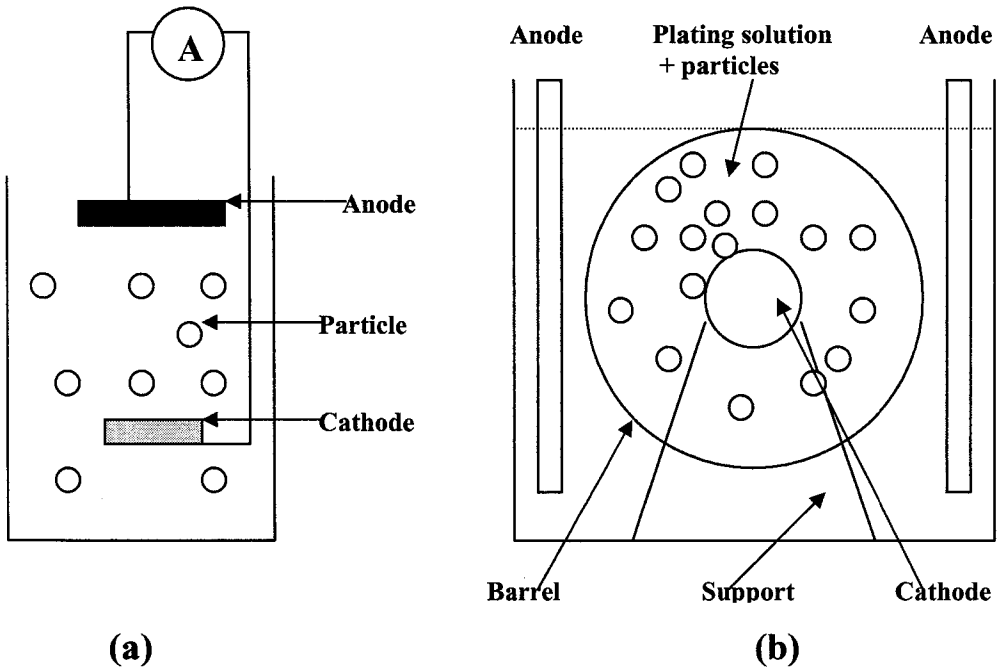

Figure 1-4. The setups of two different electroplating techniques using horizontal cathode: (a) Sediment co-deposition; (b) Barrel plating [36].

In the sediment co-deposition (Fig. 1-4 (a)), the cathode is set horizontally beneath the anode. Periodic stirring keeps particles suspended in the bath or attached to sediment on the cathode. A maximum of 50vol% particle content was obtained for Ni-graphite [76] and Ni-WS_2 [77], and 45vol% for Ni-MoS_2 [77] via SCD with a particle loading of less than 50g/l. Recent work by Napłoszek-Bilnik et al. [47, 48] resulted in Ni-Ti and Ni-Al composite coatings containing maximum 68wt% Ti particle and 44wt% Al particle respectively.

Foster et al. [36] and Honey et al. [37] had proposed a barrel plating technique to co-deposit Ni-CrAlY composite coatings. The cathode and particles are held in a semi-permeable membrane barrel (Fig. 1-4 (b) [36]), through which only current and plating solution can pass. The cathode and the barrel rotate at the same rate. Particles stay suspended in the bath, but do settle on the cathode due to barrel rotation. As a result, particles can be utilized with little wastage, something not possible for other plating processes. A bath loading as low as 10 g/L can result in maximum particle content of 40vol% in the composite coatings [36, 37]. However, because it requires special equipment and processes, barrel plating is more complex than sediment co-deposition.

1.2.1.4 Co-deposition Mechanism

In 1968, Saifullin et al. [69] proposed the first mechanical-entrapment model to predict the particle content. It was assumed that particles were delivered to the cathode surface by agitation and mechanically entrapped by the metal matrix coating. This model, however, was criticized because the entrapment of particles was more likely to be an electrophoretic or electrochemical step [55, 65, 69, 78, 79]. Bazzard et al. [32] gave a simple mathematical expression for the co-deposition of Cr particles in a Ni matrix. They believe that only those particles with a sufficiently low velocity and enough "residence" time on the cathode could be incorporated in a Ni matrix after colliding with the cathode under agitation. This model has not been found to be an effective tool to predict the particle content, as it omitted important parameters such as pH, temperature and bath compositions [78].

(a) Guglielmi Model

In 1972, Guglielmi [65] built a two-step adsorption mathematical model. The similarity between the relationship of the particle content to the particle loading and the Langmuir isothermal adsorption curve (Fig. 1-3) led Guglielmi to propose two adsorption steps, loose adsorption and strong adsorption, through which particles could be incorporated in the coatings. Particles covered by ions and solvent molecules firstly approached the cathode surface, and then became loosely adsorbed by the cathode with relatively high surface coverage. This was a physical or electrophoretic step. The second step had an electrochemical characteristic. Thin layers of ions and molecules on particles were removed under the electrical field. Particles were then strongly adsorbed by the cathode. Guglielmi [65] mathematically expressed the model as following:

$$\frac{C}{\alpha} = \frac{M i_0^{B/A}}{nF\rho_m \upsilon_0} i^{(1-B/A)} \left(\frac{1}{K} + C\right) \tag{1-1}$$

$$\sigma = \frac{KC}{1+KC}(1-\theta) \tag{1-2}$$

where α *is the volume percent of particle in coating,* C *the volume percent of particle in bath,* M *the atomic weight of deposited metal,* n *the valence of deposited metal,* F *the Faraday's constant,* ρ_m *the density of deposited metal,* υ_0 *and* B *the constants related to the particle deposition,* i_0 *and* A *the constants related to the metal deposition,* K *the adsorption coefficient,* i *the current density,* σ *the loose adsorption coverage, and* θ *the strong adsorption coverage which can be equal to* α. This model provides a direct link between the particle content and the particle concentration and current density in the bath. The Guglielmi model has been verified in various composite systems where particle content has a monotone dependence on current density, including Cu-Al_2O_3 [55], Ni-TiO_2 [65], Ni-SiC [29, 65, 80], Cr-C [61], Ag-Al_2O_3 [70], Cu-SiC [69], Cu-P [62], and Ni-PTFE [81].

A disadvantage of this model is that, because the constants such as K, υ_0, and B/A must be predetermined by fitting experiment results, it cannot predict the particle content for a specific composite system. Another limit is that it cannot explain Type 1 and Type 3 relationships (Fig. 1-1). It also cannot clearly show how agitation, pH, temperature, and bath constituents affect particle content. In spite of these limitations,

this model firstly provides a direct view into the complicated co-deposition of the particles and thus becomes the theoretical basis for the development of new co-deposition models.

(b) Celis Model

Celis et al. [78] modified the Guglielmi model and proposed a five-step mechanism of co-deposition. As shown in Fig. 1-5, particles firstly adsorb metal ions in the plating bath. Particles are then moved towards the hydrodynamic boundary layer by forced convection. In the third step, particles diffuse through the diffusion layer and approach the cathode surface. The last two steps are similar to the Guglielmi model, loose adsorption and strong adsorption. One assumption of this model is that a certain amount of adsorbed ions on the particle surface must be reduced at the cathode for the strong adsorption step to occur.

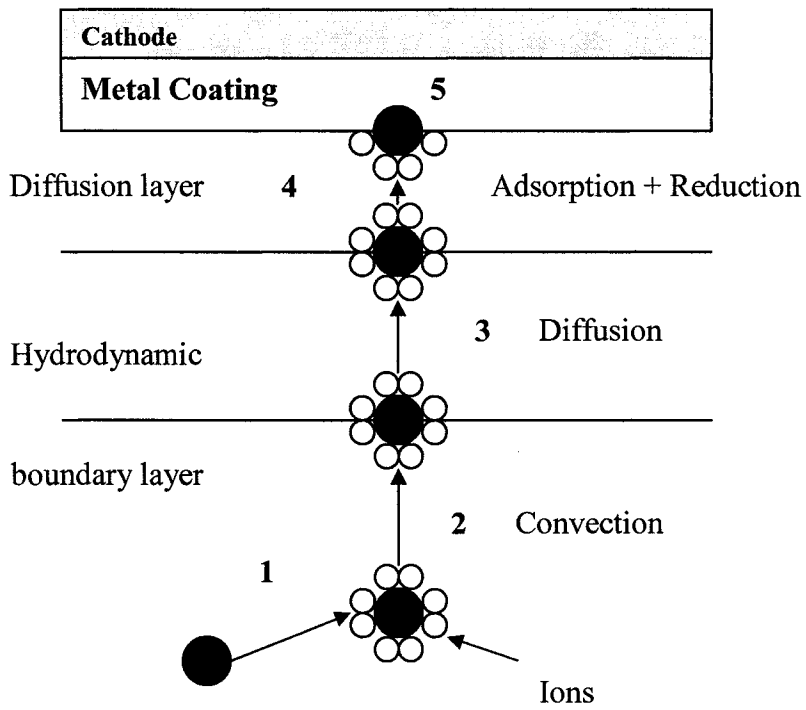

Figure 1-5. The five-step mechanism of co-deposition by Celis [78].

This model— which takes into account current density and particle bath loading as well as agitation, particle size, bath constituents, and hydrodynamic condition—results in a mathematical formula [78]:

$$w(\%) = \frac{W_p N_p P}{\frac{M_m i}{mF} + W_p N_p P} \times 100 \tag{1-3}$$

$$P = HP_{(\kappa/K,i)} \tag{1-4}$$

$$N_p = N_m \frac{C_p^*}{C_m^*} (\frac{i_{tr}}{i})^{\alpha} \tag{1-5}$$

where w *is the weight percent of particle in composite coating;* W_p *is the weight of one particle;* M_m *is the atomic weight of deposited metal,* n *the valence of deposited metal,* i *the current density, and* F *Faraday's constant;* P *is the co-deposition chance of a particle,* $P_{(\kappa/K,i)}$ *the probability of at least* κ *out of* K *adsorbed ions to be reduced;* H *is the agitation factor,* $H = 1$ *under laminar flow,* $0 < H < 1$ *under transition flow, and* $H = 0$ *under turbulent flow;* N_p *is the number of particles passing through the diffusion layer per unit time and area,* N_m *the number of ions crossing the diffusion layer per unit time and area;* C_p^* *and* C_m^* *are the number of particles and the number of ions in the bath, respectively;* i_{tr} *is the transition current density from charge transfer to concentration overvoltage control,* $\alpha = 0$ *under charge transfer control and* $\alpha \neq 0$ *under concentration overvoltage control.*

The application of the Celis model to the co-deposition of Cu-Al_2O_3 and Au-Al_2O_3 with the rotating disc electrode (RDE) has been successful [55, 78]. According to the model, Type 1 behavior in Cu-Al_2O_3 can be well explained. When current density, i, is less than the transition current density, i_{tr}, the co-deposition of particles is under the charge-transfer overvoltage control, and the reduction of adsorbed ions is the rate-limiting step. The particle content thus increases with increasing current density. If $i > i_{tr}$, the co-deposition of particles is under the control of concentration overvoltage. The diffusion of ions becomes rate-determined. Because adsorbed ions diffuse more slowly than free ions, a further increase of current density leads to decreased particle

incorporation in the composite coatings. As for Type 3 behavior in Au-Al_2O_3 system, Celis believed that there exist several i_{tr} values, which cause multiple maximum peaks of particle content.

As in the Guglielmi model, the Celis model cannot predict the particle content of a particular system without predetermining factors such as κ, K and α by fitting experimental data. The transition at i_{tr} from charge-transfer control to concentration control is still doubtful [69].

(c) Trajectory Model

In 1987, Valdes [82] developed a theoretical model for the co-deposition of particles with a RDE (Rotating Disc Electrode), which first considered possible forces on particles during transportation. Based on the Valdes model, Fransaer et al. [83] built a more precise trajectory model to describe the co-deposition of particles with a RDE. This model takes into account the flow field around the cathode and the force balance on an individual particle. As shown in Fig. 1-6 [83], forces acting on a particle can be simplified to the hydrodynamic shearing force, F_{shear} (due to various shear flows), the hydrodynamic force, F_{stagn} (owing to the stagnation point flow), the friction force, $F_{friction}$, and the adhesion force, F_{adh}. These forces can be calculated using a set of complex fluid equations. A critical shear force required to remove a particle can be related to $\kappa(F_{adh}+F_{stagn})$ according to classic friction theory, where κ is the friction coefficient. The probability of a particle remaining on the cathode would depend on the ratio of $\kappa(F_{adh}+F_{stagn})$ to the removing shear force, F_{shear}, and thus the fraction of incorporated particles could be predicted. This trajectory model predicted, with precision, the effect of particle loading on the co-deposition of particles in Cu-polystyrene. Unfortunately, this model cannot predict Type 1 behavior of current density. Fransaer proposed that a repulsive hydration force might exist, and that it would become minimal with decreasing electric field at the cathode, resulting in a peak of particle incorporation at low current density. The hydration force could also explain the effect of other parameters, such as particle type and surfactant.

By including hydrodynamic factors, the trajectory model provides a much better theoretical description of the co-deposition of particles than previous models. However, to date the validity of this model has been verified only in Cu-polystyrene and Zn-polystyrene systems [30, 83], and the existence of the hydration force hasn't yet been confirmed.

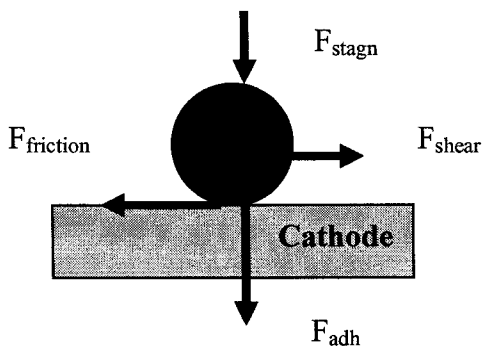

Figure 1-6. The force balance on the particle attached to the cathode [83].

(d) Co-deposition of Metal Particles

As mentioned in Section 2.1.3.1, the co-deposition of metal particles and other conducting particles is minimally affected by current density, which is different from the case with inert particles. Narayan et al. [61] found that the deposition rate of C particles (the constant B) was equal to the deposition rate of Cr matrix (the constant A) regardless of the change of current density using the Guglielmi model. This unique behavior, however, isn't completely understood. Bazzard et al. [32] had previously observed the formation of out-growing dendrites on Ni-Cr composite coatings, but not on Ni-SiO_2 composites. Based on results of polarization and conductivity measurements in a plating bath, they postulated that conducting Cr particles caused a local rise of electric field around the cathode surface, which facilitates the incorporation of Cr particles into the cathode. Deposited Cr particles act as new cathode surfaces, thereby becoming preferential deposition sites for other Cr particles and resulting in the dendrite deposits. The non-conducting SiO_2 particles may only slightly change the electric field around the cathode. The deposited SiO_2 particles cannot be the preferential sites for other particles due to the non-conducting nature so that SiO_2 particles will homogenously deposit on

cathode surface. The rough surface of coatings containing conducting particles was also confirmed by Foster et al. [53] for Co-Cr_3C_2 and Stankovic et al. [54] for Cu-C. Watson et al. [84, 85] reported that, unlike SiC particles, Cr particles can catalyze the deposition of Ni^{2+}.

1.2.2 Physical and Mechanical Properties of Ni_3Al

γ'-Ni_3Al is one nickel-based intermetallic compound with a highly ordered cubic crystal structure, and belongs to the space group of Pm3m (also designated as $L1_2$ structure). The ordered $L1_2$ structure of Ni_3Al can be retained up to its melting point, 1395 °C [86]. Fig. 1-7 shows the unit cell of Ni_3Al, where Al atoms occupy all corners, and Ni atoms locate at 6 face-centered sites. The lattice parameter of Ni_3Al is about 0.357nm, which can be altered by an addition of alloying elements [86, 87]. According to the Ni-Al equilibrium phase diagram [88], Ni_3Al has a very narrow stoichiometry range of Al content (e.g., 24~27at% of Al for single γ'-Ni_3Al phase at 400 °C).

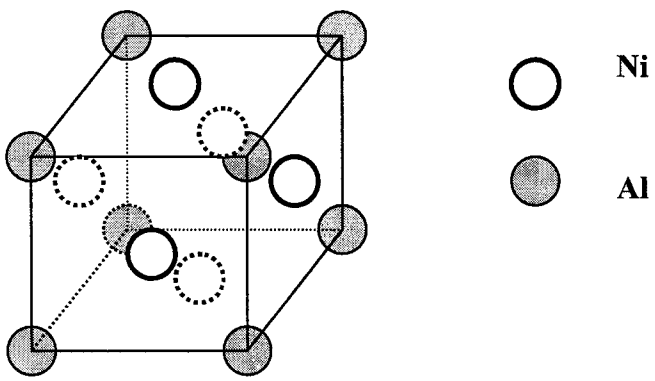

Figure 1-7. The unit cell of Ni_3Al crystal with an ordered $L1_2$ structure.

Typical physical and mechanical properties of pure Ni_3Al are summarized in Table 1-4 [87, 89, 90]. Ni_3Al shows strong characteristics of the metallic bonding along with excellent thermal and electrical conductivities, and has a large thermal expansion coefficient. A unique advantage of Ni_3Al-based alloys is its abnormal increase in strength with increasing temperature up to about 800 °C [91-93]. In contrast, commercial Ni-based superalloys experience a continuous decrease of strength. Furthermore, the density of Ni_3Al is only three-quarters of that of Ni-based superalloys [91]. The fatigue resistance

and the creep resistance of Ni_3Al are also superior to those of Ni-based superalloys even at 800~1000 °C [91-94]. Unfortunately, a major disadvantage of Ni_3Al as a structure material is its brittleness at room temperature. As shown in Table 1-4, the ductility of pure Ni_3Al is only around 2%. Recent studies have indicated that the brittleness of Ni_3Al might result from external hydrogen embrittlement [92], where the segregation of hydrogen from the moisture at Ni_3Al grain boundaries is severely weakened. It was reported that a minor addition of B could substantially enhance the ductility of Ni_3Al. As much as 40-50% total elongation had been achieved with 0.04wt% B [95, 96]. This breakthrough led to a quick development of commercial Ni_3Al-based alloys at the Oak Ridge National Lab, alloys that are designated as IC series alloyed with B and other elements such as Cr, Zr, Mo and Si. Alloying elements offer Ni_3Al-based alloys the excellent combination of mechanical properties and high temperature resistances. Applications of Ni_3Al-based alloys to date include heat-treating trays, furnace rolls, radiant burner tubes, reactive vessels, forging dies, cracking tubes and jet-engine blades [92, 94, 97].

Table 1-4. Typical physical and mechanical properties of pure Ni_3Al compound.

Properties	Ni_3Al
Density (g/cm^3)	7.65
Melting Temperature (°C)	1395
Bonding	Covalent / metallic
Thermal expansion coefficient ($\times 10^{-6}/K^{-1}$)	12.5
Thermal conductivity (W/m•K)	28.85
Electrical resistivity ($10^{-8}\Omega$•m)	32.59
Heat capacitivity (J/g•K)	0.54
Young's modulus (GPa)	168
0.2%Yield strength (MPa)*	280
Ultimate Tensile Stress at RT (MPa)*	333
Elongation*	2.6%

*: Data collected at room temperature in air.

1.2.3 Oxidation of Ni_3Al

1.2.3.1 Oxidation Thermodynamics

Like that of other alumina-forming metals or alloys, the oxidation resistance of Ni_3Al alloys relies on the formation of Al_2O_3. The reaction formula can be expressed as:

$$2Al(s)+\frac{3}{2}O_2 \rightarrow Al_2O_3(s) \tag{1-6}$$

$$\Delta G = \Delta G^\circ + \frac{3}{2}RT\ln(\frac{1}{p_{O_2}}) \tag{1-7}$$

$$\text{At equilibrium, } p_{O_2} = \exp(\frac{2}{3}\frac{\Delta G^\circ}{RT}) \tag{1-8}$$

Where ΔG is the free energy of the reaction; ΔG° the standard free energy of formation of oxides; p_{O_2} the partial pressure of oxygen; R the gas constant; and T is the absolute temperature. Fig. 1-8 shows ΔG° for some common oxides [98]. Based on Fig. 1-8, Al_2O_3 has more negative ΔG° than Cr_2O_3 and SiO_2, suggesting a larger driving force for the formation of Al_2O_3. From Equation (1-8), the equilibrium partial pressure of oxygen of formation of Al_2O_3 is much lower than that of formation of Cr_2O_3 and SiO_2, indicating a higher thermodynamic stability of Al_2O_3.

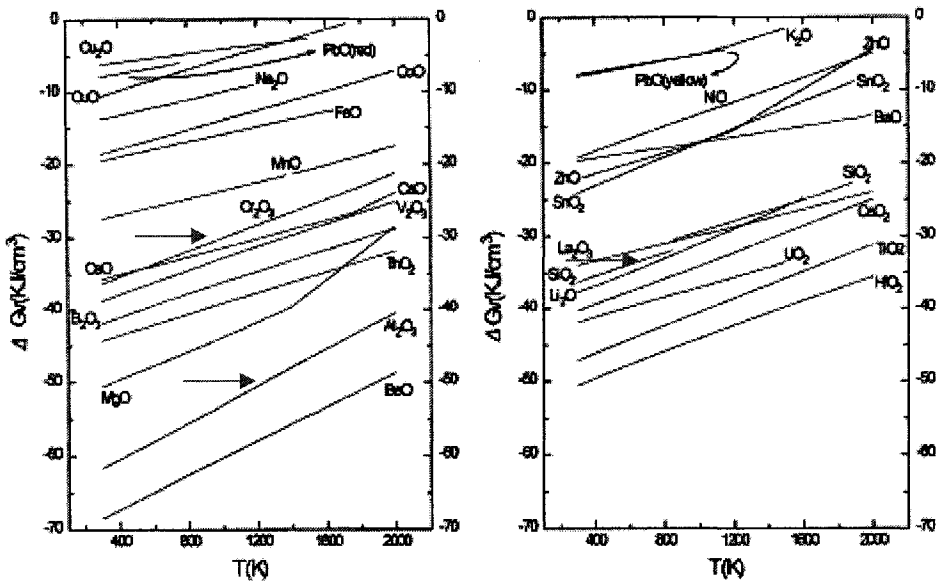

Figure 1-8. The standard free energy change of formation of oxides [98].

1.2.3.2 Oxidation Kinetics

High-temperature oxidation of metals or alloys (including Ni_3Al alloys) generally follows three stages: transient oxidation, stead-state oxidation and breakaway [99]. The transient stage features a rapid increase of weight gain due to selective oxidation of the active metal elements. After the formation of the protective oxide scale, the oxidation rate curve quickly flattens out. In the final stage, the protective scale is broken, and base metals or alloys suffer accelerated oxidation. The second stage is often used to determine the oxidation kinetics in terms of the relationship of weight change to exposure time. Three oxidation mechanisms that have been recognized are the logarithmic law, the parabolic law and the linear law (Fig. 1-9). The logarithmic mechanism is manifested only in metals oxidized at low temperatures (300-400 °C) [100]. For most alloys, the linear law and the parabolic law are more commonly observed.

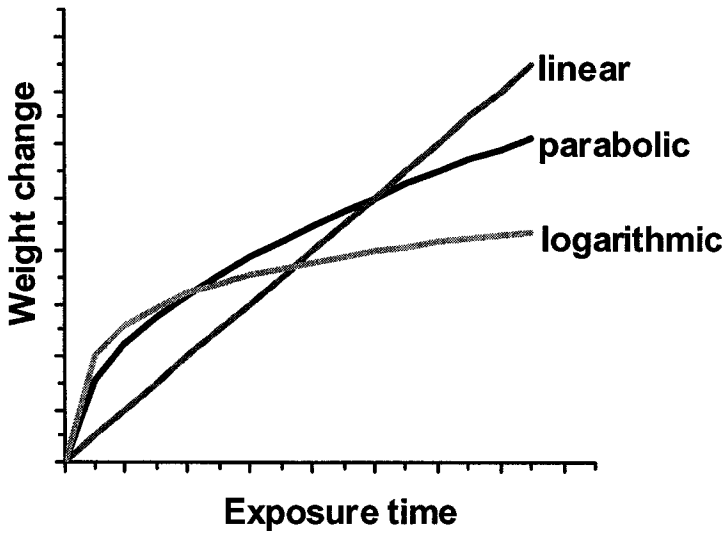

Figure 1-9. Typical oxidation mechanisms of metal and alloys.

In case of parabolic oxidation, one assumes that metals and alloys form a dense and single-phase oxide scale during oxidation. The rate-determining step is the lattice diffusion of reacting species through the oxide scale. The rate equation can be described by [100]:

$$(\frac{\Delta m}{A}) = k_p t^n + C, n = 0.5 \qquad (1\text{-}9)$$

$$\text{or } (\frac{\Delta m}{A})^{\frac{1}{n}} = k_p' t + C', n = 0.5 \quad (1\text{-}10)$$

where Δm is the weight change; A is the area of base metals or alloys; t is the exposure time; C and C' are the constants; n is the rate component, and $n = 0.5$ for the parabolic oxidation; k_p and k_p' are the parabolic rate constants. The parabolic rate constant is temperature dependent, and it can be expressed by an Arrhenius-type equation

$$k_p = k_0 \exp(-\frac{Q}{RT}) \quad (1\text{-}11)$$

where k_0 is the constant; Q is the activation energy of oxidation.

The parabolic law is often adopted to describe the high-temperature oxidation of numerous metals and alloys including Ni_3Al. It is noted that the oxidation of Ni_3Al alloys may not exactly follow the parabolic law. It has been found that the scale structure on Ni_3Al oxidized below 1200 °C may consist of multiple oxide phases such as NiO, $NiAl_2O_4$, and Al_2O_3 [89, 99, 101-103], which does not meet the assumption of the parabolic law. Several researchers have reported that the oxidation of Ni_3Al alloys and coatings actually has a subparabolic behavior ($n < 0.5$) [51, 52, 103, 104].

The linear oxidation has a rate equation similar to that of the parabolic oxidation except for the rate component $n = 1$, which is given by:

$$(\frac{\Delta m}{A}) = k_l t + C \quad (1\text{-}12)$$

where k_l is the linear rate constant. From Equation (1-12), it is clear that the oxidation rate during linear oxidation will be independent of exposure time. This type of oxidation is often observed in metals and alloys forming porous oxide scales or cracked oxide films. The overall oxidation may be controlled by the stead-state oxidation reaction at the phase boundary or the surface [100].

1.2.3.3 Development of Protective Oxides on Ni_3Al

(a) Wagner's Internal-Oxidation Theory

The formation of protective Al_2O_3 on Ni_3Al alloys is complex, and affected strongly by composition, temperature, oxygen partial pressure and alloying element. The selective oxidation of Ni and Al exists during oxidation. Wagner has dealt with the oxidation in binary alloys (AB, B is less noble than A) [105]. It assumes that the concentration of B in the AB alloy should be high enough to form a continuous external oxide scale, and, otherwise, B can only be internally oxidized in the form of oxide precipitates. The critical concentration of B can be given by [105, 106]:

$$N_B^* = (\frac{\pi g^*}{2\upsilon}\frac{V_M}{V_{OX}}\frac{N_O D_O}{D_B})^{\frac{1}{2}} \quad (1\text{-}13)$$

where D_B is the diffusion coefficient of B in alloy; N_O and D_O are the molar fraction of oxygen on the surface and the diffusion coefficient of oxygen in the alloy, respectively; V_M and V_{OX} are the molar volume of the AB alloy and the oxide, respectively; g^* is the volume fraction of internal oxide precipitates; υ is the stoichiometry factor. If the oxidation follows the parabolic law and BO scale is formed, the critical concentration of B can be expressed by [105, 106]:

$$N_B^0 = \frac{V_M}{Z_B M_O}(\frac{\pi k_p}{D_B})^{\frac{1}{2}} \quad (1\text{-}14)$$

where Z_B is the valence of B; M_O is the atomic weight of oxygen; and k_p is the parabolic oxidation rate constant.

The addition of Cr (or Si) can promote the selective oxidation of Al due to a gettering effect [106] and thus curtail the critical concentration of Al in the alloys to form the external alumina scale. The critical Al content to form a continuous alumina scale could be decreased from 10-20wt% in Ni-Al binary system to as low as 5wt% in Ni-Al-Cr system [106]. However, theoretical modeling of internal oxidation and external oxidation of Al in ternary alloys (e.g., Ni-Al-Cr and Ni-Al-Si) is difficult. The third element of Cr (or Si) makes it hard to determine the parameters such as D_B and D_O in Equation (1-13) and (1-14). Recently, based on the Wagner's internal-oxidation theory in binary alloys (AB), Gesmundo and Niu [107-112] have established mathematical models to describe internal oxidation and transition from internal to external oxidation in the

ternary A-B-C alloys. They also discussed the possible effects of oxygen partial pressure and temperature.

(b) Effects of Temperature and Al Content

The effects of temperature and Al content on scale development on Ni-Al alloys were first studied by Pettit [113], and are summarized in Figure 1-10 (a) and (b).

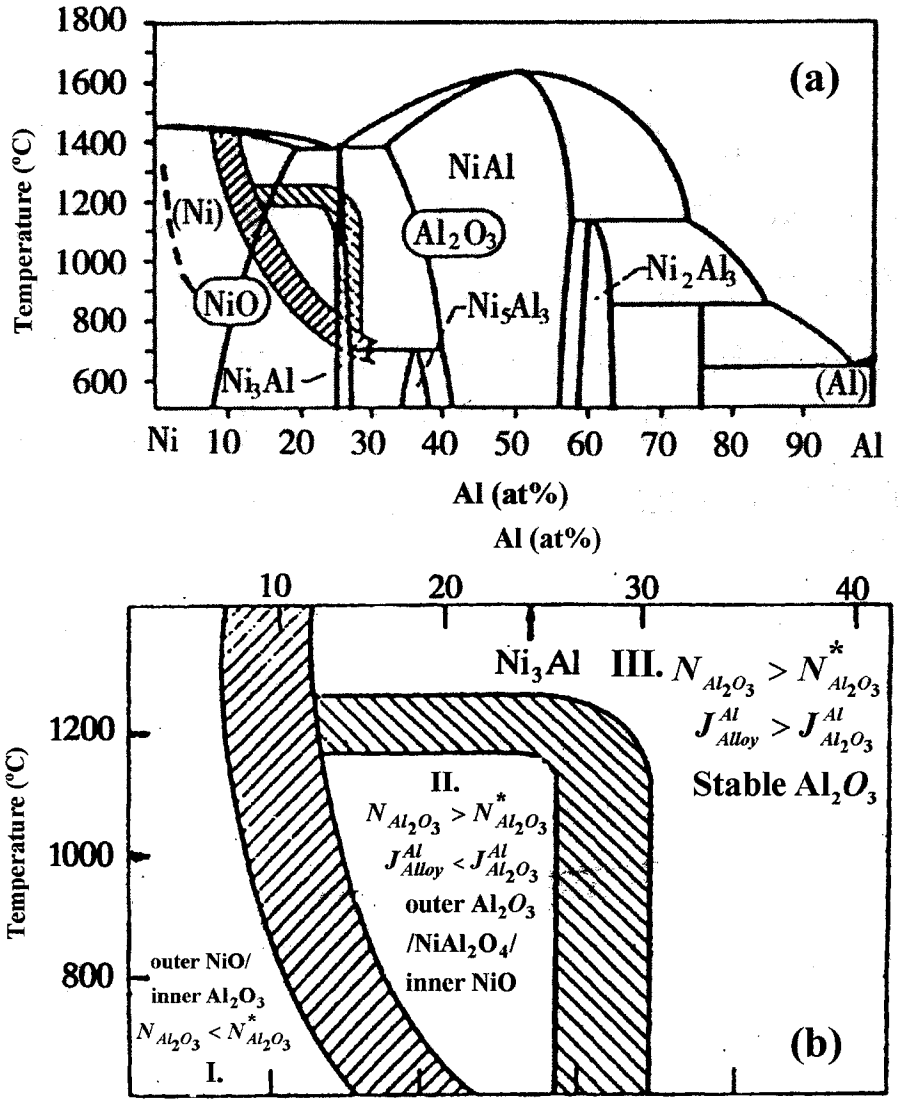

Figure 1-10. The effects of temperature and Al content on the evolution of oxide scale on Ni-Al alloys: (a) phase diagram; (b) magnified Ni-rich portion [113]. (The shadow area in (a) and (b) represent the critical Al content to form protective Al_2O_3 scale.)

Based on temperature and Al content, three regions with different oxidation mechanisms are identified in the Ni-Al binary phase diagram.

I. At low Al content and temperatures, the formation of continuous Al_2O_3 is impossible due to $N_{Al_2O_3} < N^*_{Al_2O_3}$, and NiO is selectively formed in the early stage. The final oxide structure consists of the outer pure NiO and the internal-oxidation zone containing Al_2O_3 and some $NiAl_2O_3$ precipitates.

II. For Ni-Al alloys with relatively high Al content at intermediate temperatures, the Al_2O_3 scale will be selectively formed due to $N_{Al_2O_3} > N^*_{Al_2O_3}$. Because the diffusion flux of Al in alloy (J^{Al}_{Alloy}) is less than that in Al_2O_3 scale ($J^{Al}_{Al_2O_3}$), a depletion layer of Al will be formed under Al_2O_3. The oxide structure will be outer Al_2O_3 scale / inner $NiAl_2O_4$ or probably NiO.

III. This mechanism is valid only if $N_{Al_2O_3} > N^*_{Al_2O_3}$ and $J^{Al}_{Alloy} > J^{Al}_{Al_2O_3}$, which is in the high Al portion. Hence, the stable surface oxide will be Al_2O_3.

According to Pettit [113], the oxidation of Ni_3Al alloys would follow mechanism II at 900-1300 °C, first the formation of the outer Al_2O_3 and then the inner $NiAl_2O_4$/NiO. However, Kuenzly et al. [114] argued that the oxide structure on Y-doped Ni_3Al alloys was the outer NiO/intermediate $NiAl_2O_4$/inner Al_2O_3 between 900-1200 °C. Doychak et al. [101] found a duplex oxide structure with the outer $NiAl_2O_4$ and the inner Al_2O_3 on Zr/B doped Ni_3Al alloys after oxidizing at 1200 °C for 1 min. Schumann et al. [115] also observed the simultaneous formation of outer NiO and internal-oxidation zone (IOZ) containing Al_2O_3 particles on single-crystal Ni_3Al after 1 min oxidation. Long-term exposure resulted in intermediate $NiAl_2O_4$ spinel and inner Al_2O_3. More systematic studies have been recently conducted by Pérez et al. [103] on powder-metallurgy (PM) Ni_3Al alloys. The results are summarized in Fig. 1-11 and Fig. 1-12. It was found that a transition of oxidation exists at approximately 730 °C. At the low temperature range of 535-730 °C, the IOZ was firstly formed, followed by the Ni layer and the NiO. A thin Al_2O_3 scale was developed only after a longer time. At the high temperature range of 730-1020 °C, the oxidation mechanism is more consistent with the observations of

Kuenzly [114], Doychak [101] and Schumann [115]. Pérez et al. [103] also found that the formation of voids at the oxide/alloy interface became more severe with increasing temperature.

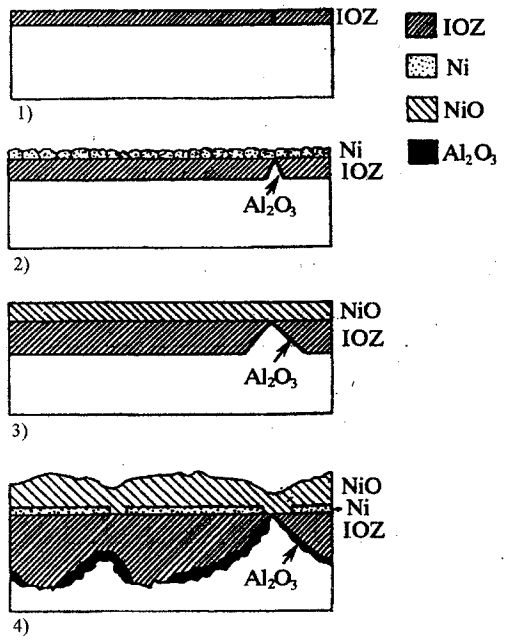

Figure 1-11. The oxidation stages of PM Ni_3Al for the low temperature range [103].

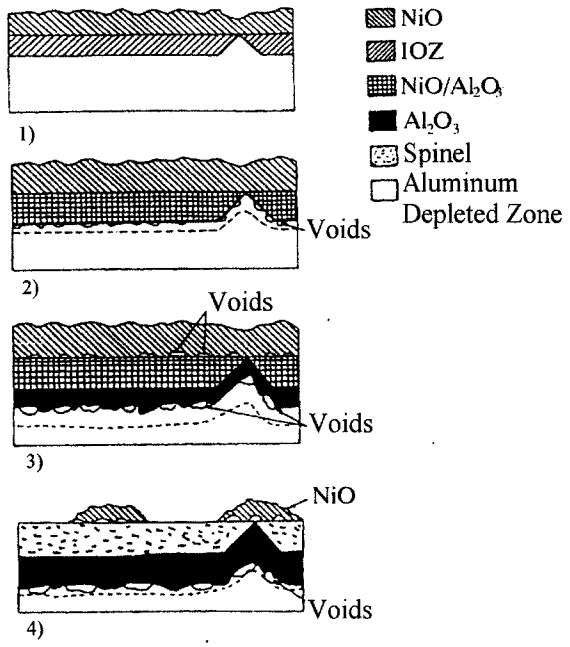

Figure 1-12. The oxidation stages of PM Ni_3Al for the high temperature range [103].

(e) Effect of Oxygen Partial Pressure

Ni_3Al alloys generally develop multiple oxides during oxidation under relatively high oxygen partial pressures, e.g., air or pure oxygen. Under low oxygen partial pressures, the oxidation behaviors of Ni_3Al are very distinct [115-119]. Venezia [116] reported that only the alumina oxide was found on Ni_3Al at low oxygen pressures. Schumann et al. [117] conducted the oxidation of single-crystal Ni_3Al at 950 °C under $p_{O_2} = 4\times10^{-19}\,atm$. They observed that only γ-Al_2O_3 formed in the initial stage, and γ-Al_2O_3 transformed to equilibrium α- Al_2O_3 in the later stage. The outward diffusion of Ni through the Al_2O_3 scale was also observed. Yi et al. [118] performed the oxidation of Ni_3Al alloys at 800 °C up to 25 hr under three different p_{O_2}, $5-9\times10^{-6}\,atm$, $1.2\times10^{-14}\,atm$, and $1.2\times10^{-19}\,atm$. The scale structure at $p_{O_2} = 5-9\times10^{-6}\,atm$ was the

outer $NiO/NiAl_2O_4$/ the inner Al_2O_3. At $p_{O_2} = 1.2\times10^{-14} atm$, the $NiAl_2O_4$ spinel was solely detected, and only the Al_2O_3 was identified at $p_{O_2} = 1.2\times10^{-19} atm$. Gao et al. [119] recently found two different oxidation behaviors of Ni_3Al alloys at $10^{-15} atm \le p_{O_2} \le 10^{-22} atm$. At $10^{-15} atm \le p_{O_2} < 10^{-18} atm$, pure Ni particles were formed first, followed by the slowly-formed Al_2O_3. In contrast, only Al_2O_3 could be found at $p_{O_2} = 10^{-22} atm$.

1.2.3.4 Transition Alumina

The equilibrium α-Al_2O_3, which is thermodynamically most stable, provides the best protection for Ni_3Al alloys. However, several transition alumina phases—such as γ-Al_2O_3, δ-Al_2O_3 and θ-Al_2O_3—would form in the transient oxidation stage of alumina-forming alloys [51, 52, 89, 101-103, 115, 120-123]. α-Al_2O_3 has a corundum crystal structure, which can be treated as hexagonally close-packed oxygen ions with trivalent Al cations occupying two-thirds of octahedral interstitial sites. The crystal structures of metastable alumina have been reviewed in [120, 122-124]. Those structures generally consist of cubic close-packed oxygen ions with Al atoms in tetrahedral and octahedral interstices. γ-Al_2O_3, with a cubic spinel structure, usually forms below 900 °C and transforms to more stable α-Al_2O_3 with time [120, 121, 123]. θ-Al_2O_3 has the monoclinic symmetry, and is more frequently seen at higher temperatures (900-1200 °C) [120-123]. δ-Al_2O_3 is a superlattice of the spinel structure. It has been proposed that the transformation of alumina generally follows a sequence of $\gamma\rightarrow\delta\rightarrow\theta\rightarrow\alpha$ [123]. Depending on temperature, α-Al_2O_3 may nucleate in γ-Al_2O_3 or θ-Al_2O_3 so that the transition alumina scale will be replaced by a α-Al_2O_3 scale [123, 124]. The mass transport in the transition alumina has been reviewed by Prescott [120, 121] and Stott [122]. The growth of γ-Al_2O_3 or θ-Al_2O_3 is controlled by the fast outward diffusion of Al via the cation lattice and the oxide surface. Platelet-like γ-Al_2O_3 or whisker-like θ-Al_2O_3 due to the outward cation diffusion is often observed in the early stage of Ni-Al alloys and coatings [51, 52, 102, 125].

1.2.3.5 Oxidation Resistance of Ni_3Al

(a) Current Understanding

Pérez [103] summarized some short-term isothermal-oxidation results of Ni_3Al alloys prepared by different methods over a large temperature range. As shown in Fig. 1-13, Ni_3Al alloys exhibit a fairly low oxidation rate even at high temperatures. Choi et al. [102] had studied the isothermal oxidation of pure cast Ni_3Al alloys at high temperatures. At the highest temperature of 1200 °C, the weight gain was less than 2.5mg/cm^2 after 60hr exposure. Pérez et al. [126] investigated the long-term isothermal oxidation of pure PM Ni_3Al alloys at the relatively low temperature of 635 °C, where the mass change after 1000 hr was less than 2 mg/cm^2. Recently, Susan et al. [51, 52] conducted long-term isothermal oxidation of electrodeposited Ni-Al coatings, containing γ-Ni and γ'-Ni_3Al, at 800 °C and 1000 °C. These coatings showed excellent oxidation resistance at 800 °C, only 0.5 mg/cm^2 after 2000 hr exposure, but accelerated oxidation at 1000 °C with a weight gain of more than 10 mg/cm^2 after 2000 hr.

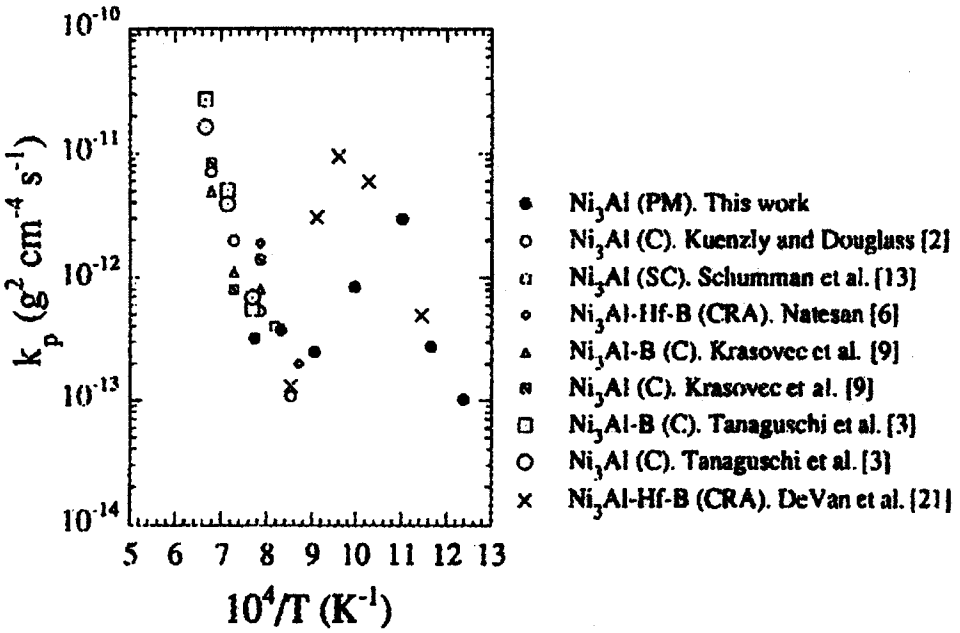

Figure 1-13. Arrhenius plot comparing data of parabolic rate constants k_p for oxidation of Ni_3Al alloys. PM: Power Metallurg, C: Cast, SC: Single crystal, CRA: Cast + Rolled +Annealed [103].

Cyclic oxidation is an issue of concern because Ni_3Al alloys are commonly served in thermal-cycling conditions. Pure Ni_3Al alloys are found to be prone to spallation at high temperatures. Choi [102] reported that the spallation of scale on pure Ni_3Al alloys occurred at 1000 °C and became much worse at 1300 °C. Alloying elements such as Cr and B, or reactive elements such as Y and Hf, were found to improve the spallation resistance of Ni_3Al [101, 114, 122, 127]. Brill [20] reported some results of long-term cyclic oxidation of alloyed Ni_3Al alloys in air at 1000 °C, which indicated a very low weight gain (less than 1.2 mg/cm^2). Brill [20] also compared the long-term cyclic oxidation results of Ni_3Al alloys with those of commercial iron-based alloy 800H and nickel-based alloy 617 at different temperatures. As shown in Figure 1-14, excellent oxidation resistance of Ni_3Al alloys was evident. Recently, Deevi et al. [92] performed longer-term tests on Ni_3Al-based alloys and alloy 800H at 1100 °C in air-5% water vapor. They reported that Ni_3Al alloys had no significant mass change even after 270 days. In contrast, alloy 800H suffered 150mg/cm^2 weight loss only after 40 days. Haanappel et al. [128] also reported fairly low weight change of Cr-doped Ni_3Al alloys (less than 0.1 mg/cm^2) at 900 °C in air for 1000 hr, and no crack or spallation was seen.

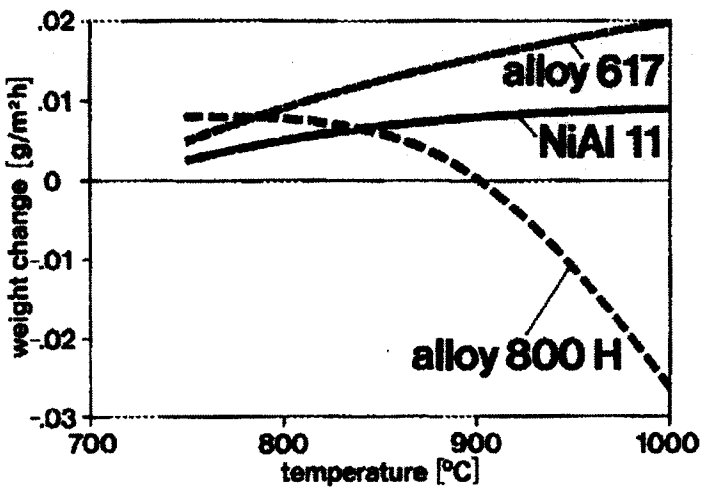

Figure 1-14. The comparison of long-term cyclic oxidation of alloy 800H and alloy 617 with the NiAl 11 alloy (Ni_3Al base alloy) [20].

(b) Effect of Microstructure

Several researchers have studied the effect of grain size on the oxidation resistance of Ni_3Al alloys or coatings, with contradictory conclusions. Takeyama et al. [129] reported that Ni_3Al alloys with finer grains had better oxidation resistance at 1000 °C due to a quick formation of protective alumina scale. Brill [20], however, argued that the fine-grain wrought Ni_3Al showed worse cyclic oxidation resistance than the cast Ni_3Al with coarse grains at 1000 °C, as shown in Fig. 1-14. Pérez et al. [104] recently studied the oxidation of PM Ni_3Al alloys with various grain sizes at different temperatures. They found that at temperature below 730 °C, the oxidation rate decreased with a decrease of grain size. The larger fraction of grain boundaries in fine-grained Ni_3Al alloys enhanced the formation of Al_2O_3 in the low-temperature range. Above 730 °C, the coarse-grain Ni_3Al alloys surprisingly showed better oxidation resistance. It was believed that fine grains easily cause the intrusion of oxide scale, and thus promote the inward diffusion of oxygen. Wang [130], however, reported that the Cr-doped Ni_3Al (50nm) had much higher cyclic oxidation resistance than the cast Ni_3Al at 1000 °C. The better cyclic oxidation behavior of nano Ni_3Al was also observed by Chen et al. [131] and Liu et al. [132]. Recently, Zhou et al. [49] found that nano grains greatly facilitated the formation of a continuous and compact alumina scale on the electrodeposited Ni-Al nanocomposite film at 1050 °C. Although the overall effect of grain size on the oxidation of Ni_3Al is still being debated, the positive role of fine grains in the formation of alumina scale is generally accepted.

(c) Effect of Alloying Element

Table 1-5 summarizes results about the effects of alloying elements on the oxidation of Ni_3Al alloys or coatings [17, 51, 99, 125, 127, 128, 130, 132-140]. Alloying elements in Ni_3Al are used primarily to improve mechanical properties or high temperature corrosion resistance. Many contradictive conclusions have been found from Table 1-5, which may be attributed to differences in doping methods, dosage, and alloy systems among various researchers. Boron significantly improves the low-temperature ductility of Ni_3Al, but deteriorates the adherence of oxide scale due to the formation of voids on Ni_3Al surface [125]. Cr can effectively decrease the critical Al content from

10~20wt% in Ni-Al binary system to 5wt% in Ni-Al-Cr system to form continuous alumina scale [106]. However, above 1100 °C, the transformation of Cr_2O_3 to vaporized CrO_3 leads to many micro-voids in the scale, which reduces the adherence of oxide scale [125]. Reactive elements (REs) such as Y, Ce, La, Zr and Hf (or their oxides, i.e., REOs) are added to enhance the adherence of the alumina scale and to improve the cyclic oxidation resistance of Ni_3Al, although some elements may cause an increase of weight gains. This so-called reactive element effect will be further discussed later.

Table 1-5. The effect of alloying elements on the oxidation of Ni_3Al, adapted from [99].

Alloying elements	Oxidation Properties	Adherence of Al_2O_3 scale	Formation of Al_2O_3 scale	Growth of Al_2O_3
B	↓(↑)	↓		+
Cr	↑ (↓)	↑(↓)	↑	+
Ni		↑		
Co	↑	↑ (↓)		+
Mo	↑			
W				-
Si			↑	
Ti	↓	↑ (↓)		+
Y	↓(↑)	↑ (↓)	↑	+
Zr	↓(↑)	↑		+
ZrO_2	↓			
Hf	↑	↑	↑	+
HfO_2	↓			
SiC	↑	↓		
Al_2O_3	↓			
Ta				+
Ce		↑		
La		↑		

↑: Improving; ↓: Deteriorating; +: Having effect; -: Having no effect.
↑ (↓) and ↓(↑): Some disputed results inside parenthesis.

(d) Effect of Interdiffusion

Interdiffusion is a practical problem for protective coating systems. It refers to the inward diffusion of coating components and the outward diffusion of substrate elements. Interdiffusion and spallation are the two main factors that can shorten the life of alumina-

forming coatings during oxidation, especially at high temperatures. In reducing or inert atmospheres, interdiffusion will become more dominant. Al can be quickly consumed either by regenerating the spalled scale or by inward diffusion. If the Al level is lower than a critical value, less protective NiO or $NiAl_2O_4$ instead of Al_2O_3 will be formed, indicating failure of coatings. Susan et al. [141] recently investigated interdiffusion in Ni-15at%Al coating / Ni matrix system during isothermal oxidation. They found that inderdiffusion was negligible at 800 °C even after 2000 hr. However, the γ-Ni + γ'-Ni_3Al two-phase zone in the coating was quickly depleted to γ-Ni when oxidized at 1000 °C for 100 hr or 1100 °C for only 50 hr. They concluded that the rapid consumption of Al owing to interdiffusion was the reason for the marginal isothermal oxidation resistance of Ni-15at%Al coating at 1000 °C [52].

1.2.3.6 Reactive-Element Effect (REE)

(a) Failure of Oxide Scale

As discussed in Section 1.2.3.5, pure Ni_3Al alloys have marginal cyclic-oxidation resistance, and easily suffer the spallation of the protective Al_2O_3, especially at temperatures above 1000 °C. The oxide scale can also fail due to buckling or cracking of the scale [122, 142-144]. The failed oxide scales lead to accelerated local oxidation and a rapid loss of Al in the alloy matrix. Although the failure mechanisms of the oxide scale are not yet been completely understood, it is generally believed that compressive residual stresses, voids and interfacial impurities are the main attributes.

Compressive residual stresses, such as thermal stress, growth stress and interfacial stress, are the major causes of scale failure. Thermal stress results from a large mismatch of thermal expansion coefficient between the Al_2O_3 scale and the Ni_3Al matrix during cooling [114, 142, 145]. Kuenzly et al. [114] reported that the thermal stress in the Al_2O_3 scale on the pure Ni_3Al alloy during cooling from 1200 °C could be 2,413 MPa, which was higher than the ultimate compressive strength of Al_2O_3, 2,068 MPa. Because thermal stress is quickly created upon cooling, there is almost no time to relieve this stress by the creep of the matrix [122, 142]. Consequently, thermal stress is the most detrimental. Growth stress is related to the volume dilation during the transformation of Al to Al_2O_3

[144, 145]. It can be relaxed to some extent by the creep of the scale [145], and thus it is less harmful than the thermal stress. Interfacial stress is induced by the irregular geometry of the oxide/substrate interface during the growth of the scale [144, 145]. As with the growth stress, it can be relieved partially by the creep of the scale.

Other than residual stresses, voids are often observed either at the grain boundaries of the scale or at the scale/substrate interface for the alumina-forming alloys during the oxidation [114, 122, 145-148]. Void formation is believed to be caused by the condensation of excessive vacancies. Vacancies can be generated by the inward diffusion of oxygen vacancies or the outward transportation of Al cations through Al_2O_3 [114, 122]. Vacancies can also be induced by selective oxidation of Al in Ni-Al alloys [114, 122, 146], which causes an Al-depleted layer beneath Al_2O_3, and the inward diffusion of Ni. Because the inward diffusivity of Ni is larger than the outward diffusivity of Al, the Kirkendall vacancies are then created. Interfacial pores significantly deteriorate the bonding between the scale and the substrate, resulting in premature decohesion of the scale. If large residual stresses exist, cracks may start to propagate at these voids.

Harmful impurities (mainly sulfur) at the scale/substrate interface play a key role in causing failure of the scale [148-150]. Sulfur atoms are surface-active, and easy to segregate at the scale/substrate interface to lower the overall energy, which weakens the interfacial bond [149, 150]. Sulfur segregation at ppm level is enough to deteriorate the interfacial bond. Grabke et al [148] proposed that the segregated sulfur could enhance the formation of interfacial voids, and thus promote the spallation of the scale.

(b) Reactive-Element Effect (REE)

The reactive element effect has been extensively studied and reported for several decades. A minor addition of REs or REOs can effectively decrease the spallation of scale on high-temperature alloys and coatings. The possible beneficial effects and underlying mechanisms have been reviewed [121, 122, 145, 149, 151-154], and are summarized below.

1) REs promote selective oxidation of alumina and also the ability of self-healing. At the early stage of oxidation, REs will be oxidized to REOs before Al, which provide sites of preferential nucleation of alumina [121, 145].
2) REs (REOs) alter the growth mechanism of alumina scale. RE ions are prone to segregation at scale grain boundaries, which retards rapid outward diffusion of Al cations owing to the defect interaction [136, 151, 154, 155], so that the slow inward transport of oxygen becomes the rate-controlling step. This will accompany the transformation of the equiaxed structure of alumina scale without REs (REOs) to a columnar structures [121, 156]. The slowly growing scale considerably decreases the internal growth stresses.
3) REs (REOs) improve scale ductility. The segregation of RE ions or REO particles effectively pin the motion of grain boundaries, leading to a fine-grained scale. Fine-grained scales are more ductile, and allow more relaxation of residual stresses, which raises the cracking threshold and spallation resistance [121, 135, 136, 151].
4) REs (REOs) suppress the formation of voids at the scale / matrix interface [114, 121, 145, 146]. REs (REOs) are good sinks for vacancy condensation. This may reduce voids at the scale/coating interface and improve the adherence of the scale to the matrix.
5) REs (REOs) eliminate the detrimental "sulfur effect" [148-150]. It is proposed that REs such as Y can react with S to form thermodynamically stable Y-S phases in the alloy matrix, which dramatically suppresses the segregation of hazardous sulfur at the scale / matrix interface. Meier et al. [149] had reported that desulfidation using hydrogen or Y doping could achieve excellent cyclic oxidation resistance of Ni-based alloys and FeCrAl alloys. Recently, Schumann et al. [150] observed Y-S phases beneath the alumina scale on Y-doped NiAl using TEM.

1.2.4 Carbonaceous Corrosions

1.2.4.1 Carbon Activity and Oxygen Partial Pressure

Fe-based and Ni-based alloy components used in modern chemical, petrochemical, energy conversion, and metallurgical industries often suffer carbonaceous corrosion when they are exposed to carbon-containing atmospheres. For research purpose, three basic gas systems—CH_4-H_2, CO-CO_2, and CO-H_2-H_2O—are usually adopted to simulate industrial carburizing atmospheres. Carbon activity and oxygen partial pressure are used to characterize the reactivity of these atmospheres, which can be given by [7, 157]:

Reaction 1:

$$CH_4 = 2H_2 + C \tag{1-15}$$

$$a_c = K_1 \frac{p_{CH_4}}{(p_{H_2})^2}, \log K_1 = \frac{4791}{T} - 5.789 \tag{1-16}$$

Reaction 2:

$$CO + H_2 = H_2O + C \tag{1-17}$$

$$a_c = K_2 \frac{p_{CO} \bullet p_{H_2}}{p_{H_2O}}, \log K_2 = \frac{7100}{T} - 7.496 \tag{1-18}$$

Reaction 3:

$$2CO = CO_2 + C \tag{1-19}$$

$$a_c = K_3 \frac{(p_{CO})^2}{p_{CO_2}}, \log K_3 = \frac{8817}{T} - 9.071 \tag{1-20}$$

where a_c is the carbon activity of atmospheres, and, specifically, a_c=1 refers to the equilibrium state of graphite. K_1, K_2, and K_3 are the reaction constant; T is the absolute temperature, °K.

The oxygen partial pressure can be determined by [157]:

$$H_2O = H_2 + \frac{1}{2}O_2, p_{O_2} = K_4 \left(\frac{p_{H_2O}}{p_{H_2}} \right)^2 \tag{1-21}$$

$$CO_2 = CO + \frac{1}{2}O_2, p_{O_2} = K_5 \left(\frac{p_{CO_2}}{p_{CO}} \right)^2 \tag{1-22}$$

Depending on the oxygen partial pressure, the environments can be divided into either the carburizing/oxidizing atmosphere or the reducing carburizing atmosphere.

Based on carbon activity (a_c) and temperature, carbonaceous corrosions can be classified into metal dusting and carburization. Metal dusting occurs at temperatures ranging from 400-800 °C, and under high carbon activities, $a_c>1$ [1, 3, 5-7]. Carburization is generally manifested at 800-1100 °C with $a_c \leq 1$ [1, 3-7].

1.2.4.2 Thermodynamic Stability Diagram

In high-temperature carburizing environments, the metal elements in Fe-based or Ni-based alloys may react with carbon or oxygen to form carbides or oxides. The phases formed are strongly influenced by temperature, carbon activity and oxygen partial pressure. At a constant temperature, a thermodynamic stability diagram can be used to predict phases in a metal-carbon-oxygen (M-C-O) system. Fig. 1-15 provides a thermodynamic stability diagram for Cr-C-O and Si-C-O systems at 1000 °C [157].

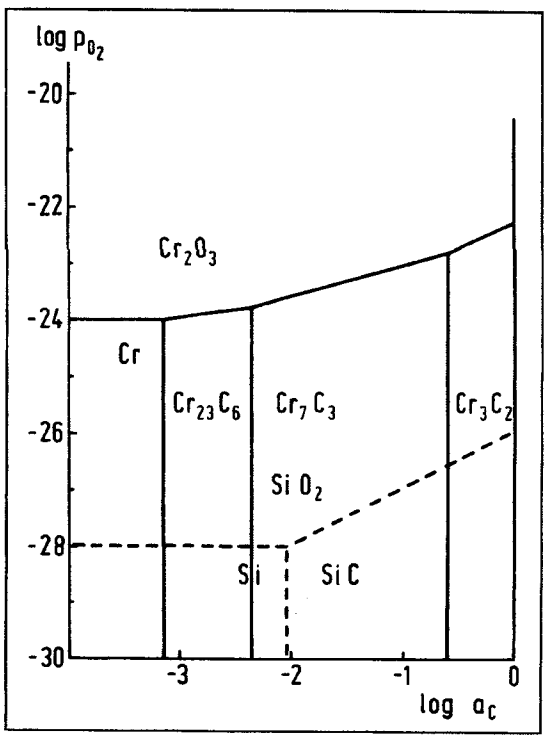

Figure 1-15. The thermodynamic stability diagram at 1000 °C for the systems of Cr-O-C and Si-O-C [157].

According to Fig. 1-15, three types of chromium carbides, Cr_2C_3, Cr_7C_3, and $Cr_{23}C_6$, can be formed. Cr_2O_3 oxide can also transform to chromium carbides under certain conditions, e.g., the decrease of oxygen partial pressure. Because it can tolerate much lower oxygen partial pressures before transforming to SiC, SiO_2 is more stable than Cr_2O_3.

1.2.4.3 Coke Formation

Coke formation is an unavoidable problem in the ethylene industry, where a thick carbon layer often form on the inner surface of Fe-Cr-Ni tubes during cracking hydrocarbon molecules. Two types of coke, namely inner catalytic coke and outer thermal coke, have been identified [10, 158-163]. Catalytic coke results from the heterogeneous reaction of hydrocarbon feedstock on some metals such as Fe and Ni, which are excellent catalysts for carbon deposition [158]. Recent studies have found that sources of catalysts also include some transiently-formed FeO, NiO and (Fe,Ni,Cr)-spinel, which could be reduced to Fe, Ni, or Fe-Ni particles [158, 162, 164]. Catalytic coke contains crystalline graphite and some metal, carbide or oxide particles, and has a filamentous and porous morphology. Thermal coke is related to the thermal cracking of hydrocarbon, from which a dense and amorphous coke layer will deposit on the tube surface. This layer is characterized by a columnar, radial and axial structure.

Coke formation occurs via several sequential steps [159, 162]. Firstly, hydrocarbons are adsorbed on the catalytic metal surface, and carbon deposition occurs due to the catalytic reaction. Carbon atoms diffuse inward along grain boundaries of the catalytic particles or the catalytic particle/matrix interface owing to thermal gradient. As carbon builds up, metal particles such as Fe or Ni will be separated and lifted up from the tube surface. With further carbon diffusion, metal particles will be transported to the top of growing carbon filaments. The deposited carbon layer gradually covers metal particles and the tube surface, thereby deactivating the entire surface, and preventing further formation of catalytic coke. The resulting outer layer will be thermal coke.

Accumulation of coke on an internal tube surface can cause many problems, e.g., a decrease of operating temperatures due to poor thermal conductivity of coke, an increase of gas pressure inside tubes owing to the reduction of effective internal tube diameter, and erosion of metal components by hard coke particles. More importantly, the coke layer on tube surface leads to carburization and metal dusting of tube materials. In a field operation, the coke must be removed periodically by gasifying the coke (decoking) at about 800-900 °C using hydrogen-vapor decoking steam.

One of the industrial approaches to control coke formation is to introduce S into the gas feedstock at the ppm level [10, 158, 159]. It is believed that S can preferentially react with Fe or Ni to form Fe-S or Ni-S compounds that can deactivate the catalytic surface for coke deposition. Another method is to introduce a protective oxide scale, such as Cr_2O_3, SiO_2 or Al_2O_3, on the alloy surface [159]. These inert oxide scales are very stable, and can block the exposure of Fe or Ni to hydrocarbon. Hence they can reduce, or at least, mitigate, the formation of catalytic coke.

1.2.4.4 Carburization

(a) Kinetics

Carburization of Fe-Ni-Cr alloys can occur in two ways: diffusion-controlled carburization and carburization with a protective scale. Diffusion-controlled carburization is always observed in Fe-Ni-Cr alloys exposed to highly reducing carburizing atmospheres, e.g., CH_4-H_2, where the formation of protective Cr_2O_3 is impossible. The internal formation of carbides is thus controlled by the diffusion of carbon in the alloys. The kinetics for this form of carburization can be described using a parabolic law [1]:

$$\left(\frac{\Delta m}{A}\right)^2 = 2kt \qquad (1\text{-}23)$$

where $\frac{\Delta m}{A}$ *is the weight gain per unit area;* k *is the carburization constant;* t *is the time.*

During carburization of Fe-Ni-Cr alloys, a two-layer zone with the inner $M_{23}C_6$ (M is Fe or Cr) and the outer M_7C_3 is often observed [1]. The thickness of total carbide zone can be written as [3]:

$$x^2 = 2\varepsilon \frac{D_c c_c}{\nu c_M} t \qquad (1\text{-}24)$$

where x is the thickness of carbides zone; ε is a labyrinth factor; ν is the stoichiometric factor for the carbide MC_ν; c_M is the concetration of the metals involved in the formation of carbide; D_c and c_c are the diffusivity and solubility of carbon in the alloy matrix; t is the time. It is obvious that the rate change of carbide layer will be affected mainly by D_c and c_c.

If oxygen partial pressure in carburizing environments is high or a pre-oxidation process is adopted, a protective chromia scale can be developed on Fe-Ni-Cr alloys. Under the circumstances, the diffusion of carbon through oxide scale becomes the rate-controlling step. Because the solubility of carbon in the oxides such as Cr_2O_3, Al_2O_3, and SiO_2 is negligible [1, 3], the ingress of carbon can be completely blocked if the oxide scale is dense and compact. The accumulated carbon in the scale in a range of 100 to 1000 ppm may take years [157]. If the oxide scale is defective, carbon can still diffuse into the substrate alloys via those short-circuit defective paths and cause precipitation of carbides.

(b) Detrimental Effects of Carburization

Excessive precipitation of carbides in Fe-Ni-Cr tube alloys due to carburization causes volume dilation and significant internal stresses, which may induce the formation of micro-cracks in the alloys. Brittle carbides also decrease the ductility of tube materials. Klöwer et al. [165] reported that nearly 100% of the Charpy notch impact energy was lost for alloy 800H and AC66 Fe-Ni-Cr alloys after carburization in CH_4-H_2 at 1000 °C for 1008 hr. Carburization leads to the loss of creep resistance of Fe-Ni-Cr tube alloys. Blocky brittle carbides precipitated along grain boundaries or in grains enhance creep rate. Excessive formation of chromium carbides significantly depletes the Cr content in alloy matrix, thereby deteriorating the ability of alloys to form Cr_2O_3 [1, 10].

(c) Control of Carburization

From Equation 1-24, the carburization rate can be reduced if the value of D_c and c_c is smaller. Grabke [1, 3, 6] has proved that the value of $D_c \bullet c_c$ in Fe-Ni binary alloy depends on the ratio of Ni/Fe. The product of $D_c \bullet c_c$ reached the minimum at Ni/Fe=4. Modern Fe-based tube alloys, e.g., 35Cr-45Ni alloys, consequently contain much higher Ni and Cr but lower Fe for better carburization and oxidation resistance. The adjustment of alloy composition, however, is limited by factors such as the cost.

Pretreatment of Fe-Ni-Cr alloys in weak oxidizing atmospheres, such as N_2-H_2-H_2O or H_2-H_2O, can exclusively induce a thin Cr_2O_3 scale free of Fe or Ni-oxides, which enhances the carburization resistance (especially in reducing environments). However, this scale suffers spallation during thermal cycling or cracking due to creep deformation. Moreover, Cr_2O_3 is not stable above 1050 °C, and converts to either chromium carbides [1, 3, 157] or volatile CrO_3 [11, 12]. To improve the spallation resistance of chromia scale, reactive elements such as Ce, Zr or Y are often added [3, 166-168]. In an early study, Hemptenmacher et al. [166] examined the effect of Ce on the carburization of alloy 800 at 1000 °C in CO-H_2O-H_2 atmospheres under different creep rates. The addition of 0.06% Ce led to strong interlocking of Cr_2O_3 scale and alloy matrix, and consequently very low carbon uptake even after 1300hr exposure. Recently, Seiersten et al. [167] reported that a thin ceria film formed by dip-coating enhanced the adhesion of Cr_2O_3 scale to Incology 800HT alloy either after pre-oxidation or during carburization in H_2-3%CH_4 at 1000 °C. Compared to uncoated pre-oxidized alloy samples, the carbon pickup rate in coated alloy samples was decreased by a factor of 2-3.

Alloying elements such as Nb, Ti, Mo, Si, and Al have been found to mitigate the carburization of Fe-Ni-Cr alloys. Mitchell et al. [168] investigated the effects of Mo, Si, and Al on the carburization of Fe-Ni-Cr cast alloys in both reducing environments and the carburizing-oxidizing atmospheres. These alloying elements all improved the carburization resistance of the alloys under both conditions. The beneficial effect of Mo was more significant than Si in highly-reducing environments, where the formation of

Cr_2O_3 and SiO_2 is impossible. One reason for this might be the precipitation of Mo_3C, which blocked the inward diffusion of carbon and the reaction of carbon with Cr. This mechanism was supported by Piekarshi et al. [169]. They observed that minor amounts of Nb and Ti decreased the carburization rate of Fe-30Ni-18Cr alloys in H_2-CO-CO_2-H_2O at 900 °C. Under carburizing-oxidizing atmospheres, alloys containing Si were more resistant to carburization. This beneficial effect resulted from the formation of a healing SiO_2 scale beneath the cracked or converted Cr_2O_3 scale because, according to Fig. 1-15, SiO_2 was more stable than Cr_2O_3. Al is similar to Si due to the formation of more stable Al_2O_3. Fe-Cr-4.5wt%Al alloy was resistant to carburization for temperatures up to 1150 °C [168]. 602CA Ni-Cr-2.3wt%Al alloys showed extremely low carbon uptake at 1100 °C for 1000hr in CH_4-H_2 [165]. It should be noted that the development of Si or Al-containing Fe-based or Ni-based alloy systems would be limited by an embrittling effect, where the addition of more than 2% Si or Al reduces the ductility of the alloys [10].

Surface coatings provide a better method for carburization control. In an early study, a CVD SiC coating was applied to Fe-Ni-Cr alloys but failed to show an improved carburization resistance owing to its poor adhesion to an alloy matrix [170]. Clark [171] had successfully produced SiC ceramic coating well-adhered to Incology reactor tubes via CVD. Under simulated cracking at 850 °C and de-coking at 800 °C, SiC coatings were found to suppress the formation of catalytic coke. Lang [172] deposited an amorphous SiO_2 scale on Incology 800H by plasma-assisted vapor deposition. The testing results showed the amorphous SiO_2 film completely stopped carburization at temperatures below 825 °C, but became ineffective at higher temperatures due to the loss of amorphous structure. Above 1000 °C, SiO_2 converted to SiC. The most successful coating systems developed to date are Cr-Si, Al-Si, and Al-Cr-Si [10, 14-16, 19], which have entered the stage of commercial application. The Al-Cr-Si coating showed excellent carburization resistance at temperatures up to 1149 °C when tested in the ethylene furnace for 27 months [14, 15]. An Al-Cr-Si coating has been successfully developed via PVD and PECVD [10, 16, 19]. After two years of field trial, the coated tubes had much lower coke buildup than the uncoated tubes.

Another trend is to use Ni_3Al-based alloys, which have their superior resistance to oxidation and carburization. Brill [20] first reported carburization of Ni_3Al base alloys in CH_4-H_2 atmospheres (a_c=0.8) at various temperatures up to 900 hr (Fig. 1-16). The superior carburization resistance of Ni_3Al-based alloy (NiAl11) to alloy 800H and alloy 617 is clear. Industrial applications of anti-carburization Ni_3Al-based components have been made in the Oak Ridge National Laboratory [91-94, 173]. Commercial Ni_3Al-based trays have been adopted by Delphi Automotive Systems Corporation in carburizing furnaces to replace stainless steel HU trays. The latter often failed after six months of in-field use. Ni_3Al-based alloys, however, did not fail even after more than 39 months [91]. The grate bars made of Ni_3Al-based alloys for calcinations of ores at high temperatures are currently being field tested [173]. Centrifugally cast Ni_3Al-based tubes with a diameter up to 675 mm have been successfully manufactured. The replacement of HU cast tubes in ethylene crackers with Ni_3Al tubes has recently been proposed [94, 173]. As in the case of other intermetallic alloys, room-temperature brittleness, long-term reliability, and complicated processing are major obstacles to their applications on a large scale. The use of Ni_3Al coatings against carburization has, however, not yet been reported.

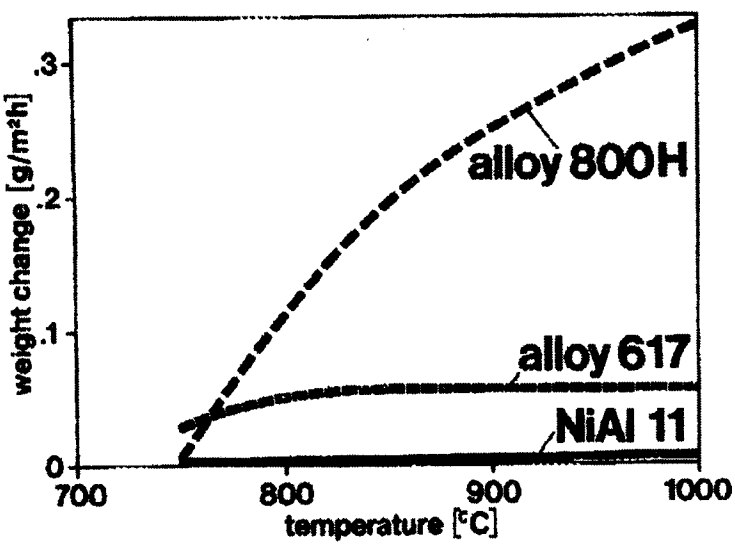

Figure 1-16. Temperature dependence of cyclic carburization of different alloys in CH_4-H_2 (a_c=0.8) [20].

1.2.4.5 Metal Dusting

Metal dusting is another form of corrosion commonly occurring in the carburizing atmospheres with $a_c>1$ at 400~800 °C [6, 7, 174-176]. For example, this type of corrosion occurs in the gas environments for the synthesis of ammonia and ethanol, and in the combustion of natural gas for the reduction of ores [7]. It is defined as the disintegration of Fe base, or Ni base alloys into a dust, consisting of very fine metallic particles and graphite, and sometimes carbides or oxides. Fine metallic particles are always Fe, Ni or both, which further catalyzes the formation of coke. A loose dusting layer causes a severe erosion problem for alloys during the transport of cracking steam. The consequence is often catastrophic. The kinetics and mechanisms of metal dusting have been thoroughly studied in recent years [6, 7, 174-179], and were found to depend mainly on base alloy compositions and temperatures.

(a) Metal Dusting in Iron and Fe-based Low Alloy Steels (Type I)

Metal dusting in iron and low alloy steels in $CO-H_2-H_2O$ at 400-650 °C generally follows the procedures shown in Fig. 1-17 [7, 174, 178].

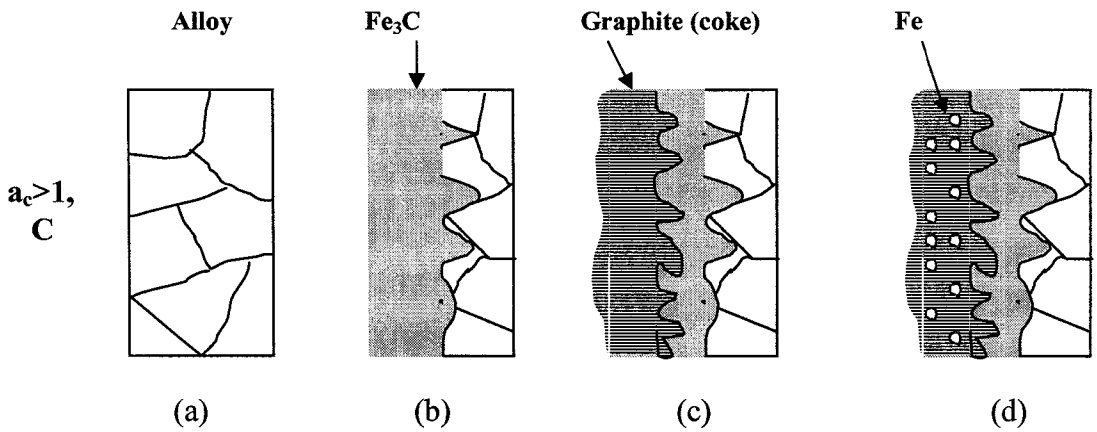

Figure 1-17. Schematic illustration of metal dusting in iron and low alloy steels: (a) surface reaction and carbon transfer; (b) formation of Fe_3C layer; (c) nucleation and growth of graphite into Fe_3C; (d) outward diffusion along graphite and segregation of Fe atom, which catalyzes the coke formation [7,174,178].

Firstly, carbon is transferred onto the surface (Fig. 1-17 (a)). Upon saturation of alloy surface, Fe_3C begins to nucleate and continues to grow into a metal matrix. A

serrated Fe_3C layer then covers the entire surface and retards the inward carbon diffusion (Fig. 1-17 (b)). This is followed by the precipitation of equilibrium graphite on the surface of the Fe_3C layer, which decreases the carbon activity on Fe_3C. Fe_3C becomes unstable and decomposes to graphitic carbon and Fe. Carbon atoms resulting from the decomposition attach to the graphite base plane and protrude into Fe_3C (Fig. 1-17 (c)). Fe atoms move outward along graphite and form fine Fe particles (about 20nm), which promotes coke formation (Fig. 1-17 (d)). Eventually, the outer coke layer continues to grow upward and the inner Fe_3C layer penetrates into the matrix. The outer coke layer usually has a filamentous morphology. The morphology of the final alloy surface after metal dusting changes slightly if the temperature is above 700 °C [7, 174]. An iron layer instead of iron particles will be formed between the coke layer and the Fe_3C layer. The final morphology is outer coke layer/iron layer/inner Fe_3C layer/metal matrix. The Fe_3C layer eventually disappears or breaks off. At higher temperatures between 900 °C and 1000 °C, the metal matrix transforms into austenite. The undergoing mechanism of metal dusting is similar to that for Ni and Ni base alloys, and will be discussed later.

The wastage of metal particles during metal dusting can be expressed by [7]:

$$\frac{\Delta m_M}{A} = k_M \bullet t \tag{1-25}$$

where $\frac{\Delta m_M}{A}$ *is the metal wastage per unit area,* k_M *the rate constant of metal wastage and* t *the time.* The catalytic coke by metal particles can be given by:

$$2(\frac{\Delta m_C}{A}) = k_C \bullet k_M \bullet f(p_i) \bullet t^2 \tag{1-26}$$

where $\frac{\Delta m_C}{A}$ *is the coke deposition per unit area,* k_C *the rate constant of coke formation, and* $f(p_i)$ *a function of the partial pressures.* The Arrhenius-plot for coking rates showed the change of kinetics at 550 °C and 750 °C [7]. Below 550 °C, coking rate is proportional to p_{CO}: it increases with p_{H_2} and decreases with p_{H_2O}. Between 550 °C and 750 °C, carbon transfer is the rate step. Above 750 °C, the metal matrix transforms to austenite, and carbon diffusion in austenite becomes rate controlling.

(b) Metal Dusting in Ni and Ni-based Alloys (Type II)

Metal dusting in Ni and Ni-based alloys is distinct from that in Fe and Fe base low alloy steels [7, 174, 179]. The formation of an intermediate carbide layer doesn't occur in Ni and Ni base alloys. In contrast, a graphite coke layer forms directly on the alloy surface and grows into an oversaturated alloy matrix with carbon, which causes a separation of Ni particles from the matrix. Because Ni particles are much larger than Fe particles in Fe and Fe-based low alloy steels, Ni and Ni-based alloys have a smaller catalytic effect and a lower coke formation. Metal dusting in Ni and Ni-based alloys is also found to depend on crystal orientation of the alloy matrix [7, 174, 179]. If graphite forms on Ni (111), it will grow epitaxially, in which case the detrimental effect of metal dusting would be minor. However, if graphite nucleates on Ni (100), the vertical growth of graphite occurs, resulting in rapid metal dusting.

(c) Metal Dusting in High Alloy Steels

High alloy steels here refer to Fe-based or Ni-based alloys with high Cr content, e.g., >11wt% in ferritic alloys and >17wt% in austenitic alloys. In CO-H_2-H_2O environments with high oxygen partial pressure at 400~800 °C, it is possible to form mainly Cr-rich oxide on these high Cr alloys. Grabke et al. [7, 174] proposed a joint mechanism of carburization, metal dusting and oxidation. If a defect-free chromia scale formed on alloy steels, metal dusting was about negligible. In fact, the scale contained some defects, and the formation of a protective chromia was difficult below 650 °C. Carbon species would reach the alloy matrix via defects in the scale. Inward diffusion of carbon results in the precipitation of chromium carbides or other alloy carbides below Cr-rich oxide scale. The following operating mechanism might be either that seen in Fe and Fe-based low alloy steels or in Ni or Ni-based alloys, depending on the alloy composition. The latter would lead to fine metal particles and outgrowth of graphitic coke layer. Chromium carbides were then oxidized and converted to oxides.

Szakálos [175, 177] recently proposed a different metal dusting mechanism (Type III). He believed that alloys react directly with CO at first, which results in chromium carbides and Cr-depleted alloy matrix. Simultaneously, chromium carbides were

selectively oxidized, and the Cr-depleted alloy matrix disintegrated due to the growth of graphite (Type II). The final dust is composed of Cr-depleted alloy matrix, oxide, and graphitic carbon. Szakálos also suggested another new mechanism for the formation of carbon nano-tubes at the final stage of metal dusting (Type IV). He proposed that the Cr-depleted matrix continued to break off to very fine particles, which catalyzed coke formation and enhanced the inward diffusion of carbon. When Fe or Ni-rich particles reached nano-size, the carbon could form only on the particle surface and grow outward to form nano-tubes. Szakálos further summarized metal dusting mechanisms occurring in ferritic FeCrAl-alloys and Cr-steels, and austentic stainless steels in $CO-H_2$ environments with different carbon activities (Fig. 1- 18). He concluded that the actual mechanism would be an integrated activity involving Type II, III and IV.

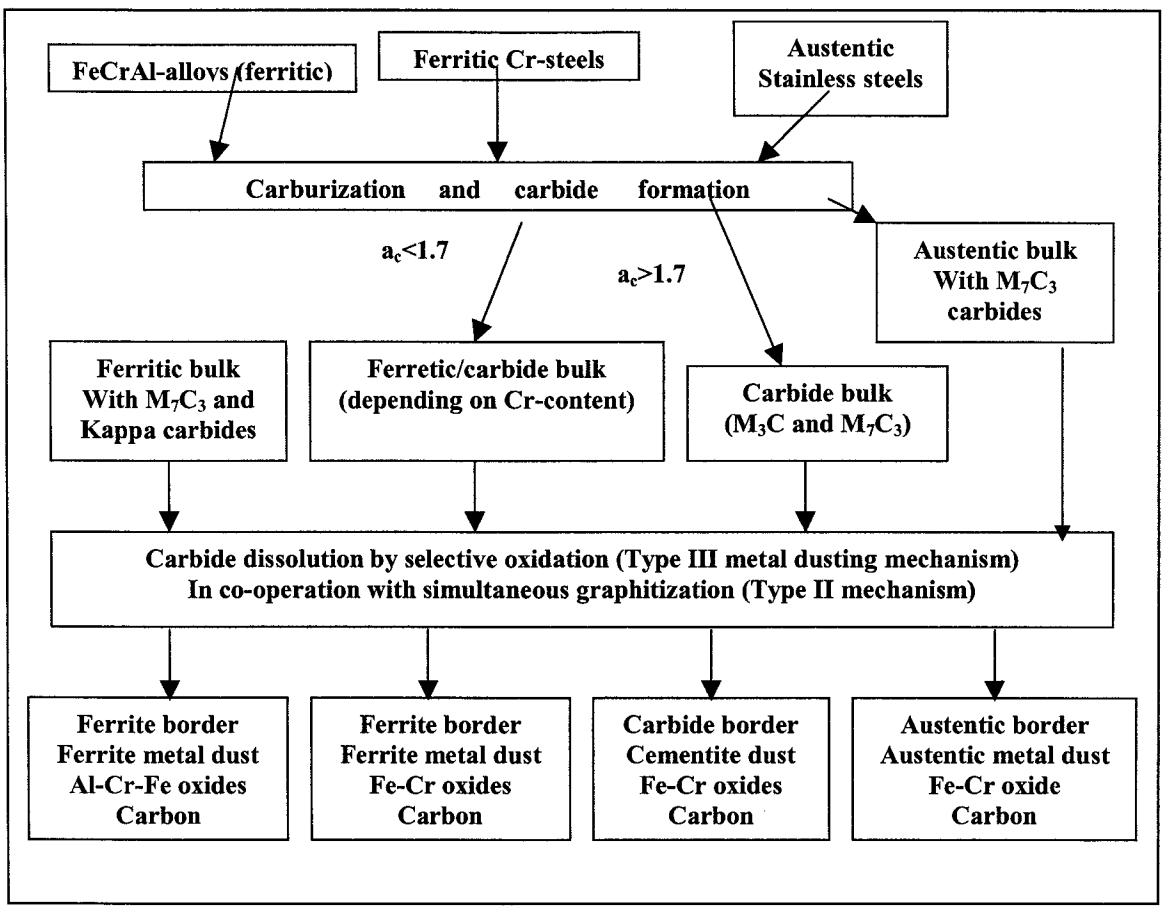

Figure 1-18. Schematic metal dusting mechanism chart for ferritic and austentic stainless steels [175].

(d) Prevention of Metal Dusting

Impurity of H_2S in gases retards metal dusting. Decomposition of H_2S releases H_2 and surface-active S. The latter is adsorbed by the alloy surface to deactivate the fresh catalyst surface required for coke formation. Grabke et al. [6, 7, 180] have investigated the effects of H_2S on metal dusting of pure iron, 2.25Cr-Mo steel, alloy 800, and Fe-25Cr-20Ni. The increase of H_2S content up to 10 ppm was found to beneficially retard the metal dusting rate. Because the minor addition of H_2S significantly improves carburization and metal dusting resistance of alloys and reduces the coke formation, this method is practically employed in modern industrial processes.

Ni alloys are more resistant to metal dusting than Fe alloys [7, 181]. Klöwer et al. [181] compared the metal dusting of commercial Fe base alloys with that of Ni base alloys in CO-H_2-H_2O at 650 °C. Fe base alloys generally showed unacceptable mass waste rate only after 190 hr. Ni base alloys, however, exhibited extremely low metal dusting rate even after 10,000 hr of exposure. A recent long-term test of Inconel alloy 693 (62Ni-29Cr) in CO-20%H_2 at 621 °C showed that only slight metal dusting occurred on alloys after 15816 hr. In contrast, Fe base Inconel alloy 800 (Fe-32Ni-21Cr) lost protection after only 1000 hr [182].

For Cr-containing alloys, rapid formation of chromia scale is a prerequisite against metal dusting. Methods that favor the formation of Cr_2O_3 and maintain the completeness of scale will result in excellent resistance to metal dusting. Increasing Cr content enhances the formation of Cr_2O_3 [6, 7, 9]. Ferritic structure is more favorable than austentic structure, as Cr diffuses faster in ferrite than in austenite [6, 7, 9]. It was previously reported that the resistance of alloys to metal dusting was affected by surface finish [183, 184]. Grabke et al. [183, 184] investigated the effects of surface finishing and grain size on the metal dusting of alloys in H_2-24%CO-2%H_2O at 600 °C and 650 °C. For Alloy 600, grinding, polishing, machining, sandblasting, and shot-peening mitigated metal dusting. These methods resulted in more defects and higher density of dislocations in superficial layer of alloys, which became short-circuit paths for the outward transport of Cr [183]. A more rapid faster establishment of Cr_2O_3 becomes possible even at low

temperatures (<650 °C). Fine grains also facilitate the formation of Cr_2O_3 scale owing to rapid diffusion of Cr via a large fraction of grain boundaries. Fine-grained 304 stainless steel (10 μm) resisted metal dusting up to 170 hr, whereas coarse-grained steel (200~300 μm) experienced excessive metal dusting after only 30 hr.

Strauß et al. [185] recently reported that alloying elements (Ti, Zr, Nb, Mo, and W) retarded metal dusting on Alloy 800. These elements have high affinities to carbon, and thus would be precipitated as carbides. This virtually reduced the loss of Cr in alloy matrix due to the formation of chromium carbides, which retained the ability of the alloy to develop Cr_2O_3. The addition of Ce, however, was found to be harmful for alloy 800. A little as 0.05% Ce reduced resistance to metal dusting. Si and Al were beneficial since these elements promoted the formation of Cr_2O_3 in the early stage, and they would be oxidized after long-term exposure to form an additional SiO_2 or Al_2O_3 scale below Cr_2O_3 scale.

Fewer investigations were conducted on the metal dusting of Fe-Al and Ni-Al. The only work reported to date was by Strauß, et al. [186] in 1996. They reported that Fe_3Al was highly susceptible to metal dusting and coke formation. The increase of Cr and Ni in $(Fe,Ni)_3Al$-Cr alloys enhanced resistance to metal dusting. Ni_3Al alloys were surprisingly invulnerable to metal dusting.

1.3 Research Objectives

There is a strong need for high-performance coatings to protect Fe base or Ni base structural components from oxidation and carburization. The novel Ni_3Al base coating may be a competitive candidate. The rapid development of the EMMC technique provides a cost-effective and viable way to bring Ni_3Al coatings into commercial use. However, systematic and definitive studies on the feasibility of the coating processing and the reliability of the coatings in oxidizing or carburizing environments have not yet been conducted. The current project aims to adopt the EMMC technique to develop Ni_3Al-based protective coatings on the Fe-Ni-Cr alloys, and secondly to investigate the

long-term resistance of Ni_3Al coatings to oxidation, carburization and metal dusting. The results are expected to provide fundamental bases for the future development and application of the electrodeposited Ni-Al base coatings. The specific objectives of this investigation and the organization of this dissertation are as follows.

1. Although several previous papers have reported electrodeposited Ni-Al composite coatings [43-49], it is still crucial to improve the process to achieve Ni-Al coatings with higher Al content and better resistance to high temperature corrosion attack in oxidizing and reducing environments. Moreover, few studies have been conducted on the electrodeposited Ni-Al-REO ternary composite coatings, and mechanisms concerning the co-deposition of metal and REO particles are still unclear. This study is aimed at depositing Ni-Al and Ni-Al-REO composite coatings with high Al particle content (30~37vol%) via electrodeposition, synthesizing Ni_3Al-based intermetallic coatings, and elucidating the behaviors and mechanisms of co-deposition of Al and REO particles. The coating processing adopted in the investigation will be presented in Chapter 2 and Chapter 3, which deal with the electrodeposition of the Ni-Al composite coating and the electrodeposition of Ni-Al-REO composite coatings respectively.
2. Chapter 4 and Chapter 5 will present the long-term cyclic oxidation behaviors of the pure and REO-dispersed Ni_3Al coatings, and possible effects of factors—coating microstructure, REO particles, and interdiffusion—on coating performances in oxidizing environments. Despite of extensive studies on the oxidation of Ni_3Al alloys and coatings via other techniques, however, only four papers [43, 49, 51, 52] have reported on the isothermal oxidation and short-term cyclic oxidation of electrodeposited Ni-Al coatings.
3. This research will examine the corrosion behavior and underlying mechanisms of Ni_3Al base coatings in simulated carburizing atmospheres, which have not been studied extensively and are poorly understood (if at all). Chapter 6 will provide the carburization behaviors of Ni_3Al-based coatings in the reducing CH_4-H_2 atmospheres, while Chapter 7 will deal with the coke

formation and metal dusting of Ni_3Al-based coatings in the CO-H_2-H_2O mixtures.

1.4 Bibliography

1. Grabke, H.J. and Wolf, I., Materials Science and Engineering, 1987. **87**: p. 23-33.

2. Hall, D.J., Hossain, M.K., and Atkinson, R.F., High Temperatures-High Pressures, 1982. **14**: p. 527-539.

3. Grabke, H.J., Corrosion, 2000. **56**(8): p. 801-808.

4. Nishiyama, Y., Otsuka, N., and Nishizawa, T., Corrosion, 2003. **59**(8): p. 688-700.

5. Ramanarayanan, T.A., Chun, C.M., and Mumford, J.D., Materials Science Forum, 2001. **369-372**: p. 55-76.

6. Grabke, H.J., Materials Science Forum, 2001. **369-372**: p. 101-108.

7. Grabke, H.J., Materials and Corrosion, 2003. **54**(10): p. 736-746.

8. Crabb, C. and Armesto, C., Chemical Engineering, 1999. **78**(1): p. 45-49.

9. Grabke, H.J. and Müller-Lorenz, E.M., Materials and Corrosion, 1998. **49**: p. 317-320.

10. Wysiekierski, A.G., Fisher, G., and Schillmoller, C.M., Hydrocarbon Processing (International Edition), 1999. **78**(1): p. 97-100.

11. Stringer, J., Materials Science and Engineering, 1987. **87**: p. 1-10.

12. Yamauchi, A., Kurokawa, K., and Takahashi, H., Oxidation of Metals, 2003. **59**(5-6): p. 517-527.

13. Lai, G.Y., Materials at High Temperatures, 1993. **11**(1-4): p. 143-150.

14. Wynns, K.A. and Bayler, G.T., *Diffusion Coated Ethylene Furnace Tubes, U.S. Patent 5,873,951*. 1999: USA.

15. Kurlekar, A. and Bayler, G.T., Hydrocarbon Processing (International Edition), 2001. **80**(1): p. 80-84.

16. Radmond, T. and Bergeron, M.P., Oil and Gas Journal, 1999. **97**(19): p. 39-42.

17. Klöwer, J., Brill, U., and Heubner, U., Intermetallics, 1999. **7**: p. 1183-1194.

18. Pourbaix, M., Materials Science and Engineering, 1987. **87**: p. 303-317.

19. Radmond, T., Chen, Y., Bailey, A., and Page, J., NACE International Corrosion/2001, 2001: p. 20.

20. Brill, U., Materials and Corrosion, 1990. **41**(12): p. 682-688.

21. Wang, Y. and Chen, W.X., Surface and Coatings Technology, 2004. **183**: p. 18-28.

22. Patnak, P.C., Materials and Manufacturing Processing, 1989. **4**(1): p. 133-152.

23. Salehi, M., Shamanian, M., and Ashrafizadeh, F., Surface Engineering (UK), 1997. **13**(6): p. 505-508.

24. Wang, K.L., Chen, F.S., and Leu, G.S., Materials and Engineering A., 2003. **357**: p. 27-38.

25. Tucker, R.C., Advanced Materials and Processes, 2004. **162**(3): p. 25-28.

26. Lee, E.C. and Choi, J.W., Surface and Coatings Technology, 2001. **148**: p. 234-240.

27. Garcia, I., Fransaer, J., and Celis, J.P., Surface and Coatings Technology, 2001. **148**(2-3): p. 171-178.

28. Wang, C.B., Wang, D.L., Chen, W.X., and Wang, Y.Y., Wear, 2002. **253**: p. 563-571.

29. Wang, S.C. and Wei, J.W.C., Materials Chemistry and Physics, 2003. **78**: p. 574-580.

30. Hovestad, A., Heesen, R.J.C.H.L., and Janssen, L.J.J., Journal of Applied Electrochemistry, 1999. **29**: p. 331-338.

31. Ghorbani, M., Mazaheri, M., Khangholi, K., and Kharazi, Y., Surface and Coatings Technology, 2001. **148**: p. 71-76.

32. Bazzard, R. and Boden, P.J., Transactions of The Institute of Metal Finishing, 1972. **50**: p. 63-69.

33. Bazzard, R. and Boden, P.J., Transactions of The Institute of Metal Finishing, 1972. **50**: p. 207-210.

34. Cameron, B.P., Foster, J., and Carew, J.A., Transactions of The Institute of Metal Finishing, 1979. **57**: p. 113-118.

35. Cameron, B.P., White, C.W., and Foster, J., Proceedings-The Electrochemical Society, 1983. **83**(12): p. 30-54.

36. Foster, J., Cameron, B.P., and Carew, J.A., Transactions of The Institute of Metal Finishing, 1985. **63**: p. 115-119.

37. Honey, F.J., Kedward, E.C., and Wride, V., Journal of Vacuum Science and Technology A., 1986. **4**(6): p. 2593-2597.

38. Saremi, M. and Bahraini, M., Transactions of The Institute of Metal Finishing, 2003. **81**(1): p. 24-27.

39. Sova, V., Transactions of The Institute of Metal Finishing, 1987. **65**: p. 21-23.

40. Osaka, T., Koiwa, I., Usuda, M., Arai, K., and Saito, I., Journal of The Electrochemical Society, 1989. **136**(4): p. 1124-1128.

41. Serek, A. and Budiok, A., Journal of Alloys and Compounds, 2003. **352**: p. 290-295.

42. Zhang, Y., Peng, X., and Wang, F., Materials Letters, 2004. **58**: p. 1134-1138.

43. Izaki, M., Fukusumi, M., Dnomoto, H., Omi, T., and Nakayama, Y., Journal of The Japan Institute of Metals, 1993. **57**(2): p. 182-189.

44. Susan, D.F., Barmak, K., and Marder, A.R., Thin Solid Films, 1997. **307**: p. 133-140.

45. Susan, D.F., Misiolek, W.Z., and Marder, A.R., Metallurgical and Materials Transactions A., 2001. **32A**: p. 379-391.

46. Barmak, K., Banovic, S.W., Petronis, C.M., Susan, D.F., and Marder, A.R., Journal of Microscopy, 1997. **185**(2): p. 265-274.

47. Napłoszek-Bilnik, I., Budiok, A., and Łągiewka, E., Journal of Alloys and Compounds, 2004. **382**: p. 54-60.

48. Napłoszek-Bilnik, I., Budiok, A., Łosiewicz, B., Pająk, L., and Łągiewka, E., Thin Solid Films, 2005. **474**: p. 146-153.

49. Zhou, Y., Peng, X., and Wang, F., Scripta Materialia, 2004. **50**: p. 1429-1433.

50. Hansen, M., *Constitution of Binary Alloys (Second Edition)*. 1958, McGraw-Hill Book Co.: New York. p. 118.

51. Susan, D.F. and Marder, A.R., Oxidation of Metals, 2002. **57**(1-2): p. 131-157.

52. Susan, D.F. and Marder, A.R., Oxidation of Metals, 2002. **57**(1-2): p. 159-180.

53. Foster, J. and Cameron, B.P., Transactions of The Institute of Metal Finishing, 1976. **54**: p. 178-183.

54. Stankovic, V.D. and Gojo, M., Surface and Coatings Technology, 1996. **81**: p. 225-232.

55. Celis, J.P. and Roos, J.R., Journal of The Electrochemical Society, 1977. **124**(10): p. 1508-1511.

56. White, C.W. and Foster, J., Transactions of The Institute of Metal Finishing, 1981. **59**: p. 8-12.

57. Stojak, J.L. and Talbot, J.B., Journal of The Electrochemical Society, 1999. **146**(12): p. 4504-4513.

58. Terizieva, V., Fransaer, J., and Celis, J.P., Journal of The Electrochemical Society, 2000. **147**(1): p. 198-202.

59. Banovic, S.W., Barmak, K., and Marder, A.R., Journal of Materials Science, 1999. **34**: p. 3203-3211.

60. Wu, G., Li, N., Zhou, D., and Mitsuo, K., Surface and Coatings Technology, 2004. **176**: p. 157-164.

61. Narayan, R. and Narayana, B.H., Journal of The Electrochemical Society, 1981. **128**(8): p. 1704-1708.

62. Graydon, J.W. and Kirk, D.W., Journal of The Electrochemical Society, 1990. **137**(7): p. 2061-2066.

63. Sombatsompop, N., Sukeemith, K., Markpin, T., and Tareelap, N., Materials Science and Engineering A., 2004. **381**: p. 175-188.

64. Müller, C., Sarret, M., and Benballa, M., Surface and Coatings Technology, 2002. **162**: p. 49-53.

65. Guglielmi, N., Journal of The Electrochemical Society, 1972. **119**(8): p. 1009-1012.

66. Moonir-Vaghefi, S.M. and Saatchi, A., Metal Finishing, 1997. **95**(6): p. 102-106.

67. White, C.W. and Foster, J., Transactions of The Institute of Metal Finishing, 1978. **56**: p. 92-96.

68. Yamada, T. and Asai, S., Journal of The Japan Institute of Metals, 2001. **65**(10): p. 910-915.

69. Hovestad, H. and Janssen, L.J.J., Journal of Applied Electrochemistry, 1995. **25**: p. 519-527.

70. Suzuki, Y. and Asai, O., Journal of The Electrochemical Society, 1987. **134**(8): p. 1905-1910.

71. Lee, C.C. and Wan, C.C., Journal of The Electrochemical Society, 1988. **135**(8): p. 1930-1933.

72. Johal, C.P.S. and Gabe, D.R., Transactions of The Institute of Metal Finishing, 1989. **67**: p. 31-34.

73. Shao, I., Vereecken, P.M., Cammarata, R.C., and Searson, P.C., Journal of The Electrochemical Society, 2002. **149**(11): p. C610-C614.

74. Ger, M.D., Materials Chemistry and Physics, 2004. **87**: p. 67-74.

75. Watson, A.S., *Organic addition agents for nickel electroplating solutions*. 1989, Toronto, Ontario, Canada: Nickel Development Institute.

76. Viswanathan, M. and Ghouse, M., Metal Finishing, 1979. **77**(10): p. 67-69.

77. Ghouse, M., Viswanathan, M., and Ramachandran, E.G., Metal Finishing, 1980. **78**(4): p. 44-47.

78. Celis, J.P., Roos, J.R., and Buelens, C., Journal of The Electrochemical Society, 1987. **134**(6): p. 1402-1408.

79. Fransaer, J., Celis, J.P., and Roos, J.R., Metal Finishing, 1993. **81**(6): p. 97-100.

80. Grosjiean, A., Rezrazi, M., Bercot, P., and Tachez, M., Metal Finishing, 1998. **96**(4): p. 14-17.

81. Bercot, P., Peña-Muñoz, E., and Pagetti, J., Surface and Coatings Technology, 2002. **157**: p. 282-289.

82. Valde, J.L., Journal of The Electrochemical Society, 1987. **134**(4): p. C223-C225.

83. Fransaer, J., Celis, J.P., and Roos, J.R., Journal of The Electrochemical Society, 1992. **139**(2): p. 413-425.

84. Watson, S.W. and Walters, R.P., Journal of The Electrochemical Society, 1991. **138**(12): p. 3633-3637.

85. Watson, S.W. and Walters, R.P., Journal of The Electrochemical Society, 1993. **140**(8): p. 2235-2238.

86. Stoloff, N.S., International Materials Reviews, 1989. **34**(4): p. 153-183.

87. Dey, G.K., Sādhanā, 2003. **28**(1-2): p. 247-262.

88. Singleton, M.F., Murray, J.L., and Nash, P., *Al-Ni (Aluminum-Nickel)*, in *Binary Alloy Phase Diagrams*, J. Massalski, Editor. 1990, ASM International Materials: Materials Park. Ohio. p. 181-184.

89. Meier, G.H., Materials and Corrosion, 1996. **47**: p. 595-618.

90. Zhang, Y.G., Han, Y.F., Chen, G.L., Guo, J.T., Wan, X.J., and Feng, D., *Structural Intermetallics*. 2001, Beijing, China: National Defence Industry Press. p. 604-609.

91. Wessel, J.K. and Long, W.G., Advanced Materials and Processes, 2003. **161**(6): p. 55-57.

92. Deevi, S.C. and Sikks, V.K., Intermetallics, 1996. **4**: p. 357-375.

93. Sikka, V.K., Deevi, S.C., Viswannathan, S., Seindeman, R.W., and Santella, M.L., Intermetallics, 2000. **8**: p. 1329-1337.

94. Stoloff, N.S., Liu, C.T., and Deevi, S.C., Intermetallics, 2000. **8**: p. 1313-1320.

95. Liu, C.T. and Stiegler, J.O., Science, 1984. **226**: p. 636-642.

96. Liu, C.T., White, C.L., and Horton, J.A., Acta Metallurgica, 1985. **33**(2): p. 213-229.

97. Xiao, C.B., Han, Y.F., Li, S.S., Wang, D.G., Song, J.X., and Li, Q., Materials Letters, 2003. **57**: p. 3843-3846.

98. He, Y.D., Li, Z.W., Qi, H.B., and Gao, W., Materials Research Innovation, 1997. **1**: p. 157-160.

99. Doychak, J., in *Intermetallic Compounds: Vol.1 Principles*, J.H. Westbrook and R.L. Fleischer, Editors. 1994, J. Wiley: New York, USA.

100. Kofstad, P., *High Temperature Corrosion*. 1988, New York, NY, USA: Elsevier Applied Science. p. 15-25.

101. Doychak, J. and Rühle, M., Oxidation of Metals, 1989. **31**(5-6): p. 431-452.

102. Choi, S.C., Cho, H.J., Kim, Y.J., and Lee, D.B., Oxidation of Metals, 1996. **46**(1-2): p. 51-72.

103. Pérez, P., González-Carrasco, J.L., and Adeva, P., Oxidation of Metals, 1997. **48**(1-2): p. 143-170.

104. Pérez, P., González-Carrasco, J.L., and Adeva, P., Oxidation of Metals, 1998. **49**(5-6): p. 485-507.

105. Wagner, C., Z. Electrochem., 1959. **63**: p. 772-782.

106. Kofstad, P., *High Temperature Corrosion*. 1988, New York, NY, USA: Elsevier Applied Science. p. 324-388.

107. Gesmundo, F. and Niu, Y., Oxidation of Metals, 2003. **60**(5-6): p. 347-370.

108. Gesmundo, F. and Niu, Y., Oxidation of Metals, 2004. **62**(5-6): p. 357-374.

109. Gesmundo, F. and Niu, Y., Oxidation of Metals, 2004. **62**(5-6): p. 375-390.

110. Niu, Y. and Gesmundo, F., Oxidation of Metals, 2003. **60**(5-6): p. 371-391.

111. Niu, Y. and Gesmundo, F., Oxidation of Metals, 2004. **62**(5-6): p. 341-355.

112. Niu, Y. and Gesmundo, F., Oxidation of Metals, 2004. **62**(5-6): p. 391-410.

113. Pettit, F.S., Transactions of TMS-AIME, 1967. **239**: p. 1296-1305.

114. Kuenzly, J.D. and Douglass, D.L., Oxidation of Metals, 1974. **8**: p. 139-178.

115. Schumann, E. and Rühle, M., Acta Metallurgica ET Materialla, 1994. **42**(4): p. 1481-1487.

116. Venezia, A.M. and Loxton, C.M., Surface and Interface Analysis, 1988. **11**(6-7): p. 287-290.

117. Schumann, E., Schnotz, G., Trumble, K.P., and Rühle, M., Acta Metallurgica ET Materialla, 1992. **40**(6): p. 1311-1319.

118. Yi, H.C., Smeltzer, W.W., and Petrix, A., Oxidation of Metals, 1996. **45**(3-4): p. 281-299.

119. Gao, W., Li, Z.W., Wu, Z., Li, S., and He, Y.D., Intermetallics, 2002. **10**: p. 263-270.

120. Prescott, R. and Graham, M.J., Oxidation of Metals, 1992. **38**(3-4): p. 73-87.

121. Prescott, R. and Graham, M.J., Oxidation of Metals, 1992. **38**(3-4): p. 233-254.

122. Stott, F.H., Wood, G.C., and Stringer, J., Oxidation of Metals, 1995. **44**(1-2): p. 113-141.

123. Yang, J.C., Schumann, E., Levin, I., and Rühle, M., Acta Materialia, 1998. **46**(6): p. 2195-2201.

124. Bagwell, R.B. and Messing, G.L., Journal of Materials Science, 2001. **36**: p. 1833-1841.

125. Choi, S.C., Cho, H.J., and Lee, D.B., Oxidation of Metals, 1996. **46**(1-2): p. 109-127.

126. Pérez, P., González-Carrasco, J.L., and Adeva, P., Corrosion Science, 1998. **40**(4-5): p. 631-644.

127. Pan, Y.C. and Chuang, T.H., Journal of Materials Science, 1991. **26**: p. 6097-6103.

128. Haanappel, V.A.C., Pérez, P., González-Carrasco, J.L., and Stroosnijder, M.F., Intermetallics, 1998. **6**: p. 347-356.

129. Takeyama, M. and Liu, C.T., Acta Metallurgica, 1989. **37**: p. 2681-2688.

130. Wang, F.H., Oxidation of Metals, 1997. **47**(3-4): p. 247-258.

131. Chen, G.F. and Lou, H.Y., Materials Science and Engineering A., 1999. **271**: p. 360-365.

132. Liu, Z.Y. and Gao, W., Oxidation of Metals, 2001. **55**(5-6): p. 481-504.

133. Pérez, P., González-Carrasco, J.L., and Adeva, P., Oxidation of Metals, 1999. **51**(3-4): p. 273-289.

134. Chen, M., Patu, S., Shi, C.X., and Shen, J.N., Journal of Materials Science, 1993. **28**: p. 5508-5513.

135. Jung, H.G. and Kim, K.Y., Oxidation of Metals, 1996. **46**(1-2): p. 147-167.

136. Jung, H.G. and Kim, K.Y., Oxidation of Metals, 1998. **49**(5-6): p. 403-430.

137. Pérez, P., González-Carrasco, J.L., Adeva, P., Haanappel, V.A.C., and Stroosnijder, M.F., Materials Science and Technology, 1999. **15**: p. 345-351.

138. Han, Y.F. and Xiao, C.B., Intermetallics, 2000. **8**: p. 687-691.

139. Xiao, C.B. and Han, Y.F., Journal of Materials Science, 2001. **36**: p. 4755-4762.

140. Lee, D.B. and Kim, D.J., Intermetallics, 2001. **9**: p. 51-56.

141. Susan, D.F. and Marder, A.R., Acta Materialia, 2001. **49**: p. 1153-1163.

142. Bull, S.J., Oxidation of Metals, 1998. **49**(1-2): p. 1-17.

143. Evans, H.E. and Lobb, R.C., Corrosion Science, 1984. **24**(3): p. 209-222.

144. Hancock, P. and Nicholls, J.R., Materials at High Temperatures, 1994. **12**(2-3): p. 209-217.

145. Rahmel, A. and Schütze, M., Oxidation of Metals, 1992. **38**(3-4): p. 255-266.

146. Grabke, H.J., Intermetallics, 1999. **7**: p. 1153-1158.

147. Pint, B.A., Oxidation of Metals, 1997. **48**(3-4): p. 303-328.

148. Grabke, H.J., Surface and Interface Analysis, 2000. **30**: p. 112-119.

149. Meier, G.H., Pettit, F.S., and Smialek, J.L., Materials and Corrosion, 1995. **46**: p. 232-240.

150. Schumann, E., Yang, J.C., and Graham, M.J., Scripta Materialia, 1996. **34**(9): p. 1365-1370.

151. Chevalier, S. and Larpin, J.P., Acta Materialia, 2002. **50**: p. 3105-3114.

152. Jedliński, J., Corrosion Science, 1993. **35**(5-8): p. 863-869.

153. Peraggi, B. and Rapp, R.A., Materials at High Temperatures, 1994. **12**(2-3): p. 229-234.

154. Haugsrud, R., Corrosion Science, 2003. **45**: p. 1289-1311.

155. Czerwinski, F. and Smeltzer, W.W., Oxidation of Metals, 1993. **40**(5-6): p. 503-527.

156. Pint, B.A., Materials Science Forum, 1997. **251-254**: p. 397-404.

157. Grabke, H.J., *Carburization: A High Temperature Corrosion Phenomenon*. 1998, St.Louis, MO, USA: MTI.

158. Tokura, S., Otsuka, N., and Kudo, T., Corrosion, 1993. **49**(7): p. 561-568.

159. Bennett, M.J., Materials and Corrosion, 1998. **49**: p. 345-351.

160. Browne, J., Broutin, P., and Ropital, F., Materials and Corrosion, 1998. **49**: p. 360-366.

161. Alstrup, I., Tavares, M.T., Bernardo, C.A., Sorensen, O., and Rostrup-Nielsen, J.R., Materials and Corrosion, 1998. **49**: p. 367-372.

162. Figueiredo, J.L., Materials and Corrosion, 1998. **49**: p. 373-377.

163. Ganser, B., Wynns, K.A., and Kurlekar, A., Materials and Corrosion, 1999. **50**: p. 700-705.

164. Steurbaut, C., Grabke, H.J., Stobbe, D., Van Buren, F.R., Korf, S.J., and Defrancq, J., Materials and Corrosion, 1998. **49**: p. 352-359.

165. Klöwer, J. and Heubner, U., Materials and Corrosion, 1998. **49**: p. 237-245.

166. Hemptenmacher, J. and Grabke, H.J., Materials and Corrosion, 1983. **34**: p. 333-340.

167. Seiersten, M., Simon, C., and Osvold, K., Materials Science Forum, 1997. **251-254**: p. 559-566.

168. Mitchell, D.R.G., Young, D.J., and Kleemann, W., Materials and Corrosion, 1998. **49**: p. 231-236.

169. Piekarski, B., Corrosion Review, 2001. **19**(5-6): p. 453-465.

170. Southwell, G., Macalpine, S., and Young, D.J., Materials Science and Engineering, 1987. **88**: p. 81-87.

171. Clark, T.J., Ceramic Engineering and Science Proceedings, 1997. **18**(3A): p. 47-54.

172. Lang, E., Bennett, M.J., and Knights, C.F., Materials Science and Engineering, 1987. **88**: p. 21-29.

173. Liu, C.T., George, E.P., Sikka, V.K., and Deevi, S.C., *Design of Ni_3Al alloys for structure use*, in *Processing and Design Issues in High-Temperature Materials*, N.S. Stoloff and R.H. Jones, Editors. 1996, Minerals, Metals & Materials Society: Warrendale, PA, USA. p. 139-157.

174. Grabke, H.J., Materials and Corrosion, 1998. **49**: p. 303-308.

175. Szakálos, P., Materials and Corrosion, 2003. **54**(10): p. 752-762.

176. Grabke, H.J. and Spiegel, M., Materials and Corrosion, 2003. **54**(10): p. 799-804.

177. Szakálos, P., Pettersson, R., and Hertzman, S., Corrosion Science, 2002. **44**: p. 2253-2270.

178. Pippel, E., Woltersdorf, J., Grabke, H.J., and strauß, S., Steel Research, 1995. **66**(5): p. 217-221.

179. Schneider, R., Pippel, E., Woltersdorf, J., Strauß, S., and Grabke, H.J., Steel Research, 1997. **68**(7): p. 326-332.

180. Schneider, R., Viefhaus, H., Inden, G., Grabke, H.J., and Müller-Lorenz, E.M., Materials and Corrosion, 1998. **49**: p. 336-339.

181. Klöwer, J., Grabke, H.J., and Müller-Lorenz, E.M., Materials and Corrosion, 1998. **49**: p. 328-329.

182. Baker, B.A., Hartmann, V.M., Shoemaker, L.E., McCoy, S.A., and Rajendran, S., Transactions of The Indian Institute of Metals, 2003. **56**(3): p. 327-333.

183. Grabke, H.J., Müller-Lorenz, E.M., Strauss, S., Pippel, E., and Woltersdorf, J., Oxidation of Metals, 1998. **50**(3-4): p. 241-254.

184. Grabke, H.J., Müller-Lorenz, E.M., and Zinke, M., Materials and Corrosion, 2003. **54**(10): p. 785-792.

185. Strauß, S. and Grabke, H.J., Materials and Corrosion, 1998. **49**: p. 321-327.

186. Strauß, S., Krajak, R., Palm, M., and Grabke, H.J., Materials and Corrosion, 1996. **47**(12): p. 701-702.

Chapter 2

Electrodeposited Ni–Al Composite Coatings with High Al Content via Sediment Co-deposition*

* A version of this chapter has been published. Liu, H.F. and Chen, W.X., **Surface and Coatings Technology**, 2005. 191: p. 341-350.

2.1 Introduction

In recent years, Ni_3Al intermetallic alloys have attracted considerable attention because of their great potential for high-temperature structural applications due to low density, high strength at elevated temperature, and excellent resistance to high-temperature corrosion [1-6]. However, poor ductility at room temperature limits wide use of intermetallics as structural materials. Although major strides have been made to overcome the drawbacks of intermetallic-compound-based alloys, much progress has yet to be made to reduce processing cost and improve ductility and creep properties before the alloys can be widely utilized in monolithic or bulk form. Nevertheless, these shortcomings are not expected to impose much difficulty when the alloys are used as protective coating materials.

Currently, many coating techniques—for example, physical vapor deposition (PVD) [7], Self-propagating high-temperature synthesis (SHS) [8] and thermal spraying [2]—have been employed to produce Ni_3Al intermetallic coatings on various substrates. Recent interests are to adopt conventional electrodeposition (CED) to prepare nickel aluminide coatings [9, 10]. This is a two-step process involving co-deposition of metal matrix (e.g., Ni)/metal particle (e.g., Al) composites and, secondly, diffusion treatment to form alloy coatings. Compared to other coating techniques, CED is a low-cost and can be performed at low temperature. It is particularly suitable for tubes with complex shapes and the internal surfaces of small tubes, which are difficult or impossible to coat by other methods. Furthermore, CED coatings have excellent surface quality and adhesion to substrate. To date, several composite systems, including Ni-Al, Ni-Ti, Ni-Cr, Ni-Zr and Ni-CrAlY, have been reported [9-17].

Izaki et al. [9] reported electrodeposited Ni-Al coatings from Watt's nickel solution using 9 μm Al particles. When heated in vacuum at 800 °C for 3 hr, the microstructure of alloy coatings changed from single γ-Ni phase to single γ'-Ni_3Al phase with increasing Al content. More recently, Susan et al. [10] produced Ni-Al coatings from nickel sulphamate solution, which contained maximum 20vol% Al particles. Two-phase Ni-Al coatings (γ-Ni + γ'-Ni_3Al) were obtained after diffusion treatment at 825 °C

for 3hr in vacuum. Results showed that these Ni-Al coatings have good oxidation resistance below 900 °C [18, 19]. To achieve good oxidation resistance above 900 °C, Al content in composites should be increased so that more thermodynamically stable phases such as γ'-Ni_3Al or β-NiAl can be formed. For example, the formation of single-phase γ'-Ni_3Al requires an Al content of 22~28mol% (30~37vol%) in the coating [9].

Most Ni-Al composite coatings are produced with the CED technique, in which the anode and cathode are vertically inserted in the bath. The work by Susan et al. [10] showed that a maximum of 20vol% Al was produced at about 300g/l of particle loading, and further increase in particle loading didn't yield a higher particle volume fraction in coating. One may use surfactants to obtain more incorporation of particles in composites. Ni-PTFE composite coatings with 70vol% PTFE particles were obtained using cationic and nonionic surfactants [20]. However, excessive surfactants will reduce the cathode efficiency [21] and increase the brittleness of deposits [20].

A novel coating technique called sediment co-deposition (SCD) has been developed by Viswanathan [22]. In this technique, the cathode is horizontally set in the bath. Periodic stirring is used to keep particles suspended in solution and sediment on the cathode. A maximum of 50vol% particles in the coating was obtained for Ni-graphite [22] and Ni-WS_2 [23], and 45vol% for Ni-MoS_2 [23] via SCD that required low particle loading in the bath. Recently, Napłoszek-Bilnik [11, 12] reported that 44wt% Al particles were deposited in Ni-Al coatings via SCD. However, rough surface made coatings inapplicable. Another sediment technique called barrel plating was introduced by Foster et al. [15] and Honey et al. [16] to deposit MCrAlY coatings. Up to 40vol% of CrAlY particles was successfully deposited in composites. However, compared to SCD, because it requires specialized equipments, barrel plating is more complicated.

This chapter is aimed at extending the SCD technique to develop applicable Ni-Al composite coatings on the centrifugally cast Fe-Ni-Cr tube alloys from a Watt's type bath. The objectives were firstly to produce Ni-Al composite coatings with high Al content to form single-phase γ'-Ni_3Al coatings after diffusion treatment, and secondly to

understand the effects of deposition parameters on the Al particle deposition in the coatings, as most of the SCD deposition involves inert (non-conductive) particles.

2.2 Experimental

2.2.1 Sediment Co-deposition

The basic setup of the SCD technique is depicted in Fig. 2-1. The anode is located on top of the plating bath, and the cathode (substrate to be coated) is positioned horizontally below the anode. One "On/Off" controller provided periodic stirring through a stir bar.

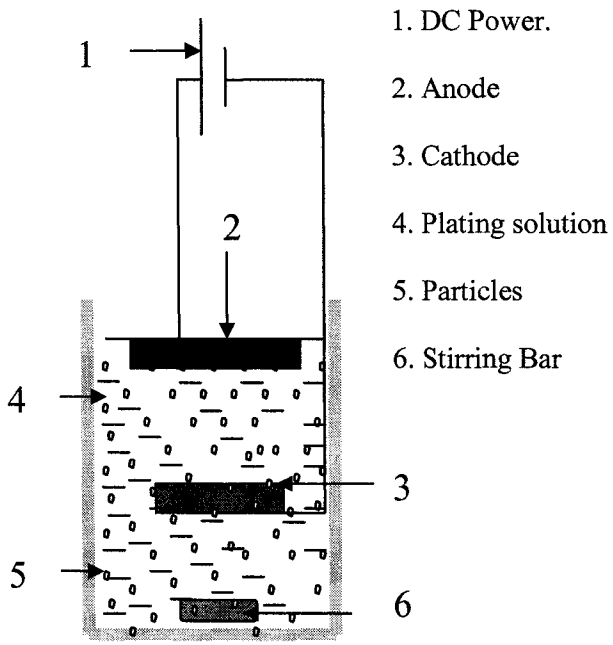

Figure 2-1. Schematic diagram of sediment co-deposition (SCD) setup.

The centrifugally cast high-performance alloy (HP alloy) was used as the coating substrate, whose chemical compositions were as follows: 35wt% Ni, 25wt% Cr, 0.4wt% C, <1.5wt% Si, <1.5wt% Mn, <1.5wt% Nb, and balanced Fe. Coupons of HP alloy of dimensions 20mm×10mm×2mm were machined and ground using SiC papers up to 600-grit finish. Coatings were deposited on the 20mm×10mm surface. The anode was a pure Ni plate ground by SiC paper to 240-grit finish.

The composition of the Watt's type nickel bath and typical operating conditions are given in Table 2-1. Al powder purchased from Valimet Inc. (Stockton, CA, USA) had a size distribution of 3.0~4.5 μm. Before electroplating, the anode and cathode were pretreated according to ASTM B343-92a [24] and ASTM B558-79 [25] respectively. For characterization, some as-plated coupons were sectioned, mounted, and polished with diamond slurry from 6 μm to 1 μm. All samples were finally polished with 0.05 μm colloidal silica.

Table 2-1. Watt's type nickel bath and typical operating conditions.

Watt's type nickel solution:	**Operating conditions**:
Nickel sulfate ($NiSO_4 \cdot 6H_2O$): 270 g/l	Anode: pure Ni
Nickel Chloride ($NiCl_2 \cdot 6H_2O$): 45 g/l	pH: ~4.0
Boric acid (H_3BO_3): 40 g/l	Temperature: room temperature
Sodium dodecyl sulphate	Current density: 20-90 mA/cm^2
($CH_3(CH_2)_{10}CH_2OSO_3Na$): 0.2 g/l	
Particle: pure Al particle, ~3 μm	Stirring rate: 400 rpm
	Particle loading: 5-150 g/l
	Off/On time: typically 10s/1200s
	Plating time: 3 hr

2.2.2 Volume Fraction of Al Particles

The as-plated Ni-Al coatings were examined on a JSM-6302FXV Field Emission Scanning Microscope. To determine the volume fraction of Al particles in composite coatings, backscattered electron (BSE) images at 1000× magnification were taken from various locations of each coupon, which were then processed using Image software, Image-Pro® Plus Version 4.0.0, to obtain the volume fraction of Al particles. In this software, areas or phases of different darkness can be separated and analyzed by adjusting the threshold level of darkness. The area percent of spherical Al particles obtained from the measurements was assumed to be the volume fraction of Al particles in the composite coatings.

2.2.3 Diffusion treatment

Izaki et al. [9] and Susan et al. [26] have provided details of reaction synthesis for Ni-Al composite coatings. Although the formation of an intermetallic phase can occur at temperaures as low as 500 °C, practically, a temperature of diffusion treatment about 800 °C is preferred due to shortened processing time. In this investigation, as-plated samples were annealed in vacuum under different conditions (Table 2-2). The phase structure of the treated coatings was determined using small-angle X-ray diffraction (XRD), which was performed on a Rigaku X-ray diffractometer with the Cu K_α incident radiation generated at 40kV and 110 mA. A fixed incident angle of 4 degrees and a 2θ range of 20 to 90 degrees were adopted to collect the X-rays. The XRD patterns were then analyzed with the aid of Jade Version 2.1.

Table 2-2. Conditions of diffusion treatment of Ni-Al particles composite coatings.

Samples	Conditions
Particle loading: 80 g/l	1: 550 °C, 2 hr 2: 550 °C, 2 hr + 670 °C, 2hr 3: 550 °C, 2 hr + 670 °C, 2hr + 800 °C, 3hr 4: 800 °C, 3 hr

2.3 Results and Discussion

2.3.1 Morphology of SCD Coatings

A typical SCD Ni-Al composite coating is shown in Figs. 2-2 (a) and (b). The composite coating is uniform in thickness, which was controlled to be about 100 μm (Fig. 2-2). Spherical Al particles (black phase) are homogeneously distributed in Ni matrix coating (white phase). No defects such as pores and cracks were observed in the coatings. It should be noted that some particles with gray color are also present in the figure, which are Al particles beneath a thin layer of nickel matrix. To reduce the error of analysis, these gray particles were excluded by adjusting the threshold level above their darkness.

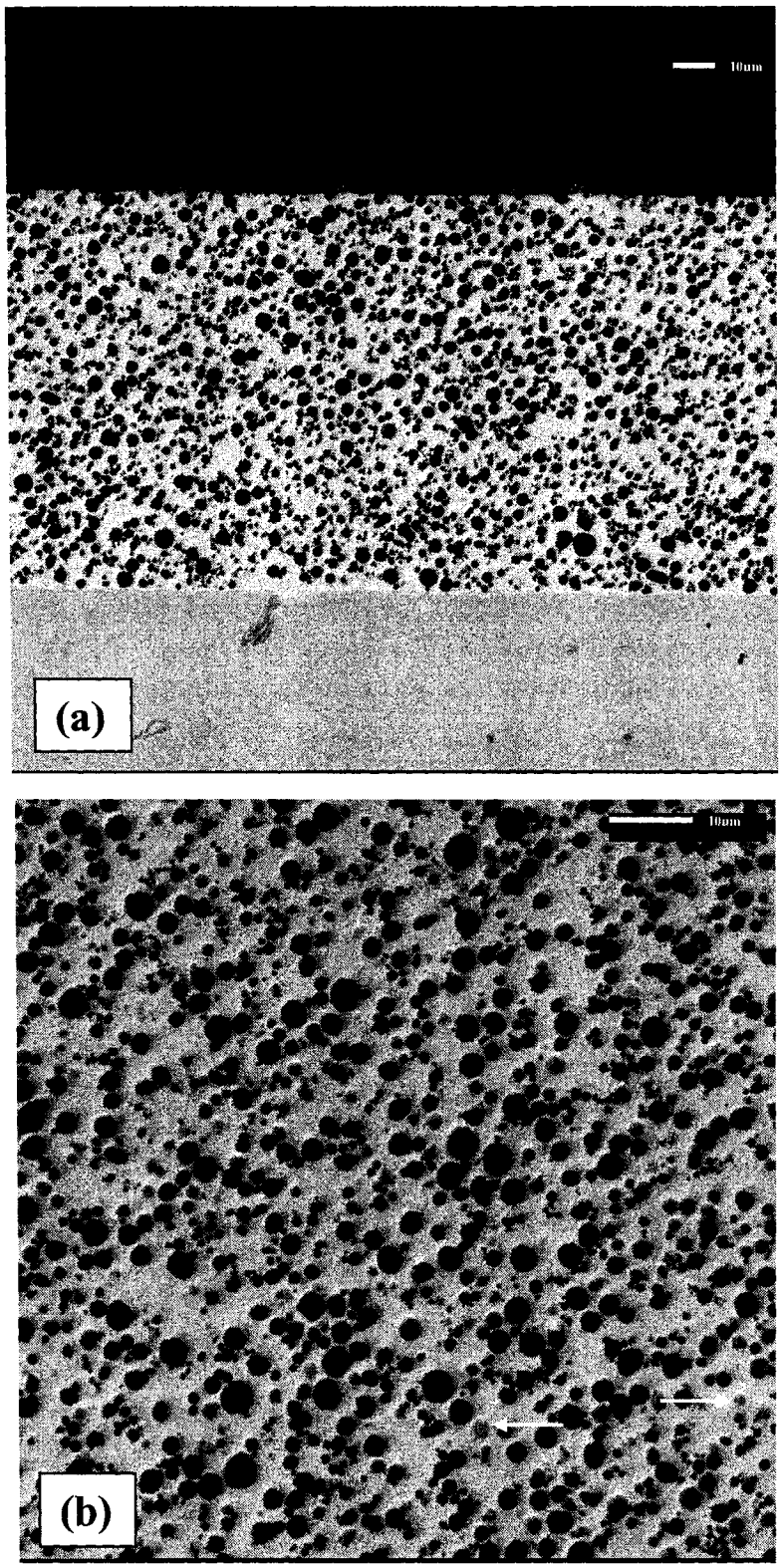

Figure 2-2. Typical BSE micrographs of SCD Ni-Al composite coating (80 g/l, 10s/1200s): (a) low magnification; (b) high magnification.

2.3.2 Effects of Processing Parameters

2.3.2.1 Current Density

The effect of current density on the volume fraction of Al particles is shown in Fig. 2-3 for three different particle loadings, 15 g/l, 40 g/l, and 80 g/l. The stirring Off/On time is set to be 10s/1200s for all tests. Generally, the volume fraction of Al particles with 15 g/l is relatively lower than that with 40 g/l. According to Fig. 2-3, little change in the Al volume fraction with increasing current density was observed at 15g/l and 40g/l loadings. This behavior is similar to that of SCD Ni-graphite system [22] and CED Cr-graphite system [27]. Barmak et al. [28] and Susan et al. [10] reported similar phenomena in CED Ni-Al system, although there was a small peak of particle fraction at 50 mA/cm^2. The current-density dependence in the present work is different from those reported for non-conducting particle systems such as Ni-WS_2 and Ni-MoS_2 [23], Ni-Al_2O_3 [28], Cu-Al_2O_3 [29], Ni-SiC [30], Cu-SiO_2 [31] and ZnNi-SiC [32], where one or multiple peaks of particle content with increasing current density were observed.

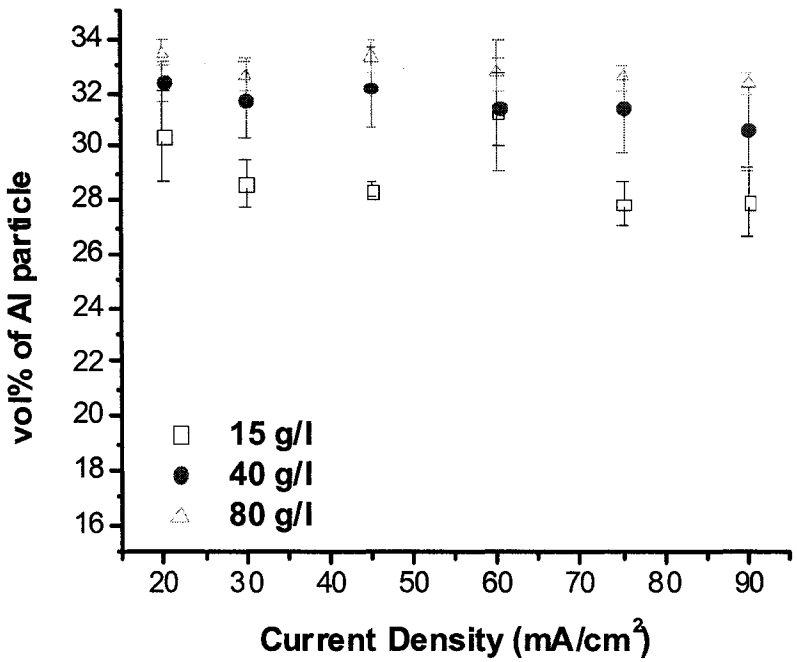

Figure 2-3 The effect of current density on the Al content in composite coatings.

2.3.2.2 Particle Loading

Deposition with particle loadings ranging from 5 g/l up to 150 g/l was performed at a fixed current density of 45 mA/cm^2 and Off/On time of 10s/1200s. The variation of the Al content in the coatings with the particle loading in the bath and the volume fraction of Al particles in the bath is plotted in Figs. 2-4 (a) and (b) respectively.

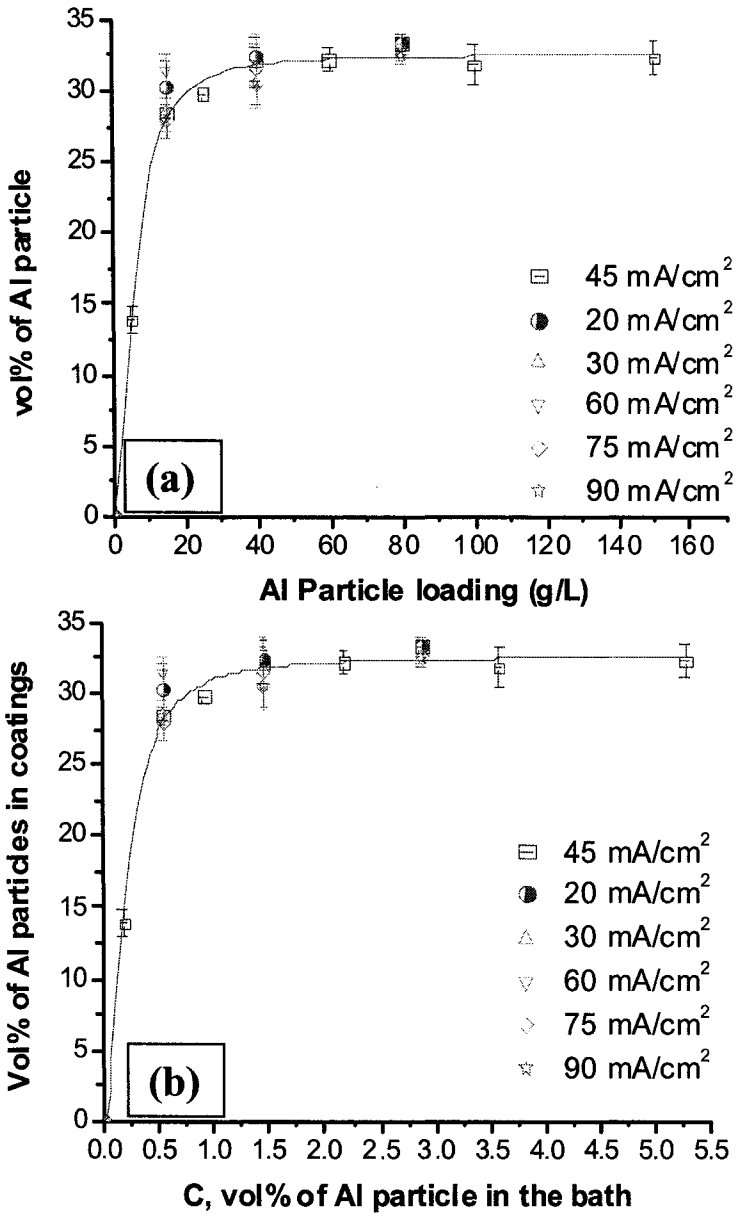

Figure 2-4. The effect of particle loading (or particle concentration) on the volume fraction of Al particles in composite coatings: (a) particle loading; (b) particle concentration.

Two regions are apparent in both Fig. 2-4 (a) and Fig. 2-4 (b). In region I, where the particle loading was varied from 0 g/l to 40 g/l (0vol% ~ 1.46vol%), the volume fraction of Al particles increased abruptly with an increase in particle loading. Beyond 40 g/l (region II), the volume fraction is seen to be insensitive to the change in particle loading. This trend is similar to those reported in other coating systems including Ni-graphite [22], Ni-MoS_2 and Ni-WS_2 [23], Ni-Al [26], Cr-graphite [27], Ni-SiC [30], and Zn-polystyrene [33]. Susan [26] also reported that the particle size had little effect on the co-deposition of Al particles, and hence the curves in Fig. 2-4 (a) and (b). According to Fig. 2-4 (a) and (b), the particle content in region II fluctuates between 30vol% and 35vol%, which is lower than a maximum 50vol% of graphite in SCD Ni-graphite (conducting particles) composites [22] but significantly higher than maximum 20vol% of Al in CED Ni-Al composite [26]. Compared to CED Ni-Al coatings, the particle content in SCD Ni-Al coatings is saturated at a much lower bath loading. The critical particle loading is 40 g/l (1.46vol%) in the current SCD Ni-Al system, but was as high as 300 g/l (10.53vol%) in the CED Ni-Al system.

2.3.2.3 Off/On Time

As shown in Fig. 2-5, the particle content in the coating is independent of the Off/On time ratio from 0 to 1, although considerable scatter is seen in the data at a loading of 40 g/l. Fig. 2-6 (a) shows the effect of the Off time on the incorporation of Al particles in coatings when the On time is fixed at 1200s. It is clear that the Off time has little effect on the volume fraction of Al particles. When the Off time is set at 10s, decreasing the On time also has an insignificant influence on the volume fraction of Al particle according to Fig. 2-6 (b). The Off/On time controls the sediment and suspension of Al particles during deposition. Longer Off time may allow more Al particles to settle on the cathode and to be embedded in composite coatings. However, this beneficial effect of the Off time is not shown in Fig. 2-5 and Fig. 2-6, even at a low particle loading of 15 g/l.

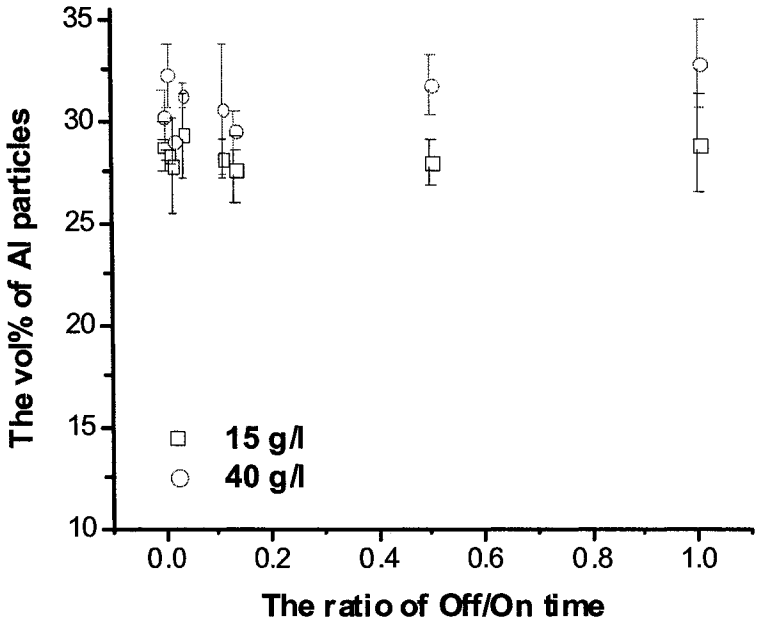

Figure 2-5. The effect of the ratio of Off/On time on Al particle content in composite coatings.

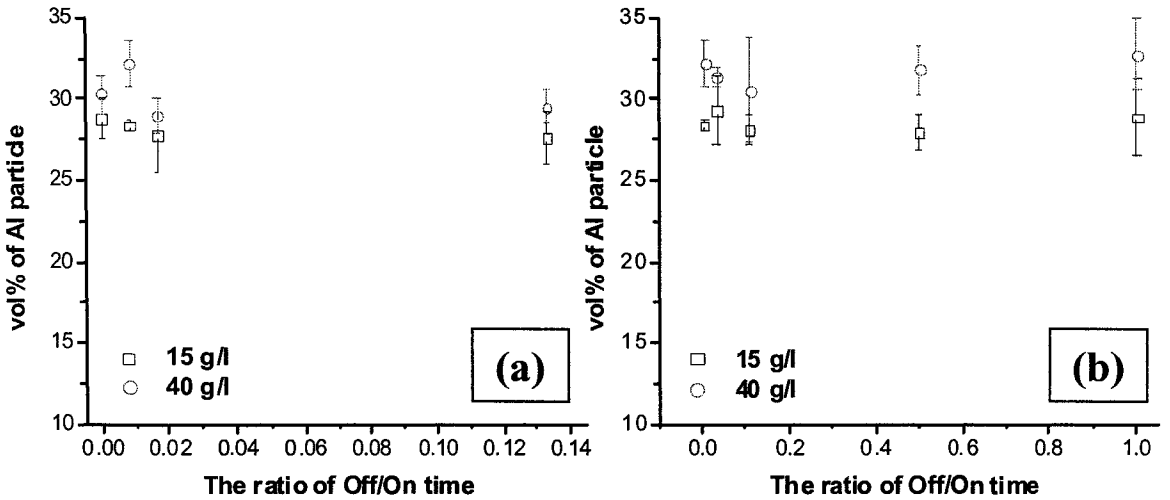

Figure 2-6. The Al particle content in coatings vs the ratio of Off/On time with: (a) fixed On time, 1200s; (b) fixed Off time, 10s.

2.3.3 Co-deposition Mechanism

Although various effective electrodeposited composite coatings have been successfully developed, the co-deposition mechanisms of particles are not fully understood. To date, several mathematical models such as Guglielmi model [34], Celis model [29, 35] and trajectory model [36] have been established to explain the co-

deposition nature of particles and the effects of processing parameters. The Guglielmi model is the first general mathematical model considering the co-deposition mechanism. In this model, the co-deposition occurs through two sequential steps: first, particles adsorbing metal ions are loosely adsorbed on the cathode, and then the reduction of ions provides strong adsorption between particles and the cathode. This model has been proven valid in a number of composite systems [27, 30, 34, 35, 37, 38]. As it is relatively simple in explaining the effect of current density and particle loading, the Gugliemi model is also adopted in the current SCD Ni-Al system.

Generally, the Guglielmi model is expressed by:

$$\frac{C(1-\alpha)}{\alpha} = \frac{Mi_0}{nF\rho_m \upsilon_0}\exp[(A-B)\eta].(\frac{1}{K}+C) \qquad (2\text{-}1\text{-}1)$$

$$\text{when}\,\alpha << 1,\ \frac{C}{\alpha} = \frac{Mi_0}{nF\rho_m \upsilon_0}\exp[(A-B)\eta].(\frac{1}{K}+C) \qquad (2\text{-}1\text{-}2)$$

$$i = (1-\theta)i_0 \exp(A\eta) \qquad (2\text{-}2)$$

where α *is the volume percent of particle in coating,* C *the volume percent of particle in bath,* M *the atomic weight of deposited metal,* n *the valence of deposited metal,* F *the Faraday's constant,* ρ_m *the density of deposited metal,* υ_0 *and* B *the constants related to the particle deposition,* i_0 *and* A *the constants related to the metal deposition,* K *the adsorption coefficient,* η *the cathodic overpotential,* i *the current density, and* θ *the strong adsorption coverage which can be equal to* α. Equation (2-1-1) is a generalized expression that defines links among the volume fraction of particles in the coatings, the current density and the particle concentration in bath. In certain inert particle systems, where the particle content in coatings is fairly low, the factor $(1-\alpha)$ can be omitted and Equation (2-1-2) used. However, in the present SCD Ni-Al system, Equation (2-1-1) should be adopted due to the high Al particle concentration.

According to the Guglielmi model [34], if this model is valid in the SCD Ni-Al system, two characteristics must be met. Firstly, the curve of α vs C must be similar to a Langmuir adsorption isothermal curve. Fig. 2-4 (b) displays this characteristic. Secondly,

a linear relationship must exist between $\frac{C(1-\alpha)}{\alpha}$ and C at a given current density and lines obtained at different current densities must converge at one point where C=-1/K. The slopes of these lines are given by:

$$\tan\psi = \frac{Mi_0}{nF\rho_m \upsilon_0}\exp[(A-B)\eta] \tag{2-3}$$

In Equation (2-2), as α <<1 for some inert particle systems, $(1-\theta)$ can be neglected. Thus Equation (2-2) can be written as:

$$i = i_0 \exp(A\eta) \tag{2-2-1}$$

Therefore, replacing η in Equation (2-3) with Equation (2-2-1) and taking logarithms on the resulting equation yield:

$$\log\tan\psi = \log\frac{Mi_0 B/A}{nF\rho_m \upsilon_0} + (1-\frac{B}{A})\log i \tag{2-4}$$

For current SCD Ni-Al, because α is large, (1-θ) cannot be omitted. However, as the surface of conducting Al particle can be a new cathode for deposition, the effective cathode surface area available for deposition may not decrease, and the correction factor (1-θ) can be neglected here. Thus, Equation (2-4) is also valid in the SCD Ni-Al system.

Fig. 2-7 shows the curve of $\frac{C(1-\alpha)}{\alpha}$ vs C at various current densities. A single line is obtained by fitting these data, for which 1/K=0.181 and K=5.512. Furthermore, one single line rather than a series of lines at various current densities is shown in Fig. 2-7. This means that the slopes of these lines, $\tan\psi$, are independent of current density i. Therefore, in the $\log\tan\psi$ *vs* $\log i$ plot, according to Equation (2-4), $(1-\frac{B}{A})$ must be equal to 0, or $B = A$. According to Equation (2-1-1), when $B = A$, the incorporation of Al particles in composite coatings isn't affected by current density, which is consistent with the experimental data from 20mA/cm^2 to 90mA/cm^2 in Fig. 2-3. The significance of $B = A$ is that the reduction rate of free Ni^{2+} ions in the electrolyte is equal to that of Ni^{2+} ions adsorbed by particles [30], so that the particle content in coating will not change regardless of variation of current density. This behavior, $B = A$, was also observed in the

Cr-graphite system [27], but did not hold in non-conducting particle systems [30, 35, 38] where $B \neq A$.

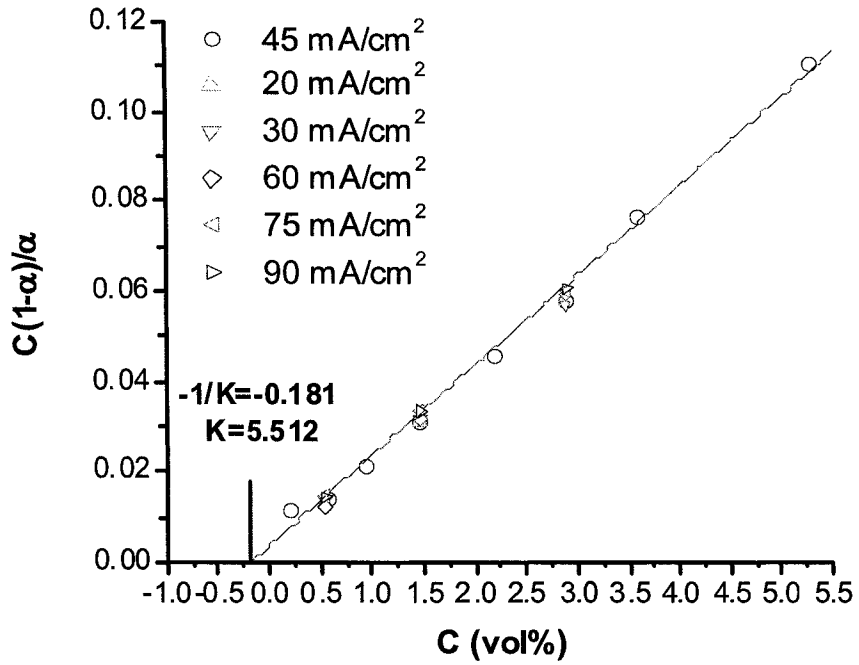

Figure 2-7. $\frac{C(1-\alpha)}{\alpha}$ vs C at different current density.

Previous studies have demenstrated that metal particles behave differently from inert particles [13, 39-41]. For example, metal particles can cause a local rise of electrical field around the cathode that is beneficial to particle deposition. Unlike SiC particles, Cr particles in plating solution can catalyze the deposition of Ni^{2+}. Moreover, the adsorption coefficient K obtained in the current SCD Ni-Al system is much higher than that in some inert particle systems [30, 34, 38]. This indicates that Al particles can be adsorbed more stably onto the cathode than the inert particles, and are less likely to be desorbed from the cathode. Different surface properties of conducting and inert particles in the electrolytic solution may be one reason for dissimilar co-deposition behaviors at various current densities. More fundamental work is necessary to fully clarify this matter.

The effect of particle loading can be explained according to the results presented in Table 2-3. The loose adsorption surface coverage σ, which is a ratio of the cathode

area overshadowed by particles loosely occupied on the cathode to the total cathode area, can be calculated by assuming that the strong adsorption surface coverage θ is equal to the volume fraction of Al particles in coatings in accordance with to Equation (2-5-1) [34]:

$$\sigma = \frac{KC}{1+KC}(1-\theta) \tag{2-5-1}$$

$$\sigma^* = \frac{KC}{1+KC} \tag{2-5-2}$$

Table 2-3. The surface coverage at different particle concentration in bath.

C (%)	θ (%)	σ (%)	σ^* (%)
0.185	13.957	42.854	49.805
0.552	28.447	53.510	74.784
0.917	29.803	58.349	83.121
1.460	32.207	60.121	88.683
2.174	31.823	62.795	92.107
2.878	33.593	62.369	93.920
3.571	31.897	64.727	95.042
5.263	32.330	65.35	96.581

In Table 2-3, σ and θ are much higher than C. Also, the strong adsorption surface coverage θ is smaller than the loose adsorption surface coverage σ, which means that the strong adsorption controls the kinetics of co-deposition of Ni-Al composites. At low particle loading, σ and θ can increase effectively as C increases. However, at high particle loading, the loosely adsorbed Al particle parameter, σ, quickly reaches the limit with a further increase of C, as does θ. One saturated layer apparently forms over the cathode surface, which further blocks the loose adsorption of Al particles. This may have occurred due to the interaction among charged particles when particle concentration is high. It should be noted that the loose adsorption coverage σ calculated using Equation (2-5-1) might be underestimated. This is so because the equation was originally proposed for inert particles, where the deposited particles reduce the effective cathode surface area for deposition. For conducting metal particles such as Al, the particle surface can be the new cathode for deposition. Therefore, the loose adsorption coverage, σ^*, as listed in Table 2-3, should be computed using Equation (2-5-2) without

considering the correction factor, $1-\theta$. Clearly σ^* is much higher than σ. As mentioned earlier, SCD Ni-Al coatings can achieve higher particle content in the coatings at lower particle loading than CED Ni-Al coatings. This can be attributed to the gravity and the position of the cathode. For the SCD technique, the gravitational force on the Al particles facilitates sediment of more particles on the horizontal cathode, which increases the opportunity of the loose and strong adsorption of the Al particle on the cathode. In addition, the horizontal cathode can hold more particles than a vertical cathode, and can enable particles to be engulfed by deposited Ni coating. One possible reason for the minor effect of the Off/On time on the particle content in coatings is that the loose adsorption σ and the strong adsorption θ on cathode have reached a saturated level regardless of the Off/On time at a certain particle loading and agitation rate.

2.3.4 Diffusion Treatment

The microstructure of coated coupons annealed at different temperatures is shown in Figs. 2-8 (Backscatter [BSE] electron images).

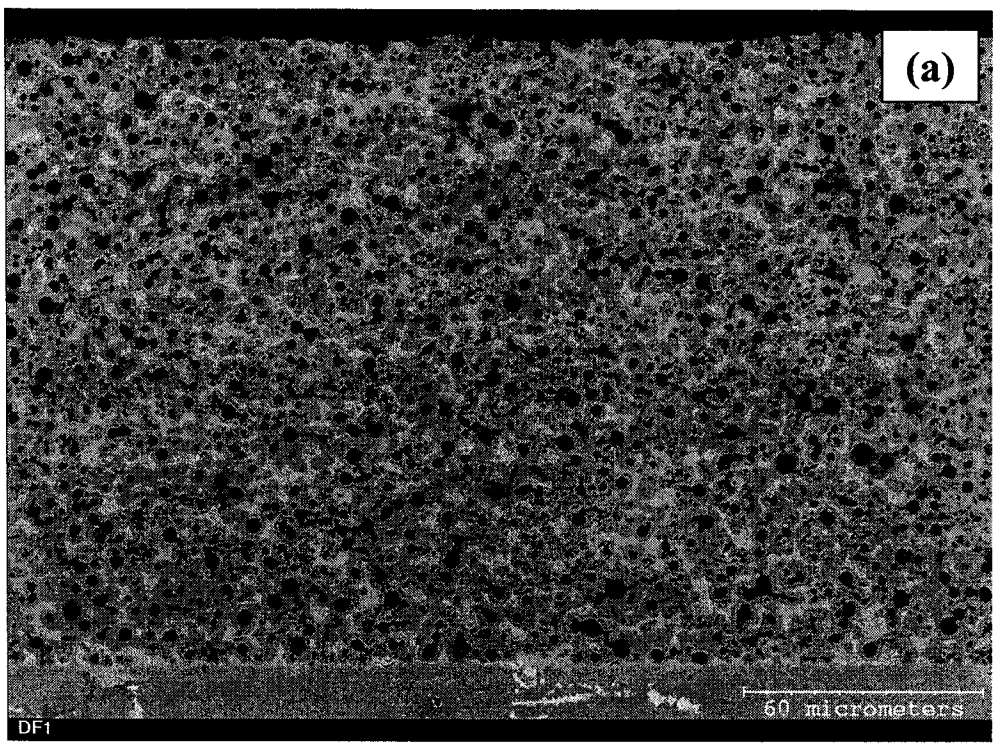

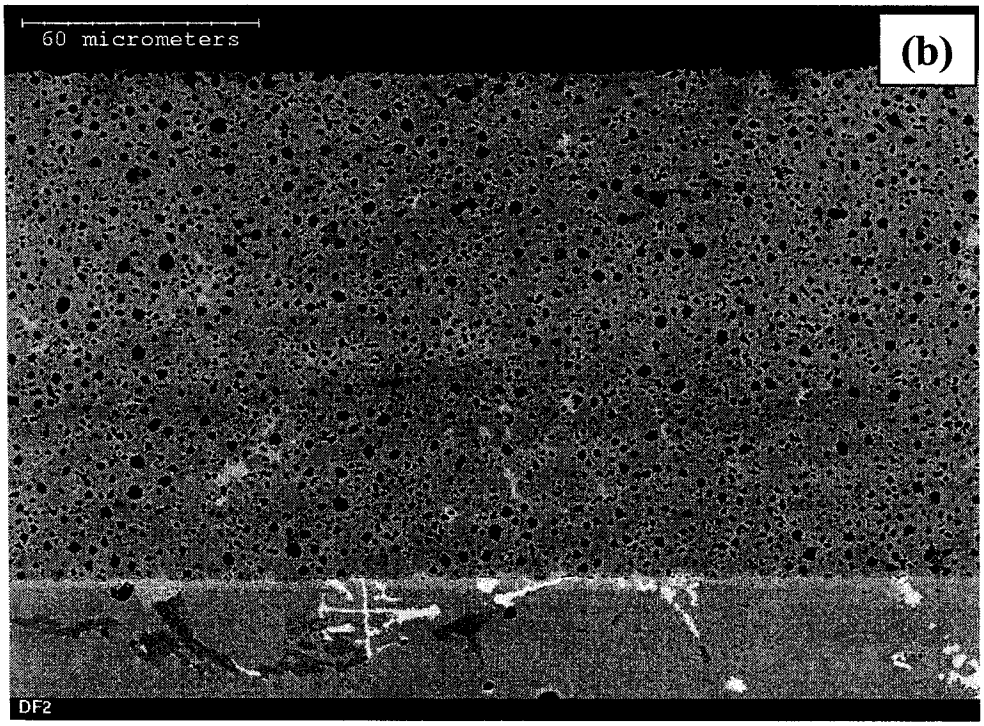

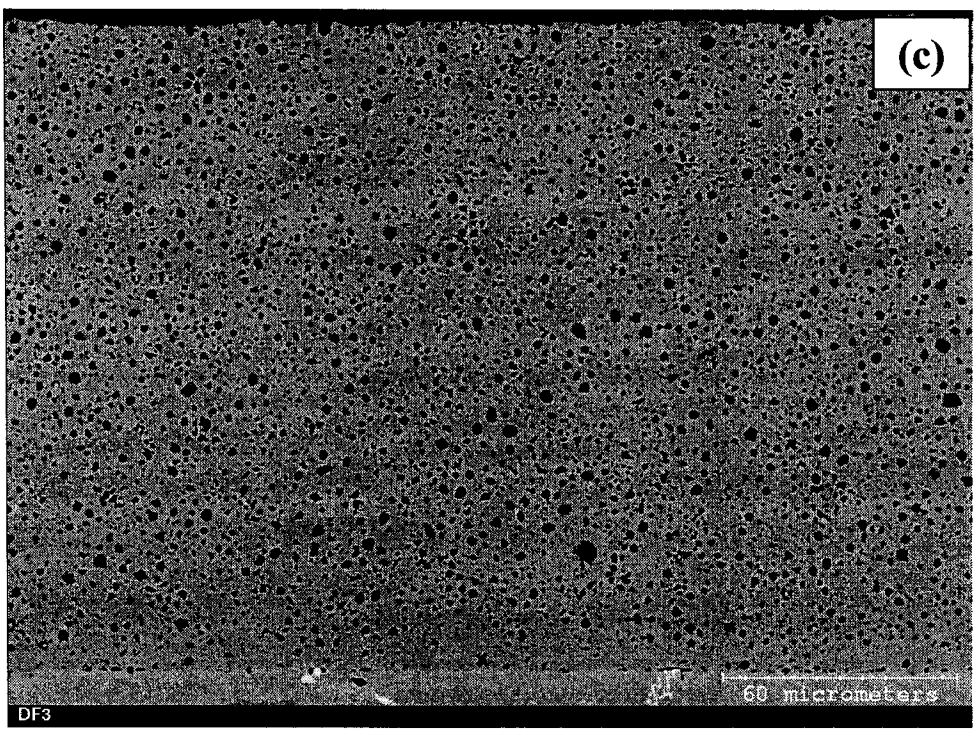

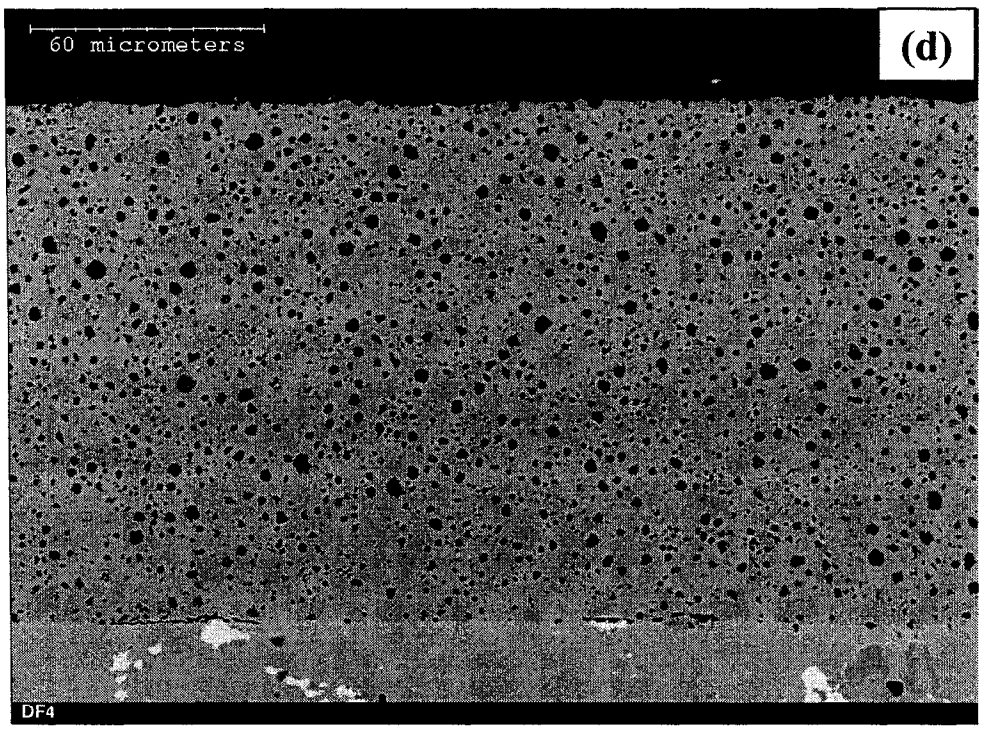

Figure 2-8. The morphologies of annealed Ni-Al composite coatings at different conditions: (a) 550 °C, 2 hr; (b) 550 °C, 2 hr +670 °C, 2 hr; (c) 550 °C, 2 hr +670 °C, 2 hr + 800 °C, 3 hr; (d) 800 °C, 3 hr.

At low temperature, 550 °C for 2hr, both the Ni-Al intermetallic phase (gray region in Fig. 2-8 (a)) and the γ-Ni phase (bright region) are observed in the coating. With an increase in diffusion temperature and time, as is seen in Fig. 2-8 (b), (c) and (d), γ-Ni phase is reduced and disappears at 800 °C, and the homogeneous Ni-Al intermetallic phase is formed.

The XRD results in Fig. 2-9 provide phase information under the different annealing conditions shown in Table 2-2. Three phases, γ-Ni, γ'-Ni_3Al and β-NiAl, are detected in annealed coating under condition 1 (550 °C for 2 hr). According to Fig. 2-9, no Al phase (the major peak of $2\theta=38.473°$) was detected. Susan [26] has also reported that the Al particles in Ni-Al composite coatings would quickly disappear upon heating to a temperature above 500 °C for a short period (less than an hour). When diffusion temperature and time are increased, 550 °C for 2 hr followed by 670 °C for 2 hr, the β-NiAl phase was not detected and the γ-Ni phase is reduced. For the annealed samples

under two other high temperature conditions, only the γ'-Ni_3Al phase is detected. These results are consistent with the SEM observations in Fig. 2-8. The detection of single Ni_3Al phase in Fig. 2-9 under condition 3 and condition 4, along with the uniform phase observed in Fig. 2-8 (c) and (d), also confirms that a volume fraction of Al particles in the as-plated coatings was indeed around 30-35vol%. Final annealed coatings contained significant amounts of porosity (Fig. 2-8 (c) and (d)). The pores might be formed due to local densification during the melting of Al, and rapid diffusion of Al into Ni matrix [9, 26].

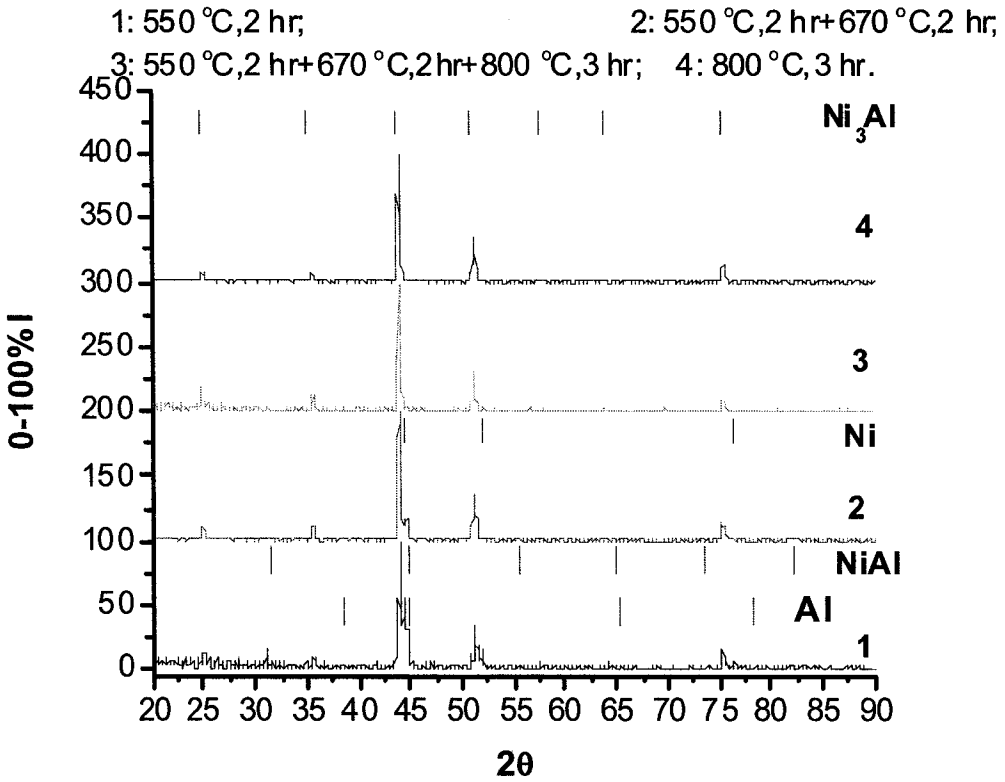

Figure 2-9. The XRD patterns of annealed Ni-Al composite coatings under four different conditions of diffusion treatment.

2.4 Concluding Remarks

Ni-Al particles composite coatings are successfully developed via sediment co-deposition (SCD) technology. Compared to the Ni-Al composites via conventional electro-deposition (CED), higher Al particle content in coatings ranging from 30vol% to

35vol% can be obtained at very low particle loading in the bath. Deposition parameters have distinct effects on particle incorporation in coatings. The volume fraction of Al particles in composite coatings is determined mainly by the particle loading in the bath. Current density and Off/On time have little or no influence on particle incorporation. The co-deposition behavior, which is different from that in inert particle systems, can be explained by the Guglielmi two-step adsorption model. Due to a high volume fraction of Al particles in Ni-Al composites coating, single phase γ'-Ni_3Al alloy coatings can be formed after diffusion treatment.

2.5 Bibliography

1. Brill, U., Materials and Corrosion, 1990. **41**(12): p. 682-688.

2. Sidhu, B.S. and S. Prakash, Surface and Coatings Technology, 2003. **166**: p. 89-100.

3. Klöwer, J., U. Brill, and U. Heubner, Intermetallics, 1999. **7**: p. 1183-1194.

4. Deevi, S.C. and V.K. Sikks, Intermetallics, 1996. **4**: p. 357-375.

5. Sikka, V.K., S.C. Deevi, S. Viswannathan, R.W. Seindeman, and M.L. Santella, Intermetallics, 2000. **8**: p. 1329-1337.

6. Stoloff, N.S., C.T. Liu, and S.C. Deevi, Intermetallics, 2000. **8**: p. 1313-1320.

7. Banerjee, R., G.B. Thompson, P.M. Anderson, and H.L. Fraser, Thin Solid Films, 2003. **424**: p. 93-98.

8. La, P.Q., M.W. Bai, Q.J. Xue, and W.M. Liu, Surface and Coatings Technology, 1999. **113**: p. 44-51.

9. Izaki, M., M. Fukusumi, H. Dnomoto, T. Omi, and Y. Nakayama, Journal of The Japan Institute of Metals, 1993. **57**(2): p. 182-189.

10. Susan, D.F., K. Barmak, and A.R. Marder, Thin Solid Films, 1997. **307**: p. 133-140.

11. Napłoszek-Bilnik, I., A. Budiok, and E. Łągiewka, Journal of Alloys and Compounds, 2004. **382**: p. 54-60.

12. Napłoszek-Bilnik, I., A. Budiok, B. Łosiewicz, L. Pająk, and E. Łągiewka, Thin Solid Films, 2005. **474**: p. 146-153.

13. Bazzard, R. and P.J. Boden, Transactions of The Institute of Metal Finishing, 1972. **50**: p. 63-69.

14. Sova, V., Transactions of The Institute of Metal Finishing, 1987. **65**: p. 21-23.

15. Foster, J., B.P. Cameron, and J.A. Carew, Transactions of The Institute of Metal Finishing, 1985. **63**: p. 115-119.

16. Honey, F.J., E.C. Kedward, and V. Wride, Journal of Vacuum Science and Technology A., 1986. **4**(6): p. 2593-2597.

17. Saremi, M. and M. Bahraini, Transactions of The Institute of Metal Finishing, 2003. **81**(1): p. 24-27.

18. Susan, D.F. and A.R. Marder, Oxidation of Metals, 2002. **57**(1-2): p. 131-157.

19. Susan, D.F. and A.R. Marder, Oxidation of Metals, 2002. **57**(1-2): p. 159-180.

20. Hovestad, H. and L.J.J. Janssen, Journal of Applied Electrochemistry, 1995. **25**: p. 519-527.

21. Watson, A.S., *Organic addition agents for nickel electroplating solutions*. 1989, Toronto, Ontario, Canada: Nickel Development Institute.

22. Viswanathan, M. and M. Ghouse, Metal Finishing, 1979. **77**(10): p. 67-69.

23. Ghouse, M., M. Viswanathan, and E.G. Ramachandran, Metal Finishing, 1980. **78**(4): p. 44-47.

24. *Standard practice for preparation of nickel for electroplating, ASTM designation: B343-92a*. October 1992, Philadelphia, PA: ASTM.

25. *Standard practice for preparation of nickel alloys for electroplating, ASTM designation: B558-79*. April 1979, Philadelphia, PA: ASTM.

26. Susan, D.F., W.Z. Misiolek, and A.R. Marder, Metallurgical and Materials Transactions A., 2001. **32A**: p. 379-391.

27. Narayan, R. and B.H. Narayana, Journal of The Electrochemical Society, 1981. **128**(8): p. 1704-1708.

28. Barmak, K., S.W. Banovic, C.M. Petronis, D.F. Susan, and A.R. Marder, Journal of Microscopy, 1997. **185**(2): p. 265-274.

29. Celis, J.P., J.R. Roos, and C. Buelens, Journal of The Electrochemical Society, 1987. **134**(6): p. 1402-1408.

30. Wang, S.C. and J.W.C. Wei, Materials Chemistry and Physics, 2003. **78**: p. 574-580.

31. Terizieva, V., J. Fransaer, and J.P. Celis, Journal of The Electrochemical Society, 2000. **147**(1): p. 198-202.

32. Müller, C., M. Sarret, and M. Benballa, Surface and Coatings Technology, 2002. **162**: p. 49-53.

33. Hovestad, A., R.J.C.H.L. Heesen, and L.J.J. Janssen, Journal of Applied Electrochemistry, 1999. **29**: p. 331-338.

34. Guglielmi, N., Journal of The Electrochemical Society, 1972. **119**(8): p. 1009-1012.

35. Celis, J.P. and J.R. Roos, Journal of The Electrochemical Society, 1977. **124**(10): p. 1508-1511.

36. Fransaer, J., J.P. Celis, and J.R. Roos, Journal of The Electrochemical Society, 1992. **139**(2): p. 413-425.

37. Grosjiean, A., M. Rezrazi, P. Bercot, and M. Tachez, Metal Finishing, 1998. **96**(4): p. 14-17.

38. Bercot, P., E. Peña-Muñoz, and J. Pagetti, Surface and Coatings Technology, 2002. **157**: p. 282-289.

39. Foster, J. and B.P. Cameron, Transactions of The Institute of Metal Finishing, 1976. **54**: p. 178-183.

40. Watson, S.W. and R.P. Walters, Journal of The Electrochemical Society, 1991. **138**(12): p. 3633-3637.

41. Watson, S.W. and R.P. Walters, Journal of The Electrochemical Society, 1993. **140**(8): p. 2235-2238.

Chapter 3

Reactive Oxide-dispersed Ni_3Al Intermetallic Coatings by Sediment Co-deposition*

* A version of this chapter has been published. Liu, H.F. and Chen, W.X., **Intermetallics**, 2005. 13: p. 805-817.

3.1 Introduction

Because of their excellent resistance to high-temperature oxidation, carburization, and hot corrosion, Ni_3Al intermetallic alloys and coatings have been studied extensively [1-3]. The high-temperature protection of Ni_3Al derives from the formation of a compacted, defect-free and slow-growing alumina scale. Unfortunately, the alumina scale is inherently susceptible to cracking and spalling during thermal cycling, which causes a significant loss of Al and a reduction in the lifetime of Ni_3Al. In practice, reactive elements (REs) such as Y, Ce, Zr, Hf and La or their oxides (REOs) have been employed to improve the alumina scale [4-6]. Benefits claimed from REs (or REOs) include an increase of scale ductility, an improvement in the adherence of scale to substrates, and a reduction of the segregation of harmful elements such as sulfur at the scale/substrate interface [4-6].

Conventionally, REs (or REOs) are dispersed in alloys via casting [7], mechanical alloying and powder metallurgy [8]. They have been deposited by using thermal spraying [6], laser cladding [9], sputtering [10], pack cementation [11] and chemical vapor deposition (CVD) [12]. In some cases, REs were preferentially applied on the substrates as thin films or doped in the surfaces of base alloys using ion implantation [5, 13] and hot dipping [14]. REO coatings such as La_2O_3 applied via atomic layer chemical vapor deposition (ALCVD) [15], Y_2O_3 by metalorganic chemical vapor deposition (MOCVD) [16], and sol-gel coatings such as CeO_2 [17] also have been reported.

Recently, conventional electrodeposition (CED) has been studied to co-deposit REO particles in the metal matrix coatings. In this process, REO particles are suspended in the plating bath under continuous stirring. During the electroplating, the particles are adsorbed on the cathode surface and then entrapped in the metal matrix coating. Peng et al. [18-20] deposited Ni-La_2O_3 composite films to protect Ni, stainless steel, and γ-TiAl from high temperature oxidation. Veleva et al. [21] produced Ni-Y_2O_3 composite coatings from a Watt's bath, which proved to be more resistant to corrosion than pure Ni coatings. Compared to other coating techniques, the CED technique is a low-cost and low-temperature coating method. It offers a simple way to apply reactive oxide-dispersed

protective coatings on various substrates. Moreover, the CED technique was introduced to produce Ni-Al binary alloy coatings [22, 23]. Ni-Al composite coatings can be co-deposited when Al metal particles are added to the nickel plating bath. Proper annealing treatment can form protective Ni-Al binary alloy coatings. For example, single-phase Ni_3Al coatings can be formed provided that sufficient Al particles (30~37vol%) are present in the Ni-Al composite coatings [22]. Therefore, one may produce more complex Ni-Al-REO ternary composite coatings from a nickel plating bath containing Al particles and REO particles, and then induce the *in situ* synthesis of REO-dispersed Ni_3Al coatings by annealing the composites. Barkmak et al. [24] did the initial research on the CED Ni-Al-Al_2O_3 ternary composite coatings. They found that Ni-Al-Al_2O_3 ternary composite coatings with a maximum of 20vol% Al particles can be formed, and that the particle content depends on process parameters such as particle concentration and current density. However, electrodeposited Ni-Al-REO ternary systems have not been reported to date.

In Chapter 2, we successfully employed sediment co-deposition (SCD) to deposit Ni-Al composite coatings, with as high as 30~35vol% of Al particles, from a Watt's nickel bath. Single-phase Ni_3Al intermetallic coatings were formed after the annealing treatment. In this chapter, we extend this SCD technique to co-deposit Ni-Al-REO ternary composite coatings. In order to form single-phase Ni_3Al, it is important to maintain adequate Al content in the coatings. This, however, could not be achieved when REO oxide particles co-existed in the plating bath, and the phase structures in annealed Ni-Al-REO composite coatings could be different.

3.2 Experimental Procedures

3.2.1 Coating Process

Sediment co-deposition (SCD) was used to deposit Ni-Al-REO composite coatings (See Chapter 2 for details). The basic principle of SCD is that the anode is located on top of the plating bath, and the cathode (substrate to be coated) is positioned horizontally below the anode. One On/Off controller provided periodic stirring through a stir bar. Particles were suspended in the solution during On time, and settled on the

cathode in the Off portion of the cycle. Compared to CED, the SCD technique produced a higher particle content in coatings.

The composite coatings were electroplated from a Watt's nickel solution. The composition of the bath and some typical operating conditions are provided in Table 3-1. The centrifugally-cast HP alloy was used as the coating substrate. This alloy contains mainly 35wt% Ni, 25wt% Cr, 0.4wt% C, <1.5wt% Si, <1.5wt% Mn, <1.5wt% Nb, and the balance Fe. Coupons of HP alloy of dimensions 20mm×10mm×2mm were machined, and then ground using SiC paper to a 600-grit finish. Coatings were deposited on the 20mm×10mm surfaces. Al powders, purchased from Valimet Inc. (Stockton, CA, USA), had an average size of 3 μm. Two reactive oxides, CeO_2 and Y_2O_3, purchased from Alfa Aesar, USA, were used in this study. The CeO_2 powders had average sizes of 5 μm and 9~15 nm, and Y_2O_3 powder a particle size less than 1 μm.

Table 3-1. The composition of plating bath and typical operating conditions.

The Watt's nickel bath:	
Nickel sulfate ($NiSO_4 \cdot 6H_2O$): 270 g/l;	Nickel Chloride ($NiCl_2 \cdot 6H_2O$): 45 g/l;
Boric acid (H_3BO_3): 40 g/l;	
Sodium dodecyl sulphate ($CH_3(CH_2)_{10}CH_2OSO_3Na$): 0.2 g/l	
pH: ~4.0	
Operating conditions:	
Anode: pure Ni;	Cathode: Fe-Cr-Ni
Temperature: room temperature;	Current density: 45 mA/cm^2
Stirring rate: 400 rpm;	Off/On time: typically 10s/1200s
Plating time: 4 hr	

3.2.2 Characterization

Prior to plating, coupons were cleaned using acetone and then air-dried. Some coated coupons were annealed in vacuum. A vacuum furnace was pumped down to

around 0.8 mtorr, and heated to 800 °C for 3 hr. Some as-plated and annealed coupons were sectioned, mounted, and then polished with a diamond slurry from 6 μm to 1 μm and finally with 0.05 μm colloid silica.

The microstructure and morphology of the coatings were examined using a S-2700 Scanning Electron Microscope (SEM) (HITACHI, Japan) in the backscattered electron (BSE) mode. The phases of annealed coatings was determined using X-ray diffraction (XRD) in powder mode, which was performed on a Rigaku Geigerflex 2173 diffractometer with the Co K_α incident radiation generated at 40kV and 30mA. A 2θ range of 2 to 120 degrees was adopted to collect the X-rays.

To determine the volume fraction of Al particles in composite coatings, BSE images at 1000× magnification were taken from various locations of each as-plated coupon, which were then processed using Image-Pro® Plus Version 4.0.0 software to obtain the volume fraction of Al particles. Using this software, areas or phases of varying darkness can be separated and analyzed by adjusting the threshold level of darkness. The area fraction of the particles was assumed to be the volume fraction of the particles in the composite coating. The validity of this method was verified in Chapter 2.

3.3 Results

3.3.1 Ni-Al Composite Coatings

According to Chapter 2, the Al particle content in Ni-Al composite coatings strongly depends on the Al bath loading. The volume fraction of Al particles in coatings rapidly increased up to 40 g/l Al bath loading. It then leveled off beyond 40 g/l and produced coatings containing 30vol% to 35vol% Al. The typical morphology of Ni-Al composite coatings obtained with Al particle loading at 80 g/l is shown in Fig 3-1 (a). Spherical Al particles (black phase) are homogeneously distributed in a Ni matrix (light phase). The composite coating shown in Fig. 3-1 (a) contained about 33.5vol% (24.9at%) of Al particles. The coating that was annealed at 800 °C for 3 hr is shown in Fig. 3-1 (b). It can be seen in the micrograph that the annealing treatment produced a uniform single-

phase alloy, which was identified to be single-phase γ'-Ni_3Al, according to the XRD spectrum shown in Fig. 3-2 with diffraction peaks at 2θ=29.024°, 41.550°, 51.490°, 60.175°, 90.346°, and 112.543°. It should be noted that final annealed coatings contained pores (dark phase) as shown in Fig. 3-1(b). The pores were formed due to local densification during melting of Al, and rapid diffusion of Al into the Ni matrix [22, 23].

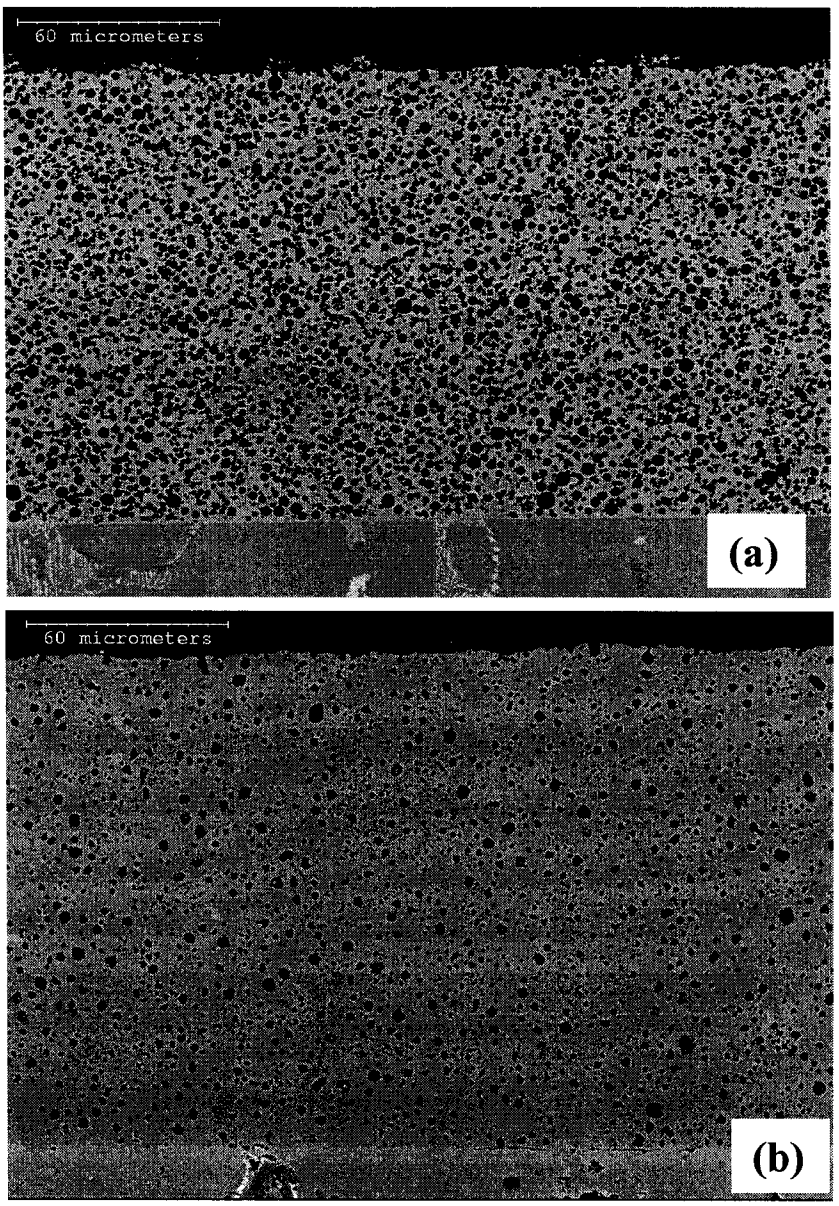

Figure 3-1. Typical BSE micrographs of Ni-Al binary composite coatings with the 80 g/l Al bath loading: (a) as-plated coating, (b) annealed coating.

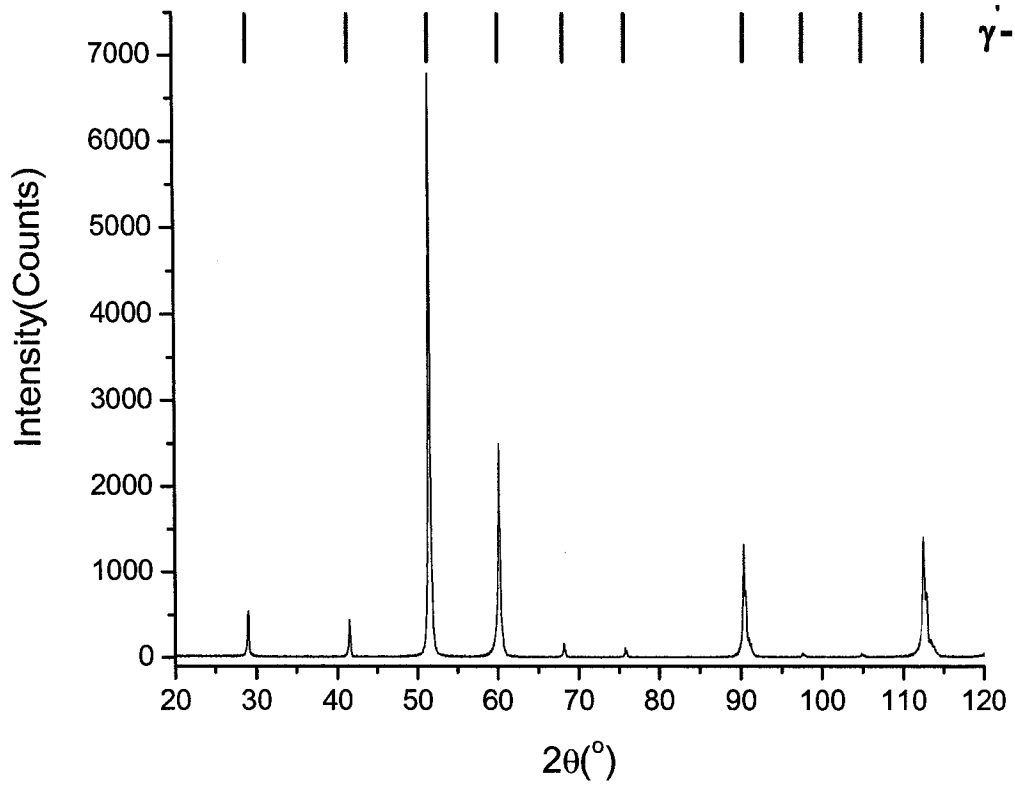

Figure 3-2. The X-ray pattern of the annealed Ni-Al composite coating with the 80 g/l Al bath loading.

3.3.2 Ni-Al-REO Composite Coatings

Ni-Al-REO composite coatings were deposited from a plating bath containing both Al particles and REO particles. The Al particle loading in the plating bath was kept at 80 g/l for all tests. The effects of REO particle loading on the volume fraction of Al particles in composite coatings are illustrated in Fig. 3-3. The phases formed in annealed Ni-Al-REO composite coatings are summarized in Table 3-2.

3.3.2.1 Nano CeO_2 (9-15 nm)

Six bath loadings of nano CeO_2 at 1 g/l, 5 g/l, 10 g/l, 20 g/l, 40 g/l and 80 g/l respectively, were used to deposit Ni-Al-nano CeO_2 composite coatings. According to Fig. 3-3, the volume fraction of Al particles decreased continuously with increasing oxide bath loading. When the oxide particle loading was greater than 5 g/l, the Al content in the

Table 3-2. The phase information of annealed Ni-Al-REO Coatings.

Ni-Al-CeO_2 (9~15 nm)	Phases
1 g/l (30.98±0.60vol%)*	Ni_3Al (major)
5 g/l (29.83±1.81vol%)	Ni_3Al (major)
10 g/l (27.07±1.86vol%)	Ni_3Al (major)
20 g/l (17.25±0.30vol%)	Ni (major), Ni_3Al (weak), $CeAlO_3$ (weak)
80 g/l (3.38±0.26vol%)	Ni (major), $CeAlO_3$ (weak)

Ni-Al-CeO_2 (5 μm)	Phases
0.5 g/l (32.66±0.6vol%)	Ni_3Al (major)
1 g/l (30.58±0.52vol%)	Ni_3Al (major), CeO_2 (very weak)
5 g/l (31.03±0.4vol%)	Ni_3Al (major), CeO_2 (weak)
10 g/l (27.89±0.76vol%)	Ni_3Al (major), CeO_2 (weak)

Ni-Al-Y_2O_3 (<1 μm)	Phases
0.5 g/l (30.41±0.56vol%)	Ni_3Al (major)
1 g/l (26.77±0.90vol%)	Ni_3Al (major), Y_2O_3 (weak)
5 g/l (18.69±0.55vol%)	Ni_3Al (major), Ni (major), Y_2O_3 (moderate)
10 g/l (13.72±0.99vol%)	Ni_3Al (weak), Ni (major), Y_2O_3 (moderate)

*: The vol% of Al particles in as-plated composite coatings

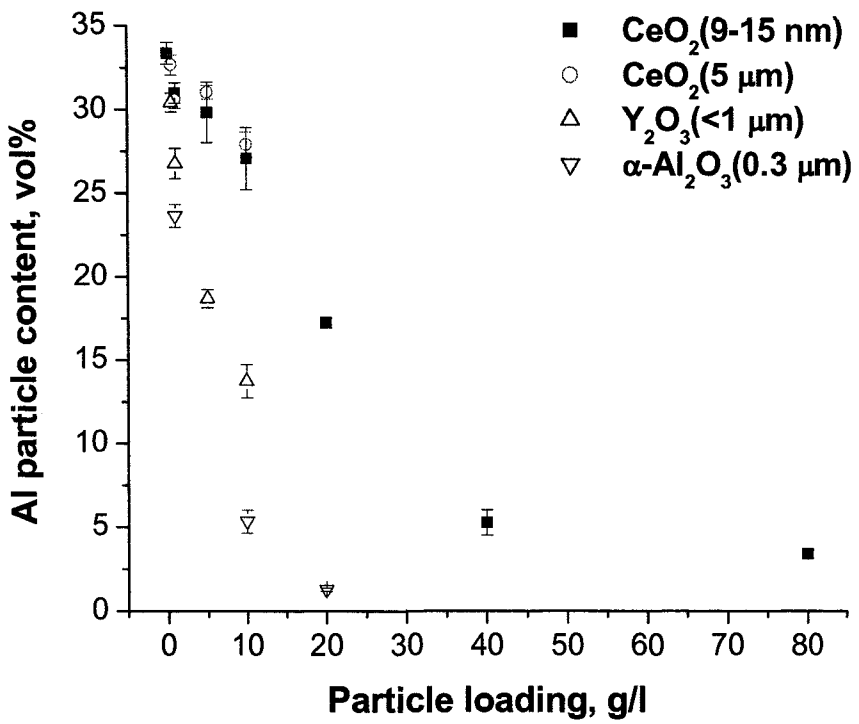

Figure 3-3. The effect of the REO bath loading on the volume fraction of Al particles in Ni-Al-REO composite coatings.

coating fell below 30vol%, which is the minimum Al level required for the formation of single-phase Ni_3Al coatings. Al contents as low as less than 5vol% were observed in Ni-Al-nano CeO_2 samples at a CeO_2 bath loading of 40 g/l and 80 g/l. The typical morphology of as-plated coatings with 1 g/l CeO_2 and 20 g/l CeO_2 are shown in Fig. 3-4 (a) and Fig. 3-5(a) respectively.

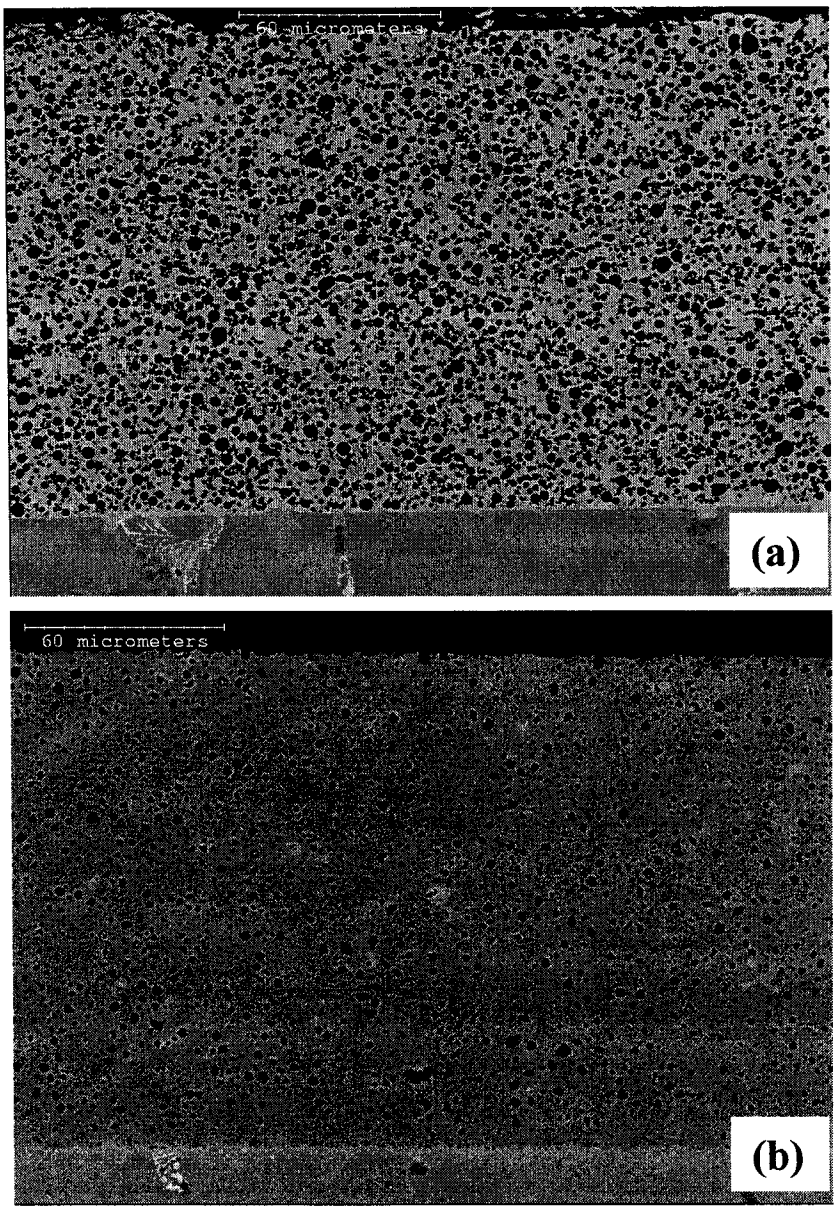

Figure 3-4. Morphology of Ni-Al-nano CeO_2 composite coatings with 1 g/l nano CeO_2: (a) as-plated, (b) annealed.

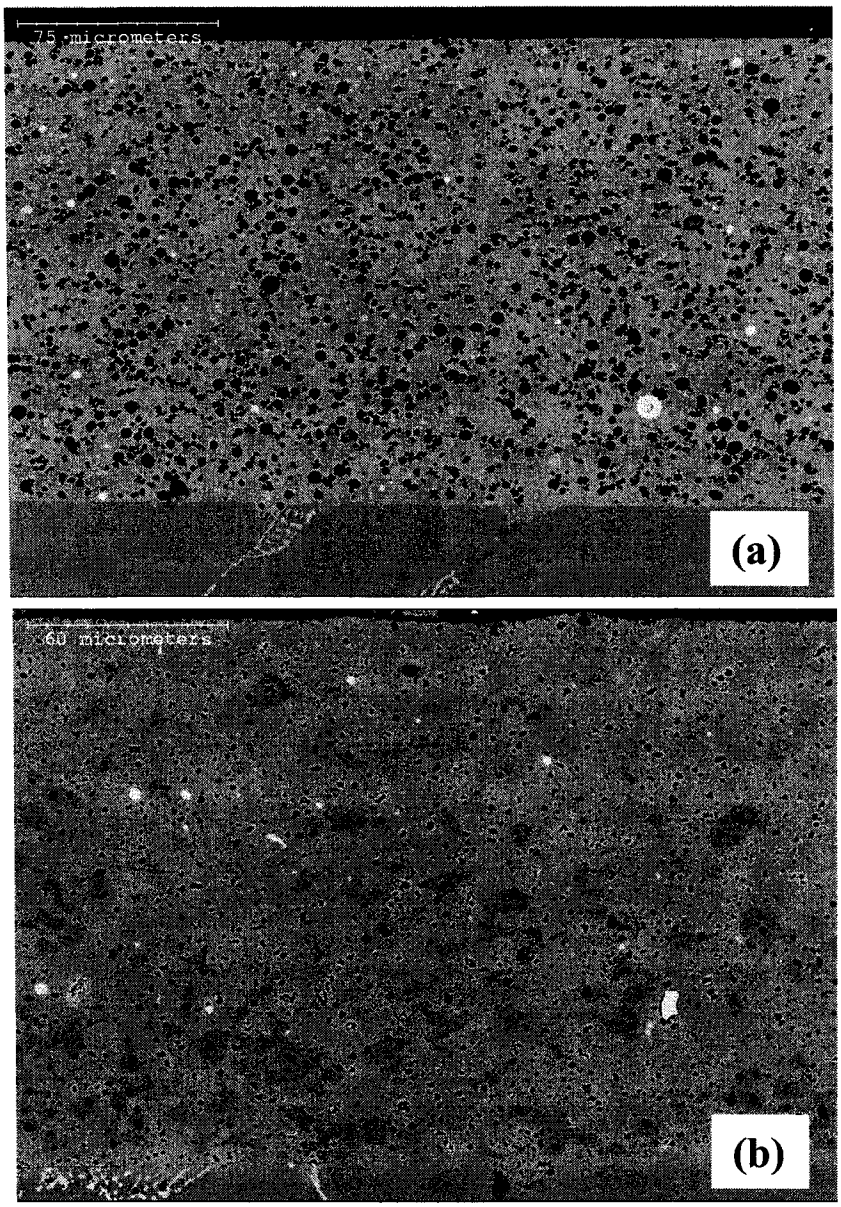

Figure 3-5. Morphology of Ni-Al-nano CeO_2 composite coatings with 20 g/l nano CeO_2: (a) as-plated, (b) annealed.

The coating with 1 g/l ceria loading contained significantly more Al particles (dark phase) than that with 20 g/l. Although the observation of nano ceria particles is beyond the resolution limit of the SEM used, ceria particles (white phase) larger than 1 μm were occasionally observed. According to Table 3-2, the phase structures of the annealed Ni-Al-nano CeO_2 coatings were strongly affected by the oxide particle loadings. With a ceria particle loading below 5 g/l, single-phase γ'-Ni_3Al was identified. With

increasing oxide bath loading, the coating consisted of γ'-Ni_3Al and γ-Ni, due to the reduction of Al content. At CeO_2 particle loadings beyond 20 g/l, the coatings were predominantly γ-Ni. Moreover, the $CeAlO_3$ phase was detected in the annealed coatings containing an increased amount of CeO_2 particles. As shown in Fig. 3-6(a), the $CeAlO_3$ phase was characterized with diffraction peaks at 2θ =27.390°, 39.085°, 48.430°, 56.587°, and 70.931°. No $CeAlO_3$ was detected in the coating with a CeO_2 bath loading of 20 g/l or less. This was probably due to the resolution limit of XRD, which can only detect second phase of 5wt% or higher. The $CeAlO_3$ phase (instead of CeO_2 phase) was detected after annealing, indicating that nano CeO_2 particles reacted with Al during the annealing treatment. Fig. 3-4(b) and Fig. 3-5(b) show the images of annealed coatings with 1 g/l and 20 g/l nano ceria loadings respectively. Fig. 3-4(b) has a uniform contrast, reflecting the nature of single-phase γ'-Ni_3Al (gray phase) with minor γ-Ni-Al phases (light phase). However, only a small fraction of γ'-Ni_3Al (darker gray phase) was observed in the annealed coating with 20 g/l CeO_2 loading in Fig. 3-5(b), and the remaining light gray regions were γ-Ni-Al phases with low Al content. The white phases in Fig. 3-5(b) are CeO_2 particles. The dark dots in the images of the annealed coatings are pores left after the annealing treatment.

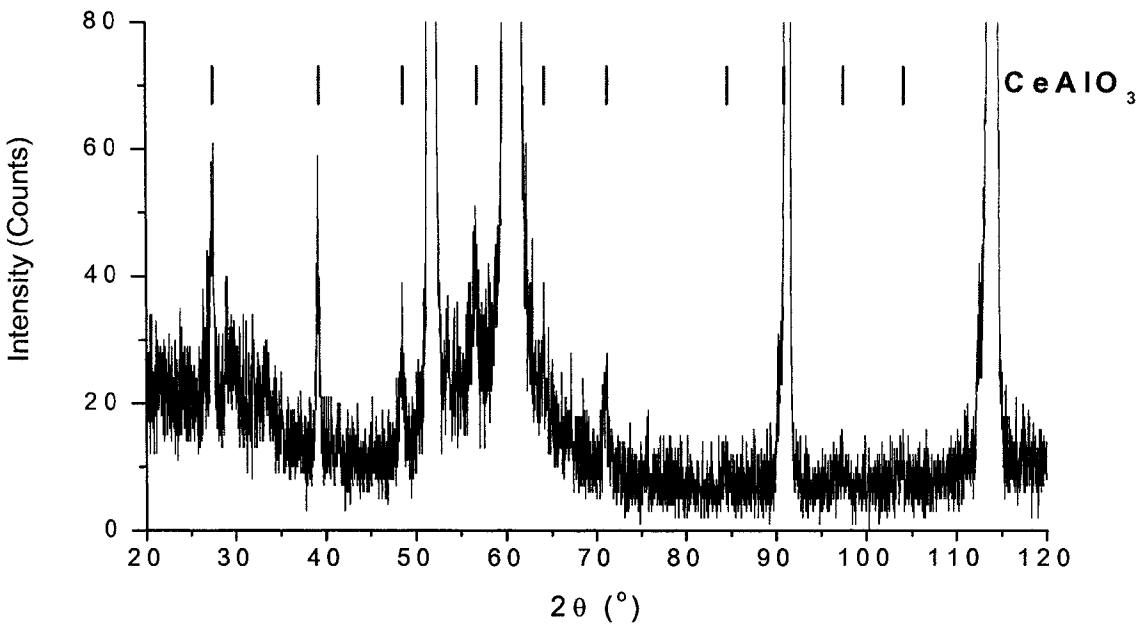

(a) $CeAlO_3$ phase in the annealed Ni-Al-nano CeO_2 coating with 20 g/l CeO_2.

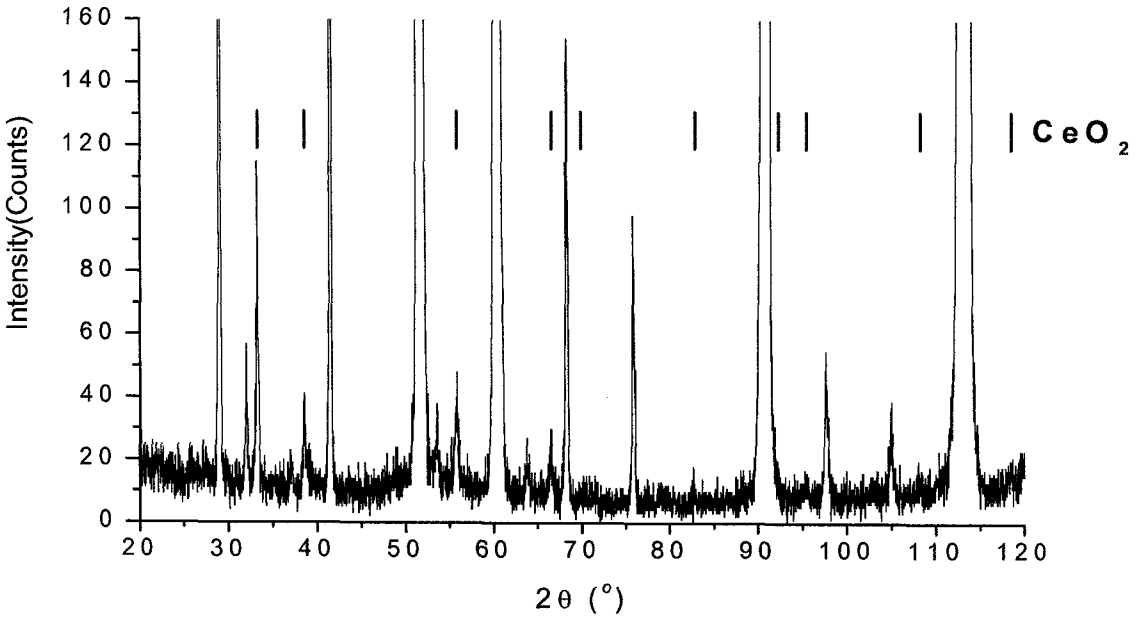

(b) CeO_2 phase in the annealed Ni-Al-5 μm CeO_2 coating with 10 g/l CeO_2.

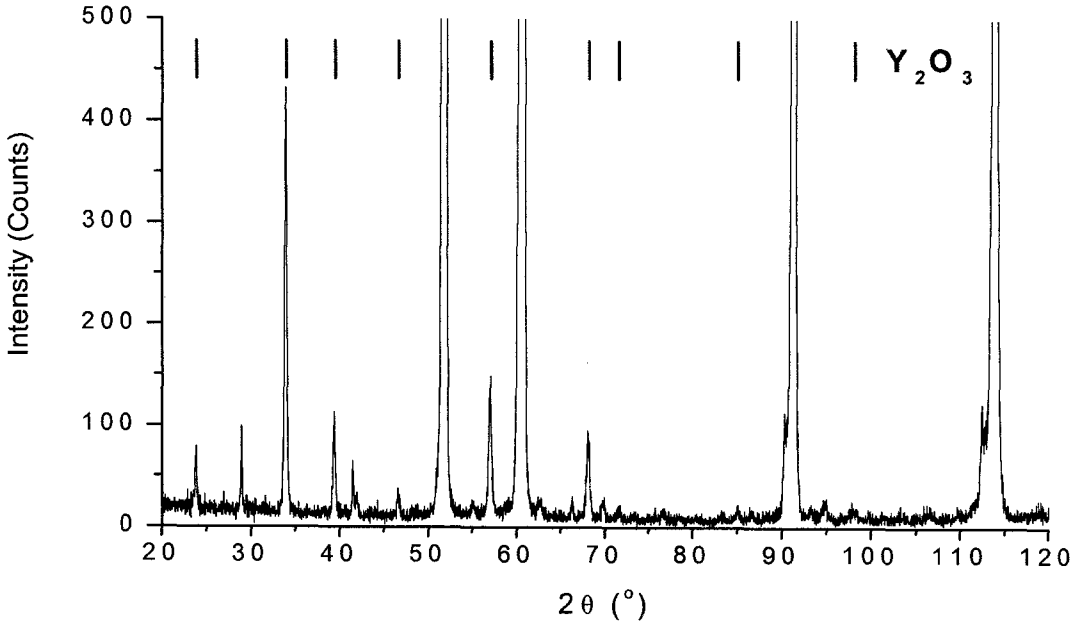

(c) Y_2O_3 phase in the annealed Ni-Al-Y_2O_3 (<1 μm) coating with 10 g/l Y_2O_3.

Figure 3-6. The X-ray patterns of REO phases in the annealed Ni-Al-REO coatings.

3.3.2.2 CeO_2 (5 μm)

Four ceria particle loadings at 0.5 g/l, 1 g/l, 5 g/l, and 10 g/l respectively were used to study the effects of loading of larger-sized ceria particles. Fig. 3-7(a) and Fig. 3-8(a) show as-plated coatings with 1 g/l and 10 g/l CeO_2 respectively. Al particles (dark phase) and CeO_2 particles (white phase) were evenly dispersed in both coatings. The coating with 10 g/l CeO_2 contained more ceria particles, but fewer Al particles, than the coating with 1 g/l CeO_2.

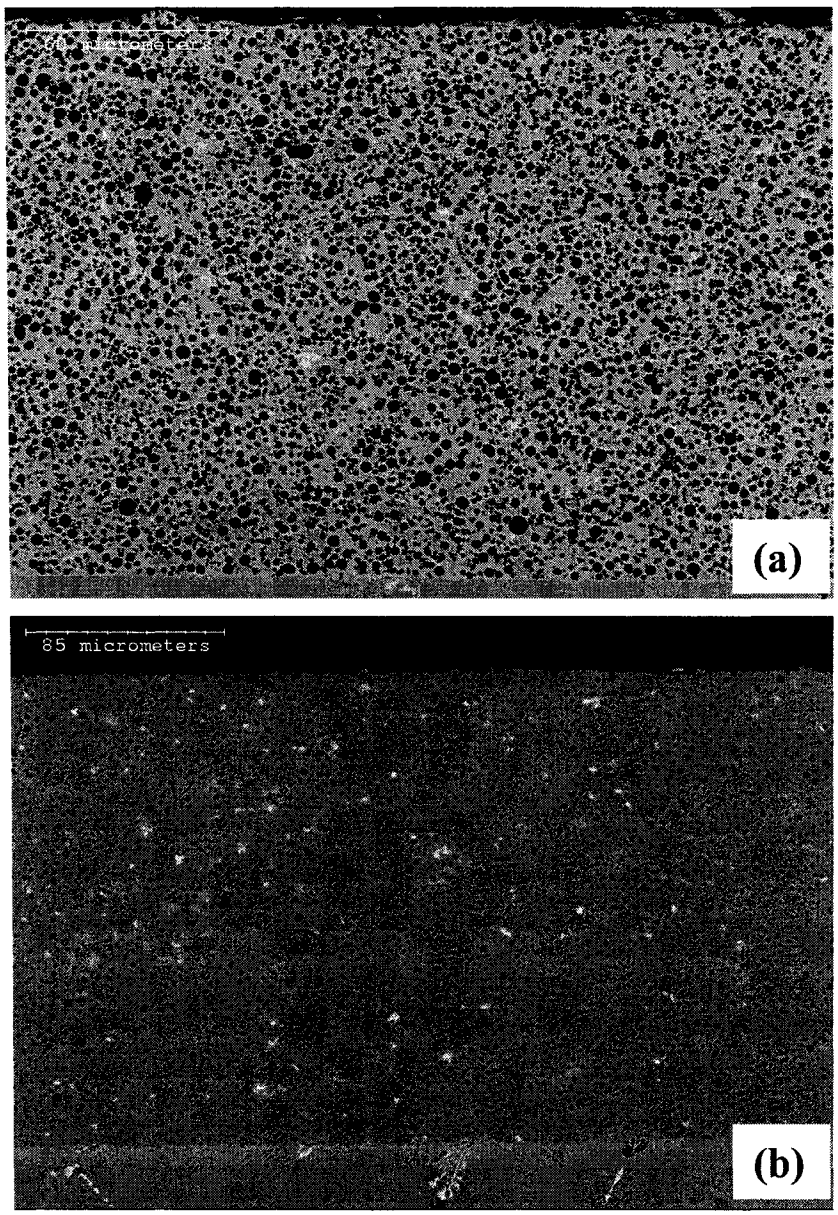

Figure 3-7. Typical pictures of Ni-Al-5 μm CeO_2 composite coatings with 1 g/l CeO_2 particle loading: (a) as-plated, (b) annealed.

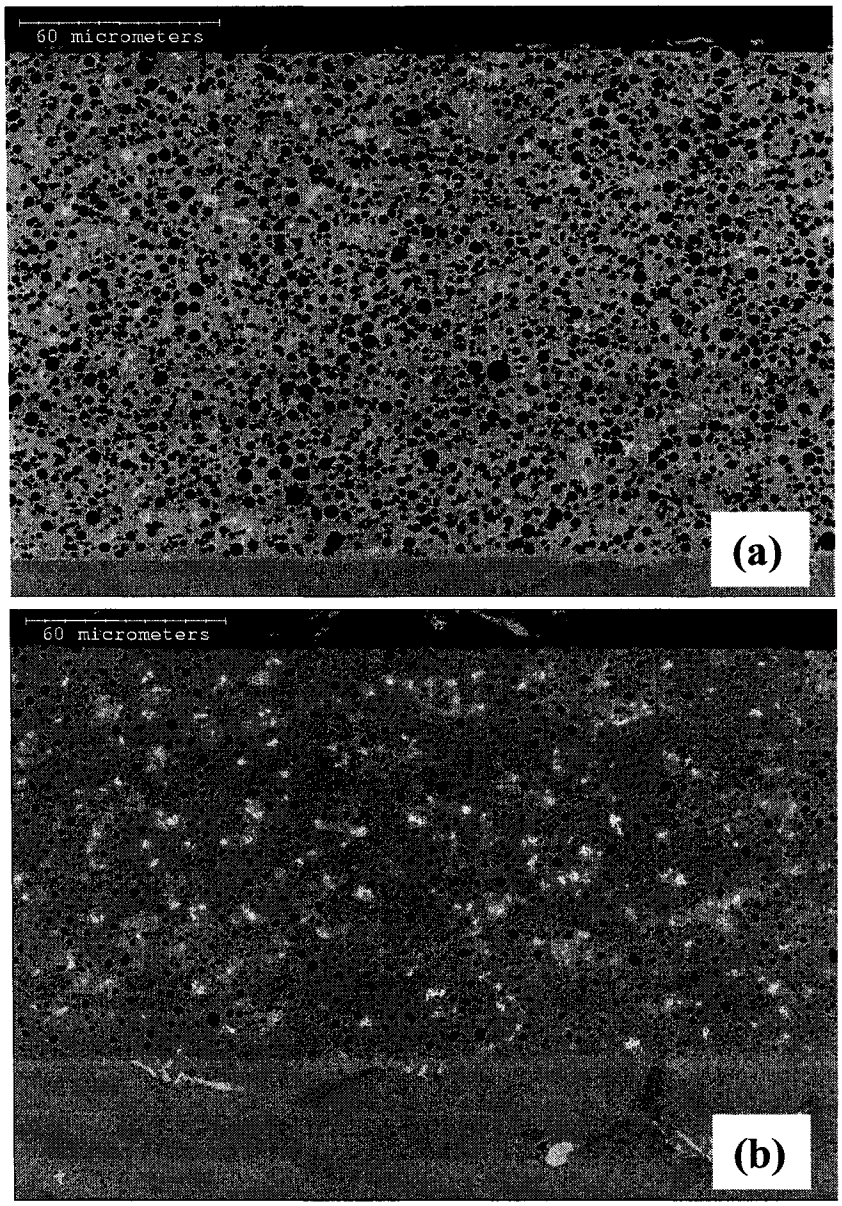

Figure 3-8. Typical pictures of Ni-Al-5 μm CeO_2 composite coatings with 10 g/l CeO_2 particle loading: (a) as-plated, (b) annealed.

As shown in Fig. 3-3, large ceria particles behaved the same as nano ceria particles in terms of the Al particle content in coatings, where the increase of CeO_2 bath loading significantly reduced the Al particle content in the composite coatings and the ceria particle size seemed to have little effect on Al particle content. According to Table 3-2, the phase structures of annealed Ni-Al-5μm CeO_2 coatings with a CeO_2 bath loading less than 10 g/l showed predominantly γ'-Ni_3Al phase. Fig. 3-7(b) shows almost 100% intermetallic phase in the annealed coating with 1g/l CeO_2 particles. The small fraction of

γ-Ni-Al phase (lighter gray phase) in the annealed coating with 10 g/l CeO_2 particles, as shown in Fig. 3-8(b), was not detected by the current XRD due to its low resolution. Based on Fig. 3-7(b) and Fig. 3-8(b), it is clear that higher CeO_2 concentration in the plating bath yielded more oxide particles (white phase) in the coatings.

However, the size of CeO_2 particles had an influence on the oxide particle content in the composite coatings. The CeO_2 phase was detected in Ni-Al-5μm CeO_2 coatings with an oxide bath loading as low as 1 g/l, while it was not detected in Ni-Al-nano CeO_2 coatings even with 10 g/l CeO_2. Furthermore, the size of the oxide particles affected the reaction of CeO_2 with Al during the annealing treatment. Only the CeO_2 phase, instead of the $CeAlO_3$ phase as was seen in Ni-Al-nano CeO_2, was present in the Ni-Al-5 μm CeO_2 coatings. The characteristic peaks of CeO_2 at $2\theta = 33.226°$ and 55.808° are shown in Fig. 3-6(b). This suggests that large CeO_2 particles did not react with Al to form a new compound during the heat treatment, or that the reaction might have produced amounts below the detection limit of XRD.

3.3.2.3 Y_2O_3 (<1 μm)

Ni-Al-Y_2O_3 composite coatings were prepared with four bath loadings at 0.5 g/l, 1 g/l, 5 g/l, and 10 g/l respectively. Fig. 3-3 indicates that the Y_2O_3 particle concentration in the plating bath had a significant effect on the Al particle content. The Al content dropped sharply from about 30vol% at 0.5g/l Y_2O_3 bath loading to as low as 14vol% at 10 g/l. Compared to CeO_2 particles, the Y_2O_3 particle had a more negative effect on the Al particle content in composite coatings. On the other hand, the Y_2O_3 particle content increased rapidly with oxide bath loading, which is shown in Fig. 3-9(a) and Fig. 3-10(a) for the as-plated coatings at 1 g/l and 10 g/l Y_2O_3 respectively. Fewer Al particles (dark phase) and a larger number of Y_2O_3 particles (gray needle phase) were contained in the coating with 10 g/l Y_2O_3 than in that with 1 g/l Y_2O_3.

The phases in the annealed Ni-Al-Y_2O_3 coatings changed from predominantly γ'-Ni_3Al phase at low Y_2O_3 bath loading, to mainly γ-Ni at high Y_2O_3 bath loading, the details of which are summarized in Table 3-2. Due to the considerable number of Y_2O_3

particles in the coatings, the Y_2O_3 phase was detected even in the coatings with 1g/l. Y_2O_3 peaks at 2θ= 23.849°, 33.899°, 39.369°, 57.007°, and 68.022° were identified in the annealed Ni-Al-Y_2O_3 coating with 10 g/l Y_2O_3, as shown in Fig. 3-6(c). No other Al/Y mixed oxide phases were found in any of the annealed composite coatings, which is similar to the experience with annealed Ni-Al-5μm CeO_2 composite coatings. The typical morphologies of annealed Ni-Al-Y_2O_3 coatings with 1 g/l Y_2O_3 and 10 g/l Y_2O_3 are shown in Fig. 3-9(b) and Fig. 3-10(b) respectively.

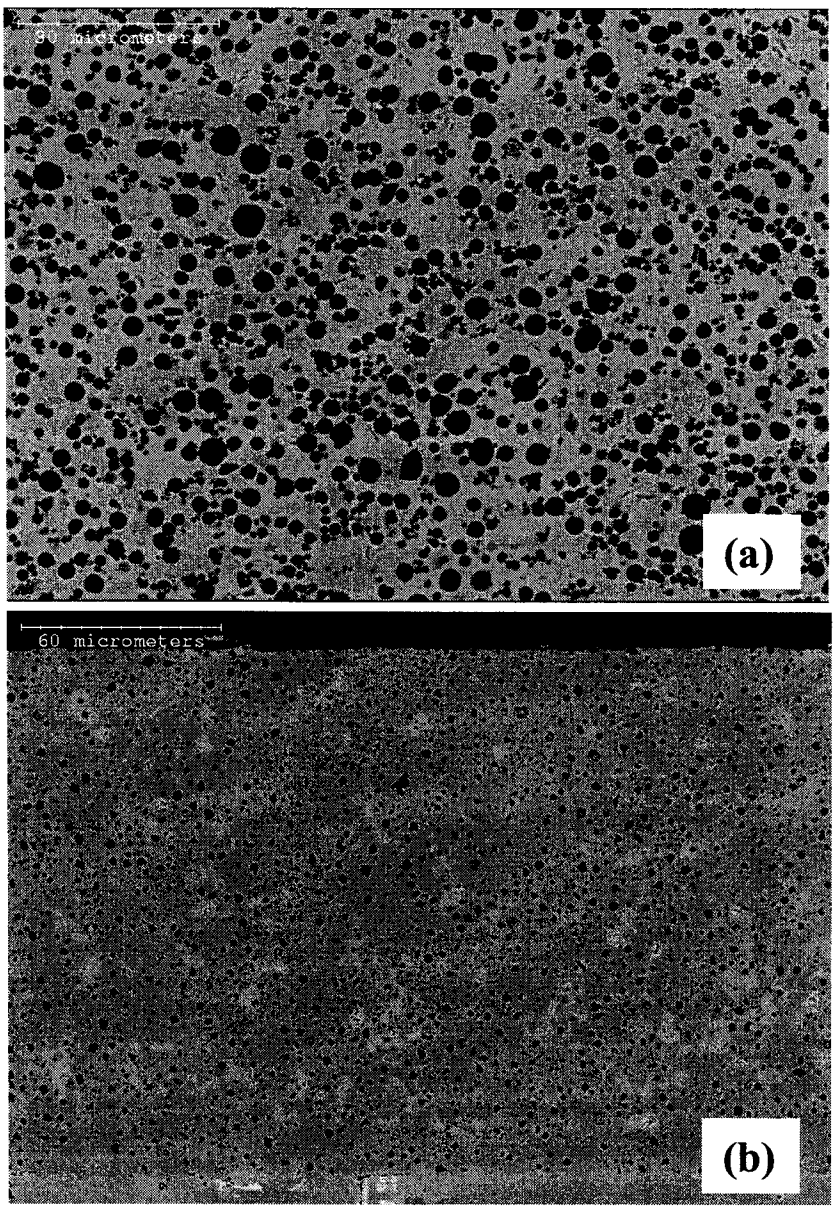

Figure 3-9. Ni-Al-Y_2O_3 (<1 μm) coatings with 1 g/l Y_2O_3: (a) as-plated, (b) annealed.

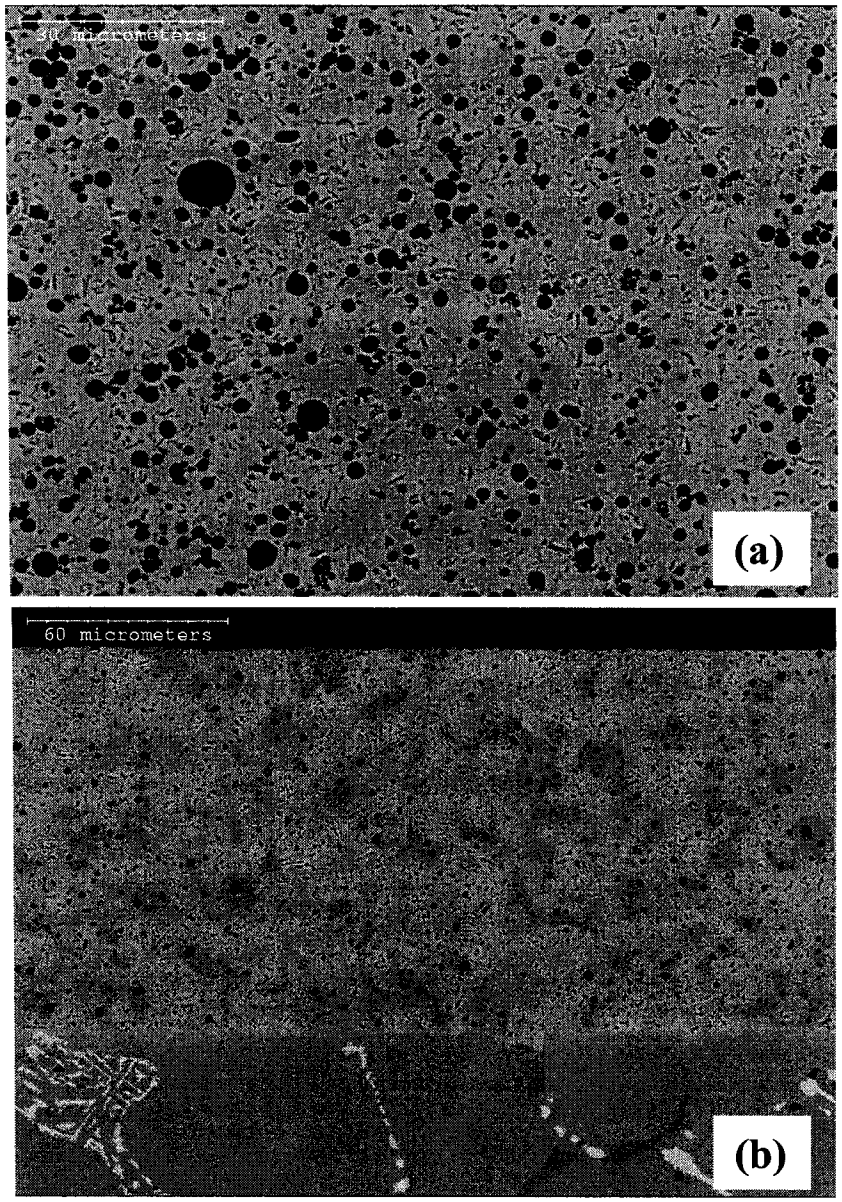

Figure 3-10. Ni-Al-Y_2O_3 (<1 μm) coatings with 10 g/l Y_2O_3: (a) as-plated, (b) annealed.

3.4 Discussion

3.4.1 Interfering Effect

It is clear in Fig. 3-3 and Table 3-2 that an increase in the REO particle loading, particularly Y_2O_3, significantly reduced the Al particle content in the coatings. In contrast, the REO particle content in the composite coatings generally increased with the REO bath loading. It is evident that REO particles in the bath interfere with the deposition of Al particles. Barmak et al. [24] found a similar interfering effect in CED

Ni-Al-α-Al_2O_3 (0.6~0.8μm) ternary composition coatings, where the Al particles in the plating bath altered the deposition behavior of the Al_2O_3 particles. The enhanced deposition of Al_2O_3 particles at low current density occurring in the Ni-α-Al_2O_3 binary systems was not observed in the Ni-Al-α-Al_2O_3 ternary systems. However, no interference of Al_2O_3 particles with the deposition of the Al particles was observed. To further clarify the effect of α-Al_2O_3 particles on the deposition of Al particles, Ni-Al-α-Al_2O_3 (0.3μm) ternary composite coatings were produced via the SCD technique (the results were also presented in Fig. 3-3). The interfering effect of α-Al_2O_3 particles on Al particles is clearly seen in Fig. 3-3, which indicates that α-Al_2O_3 particles have a more detrimental effect on the deposition of Al particles in these coatings than the other kinds of oxide particles examined. This is quite different from the results of Barmak's work. A clear explanation for this difference is not yet available, although the difference could be due to dissimilar coating techniques and bath compositions. For example, the CED technique and the nickel sulphamate bath were used in Barmak's work, whereas a sediment deposition technique and the Watt's nickel solution were used in our experiments.

Although many binary electrodeposited composite coatings were successfully produced, the co-deposition mechanisms of particles are not yet fully understood. It is generally believed that particles in the plating bath are physically adsorbed on the cathode surface, and then permanently incorporated in the metal matrix coating [25-27]. The physical adsorption is an electrophoretic step, where the particles in the plating bath will adsorb ions such as Ni^{2+} or solvent molecules, and be loosely attached to the cathode. The fraction of particles loosely attached to the cathode surface is proportional to the particle concentrations in the bath, and can be very large at high particle concentration, sometimes close to 100% [25, 28, 29]. The surface charge of the particles in the plating bath plays an important role in this physical adsorption step [30-32].

For the current SCD Ni-Al binary composite system, the Al particle content in the composite coatings was large, even at a low particle bath loading of 40 g/l. As for the

SCD Ni-REO binary composite system, for example Ni-Y_2O_3, the volume fraction of the oxide particle also was high (Fig. 3-11).

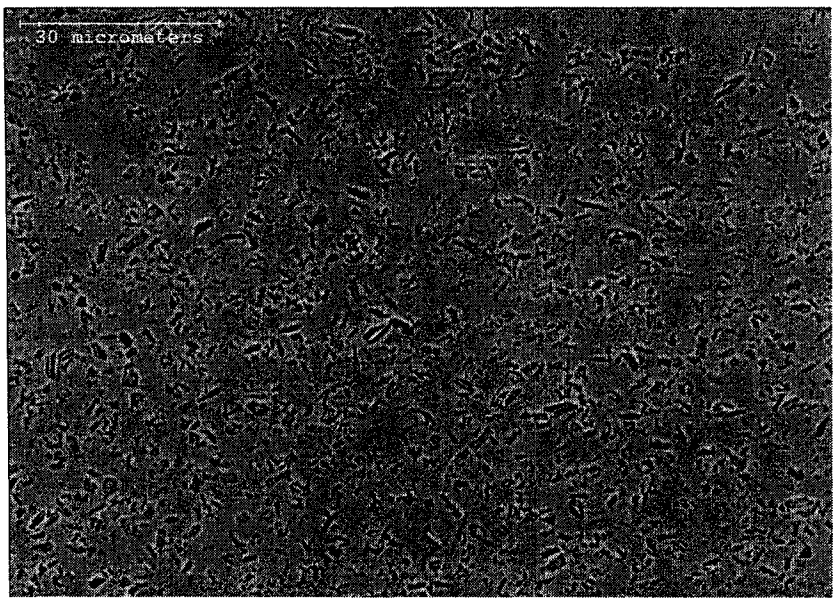

Figure 3-11. Ni -Y_2O_3 (<1μm) binary composite coatings with 40 g/l Y_2O_3.

This indicates that the metallic Al particle and the non-conducting Y_2O_3 particle can be deposited easily from the current Watt's nickel solution via the SCD technique. The surface state of the Al particle and the Y_2O_3 particle in the solution is favorable for adsorption on the cathode. When both particles co-exist in the bath, the Y_2O_3 particle content in the coatings was found to increase with the Y_2O_3 bath loading, while the Al content sharply decreased. The observation of a high volume fraction of the Y_2O_3 particles and an extremely low level of the Al particles in the ternary Ni-Al-Y_2O_3 composite coatings suggests that the Y_2O_3 particles are preferentially deposited on the cathode. Consequently, the deposition of the Al particle is retarded. This interfering effect might result from the different surface charge states of the Y_2O_3 and the Al particles in the Watt's bath. For example, if the surface charge of the Y_2O_3 particle in the bath was more positive than that of the Al particle, the Y_2O_3 particle would be more likely to be adsorbed by the cathode. As adsorption sites on the cathode are limited, the fraction of Al particles loosely adsorbed on the cathode would be reduced due to the preferential adsorption of Y_2O_3 particles, particularly at increased Y_2O_3 particle

concentrations. High Y_2O_3 particle loadings on the cathode surface would block the adsorption of Al particles, and result in extremely low Al particle contents in coatings (as was observed in the Ni-Al-Y_2O_3 composite coatings). Further work is needed to verify the above assumption.

3.4.2 Formation of REO-dispersed Ni_3Al

3.4.2.1 Ni-Al Intermetallic Phases

The formation of intermetallic phases in Ni-Al binary composite coatings during the annealing treatment results from interdiffusion between Al particles and the Ni matrix. It is affected by Al content, annealing temperature and time [22, 23, 28]. The phase structures in the fully-annealed Ni-Al composite coatings obviously depend on the Al content in the coatings. Based on the equilibrium Ni-Al binary diagram [33], the Al content in the Ni-Al composite coatings should be 22~28at% (30~37vol%), corresponding to single-phase γ'-Ni_3Al. The coating would consist of γ'-Ni_3Al and γ-Ni when the Al content was between 10at% (14.5vol%) and 22at% (30vol%). Below 10at% (14.5vol%), the solid solution of γ-Ni is obtained.

The phases identified in fully-annealed Ni-Al-REO coatings were generally consistent with the Ni-Al binary phase diagram. According to Table 3-2, a single-phase Ni_3Al coating was formed only at high Al contents. A decrease in the Al content resulted in γ'-Ni_3Al+γ-Ni dual phases in the coatings, and finally the single γ-Ni phase at low Al levels. However, for Ni-Al-REO coatings with high REO particle content, the phases present may deviate from the Ni-Al binary diagram to some extent. For example, although the Al level (14vol%) in the Ni-Al-Y_2O_3 composite coating was below the minimum Al content (14.5vol%) for the formation of γ'-Ni_3Al, γ'-Ni_3Al was still present. This happens due to the reduction of Ni in the coating in the presence of Y_2O_3 particles (around 9vol%), so that the actual ratio of Ni/Al (5.5) will still fall into the two-phase region (5.9~2.3). We believed that the volume fraction of Y_2O_3 particles in the coating was underestimated because Y_2O_3 particles can't all be separated from the Ni matrix, due to the poor contrast between them; only those Y_2O_3 particles with enough darkness were measured.

3.4.2.2 The Limit of REO Bath Loading

For the current SCD Ni-Al binary composite coatings with 80 g/l Al bath loading, the Al particle content was adequate to form single-phase Ni_3Al intermetallic coatings. When REO particles are added to the plating bath, the incorporation of REO particles in the composite coatings will be at the expense of the Al content, due to the interfering effect. The REO bath loading should be controlled to maintain sufficient Al in the coatings (30~37vol%) to form single-phase γ'-Ni_3Al. According to the results shown in Fig. 3-3, the maximum particle loading for nano CeO_2, 5 μm CeO_2, and Y_2O_3 (<1 μm) should be 5 g/l, 5 g/l, and 1 g/l respectively. Beneficial effects of reactive oxides on the high-temperature performances of alloys or coatings generally occur when the REO content is low, typically less than 5wt%, which is below the detectable limit of XRD. As a result, the preferred REO bath loading in three Ni-Al-REO systems can be lower than those maximum limits required for the formation of single-phase Ni_3Al. Therefore, REO-dispersed Ni_3Al intermetallic coatings with the preferred REO content and sufficient Al particles can be produced via SCD.

3.4.2.3 Phase Transformation of REO-Contained Phases

Table 3-2 indicates that the $CeAlO_3$ phase instead of CeO_2 phase was observed in annealed Ni-Al-nano CeO_2 coatings at high particle loadings. However, the oxide phases in the annealed Ni-Al-5 μm CeO_2 and Ni-Al-Y_2O_3 (<1 μm) coatings were identified as mainly CeO_2 and Y_2O_3 respectively, and no REO phase transformation was observed. The $CeAlO_3$ phase normally results from the reaction of ceria oxides such as CeO_2 or Ce_2O_3 with Al_2O_3 in inert or reducing atmospheres [34-36]. It has a perovskite-like structure, and is more thermodynamically stable than CeO_2 in reducing atmospheres above 500 °C [34]. The formation of $CeAlO_3$ in reducing and inert atmospheres will start above 1000 °C [35, 36]. Wang et al. [37] also observed the formation of $CeAlO_3$ in thermal-sprayed, CeO_2-modified NiAl coatings after carburizing at 1100 °C in CH_4-H_2 reducing atmospheres. In the present study, the annealing of Ni-Al-REO composite coatings was conducted in vacuum at 800 °C, which is lower than the temperature required to form $CeAlO_3$ phases. Because this phase was detected only in the annealed

Ni-Al-nano CeO_2 coatings, the presence of $CeAlO_3$ may be attributed to the particle size of CeO_2. It can be calculated that the total surface area of a nano CeO_2 particle (~12 nm) is about 417× that of a 5 μm-sized CeO_2 particle at the same weight fraction. Because reaction to form $CeAlO_3$ might be limited to the outer surface of the CeO_2 particles and to a small surface area, the $CeAlO_3$ formed on micro-CeO_2 may be too small to be detected by the XRD used.

3.5 Concluding Remarks

(1) Electrodeposited Ni-Al-REO ternary composite coatings could be deposited from the Watt's bath containing both Al and REO particles via the sediment co-deposition technique. The volume fraction of Al particles in composite coatings strongly depends on the REO bath loading. For the current Ni-Al-nano CeO_2, Ni-Al-5μm CeO_2, and Ni-Al-Y_2O_3 (<1μm) systems, the Al content decreased with increasing REO particle loading. The reduction of the Al content was more significant in the Ni-Al-Y_2O_3 (<1μm) systems. This behavior is believed to be caused by interference of REO particles with the deposition of Al particles. The REO particles in the plating bath are preferentially adsorbed by the cathode, and thus block the adsorption of Al particles to the cathode.

(2) Ni-Al intermetallic phases formed in the annealed Ni-Al-REO coatings were consistent with those defined in the equilibrium Ni-Al phase diagram. To form REO-dispersed Ni_3Al intermetallic coatings, the REO bath loading should be controlled below a critical level, depending on the types of REO particles.

(3) Nano CeO_2 particles reacted with Al to form $CeAlO_3$ phase during the annealing treatment at 800°C in vacuum. However, this transformation was not observed using XRD in the annealed Ni-Al-5μm CeO_2 and Ni-Al-Y_2O_3 (<1μm) systems. This may result from the high surface area of nano CeO_2 particles, which makes the reaction possible at lower temperatures.

3.6 Bibliography

1. Brill, U., Materials and Corrosion, 1990. **41**(12): p. 682-688.

2. Klöwer, J., Brill, U., and Heubner, U., Intermetallics, 1999. **7**: p. 1183-1194.

3. Sidhu, B.S. and Prakash, S., Surface and Coatings Technology, 2003. **166**: p. 89-100.

4. Choi, S.C., Cho, H.J., and Lee, D.B., Oxidation of Metals, 1996. **46**(1-2): p. 109-127.

5. Jung, H.G. and Kim, K.Y., Oxidation of Metals, 1996. **46**(1-2): p. 147-167.

6. Jedliński, J., Corrosion Science, 1993. **35**(5-8): p. 863-869.

7. Wrigth, I.G., Srinivasan, and Vedula, K.M., Materials at High Temperatures, 1993. **11**(1-4): p. 160-166.

8. Wrigth, I.G., Pint, B.A., and Tortorelli, P.F., Oxidation of Metals, 2001. **55**(3-4): p. 333-357.

9. Wang, K.L., Zhang, Q.B., Sun, M.L., Wei, X.G., and Zhu, Y.M., Applied Surface Science, 2001. **174**: p. 191-200.

10. Wang, F.H., Lou, H.Y., and Wu, W.T., Vacuum, 1992. **43**(5-7): p. 749-752.

11. Bianco, R. and Rapp, R.A., Journal of The Electrochemical Society, 1993. **140**(4): p. 1181-1190.

12. Warnes, B.M., Surface and Coatings Technology, 2001. **146-147**: p. 7-12.

13. Paúl, A., Elmrabet, S., Ager, F.J., and Odriozola, J.A., Oxidation of Metals, 2002. **57**(1-2): p. 33-51.

14. Saremi, M. and Bahraini, M., Transactions of The Institute of Metal Finishing, 2003. **81**(1): p. 24-27.

15. Haugsrud, R., Corrosion Science, 2003. **45**: p. 1289-1311.

16. Chevalier, S. and Larpin, J.P., Acta Materialia, 2002. **50**: p. 3105-3114.

17. Patil, S., Kuiry, S.C., and Vanfleet, R., Journal of Nanaoparticle Research, 2002. **4**: p. 433-438.

18. Peng, X., Li, T.F., and Wu, W.T., Oxidation of Metals, 1999. **51**(3-4): p. 291-315.

19. Peng, X., Li, T.F., and Wu, W.T., Transactions of Nonferrous metal Society of China, 1997. **7**(3): p. 14-20.

20. Peng, X., Tang, Z., Li, T.F., and Wu, W.T., Oxidation of Metals, 1999. **51**(3-4): p. 317-331.

21. Veleva, L., Diaz_Ballote, L., and Wipf, D., Journal of The Electrochemical Society, 2003. **150**(1): p. C1-C6.

22. Izaki, M., Fukusumi, M., Dnomoto, H., Omi, T., and Nakayama, Y., Journal of The Japan Institute of Metals, 1993. **57**(2): p. 182-189.

23. Susan, D.F., Misiolek, W.Z., and Marder, A.R., Metallurgical and Materials Transactions A., 2001. **32A**: p. 379-391.

24. Barmak, K., Banovic, S.W., Petronis, C.M., Susan, D.F., and Marder, A.R., Journal of Microscopy, 1997. **185**(2): p. 265-274.

25. Guglielmi, N., Journal of The Electrochemical Society, 1972. **119**(8): p. 1009-1012.

26. Celis, J.P. and Roos, J.R., Journal of The Electrochemical Society, 1977. **124**(10): p. 1508-1511.

27. Masalski, J., Szczygiel, B., and Gluszek, J., Transactions of The Institute of Metal Finishing, 2002. **80**(3): p. 101-104.

28. Liu, H.F. and Chen, W.X., Surface and Coatings Technology, 2005. **191**: p. 341-350.

29. Wang, S.C. and Wei, J.W.C., Materials Chemistry and Physics, 2003. **78**: p. 574-580.

30. Lee, C.C. and Wan, C.C., Journal of The Electrochemical Society, 1988. **135**(8): p. 1930-1933.

31. Shawki, S. and Hamid, Z.A., Anti-Corrosion Methods and Materials, 1997. **44**(3): p. 178-185.

32. Lee, E.C. and Choi, J.W., Surface and Coatings Technology, 2001. **148**: p. 234-240.

33. Hansen, M., *Constitution of Binary Alloys (Second Edition)*. 1958, McGraw-Hill Book Co.: New York. p. 118.

34. Angove, D.E., Cant, N.W., French, D.H., and Kinealy, K., Applied Catalysis A-General, 2000. **194**: p. 27-34.

35. Tas, A.C. and Akinc, M., Journal of The American Ceramic Society, 1994. **77**(11): p. 2961-2967.

36. Yao, M.H., Baird, R.J., Kunz, F.W., and Hoost, T.E., Journal of Catalysis, 1997. **166**: p. 67-74.

37. Wang, Y. and Chen, W.X., Surface and Coatings Technology, 2004. **183**: p. 18-28.

Chapter 4

Cyclic Oxidation Behavior of Electrodeposited Ni_3Al-CeO_2-Based Coatings at 850 °C and 1050 °C*

* The work on the cyclic oxidation at 850 °C has been published. Liu, H.F. and Chen, W.X., **Oxidation of Metals**, 2005, 64(5-6): p. 331-354.

* The work on the cyclic oxidation at 1050 °C has been submitted for publication. Liu, H.F. and Chen, W.X., submitted to **Corrosion Science**, 2005.

4.1 Introduction

Electrodeposited metal matrix (e.g., nickel-based)/metal particle (e.g., aluminum) composite coatings have been developed as protective coatings against high-temperature degradation. Usually, the composite coating is first co-deposited from a nickel plating bath containing conducting metal particles, and then annealed in vacuum or an inert atmosphere to allow the diffusion reaction between the matrix and the metal particles to form a uniform alloy. Various composite systems, such as Ni-Al [1-8], Ni-Cr [9, 10] and Ni-CrAlY [11-13], have been reported. Because it is simple, low-cost, and feasible for in situ deposition on various substrates [1, 2, 4, 7, 8], the electrodeposition of Ni-Al composite coatings has received extensive attention. These Ni-Al coatings can provide oxidation resistance in high-temperature oxidizing environments by forming a thermodynamically-stable Al_2O_3 scale on the coating surface. Izaki [1] first studied the high-temperature oxidation of such electrodeposited composite coatings. It was found that coatings with more than 16at% Al have superior short-term isothermal and cyclic oxidation resistance to 304 stainless steels at temperatures from 900 to 1100 °C. Susan [14, 15] reported that the oxidation resistance of electrodeposited two-phase, γ-Ni+γ'-Ni_3Al, Ni-Al coatings was better than that of pure nickel and a two-phase Ni superalloy containing γ-Ni+γ'-Ni_3Al at 800 °C and 1000 °C. More recently, Zhou [4] conducted the short-term cyclic oxidation experiments on electrodeposited Ni-28wt%Al nanocomposite coatings at 1050 °C, where the oxidation rate were much lower than those of the nickel and the Ni-base superalloy.

Electrodeposited Ni-Al coatings with low Al contents have usually satisfied long-term oxidation resistance at temperatures below 900 °C [14]. However, to achieve good oxidation resistance at higher temperatures, an increased Al content is required to form single-phase γ'-Ni_3Al or β-NiAl intermetallic coatings. Ni_3Al intermetallic coatings have received much attention due to fairly low weight gains during oxidation (even at temperatures above 1000 °C), carburization resistance, and sound resistance to oxidizing/chlorizing environments and molten salts [16-18]. The high-temperature protection of Ni_3Al results from the formation of compact, defect-free and slow-growing alumina scale. Unfortunately, such scales are inherently susceptible to cracking and

spalling during thermal cycling [19]. Small amounts of reactive elements (REs), such as Y, Zr, La or Ce, and their oxides (REOs), could improve the scale adherence and suppress the spallation in Ni_3Al and NiAl alloys [19-24].

Electrodeposition can be easily extended to co-deposit REO particles in Ni-Al composite coatings. Peng et al. [25, 26] developed Ni-La_2O_3 binary composite films on Ni and γ-TiAl to protect the substrates from high-temperature oxidation. Veleva et al. [27] produced Ni-Y_2O_3 composite coatings from a Watt's bath; there were more resistant to corrosion in aqueous chloric environment than pure Ni coatings. The co-deposition of Ni-Al-REO ternary composite coatings can be achieved simply by adding REO particles and Al particles to the Ni plating bath. Barkmak et al. [28] had conducted initial work on the co-deposition of Ni-Al-Al_2O_3 ternary composite coatings. In Chapter 3, we have successfully electrodeposited Ni-Al-CeO_2 and Ni-Al-Y_2O_3 ternary composite coatings from a Watt's nickel bath. By carefully adjusting the processing parameters, such as current density and particle loading, REO-modified Ni_3Al intermetallic coatings were successfully formed. However, the high-temperature performance of electrodeposited Ni-Al-REO ternary composite coatings has not been investigated previously.

The aim of this chapter is to study the cyclic-oxidation behavior of electrodeposited pure and CeO_2-modified Ni_3Al coatings at 850 °C and 1050 °C. The focus was on possible effects of CeO_2 particle, coating structure, and interdiffusion on the cyclic-oxidation resistance of the coatings.

4.2 Experimental

4.2.1 Coating Process

Ni-Al composite coatings, and Ni-Al composite coatings containing CeO_2 particles of 9-15 nm and 5 μm respectively, were deposited onto Fe-Ni-Cr substrates from a Watt's nickel bath via sediment co-deposition (SCD). The detailed coating process was described in Chapters 2 and 3. The centrifugally-cast HP alloy was used as the coating substrate; it contained 0.4wt% C, 35wt% Ni, 25wt% Cr, <1.5wt% Si,

<1.5wt% Mn, <1.5wt% Nb, and balanced Fe. Coupons of HP alloy, 20×10×2 mm^3, were machined and then ground using SiC papers up to 600-grit finish. The coating was deposited on the 20×10mm^2 surfaces. The Al powders, with an average size of 3 μm, were purchased from Valimet Inc. (Stockton, CA, USA). The CeO_2 particles, with an average size of 5 μm and 9~15 nm respectively, were obtained from Alfa Aesar, USA.

All coatings were deposited with a constant Al bath loading of 80 g/l, but with CeO_2 particle loadings ranging from 0 g/l to 5 g/l. The average coating thickness was controlled at around 150 μm. As shown in Chapter 3, the CeO_2 particle content in the composite coatings increases with an increase in CeO_2 particle loading in the plating bath, while the Al content decreases due to an interference effect. Single-phase Ni_3Al coatings were formed when the CeO_2 particle loading was controlled below 5 g/l. Prior to oxidation testing, all the as-plated samples were annealed at 800 °C for 3 hr in a vacuum furnace pumped down to about 0.8 mtorr to achieve a uniform single-phase γ'-Ni_3Al in the coating.

4.2.2 Cyclic-oxidation Test

The cyclic-oxidation test was performed in a tube furnace. Uncoated HP alloy coupons were used as a reference. Before the test, all coupons were polished with 600-grit SiC grinding paper, cleaned using acetone, and then air-dried. Test coupons were held in high-purity (99.8%) alumina boats with one coupon per boat (Vesuvius McDanel, PA, USA). Dry air was passed through the tube at a fixed rate of 60ml/min. The test cycle consisted of heating at 5 °C/min, holding at 850 °C or 1050 °C for the specific time, and cooling at 1.5 °C/min. After each cycle, the boats were removed from the furnace for mass gain measurement. Each coupon was weighed together with the boat and any spalled oxide from the coupon. Because each coated coupon has four edge surfaces uncoated, a correction was made to the measured weight gains on the assumption that the uncoated surfaces would have the same mass change per unit area as the coupon of bare HP alloy. After measurement, sample boats were returned to the furnace for the next run cycle. One repeated oxidation test was performed (the results obtained were very reproducible). The data presented in the paper were an average of the two tests.

4.2.3 Characterization

The microstructures and the morphologies of oxidized samples were examined using a S-2700 Scanning Electron Microscope (SEM) with an Energy-Dispersive X-Ray Spectrometer (EDS) attachment, and a JAMP-9500F Field Emission Auger Microprobe. The composition profiles were obtained using a JEOL 8900 SUPERPROBE equipped with a wavelength dispersive X-ray spectrometry (WDS). The oxidation products were analyzed using a Rigaku Geigerflex 2173 X-ray diffractometer (XRD) with Co K_α incident radiation generated at 40 kV and 30 mA. A 2θ range of 2 to 120 degrees was adopted for collection of X-rays.

To determine the density of porosity in the coating, secondary electron (SE) micrographs were taken from various locations of cross-sectioned coupons after being oxidized for various lengths of time. A rectangular picture frame was positioned continuously from the coating/substrate interface to the coating surface on the cross-sectional image of the coating, and the area fraction of the porosity within each frame was determined using Image-Pro® Plus Version 4.0.0 software. This software is capable of differentiating pores with other features by adjusting the threshold level of darkness. The area fraction of pores was assumed to be the volume fraction of pores in the coating. For a given distance to the coating/substrate interface, three measurements at different locations were performed, and their average was considered to be the volume fraction of porosity at a given distance to the coating/substrate interface.

4.3 Coating Microstructures

Five different coatings were assessed in this study: one pure Ni-Al coating, 80+0; two Ni-Al-5 μm CeO_2 coatings, 80+1 (5 μm) and 80+5 (5 μm); and two Ni-Al-9-15 nm CeO_2 coatings, 80+1 (9-15 nm) and 80+5 (9-15 nm). The compositions and phase characteristics of these coatings after annealing are summarized in Table 4-1. All coatings contained mainly the γ'-Ni_3Al phase. The CeO_2 phase was observed in both

annealed Ni-Al-5 μm CeO_2 coatings. However, CeO_2-related phases in the Ni-Al-nano CeO_2 were not detected due to their low concentration and the resolution limit of X-ray diffraction. In Chapter 3, it was determined that the annealing treatment at 800 °C transforms the nano CeO_2 particles into nano $CeAlO_3$ particles. Typical morphologies of the annealed pure Ni_3Al coating and the 80+1 (5μm) coating are shown in Figs. 4-1 (a) and (b) respectively. The uniform gray matrix in the micrographs is the γ'-Ni_3Al phase. The white particles in Fig. 4-1 (b) are CeO_2. Significant numbers of pores in all annealed coatings were formed due to local densification during the melting of Al and rapid diffusion of Al into the Ni matrix [1, 3].

Table 4-1. Characteristics of the five Ni-Al-CeO_2 coatings used in the investigation.

Sample code	Deposition condition	Al content (vol%)	Phases by XRD
80+0	0 g/l CeO_2	33.50±0.64	Ni_3Al (s)
80+1 (5 μm)	1 g/l CeO_2 (5μm)	30.58±0.52	Ni_3Al (s); CeO_2 (vw)
80+5 (5 μm)	5 g/l CeO_2 (5μm)	31.03±0.40	Ni_3Al (s); CeO_2 (w)
80+1 (9-15 nm)	1 g/l CeO_2 (9-15nm)	30.98±0.60	Ni_3Al (s)
80+5 (9-15 nm)	5 g/l CeO_2 (9-15nm)	29.83±1.81	Ni_3Al (s)

s: strong; w: weak; vw: very weak

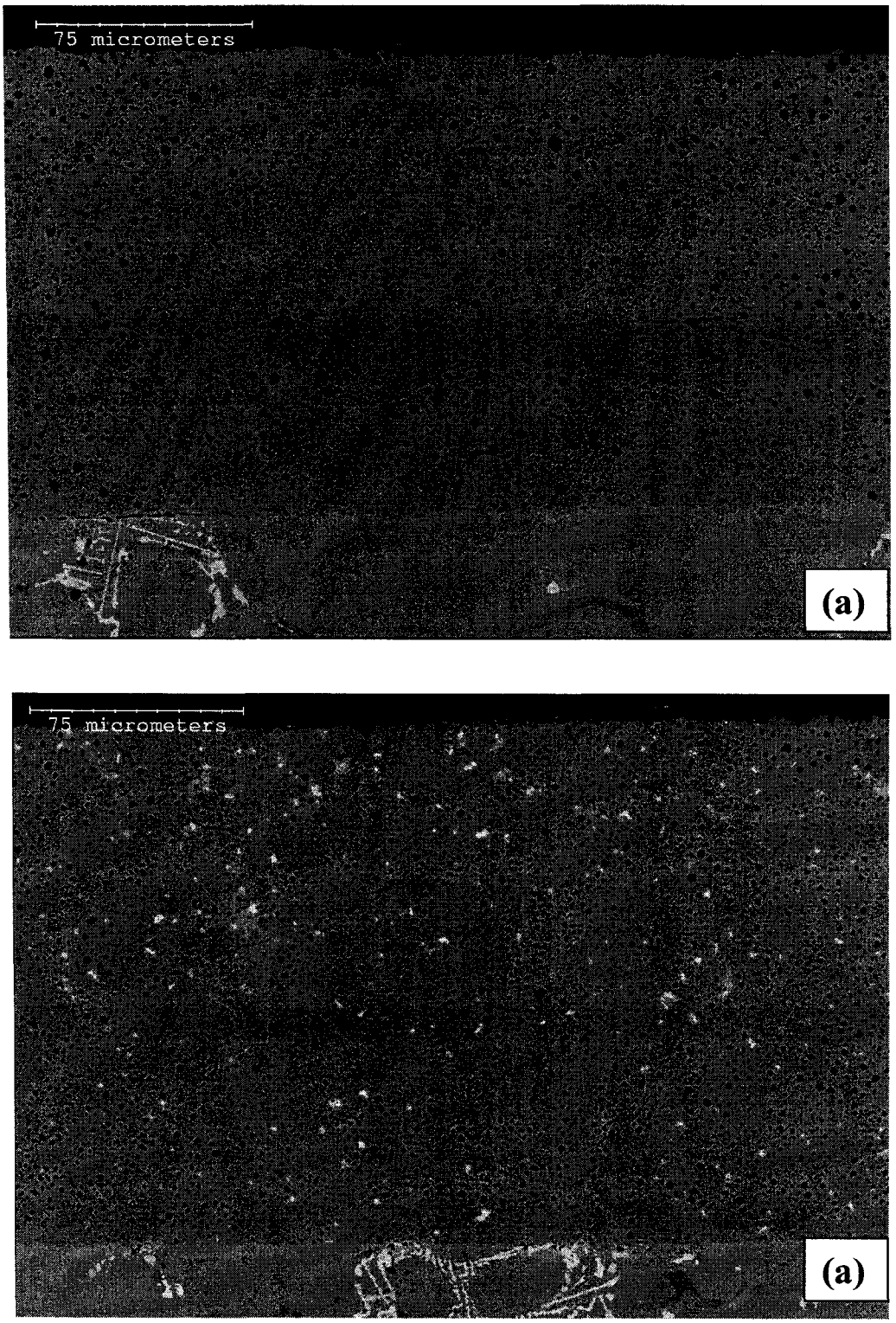

Figure 4-1. The typical morphologies of annealed Ni-Al and Ni-Al-CeO_2 composite coatings: (a) the pure Ni_3Al coating (80+0); (b) the 80+5 (5 μm) coating.

4.4 Oxidation at 850 °C

4.4.1 Oxidation Kinetics

Figs. 4-2 (a) and (b) show the mass changes of the five Ni_3Al based coatings and the uncoated alloy as a function of oxidation time. All coatings had smaller mass gains than the uncoated alloy up to 200hr (Fig. 4-2(a)). However, the uncoated alloy was characterized by a smaller mass increase after 200hr. In contrast, all coatings experienced increased rates of mass gain after 200hr (Fig. 4-2 (b)). The 80+5 (9-15 nm) coating had the lowest long-term mass change of these coatings. However, no noticeable spallation was observed for the uncoated HP alloy coupon and all coated coupons, even after 1000hr oxidation.

To understand the kinetics of cyclic oxidation, the following oxidation rate equation is used:

$$(\Delta W) = kt^n \tag{4-1}$$

$$\Delta W = \Delta m / A \tag{4-2}$$

where ΔW is the mass gain per unit area (mg/cm^2), k is the oxidation rate constant, t is oxidation time (sec), n is the rate exponent, Δm is the mass gain (mg), A is the sample surface area (cm^2). Depending on the value of n, the oxidation may follow the linear law ($n \approx 1$), the parabolic law ($n \approx 0.5$), or some other subparabolic relationship ($n < 0.5$).

Fig. 4-3 presents the log-log plots of all the coatings. All coatings quickly exhibited oxidation kinetics that were loosely consistent with the linear law. It is noted that the linear oxidation for the 80+5 (9-15nm) coating is retarded up to 300hr. A third oxidation stage with a decreased value of n was observed for all the coatings (Fig. 4-3 (a)), except the 80+5 (9-15nm) coating. The latter exhibited linear oxidation behavior almost up to 1000 hours (Fig. 4-3 (b)).

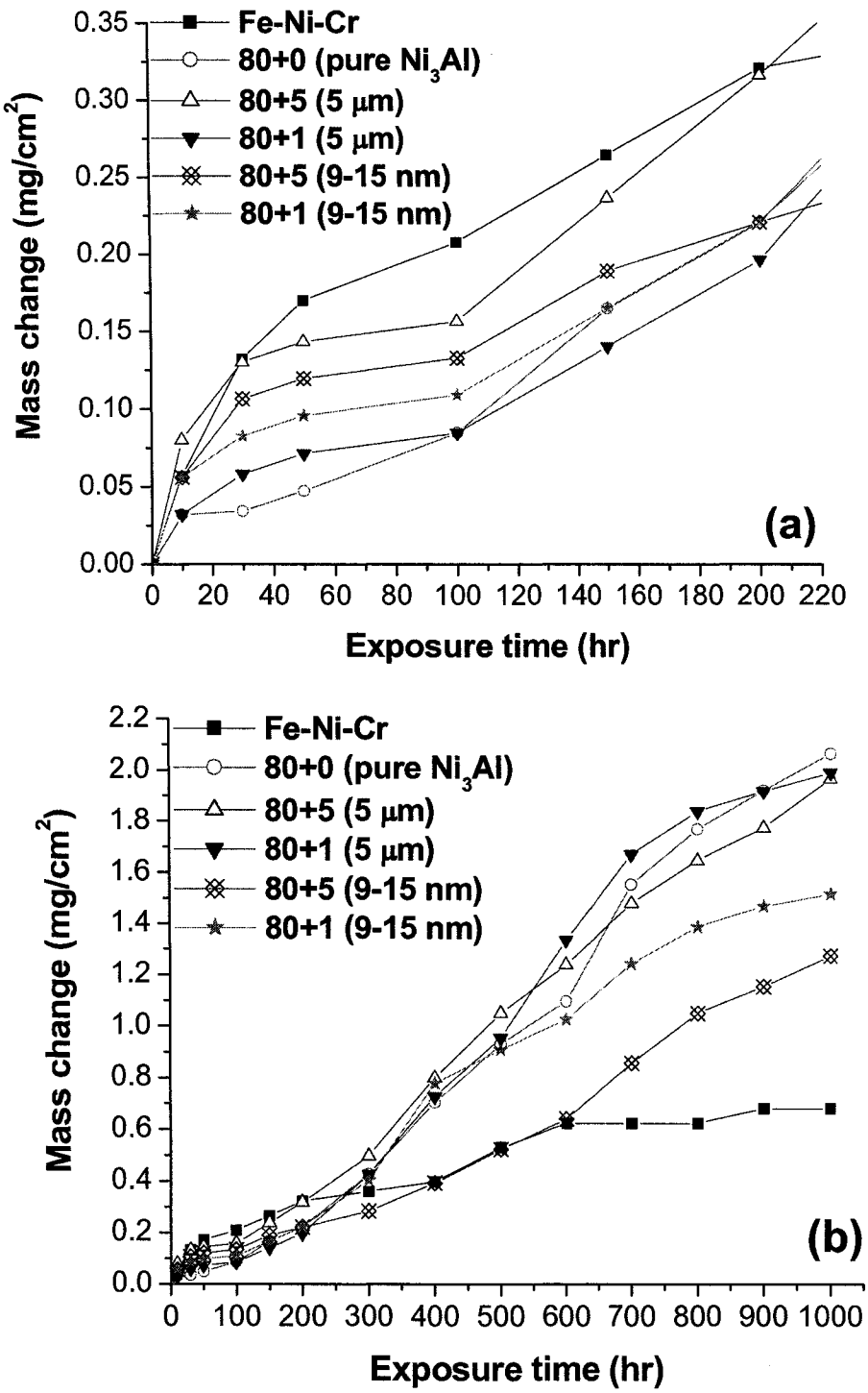

Figure 4-2. The mass change of CeO_2-modified Ni_3Al coatings during cyclic oxidation at 850 °C: (a) up to 200 hr; (b) up to 1000 hr.

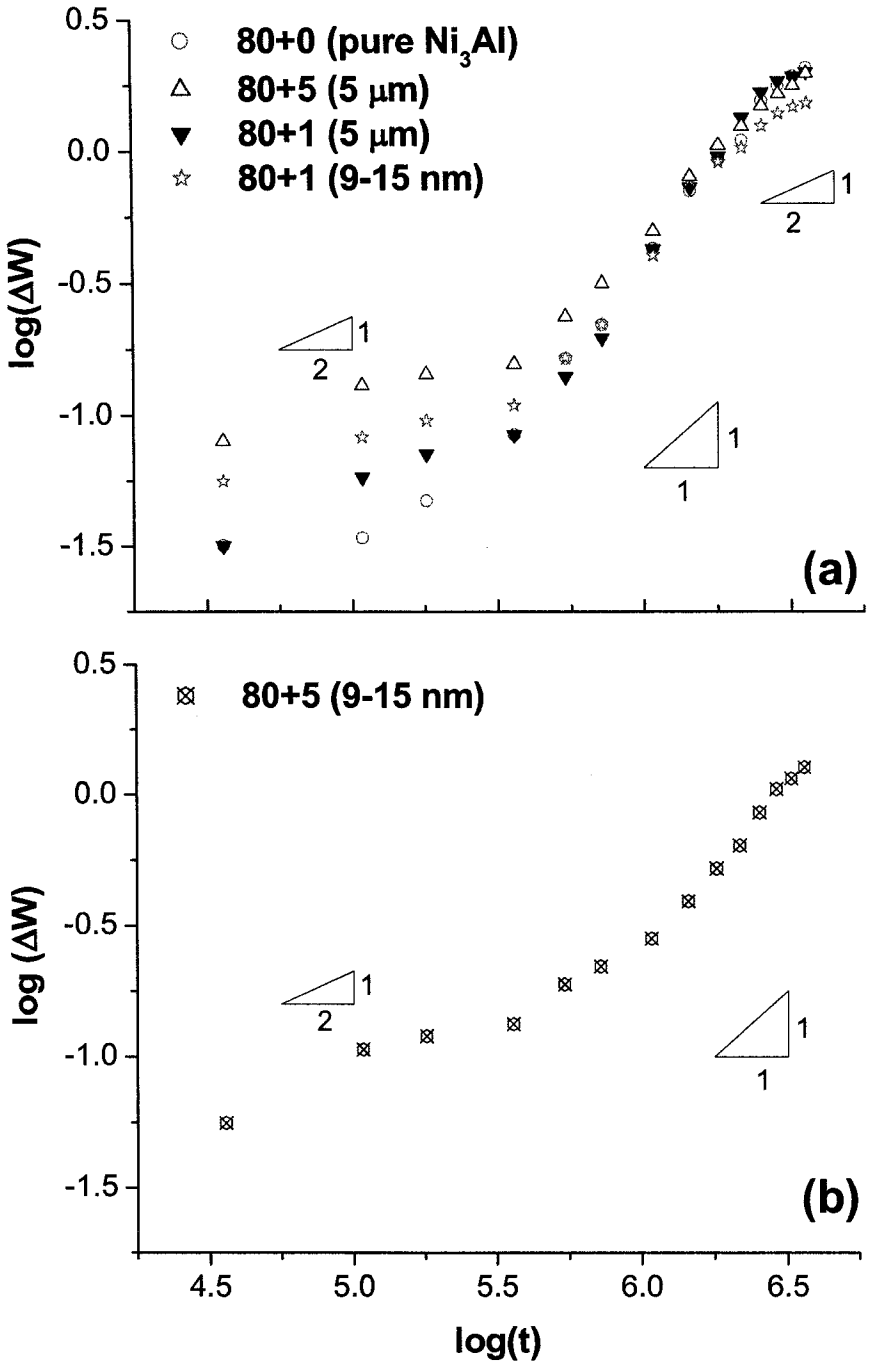

Figure 4-3. The change of oxidation rate component of Ni_3Al-based coatings during cyclic oxidation at 850 °C up to 1000 hr.

4.4.2 Morphologies of Oxide Scales

The surface morphologies (SE micrographs) of the pure Ni_3Al coating after oxidation for different times are presented in Figs. 4-4 (a)-(c). The types of oxides on the surface, as determined by XRD, are summarized in Table 4-2. According to Fig. 4-4 (a) and Table 4-2, short-term oxidation for 10 hr resulted in the formation of fine NiO crystals along the grinding tracks. By 100 hr, platelet-like γ-Al_2O_3 had covered most of coating surface (Fig. 4-4 (b)). The surface of the Ni_3Al-based coatings after 500 hr, as shown in Fig. 4-4 (c), consisted mainly of γ-Al_2O_3 and θ-Al_2O_3 mixtures according to XRD results in Table 4-2. γ-Al_2O_3 is one of the transition alumina phases that form prior to the equilibrium α-Al_2O_3 phases, and is typically formed on alumina-forming alloys or coatings during the early stage of oxidation [14, 23, 29-32]. It was proposed that γ-Al_2O_3 might transform to either δ-Al_2O_3 or θ-Al_2O_3 before it transforms into α-Al_2O_3 [33]. θ-Al_2O_3 is whisker-like or blade-like, and can easily be confused with the platelet-like γ-Al_2O_3. The formation of transition alumina is characterized by rapid outward diffusion of Al cations, which results in platelet or whisker shapes [14, 15, 23, 32].

The surface morphologies of micron and nano CeO_2- modified Ni_3Al coatings during cyclic oxidation were found to be similar to that of the pure Ni_3Al coating (nucleation of NiO crystals in the early stage and the formation of transition alumina with further oxidation). The transition Al_2O_3 grew more slowly on these CeO_2-modified coatings, especially the 80+5 (9-15 nm) coating, than on the pure Ni_3Al coating. Only a small fraction of surface area showed a noticeable amount of transition alumina on the 80+5 (9-15 nm) coating after 500 hr, as compared to the dominant transition alumina on the pure Ni_3Al coating (Fig. 4-4 (d)). The remaining (flat) areas were covered by platelet-like and whisker-like alumina that could be observed only under very high magnification. This suggests that growth of transition alumina on the 80+5 (9-15 nm) coating was suppressed.

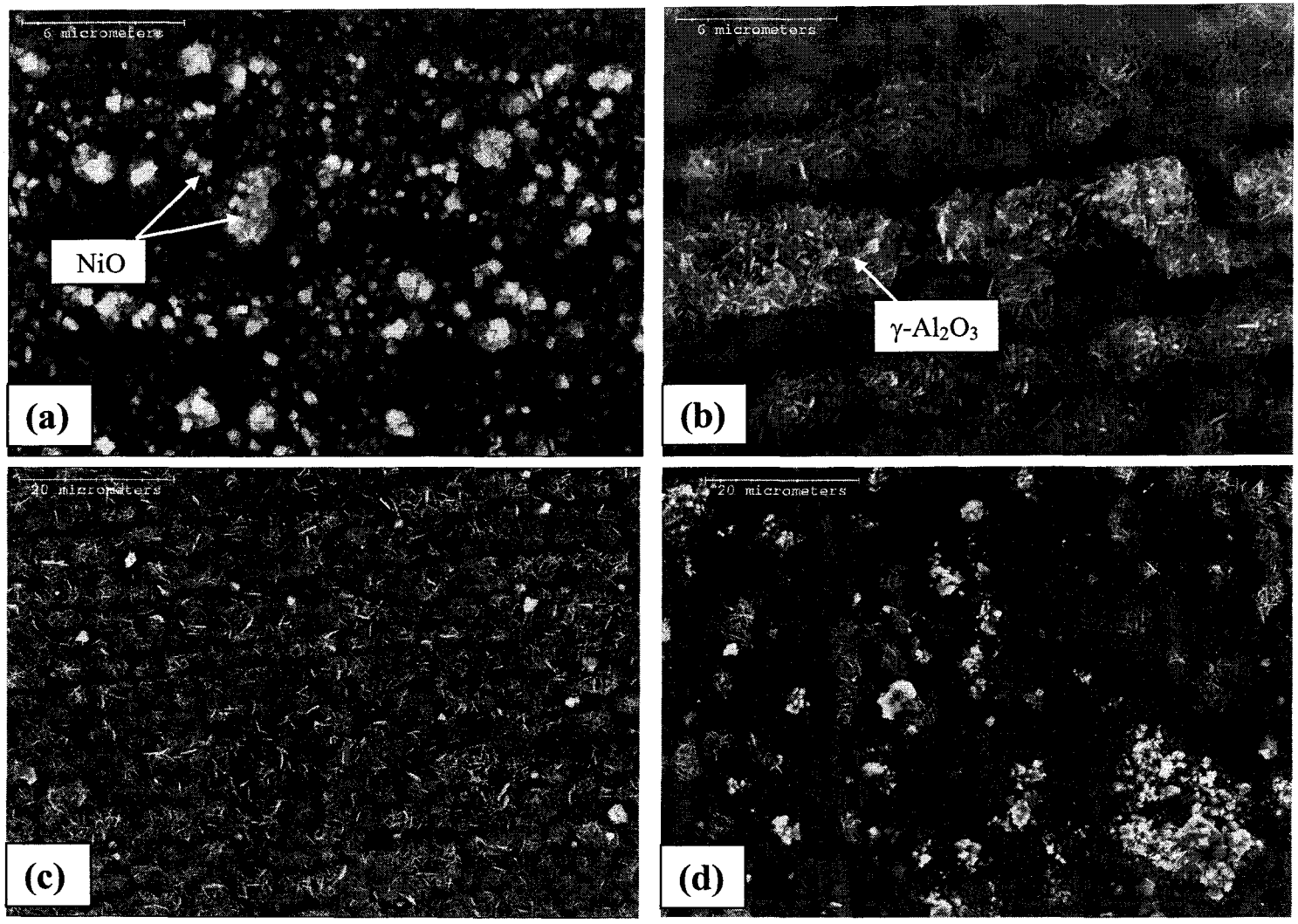

Figure 4-4. The surface morphologies of Ni_3Al-based coatings after cyclic oxidation at 850 °C: (a) 80+0 (pure Ni_3Al), 10 hr, 5000×; (b) 80+0 (pure Ni_3Al), 100 hr, 5000×; (c) 80+0 (pure Ni_3Al), 500 hr, 1500×; (d) 80+5 (9-15 nm), 500 hr, 1500×.

Table 4-2. The XRD results for oxidized coatings at 850 °C after the specified time.

Sample	10 hr	100 hr	500 hr	1000 hr
80+0	Ma: Ni_3Al* Mi: NiO	Mi: γ-Al_2O_3	Mi: Ni, NiO, $NiAl_2O_4$, γ-Al_2O_3, θ-Al_2O_3	Mo: Ni, NiO, $NiAl_2O_4$ Mi: γ-Al_2O_3, θ-Al_2O_3
80+5 (5 μm)	Mi: NiO, CeO_2	Mi: NiO, CeO_2	Mo: Ni, NiO Mi: $NiAl_2O_4$, γ-Al_2O_3, θ-Al_2O_3, CeO_2	Ma: NiO Mo: Ni, $NiAl_2O_4$ Mi: γ-Al_2O_3, θ-Al_2O_3, CeO_2
80+1 (5 μm)	Mi: NiO, CeO_2	Mi: NiO, γ-Al_2O_3, CeO_2	Mo: Ni, NiO Mi: $NiAl_2O_4$, γ-Al_2O_3, θ-Al_2O_3, CeO_2	Mo: Ni, NiO, $NiAl_2O_4$ Mi: γ-Al_2O_3, θ-Al_2O_3, CeO_2
80+5 (9-15 nm)	Mi: NiO	Mi: NiO, γ-Al_2O_3	Mi: Ni, NiO, $NiAl_2O_4$, γ-Al_2O_3, θ-Al_2O_3	Ma: NiO Mo: Ni, $NiAl_2O_4$ Mi: γ-Al_2O_3, θ-Al_2O_3
80+1 (9-15 nm)	Mi: NiO	Mi: γ-Al_2O_3	Mi: Ni, NiO, $NiAl_2O_4$, γ-Al_2O_3, θ-Al_2O_3	Mo: Ni, NiO, $NiAl_2O_4$, Mi: γ-Al_2O_3, θ-Al_2O_3

Ma: Major; Mo: Moderate; Mi: Minor.
*: Ni_3Al is the major phase in all coatings oxidized for all times.

4.4.3 Cross-sectional Morphologies of Oxide Scales

Cross-sectional micrographs of pure Ni_3Al coatings oxidized for 100 hr and 500 hr are depicted in Figs. 4-5 (a) and (b) respectively. The oxide scale after 100 hr was very thin (about 1-2 μm). A change in cross-sectional morphology was clearly evident in the

samples after long-term oxidation. The sample after 500 hr was characterized by a thin compact external oxide scale and a pore-rich region in the underlying coating (it became an oxidation zone) (Fig. 4-5 (b)). Considerable oxides were observed on the inner surfaces of these pores after 500 hr. Neighboring pores were found to be interconnected by oxidized channels, as indicated by solid arrows in Fig. 4-5 (b). The white "islands" surrounded by the oxide layer were determined by EDS to contain Ni and Al, which suggests that they were trapped in the coating matrix. With increasing oxidation exposure, these islands became richer in Ni, eventually leading to a Ni solid solution with very low Al content. Various Ni and Ni-Al phases were also detected by XRD (Table 4-2). Long-term exposure produced multiple oxide products (mainly NiO, $NiAl_2O_4$ spinel, γ-Al_2O_3, and θ-Al_2O_3). The morphologies of the oxidized zone of the two CeO_2 (5 μm)-modified Ni_3Al coatings and the 80+1 (9-15 nm) coating were similar to that of the pure Ni_3Al coating. Fig. 4-5 (c) shows a typical micrograph of the 80+5 (5 μm) coating oxidized for 500 hr, which is similar to pure Ni_3Al, as shown in Fig. 4-5 (b).

According to Figs. 4-2 and 4-3, the 80+5 (9-15 nm) coating exhibited a cyclic oxidation behavior different from that of the other coatings. This observation is consistent with the cross-sectional micrograph shown in Fig. 4-5 (d). Unlike that of the other coatings, the surface of the 80+5 (9-15 nm) coating was covered by a thin Al-rich oxide layer, and no porous oxidation zone was observed in the underlying alloy. It is evident that the formation of oxidized channels in 80+5 (9-15nm) coating was retarded.

After 1000 hr, the oxide layer in the Ni_3Al coating was porous and thick, more than 10 μm (Fig. 4-6 (a)). The morphologies of the oxidation zones on all the other coatings were similar after oxidation for 1000 hr, although their thicknesses appeared to vary (Fig. 4-6). The 80+5 (9-15 nm) coating showed the thinnest oxidation zone, which is consistent with the lowest weight gains (Fig. 4-2).

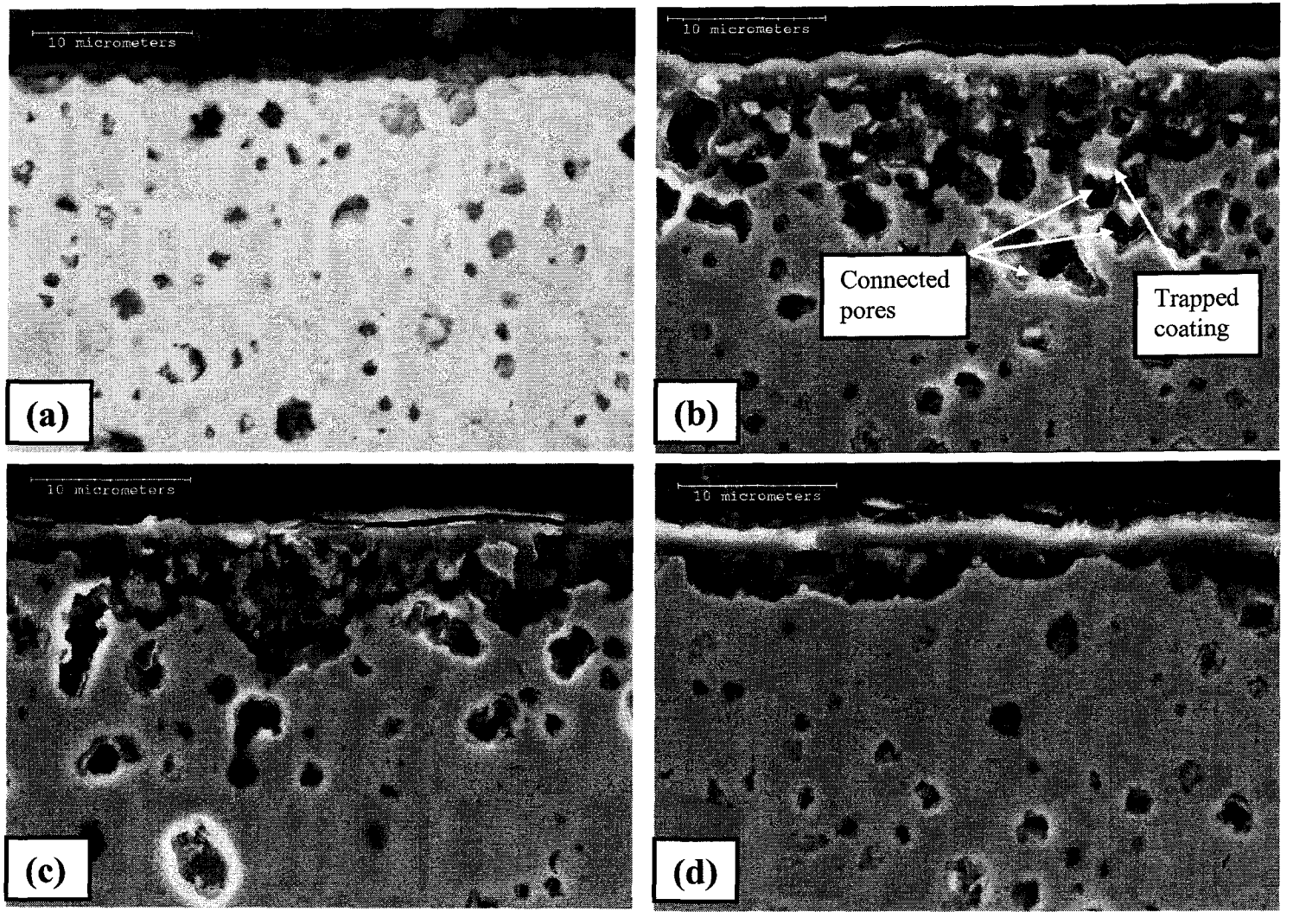

Figure 4-5. The cross-sectional images of coatings oxidized at 850 °C: (a) 80+0 (pure Ni_3Al), 100 hr; (b) 80+0 (pure Ni_3Al), 500 hr; (c) 80+5 (5 μm), 500 hr; (d) 80+5 (9-15 nm), 500 hr.

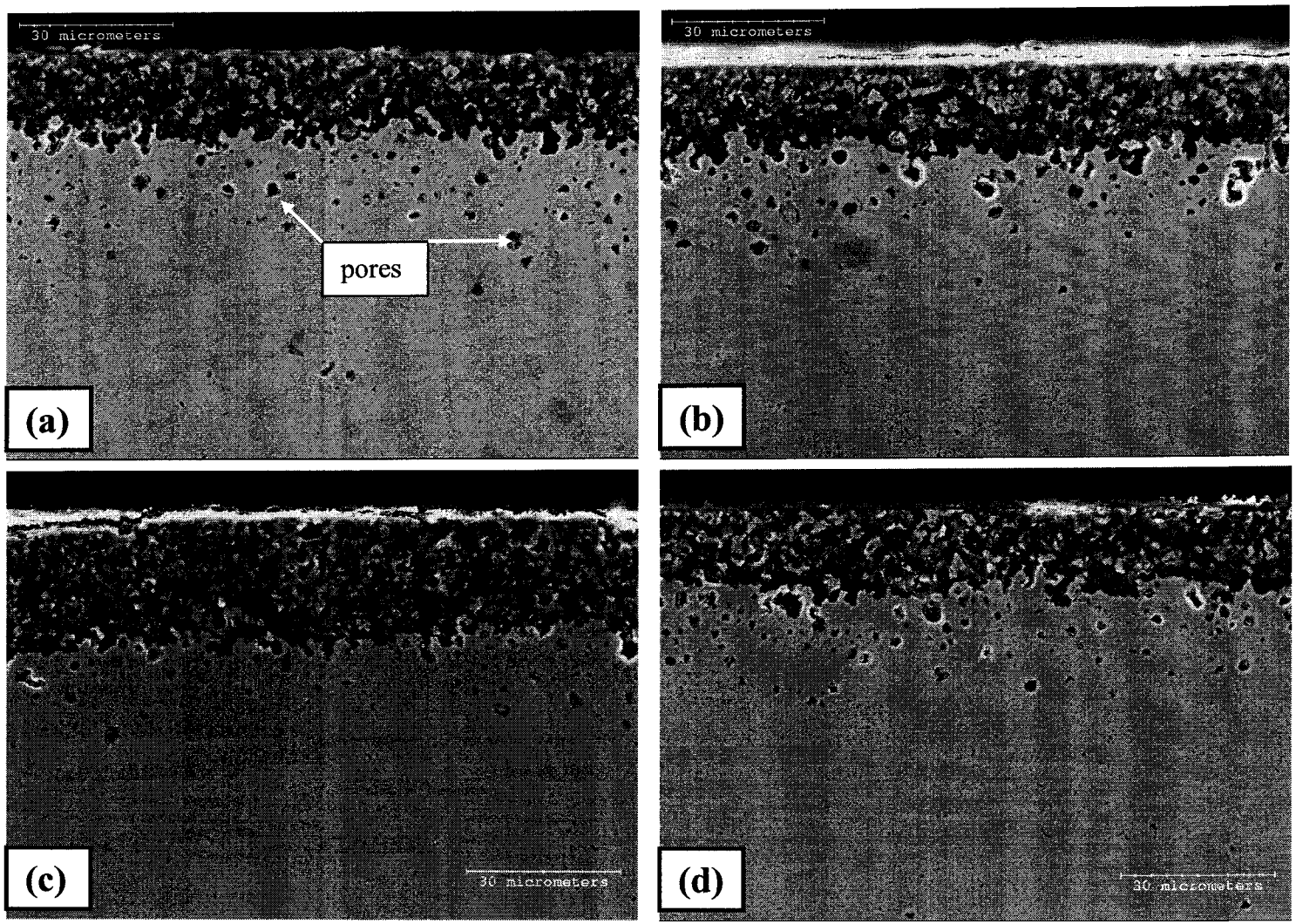

Figure 4-6. The cross-sectional images of coatings oxidized at 850 °C for 1000 hr: (a) 80+0 (pure Ni_3Al); (b) 80+5 (5 μm); (c) 80+1 (9-15 nm); (d) 80+5 (9-15 nm).

4.4.4 Cross-sectional Microstructures of Coating Layer

Fig. 4-7 (a) shows micrographs in the pure Ni_3Al coating/Fe-Ni-Cr substrate after cyclic oxidation for 500 hr.

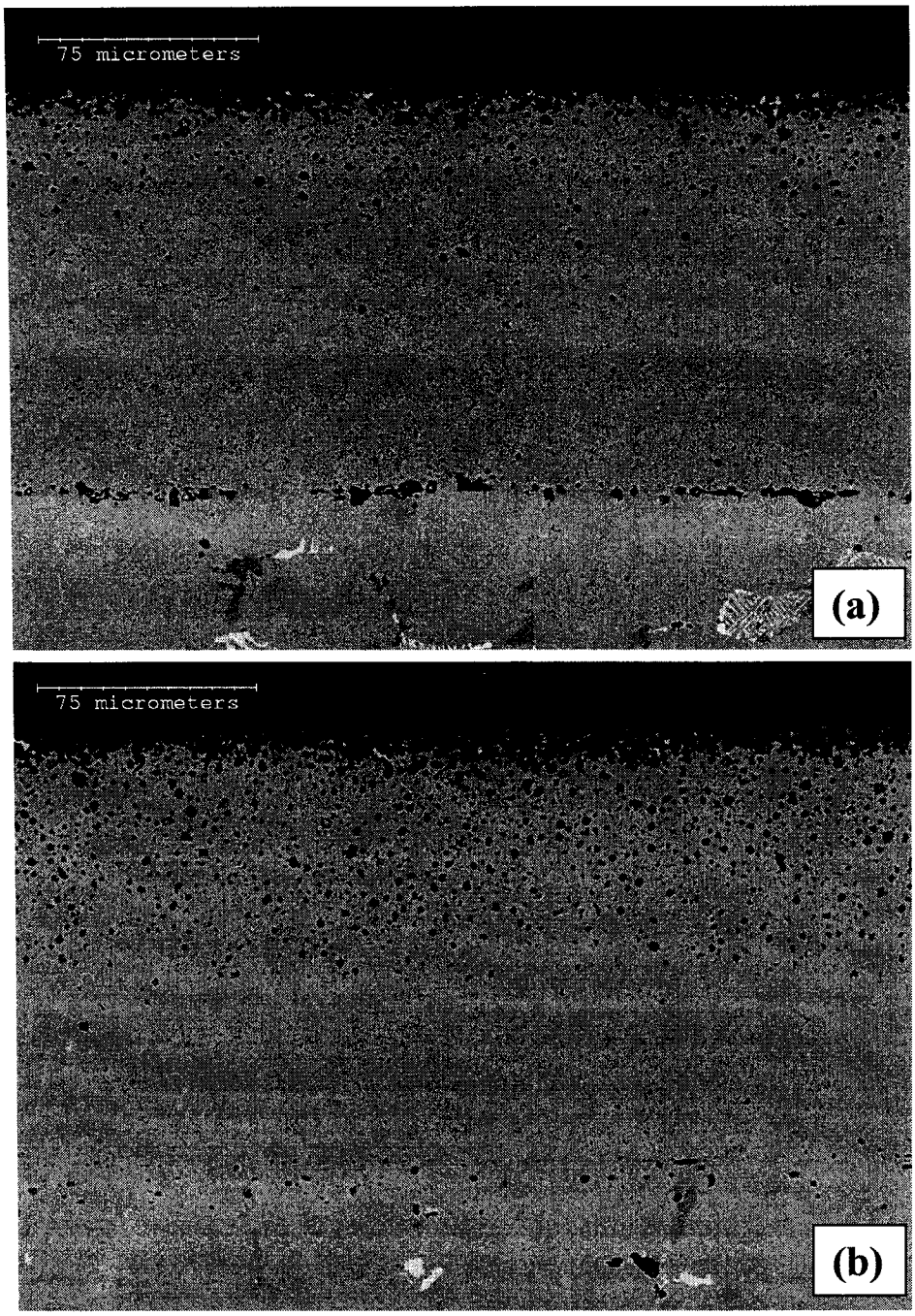

Figure 4-7. The cross section of the Ni_3Al-based coatings and Fe-Ni-Cr alloy substrate after cyclic oxidation for 500 hr: (a) 80+0; (b) 80+5 (5 μm).

In addition to the oxidation zone adjacent to the surface, the coating was characterized by a pore-rich zone beneath the oxidation zone and a pore-free zone in the coating next to the substrate. These characteristics differ from the un-oxidized coating shown in Fig. 4-1 (a), where the pores are homogeneously distributed across the coating. This suggests that the pore-free zone was formed as a result of a healing process during oxidation. This healing was actually observed after as little as 100 hr. It should be noted in Fig. 4-1(a) that the pore-free zone in the pure Ni_3Al coating was much wider than that in the 80+5 (5μm) coating (Fig. 4-7 (b)), indicating that pore-healing was affected by CeO_2 particles in the coating.

The above characteristics can be also found in Figs. 4-6 (a)-(d), which depict cross-sectional morphologies of various coatings after 1000 hr of oxidation. In these micrographs, the pore-free zone has almost met the oxidation zone on the top, particularly in the cases of the pure Ni_3Al and the 80+1 (9-15 nm) coatings. Pore healing was slower in the cases of the 80+5 (5 μm) and 80+5 (9-15 nm) coatings.

Compositional profiles across the coating and the substrate after cyclic oxidation were obtained by EPMA (Figs. 4-8 (a)-(d)). The zero point on the X axis is the location of the gas/oxide scale interface. Inward diffusion of Ni from the coating layer into the alloy substrate is significant, while that of Al is negligible even after 1000 hr (Figs. 4-8 (a) and (b) respectively). The substrate elements (mainly Cr and Fe) were detected in the coating (Figs. 4-8 (c) and (d) respectively). Evidence for diffusion of small amounts of Mn and Si were obtained. This behavior was observed for all the CeO_2-modified Ni_3Al coatings as well.

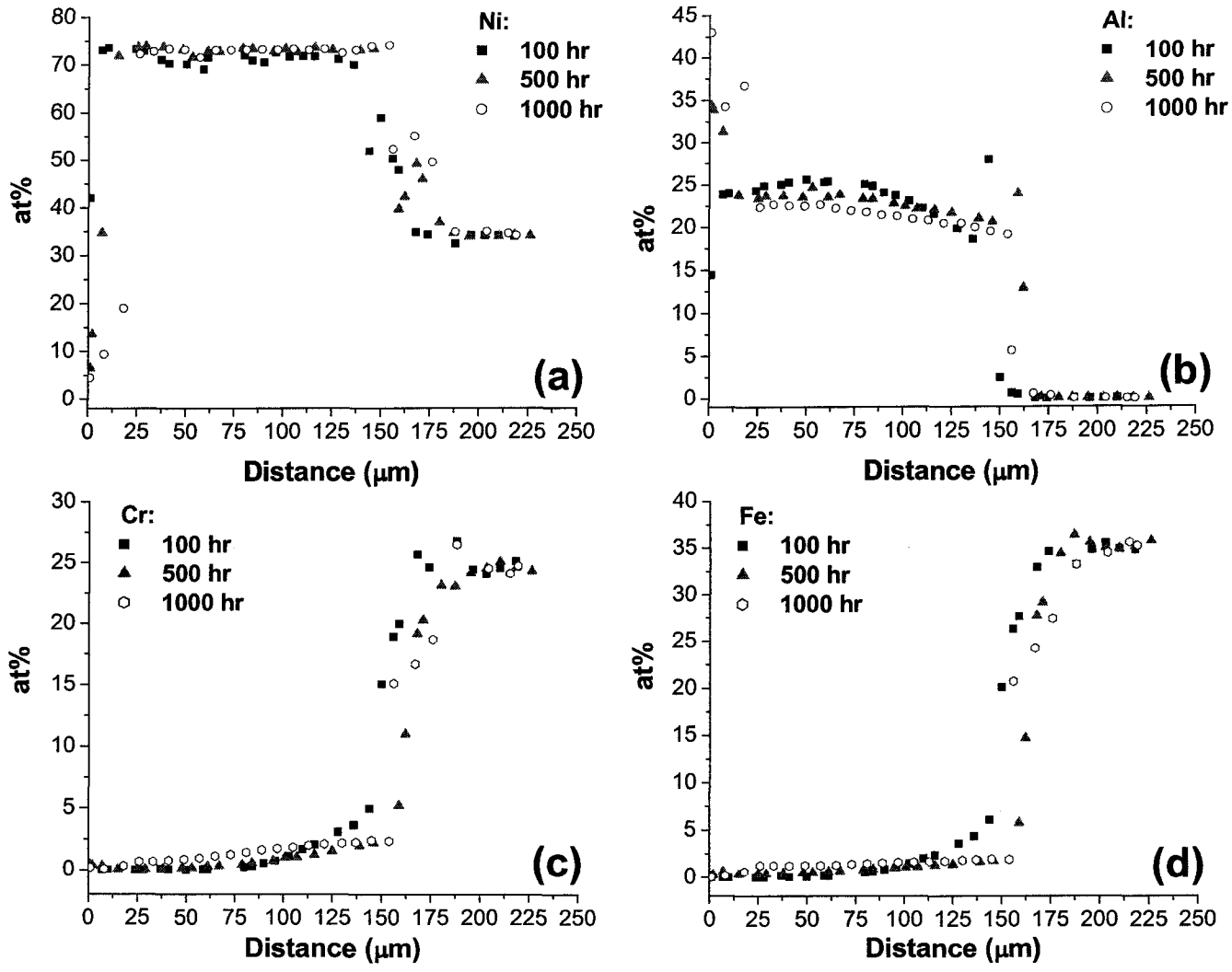

Figure 4-8. Compositional profile in the pure Ni_3Al coating/Fe-Ni-Cr substrate system after cyclic oxidation at 850 °C.

Figs. 4-9 (a)-(d) show the variations in pore density (vol %) with distance into the coating and the position of the oxidation zone as a function of oxidation time. The zero point on the X axis is the location of the coating/alloy interface, and the normalized distance of 1.0 marks the location of the outer surface of the oxide scale. The vertical lines in Fig. 4-9 represent the location of the coating/oxide interface. As the thickness varied for individual coupons, the normalized distance rather than the actual distance was used for purposes of comparison. After 1000 hr, the volume fraction of pores in the coating next to the oxidization zone had decreased to about 3 vol% or less in the pure Ni_3Al and 80+1 (9-15 nm) coatings, about 4% in the 80+5 (5μm) coating, and 6% in the 80+5 (9-15nm) coating (Figs. 4-9 (a)-(d)). The decrease in amount of pore healing in the CeO_2-modified coatings compared with that in the pure N_3Al coating after shorter exposure times was even more profound at the intermediate length of exposure. Pore-healing in the coating layer always started from coating/substrate interface and extended to the coating surface with increasing time (Figs. 4-9 (a)-(d)). This, as well as the observation of significant diffusion of substrate elements in the coating during oxidation (Figs. 4-8 (c) and (d)), suggests that pore healing is related to interdiffusion.

The 80+5 (9-15nm) coating was characterized by a very slow pore-healing rate and little advance of the oxidation zone within the first 500 hr (Fig. 4-9 (d)), which is quite different from other coatings. In the second 500 hr, the oxidation zone in the 80+5 (9-15nm) coating had advanced significantly, but those in the other four coatings had advanced much less. This observation is consistent with the fact that the 80+5 (9-15 nm) coating did not exhibit a third stage of oxidation with a lower oxidation rate, Fig. 4-3. Pore healing in the second 500 hr period for the 80+5 (9-15 nm) coating was accelerated, but as much as 6vol% pores still remained adjacent to the oxidized zone after 1000 hr.

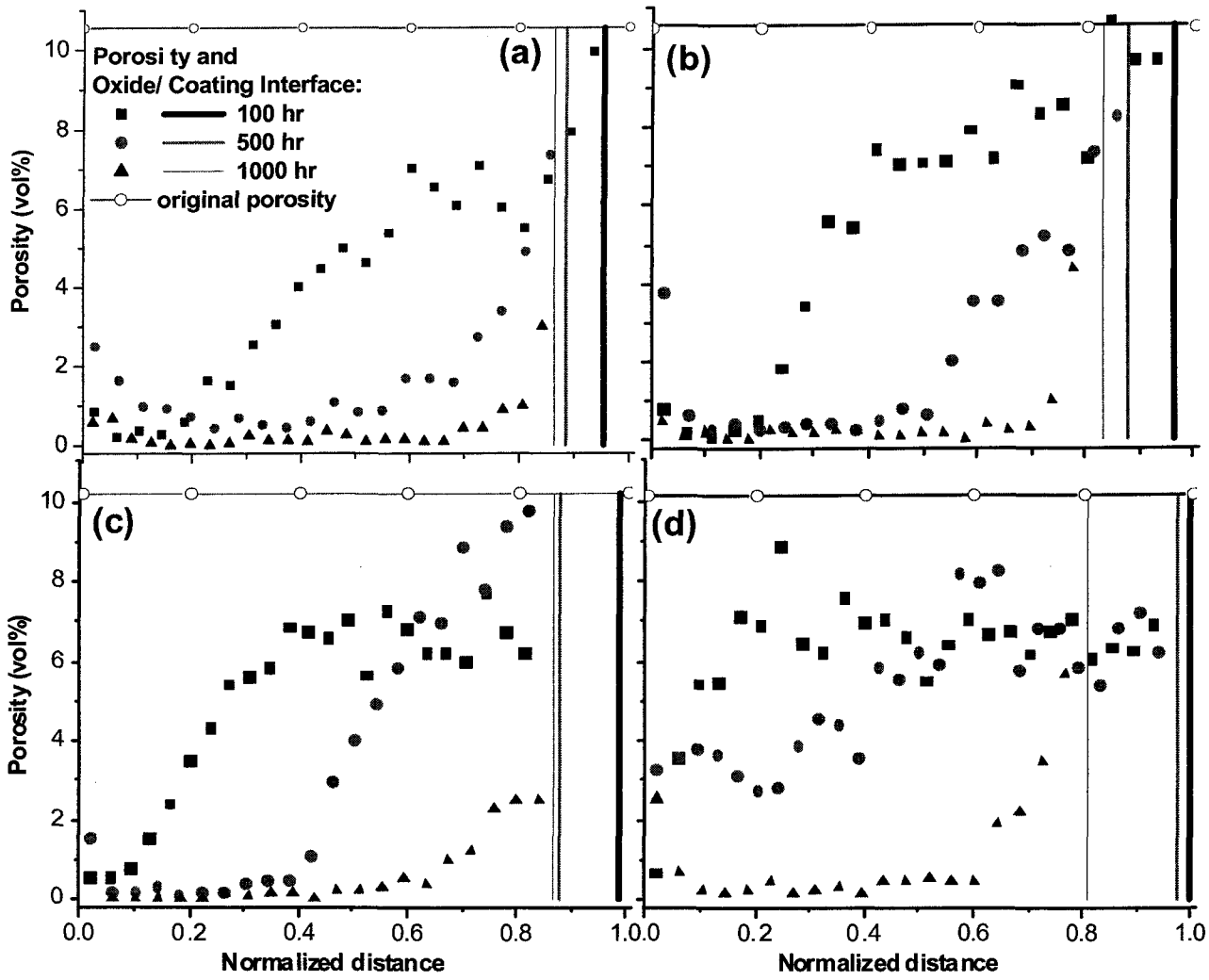

Figure 4-9. The variation of pore density (vol%) with time and the position of oxidation zone in Ni_3Al-based coatings during cyclic oxidation: (a) 80+0 (pure Ni_3Al); (b) 80+5 (5 μm); (c) 80+1 (9-15 nm) (d) 80+5 (9-15 nm).

4.4.5 Discussion

It has been suggested that Ni_3Al alloys or coatings should form one slowly-growing alumina oxide scale beneath an outer NiO layer and an intermediate $NiAl_2O_4$ layer when oxidized at temperatures less than 1000 °C, and should therefore possess excellent oxidation resistance [14, 23, 30]. The current electrodeposited Ni_3Al base coatings during cyclic oxidation at 850 °C have shown similar behavior. However, the formation of alumina scales did not ensure good long-term cyclic oxidation resistance for the coatings. In our opinion, this inconsistency can be accounted for by considering other influential factors for the current coating system. Such factors include porosity in the coating, presence of CeO_2 particles, and interdiffusion between the coating and the substrate.

4.4.5.1 Effect of Porosity

The Ni_3Al-based coatings studied contain large volume fractions of pores of micron-level diameter (Figs. 4-1 (a)-(b)). The pores in the coating matrix are closed, while those on the surface are open. The latter would increase the effective exposure area for oxidation, resulting in a higher apparent oxidation rate. Susan [14] reported that pores do not have a detrimental effect on the oxidation resistance of electrodeposited Ni-Al alloy coatings at 800 °C for periods up to 2000 hr. However, a detrimental effect of the pores was clearly observed in the Ni_3Al-based coating we obtained. This inconsistency may derive from a higher pore density, more than 10vol% in the current Ni_3Al base coatings, compared to only 8vol% in the Ni-Al coatings studied by Susan [3, 14]. Different testing conditions may also have contribution to this inconsistency.

The pores in the coating not only increase the exposed surface area, but also act as stress enhancers in the presence of stresses. Residual stresses are commonly generated in the coating system due to the growth of oxide scale and thermal cycling [34-37]. Growth stress is related to the growth of the oxide scale during oxidation [34-37], while thermal stress is caused by thermal expansion mismatch between the coating and the oxide scale during cooling. By assuming a scale of equal thickness on each 20×10 mm^2 face of the coated coupon, the thermal stress can be estimated as [35, 37]:

$$\sigma_{ox} = \frac{E_{ox}\Delta T(\alpha_{ox} - \alpha_{m})}{1 + 2(\frac{E_{ox}}{E_m} \bullet \frac{t_{ox}}{t_m})} \quad (4\text{-}3\text{-}1)$$

$$t_m \sigma_m + 2t_{ox}\sigma_{ox} = 0 \quad (4\text{-}3\text{-}2)$$

where α_{ox} and α_m are the thermal expansion coefficients of the metal coating and the oxide, respectively; ΔT is the difference between room temperature and the oxidation temperature; σ_{ox} is the thermal stress in the oxide layer; E_{ox} and E_m are the Young's modulus for the oxide and the metal coating respectively; t_{ox} and t_m are the thickness of the oxide and the thickness of the coating plus substrate respectively; σ_m is the stress in the matrix. Most oxides such as $NiAl_2O_4$, α-Al_2O_3 and γ-Al_2O_3 have lower thermal expansion coefficients than the Ni_3Al alloy (Table 4-3). Therefore, according to Equation (4-3), tensile stresses in the current Ni_3Al coatings can be expected upon cooling.

Table 4-3. Some mechanical properties of oxides and the coating matrix.

	Ni_3Al	γ-Al_2O_3	α-Al_2O_3	NiO	$NiAl_2O_4$
Theraml expansion coefficient, α ($\times 10^{-6}$/K)	12.5	2.60	8.10	15	10
Poisson's ratio, ν	0.305	0.24	0.23		
Young's modulus, E (Gpa)	168	253	340		
Density, g/cm^3	7.65	3.67	3.78	6.67	
Reference	[38, 39]	[40]	[41]	[42]	[42]

In the early stage of cyclic oxidation, the coating surface and the inner surfaces of the open pores were oxidized slowly (Fig. 4-10 (a)). Compressive stresses would develop in the oxide layer, and tensile stresses in the Ni_3Al base coating. The latter can be magnified around the tips of pores in the coatings. Because the pores can be treated as internal notches, the stress concentration can be calculated by [43]:

$$\sigma_{tip} = 2\sigma_{app}\sqrt{\frac{c}{\rho}} \tag{4-4}$$

where σ_{tip} is the stress at the notch tip; σ_{app} is the tensile stress on the Ni_3Al coating; c is the notch length; ρ is the radius of curvature of the notch. For brittle materials, such as Ni_3Al, a crack can be propagated if the local stress at the tip exceeds the tensile fracture stress σ_c of Ni_3Al, which was determined to be about 500MPa for the pure stoichiometric Ni_3Al [44]. Considering only the thermal stress during cooling after 100hr, σ_{app} was calculated to be 3.60 MPa using Equation (4-3-1) and (4-3-2). This calculation is based on the assumptions that only a γ-Al_2O_3 layer with a thickness of 1.5 μm is formed on a coating that is 150 μm thick, and secondly that c can be given an average value of 1.0 μm according to the SEM micrographs. From Equation (4-4), ρ must be less than 2×10^{-4} μm in order for σ_{tip} to exceed σ_c.

Although the direct propagation of a crack by thermal stress alone seems unlikely, the plastic deformation by the magnified stress at the tip is quite possible. Internal diffusion of oxygen through dislocation pipes may produce sharp oxidized channels connecting other nearby pores (Fig. 4-10). This oxidation mechanism can become dominant as the time of oxidation is increased, when the growth stress is increased due to thicker oxide scale. The formation of interconnected channels between the pores increases the dimensions of defects and their sharpness in the coating; this, in turn, causes an increase in the tensile stresses acting at the tip of the defects. This would further accelerate the process of oxidation.

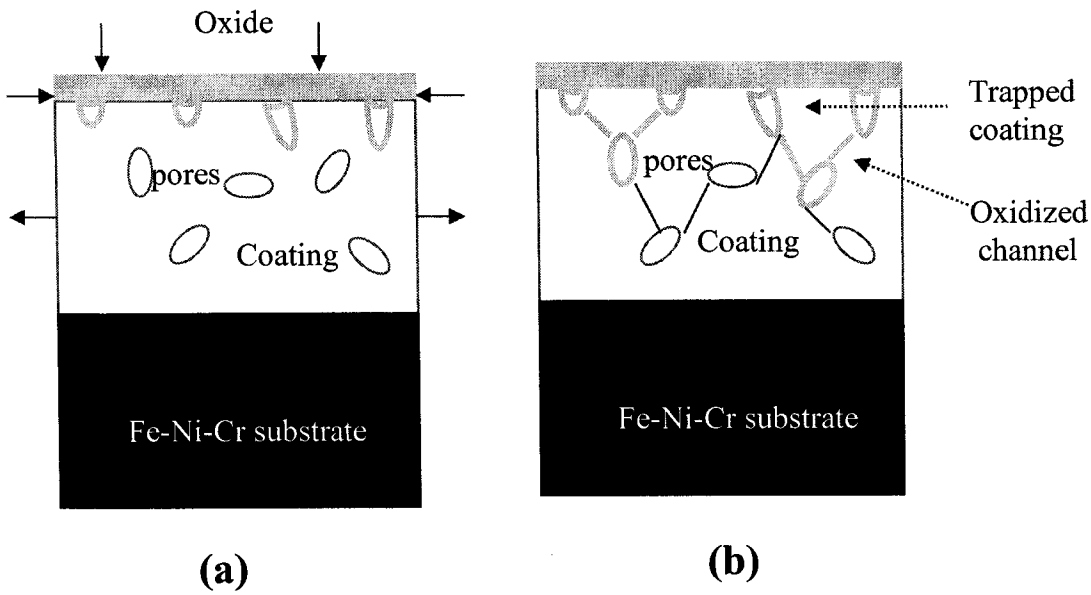

Figure 4-10. Schematic illustration showing the formation of oxidized channels in porous Ni_3Al-based coatings during cyclic oxidation: (a) Initial stage of oxidation; (b) Formation of interconnected oxidized channels.

The formation of interconnected oxidized pores may also result from the Kirdendall diffusion effect, as observed in dense Ni-Al alloys [24, 45-47]. At 850 °C, the growth of Al_2O_3 on the surface of pure Ni_3Al coating or on the inner surface of a pore is characterized by the dominant outward diffusion of Al (Figs. 4-4). As a result, the inward vacancy flux would occur and may be condensed at the scale/coating matrix interface into voids. For the coating matrix adjacent to the scale, the depletion of Al due to the formation of Al_2O_3 causes the inward diffusion of Ni. The Kirdendall vacancies could also lead to the formation of voids at the scale/coating interface or at the grain boundaries of the coating.

Due to high porosity, the active path of diffusion was readily formed between the oxidized and non-oxidized pores, allowing inward diffusion of oxygen [24, 46, 47]. This is evidenced in Figs. 4-5 (b) and (c), where the oxide layer appears defective and thickened (probably as a result of cracking of oxide scale and/or oxidized channels between pores by high residual stresses). The latter would increase the direct exposure of

the coating matrix to oxygen, which would result in higher mass change of the coating (as was observed in the intermediate stage).

The above discussion provides an explanation for the low oxidation rate observed in the early stage of oxidation and the high oxidation rate in the intermediate stage. The occurrence of the third oxidation stage with a decreased oxidation rate in some coatings is also consistent with the model. The rapid healing of pores in the pure Ni_3Al, 80+5 (5 μm), 80+1 (5 μm) and 80+1 (9-15 nm) coatings greatly decreases the stress concentration in the coatings and thus the risk of forming interconnected oxidized channels. Therefore, an improvement in oxidation resistance of these coatings can be expected. The absence of the third oxidation stage in the 80+5 (9-15 nm) coating, on the other hand, can be attributed to the slow pore-healing in the coating. This abnormal behavior in the 80+5 (9-15 nm) coating is related to the effect of CeO_2 particles, which are further discussed in the following section.

4.4.5.2 Effect of CeO_2 Particles on The Stability of The Scale

The 80+5 (9-15 nm) coating has a low pore-healing rate, but maintains a stable oxide scale for up to 500 hr. These two factors should have opposing effects on the oxidation resistance, but a low oxidation rate was observed. The underlying cause of this behavior is related to the presence and the size of the CeO_2 particles, in terms of supplying Ce^{+4} ions, which are believed to be beneficial to the oxidation resistance of alloys or coatings. Ce^{+4} ions were found to segregate at the grain boundaries of the protective oxide, which blocks the outward diffusion of metal via oxide grain boundaries, prevents coarsening of the oxide grains, and decreases the growth rate of the oxide layer [20, 32, 48-50]. In the present study, the fine–grained thin oxide film could lead to lower growth stress and thermal stress in the oxide layer, and thus the level of tensile stresses in the coating. The oxide film also helps to improve the resistance of the oxide layer to cracking. The suppressed outward Al flux can reduce Kirkendall vacancies and the formation of voids. These beneficial effects, in turn, can maintain a thin compact scale against the inward diffusion of oxygen, and thus retard the oxidation in the intermediate stage.

It has been reported that ceria particles above 10 nm cannot serve as effective sources of Ce^{+4} ions [49]. This appears to be true for the micron CeO_2 (5 μm)-modified Ni_3Al coatings obtained in this study, as the ceria particles remained detectable even after long-term exposure, indicating that large fraction of CeO_2 did not decompose into Ce^{+4} ions. On the other hand, these large ceria particles themselves may provide short-circuit paths for oxygen diffusion, resulting in higher oxygen pickup in coatings [32, 49]. It was determined that nano CeO_2 particles transformed into $CeAlO_3$ during the annealing treatment in Chapter 3. In an oxidizing environment, $CeAlO_3$ decomposes to Al_2O_3 and CeO_2. Due to their large surface areas, these nano CeO_2 particles and the decomposed $CeAlO_3$ phases are probably more effective in providing Ce^{4+} ions.

The slowly-growing thin oxide layer observed on the 80+5 (9-15 nm) coating is attributed to its ability to supply Ce^{4+} ions. It has relatively high nano CeO_2 content, and can supply enough Ce^{4+} ions into the oxide layer to maintain a high-quality scale. Consequently, the formation of interconnected oxidized channels does not occur until a later stage. This beneficial effect is eventually compromised by the formation of interconnected oxidized channels due to a high volume fraction of pores and increased residual stresses in the coating even after long-term oxidation. In the 80+1 (9-15 nm) coating, rapid formation of interconnected oxidized channels during long-term exposure might be caused by insufficient CeO_2 in the coating to stabilize the protective oxide scale. Both micron CeO_2-modified coatings lack Ce^{4+} ions due to slow decomposition of the large CeO_2 particles in the early stage, resulting in the rapid formation of a severely oxidized zone (similar to the CeO_2-free pure Ni_3Al coating).

4.4.5.3 Effect of Interdiffusion

Interdiffusion is a common problem in protective coating systems at high temperatures. In the Ni_3Al-based coating/Fe-Ni-Cr systems studied here, interdiffusion becomes obvious even in the early stage of oxidation (100 hr). In addition to the existence of a concentration gradient between the coating and the substrate, the pores in the coatings accelerate interdiffusion by creating a high vacancy flux and providing short-

circuit paths for diffusion. Interdiffusion was found to change the coating morphology by healing inherent pores. The Ni_3Al-based coatings were formed via a solid diffusion reaction between the Al particles and the Ni matrix, which is similar to the sintering of powders in powder metallurgy. Pores are healed by a rapid atom flux to the pores, and by vacancy flux from the pores to vacancy sinks such as grain boundaries, interfaces, and free surfaces [51]. During cyclic oxidation at 850 °C, the healing of pores is not uniform across the coating thickness, suggesting that sintering is not the only mechanism for healing. It is believed that the rapid healing of pores in the current coatings was caused mainly by the outward flux of substrate elements such as Fe, Cr, Mn, Nb and Si.

The fact that the depths of interdiffusion of Ni and Al into the substrate are much shorter than those of Cr and Fe into the coating (Figs. 4-8) suggests that the outward flux of substrate elements into the coating might be larger than the inward flux of Ni and Al to the substrate. Consequently, a net inward flux of vacancies to the substrate would occur. This can account for the observation that the pore-free zone began at the coating/substrate interface, and gradually extended to the coating surface with time. Further theoretical calculation of the interdiffusion rate for each element is required to verify this explanation.

The existence of substrate elements in the coatings may affect their oxidation resistance. Cr was found to improve the isothermal oxidation resistance of Ni_3Al [23, 52, 53], but to decrease the cyclic oxidation resistance [52]. Si has been reported to have little effect on the isothermal oxidation of Ni-Al coatings in air [14, 15]. The effects of Fe and Mn on the oxidation of Ni_3Al have not been reported to date. The effects of substrate elements due to interdiffusion on cyclic oxidation of the current Ni_3Al-based coatings are probably small, as, according to the EPMA analysis, the content of these elements was low at the external surface of the coating even after 1000 hr,.

4.4.5.4 Pore-healing Behavior

Fig. 4-11 shows the pore-healing behaviors of the five coatings after 500hr.

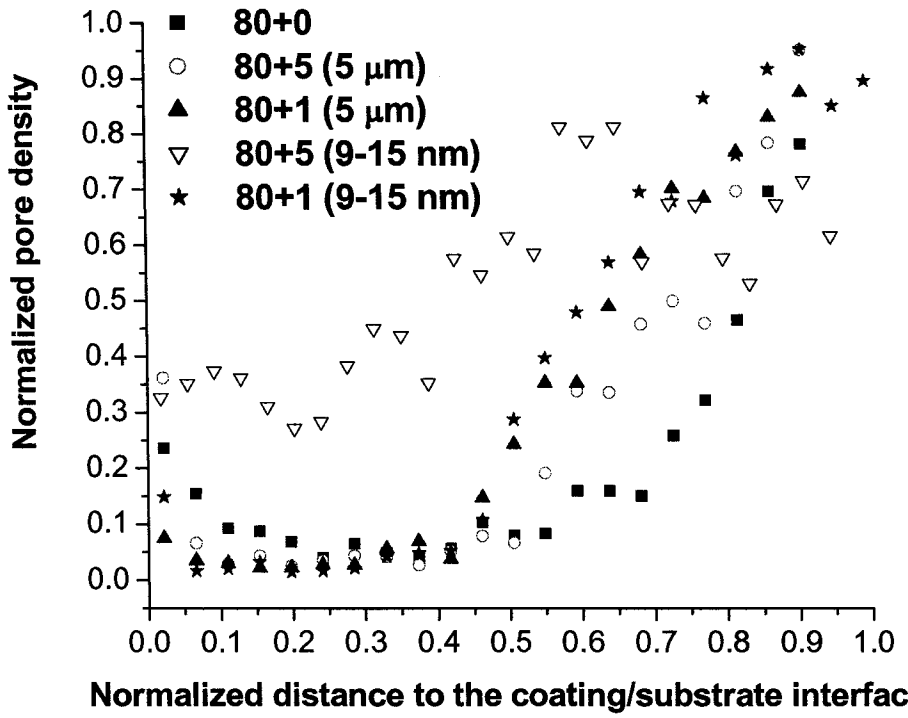

Figure 4-11. Pore density (vol%) as a function of normalized distance to the coating/matrix interface in various Ni_3Al based coatings after cyclic oxidation at 850 °C for 500 hr.

Pore healing in the pure Ni_3Al coating is obviously more rapid than that in the CeO_2-modified coatings. A decrease in the pore healing is clear in the 80+5 (9-15 nm) coating. The pure Ni_3Al coating, as well as the 80+1(5 μm) and 80+1 (9-15 nm) coatings with low CeO_2 content, display more rapid pore healing during long-term oxidation than the 80+5 (5 μm) and 80+5 (9-15 nm) coatings (Fig. 10). Based on the above observations, the different pore-healing behaviors may be linked to ceria additions in the coatings. It was reported that the mobility of metal vacancies can be significantly decreased by large reactive ions such as Ce^{4+} and La^{3+} due to defect interaction [50]. It is reasonable to assume that Ce^{4+} ions in the current coatings would interfere with the vacancy flux to vacancy sinks, such as the external coating surface or the coating/alloy interface, which slows the rate of pore healing. Because it is rich in Ce^{4+} ions, a slow rate of pore healing in the 80+5 (9-15 nm) coating can be expected. The 80+5 (5 μm) coating, due to higher CeO_2 content, may provide more Ce^{4+} ions by decomposition than the two 80+1 coatings. In addition, the oxide scale on the coating will affect the extent of pore healing, particularly for the 80+5 (9-15 nm) coating. The pores were quickly healed after

500 hr, in accordance with the breakdown of the dense and compact Al_2O_3 scale and the formation of the severely oxidized zone. The severely oxidized zone provides more short-circuit paths for the flow of vacancies to the external coating surface, and thus accelerates healing of the pores.

4.4.6 Conclusions

The cyclic oxidation behaviors of a pure Ni_3Al coating, two CeO_2 (5 μm)-modified coatings and two CeO_2 (9-15 nm)-modified Ni_3Al coatings on Fe-Ni-Cr substrates at 850 °C for periods of up to 1000 hr were investigated. Some conclusions are as follows:

1. All the Ni_3Al-based coatings showed good cyclic-oxidation resistance in the early stage, followed by a lower oxidation resistance in the intermediate stage of exposure. With further increase in oxidation time, however, the oxidation resistance was observed to be improved for all coatings except the one modified by a high content of nano CeO_2 particles.
2. The presence of a high volume fraction of pores in all the coatings was found to be responsible for the deterioration in oxidation resistance in the intermediate stage; this was due to the formation of oxidized channels between neighboring pores.
3. The pores in the coating were observed to become self-healed with increasing exposure time. Pores close to the interfaces between the coating and the substrate were healed first, followed by those near the coating surface. An improvement in oxidation resistance was observed after long-term exposure, when the pore-free zone extended to the oxidation zone close to the surface.
4. The healing of pores and the stability of the oxide scale can be greatly influenced by CeO_2 particles in the coating, particularly nano particles. Ni_3Al coatings containing a large number of nano CeO_2 particles formed much more stable oxide scale, but showed very slow pore-healing. This behavior was attributed to an abundance of Ce^{4+} ions in the coating, following decomposition of the nano CeO_2 particles.

4.5 Oxidation at 1050 °C

4.5.1 Oxidation Kinetics

Fig. 4-12 presents the mass changes of pure and CeO_2-modified Ni_3Al coatings after oxidation at 1050 °C for periods up to 500 hr.

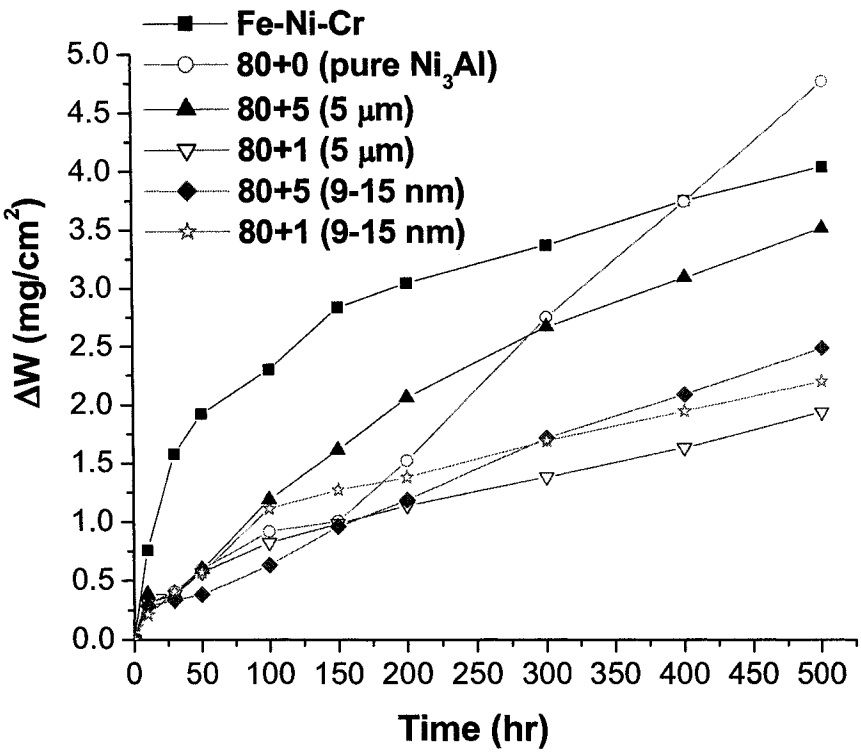

Figure 4-12. The cyclic oxidation results of the pure and the CeO_2-dispersed Ni_3Al coatings after oxidation at 1050 °C for 500 hr.

The uncoated HP alloy experienced severe spallation during cyclic oxidation, and exhibited high mass gains after 500hr. The pure Ni_3Al coating exhibited a low mass change in the initial stage of oxidation, but a rapid increase of mass gain after 150 hr, indicating the breakaway oxidation. Similar to the Fe-Ni-Cr alloy, the pure Ni_3Al coating suffered severe spallation during thermal cycling. The CeO_2-dispersed Ni_3Al coatings, especially the 80+1 (5 μm) coating and the 80+1 (9-15 nm) coating, had much better cyclic oxidation resistance and much less spallation than Fe-Ni-Cr alloy and the pure Ni_3Al coating. The 80+5 (5 μm) coating had a higher mass gain than the other three CeO_2-dispersed Ni_3Al coatings (Fig. 4-12).

4.5.2 Morphologies of Oxide Scales

4.5.2.1 Pure Ni_3Al Coating

Fig. 4-13 (a) depicts the surface morphology of the pure Ni_3Al coating after oxidation for 10 hr. Spallation is clearly evident on the pure Ni_3Al coating after the first run of the cycle. The spallation left behind bare Ni-Al grains, pores, and some residual oxides. In addition to those formed during annealing treatment, pores were observed in oxide scales left on the surface (black arrow in Fig. 4-13 (a)). In the non-spalled areas (Fig. 4-13 (b)), whisker-like oxides and some blocky oxide crystals were observed, formed preferentially along the grinding tracks. EDS analysis demonstrated that the whisker-shape oxides were rich in Al, whereas the blocky oxide crystals were rich in Ni. Those Al-rich oxides were possibly the transition alumina, θ-Al_2O_3, which has often been observed in the early stage of oxidation for Ni-Al alloys at temperatures above 900 °C [15, 23, 54, 55]. Whisker-like θ-Al_2O_3 is formed due to a dominant outward diffusion of Al cations [15, 31, 54]. θ-Al_2O_3 can either react with the initially-formed NiO to form $NiAl_2O_4$ or transform into equilibrium α-Al_2O_3 in the later stage of oxidation [15, 54, 55], both of which were detected by XRD after 100 hr oxidation (Table 4-4).

Table 4-4. The XRD analysis of oxide products on oxidized coating samples.

Sample	100 hr	500 hr
80+0	w: α-Al_2O_3, $NiAl_2O_4$	m: α-Al_2O_3 w: $NiCrO_3$, Cr_2O_3
80+5 (5 μm)	w: α-Al_2O_3, $NiAl_2O_4$, CeO_2	m: α-Al_2O_3, $NiAl_2O_4$ w: CeO_2, Cr-O
80+1 (5 μm)	w: α-Al_2O_3, $NiAl_2O_4$, w: CeO_2	m: α-Al_2O_3, $NiAl_2O_4$ w: CeO_2, Cr-O
80+5 (9-15 nm)	w: α-Al_2O_3, $NiAl_2O_4$, $MnCrO_4$	m: α-Al_2O_3, $NiAl_2O_4$ w: Cr-O
80+1 (9-15 nm)	w: α-Al_2O_3, $NiAl_2O_4$	m: α-Al_2O_3, $NiAl_2O_4$ w: Cr-O

Ni_3Al is the strong peak for all samples.
m: moderate; w: weak.

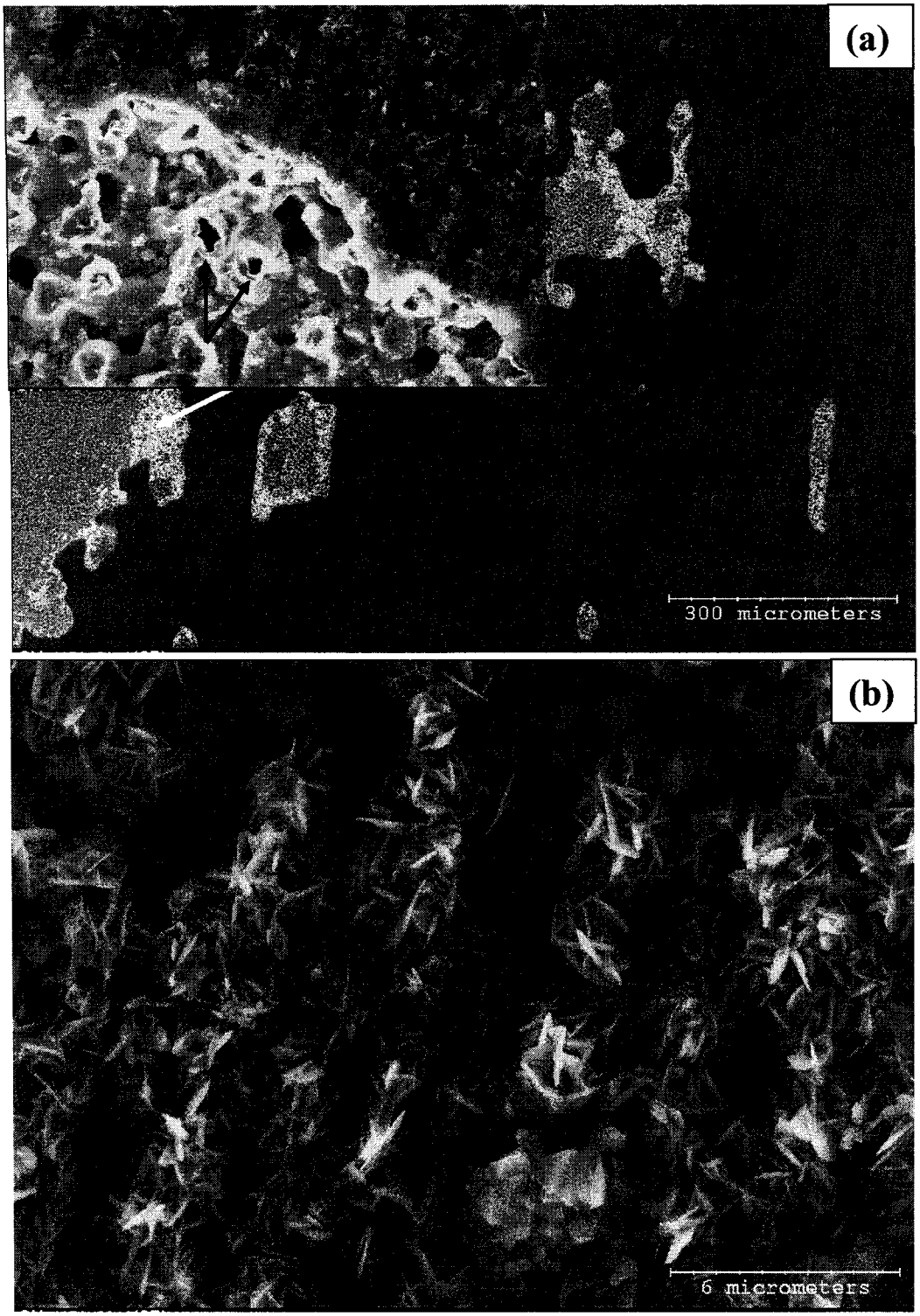

Figure 4-13. The surface morphology of the pure Ni_3Al coating after oxidation at 1050 °C for 10 hr: (a) a low-magnification view; (b) a high-magnification view.

Spallation continued with increasing cyclic oxidation. By 500 hr, the original grinding tracks all disappeared (Fig. 4-14 (a)). Fig. 4-14 (b) shows the surface morphology at higher magnification. The surface is featured with dominant fine particles and some large block-like crystals (white solid arrows), which were determined by EDS and XRD to be α-Al_2O_3 and $(Ni,Cr)O_3$ or Cr_2O_3 respectively (Table 4-4). The observation of $(Ni,Cr)O_3$ or Cr_2O_3 indicates the diffusion of substrate elements to the coating surface.

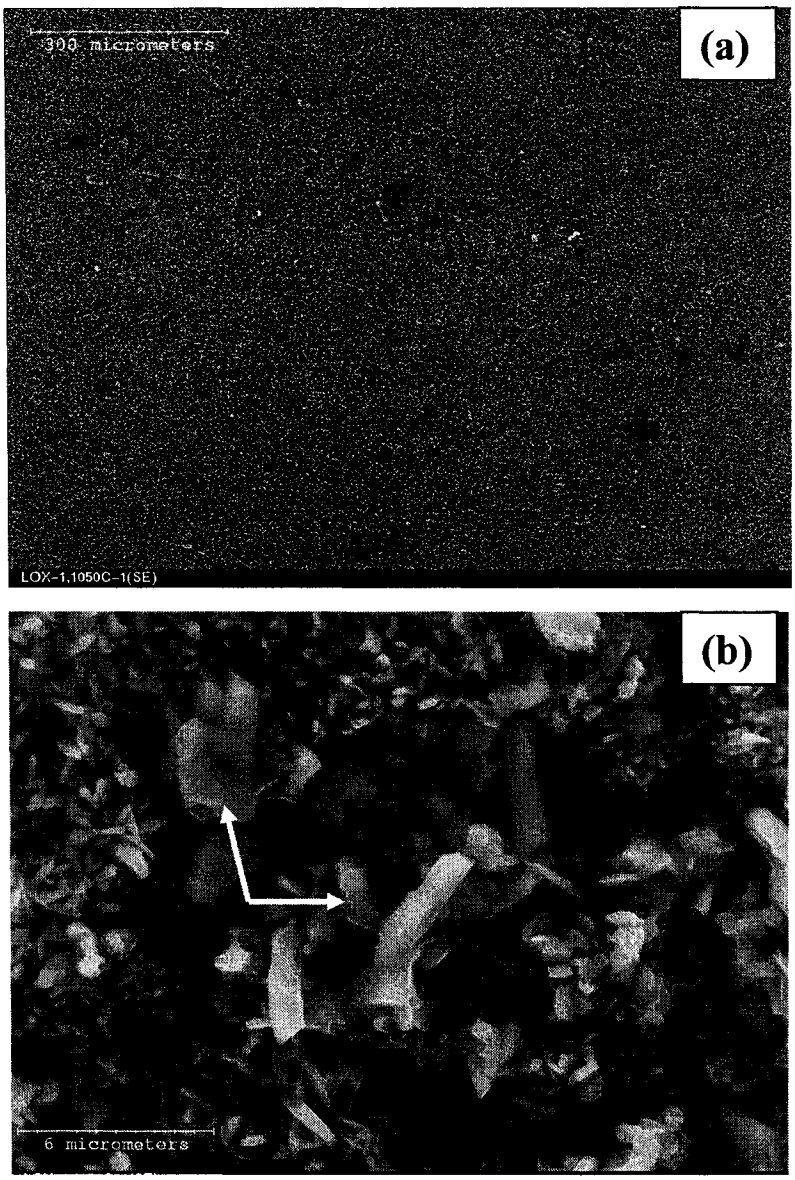

Figure 4-14. The surface morphology of the pure Ni_3Al coating after oxidation at 1050 °C for 500 hr: (a) a low-magnification view; (b) a high-magnification view.

Fig. 4-15 (a) shows the polished cross-section of the oxide scale on the pure Ni_3Al coating after 500 hr. Only an Al-rich oxide layer of about 6 μm thick, determined to be α-Al_2O_3 by XRD analysis (Table 4-4), was observed on the pure Ni_3Al coating. Many large voids (white arrows) several microns in diameter were observed in the α-Al_2O_3 scale. The fractured Al_2O_3 scale had a dominant equiaxed grain structure (Fig. 4-15 (b)), suggesting the outward diffusion of Al cations along the grain boundaries during the growth of Al_2O_3 scale [32, 48]. Some tiny voids were also seen at the scale/coating interface and at the scale grain boundaries, as shown in Figs. 4-15 (c) and (d) respectively.

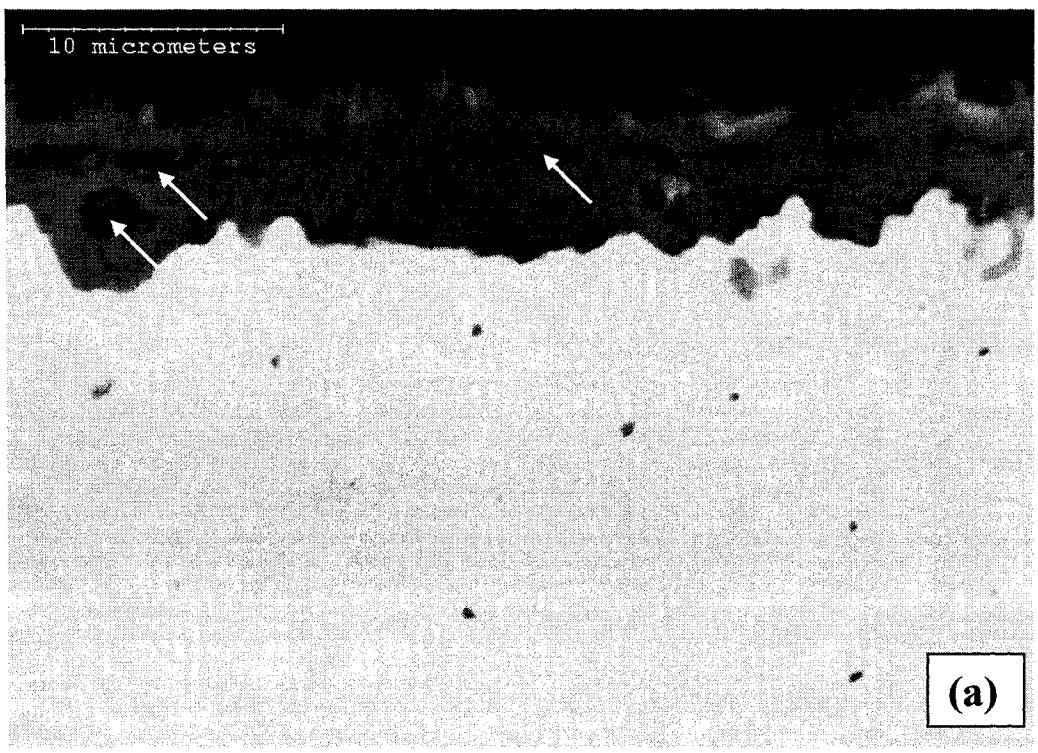

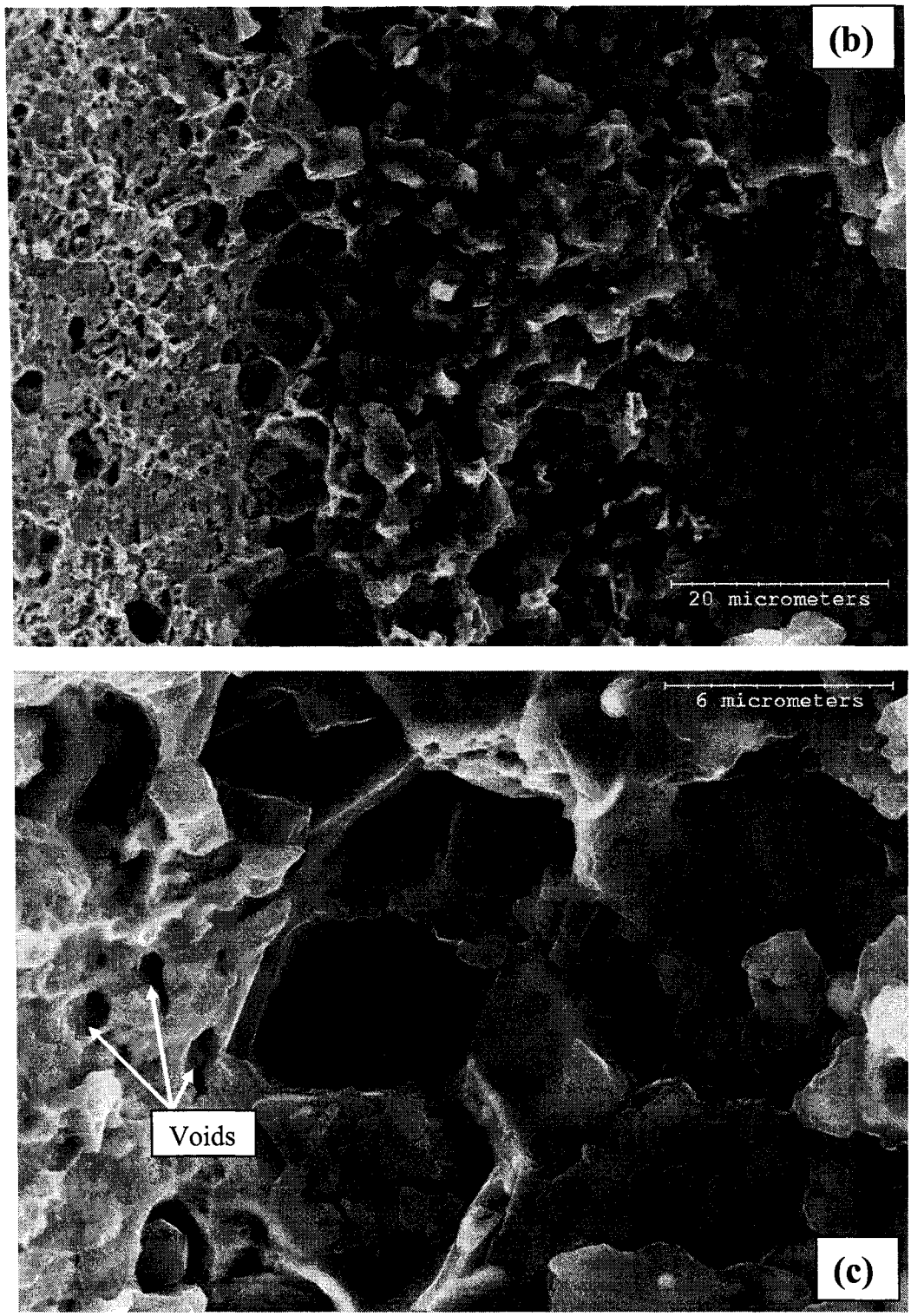

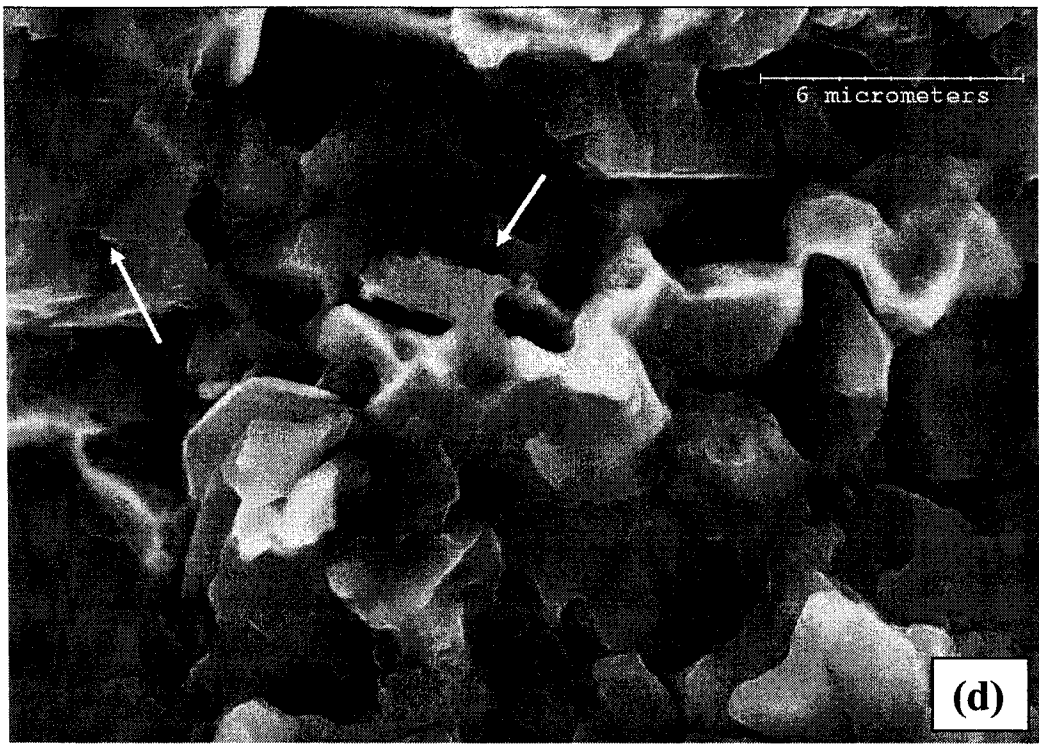

Figure 4-15. The morphology of Al_2O_3 scale on the pure Ni_3Al coatings after oxidation at 1050 °C for 500 hr: (a) the polished cross section; (b) the fracture surface (low-magnification view; (c) the scale/coating interface; (d) the fractured oxide surface (high-magnification view).

4.5.2.2 CeO_2-dispersed Ni_3Al Coatings

However, the four CeO_2-dispersed Ni_3Al coatings did not suffer spallation after the first 10 hr run. A typical surface morphology of the 80+1 (9-15 nm) coating is evident in Figs. 4-16 (a) and (b), where the original grinding tracks remain visible throughout the surface after oxidation (an indication of little spallation). The morphology of surface oxides on the 80+1 (9-15 nm) coating after oxidation for 10 hr (Fig. 4-16 (b)) is similar to that on the pure Ni_3Al coating. Ni-rich oxide crystals were always located in the Ce-rich region (white solid arrow in Fig. 4-16 (b)). They were also observed at many other locations and in all the CeO_2-dispersed Ni_3Al coatings.

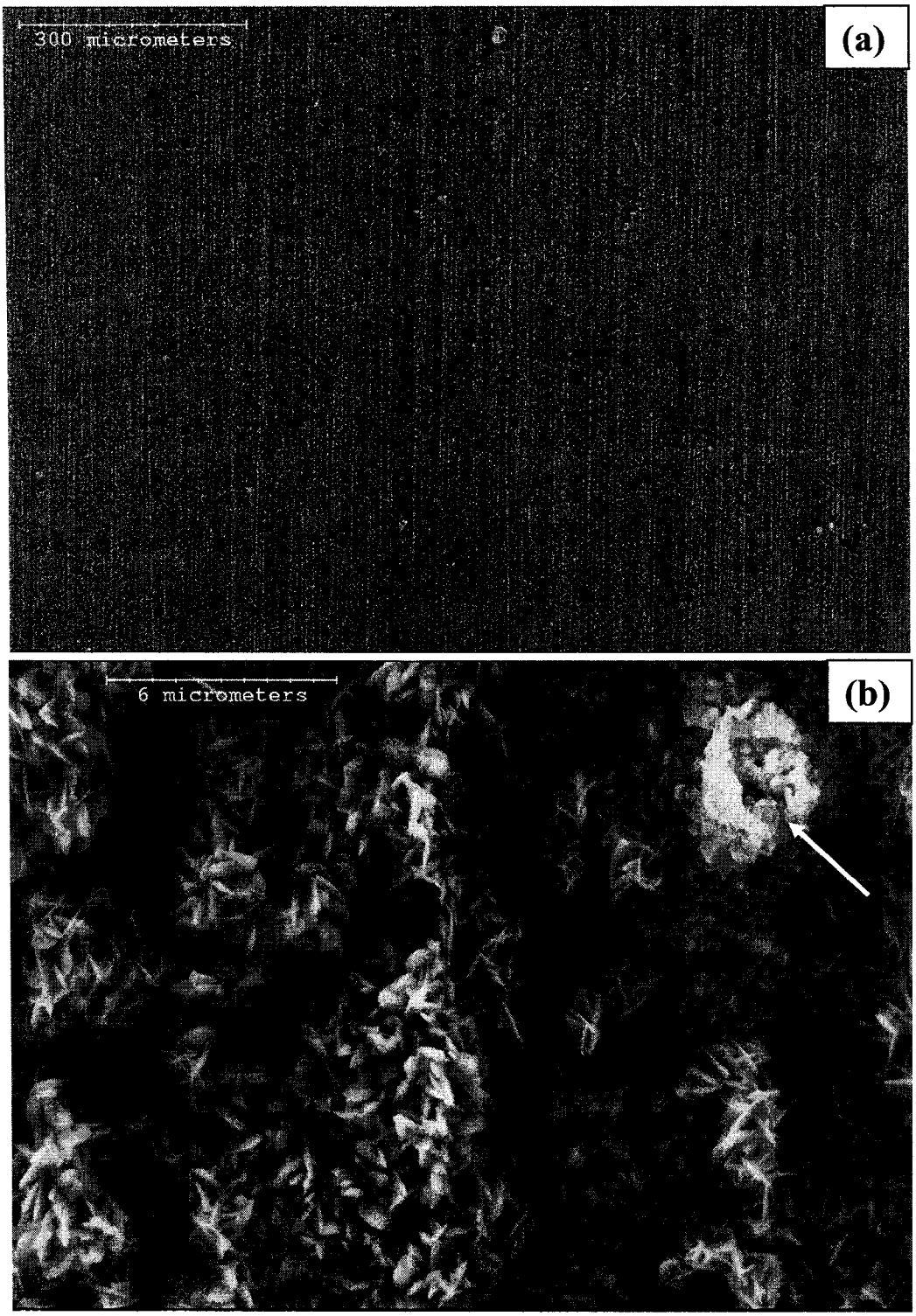

Figure 4-16. The surface morphology of the 80+1 (9-15 nm) coating after oxidation at 1050 °C for 10 hr: (a) a low-magnification view; (b) a high-magnification view.

The area fraction of whisker-like θ-Al_2O_3 oxides on the 80+5 (9-15 nm) and the 80+5 (5 μm) coating was much lower than that on the pure Ni_3Al coating coating and on the other two CeO_2-dispersed Ni_3Al coatings containing fewer CeO_2 particles, suggesting that the outward growth of θ-Al_2O_3 on the 80+5 (9-15 nm) coating and the 80+5 (5 μm) coating was retarded. All CeO_2-dispersed Ni_3Al coatings showed less spallation than the pure Ni_3Al coating during the long-term exposure. The original grinding tracks were still retained on the surface of the 80+1 (9-15 nm) coating after 500 hr exposure (Fig. 4-17 (a)), which was also observed in other three CeO_2 dispersed coatings. Surface oxides on the 80+1 (9-15 nm) coating were mainly (Ni, Al, Cr)-type and Al-rich (Fig. 4-17 (b)), which is distinct from those on the pure Ni_3Al coatings.

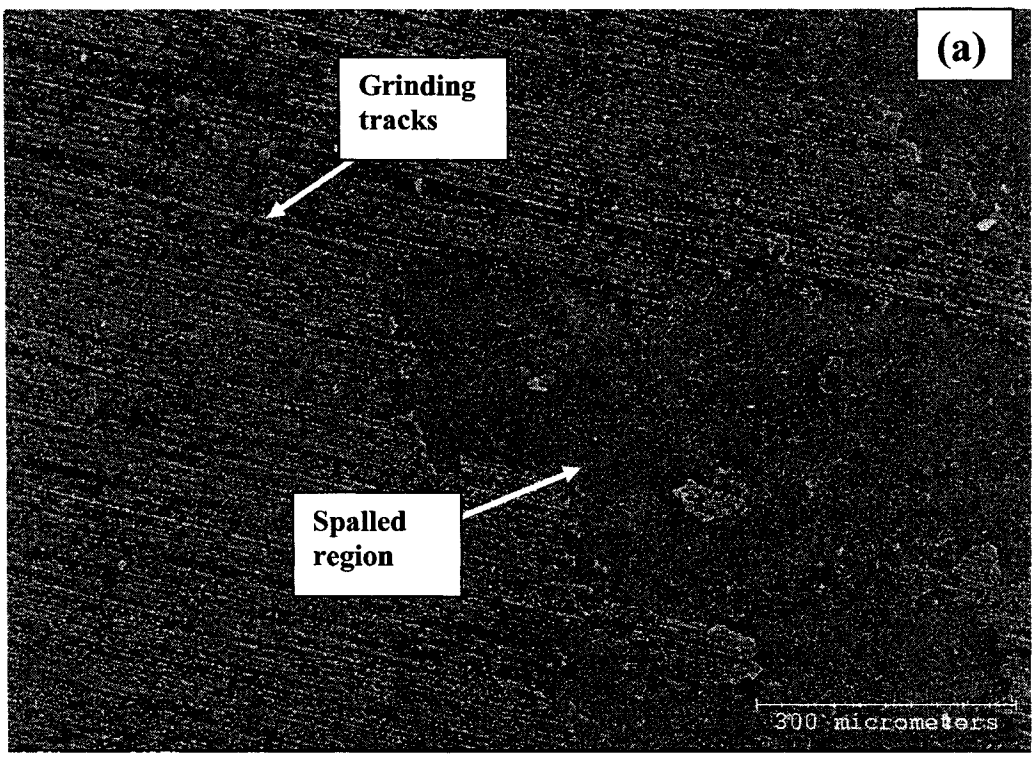

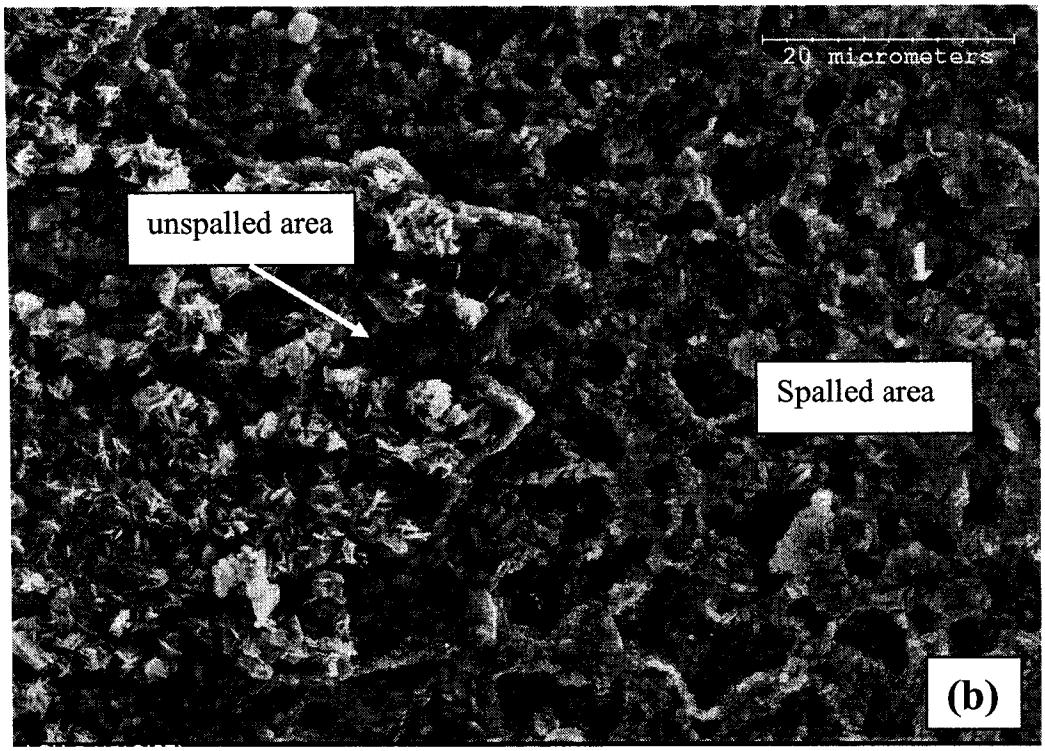

Figure 4-17. The surface morphology of the 80+1 (9-15 nm) coating after oxidation at 1050 °C for 500 hr: (a) a low-magnification view; (b) a high-magnification view.

Fig. 4-18 (a) presents the polished cross section of the 80+1 (9-15 nm) coating after 500 hr exposure. Based on the XRD analysis in Table 4-4 and the EDS analysis, a duplex-oxide structure with the outer $NiAl_2O_4$ spinel and the inner thin α-Al_2O_3 adhered to the 80+1 (9-15 nm) coating. This duplex-oxide structure was a typical characteristic of CeO_2-dispersed Ni_3Al coatings. Voids several microns in size were found mainly in the spinel layer, but less so in Al_2O_3 scale. The Al_2O_3 scale on the 80+1 (9-15 nm) coating was thinner than that on the pure Ni_3Al coating after 500 hr (Fig. 5(a)). The fractured surface of the oxide scale after 500hr is presented in Fig. 4-18 (b). The thin Al_2O_3 scale had a columnar-grain structure, which was distinct from the equiaxed grain structures found on the pure Ni_3Al coating in Fig. 4-15 (b). Formation of columnar grains was associated with the inward diffusion of oxygen during the growth of scale [32, 48]. The scale was dense, and no voids were seen at the grain boundaries.

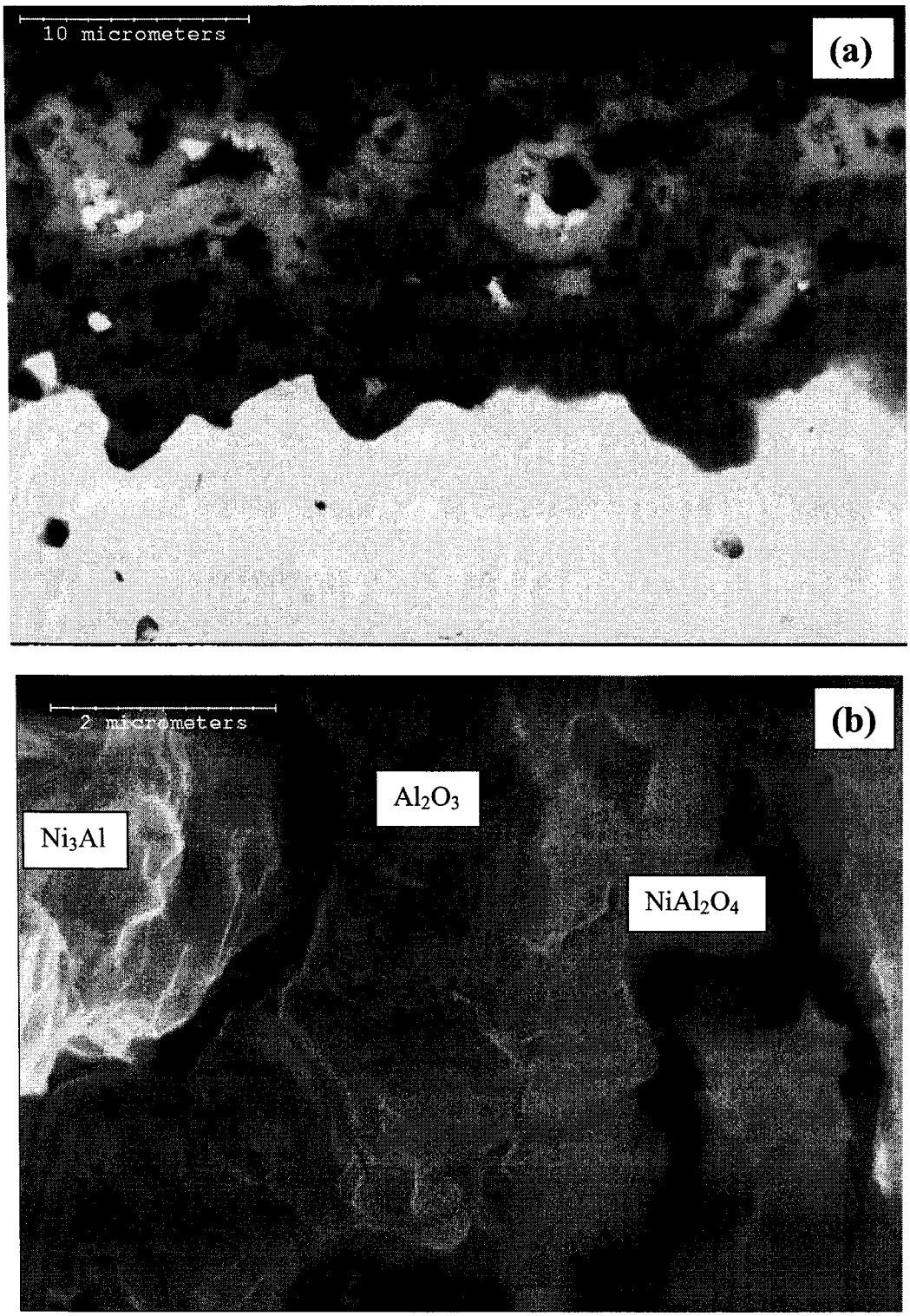

Figure 4-18. The morphology of Al_2O_3 scale on the 80+1 (9-15 nm) coatings after oxidation at 1050 °C for 500 hr: (a) the polished cross section; (b) the fracture surface.

A cross-sectional view of the 80+5 (5μm) coating is depicted in Fig. 4-19 (a). The oxide layer had a duplex structure similar to that on the 80+1 (9-15 nm), but it was much thicker than those on other CeO_2-dispsered Ni_3Al coatings after oxidation for 500 hr. This is consistent with the highest mass increase of the 80+5 (5 μm) coating during the cyclic oxidation (Fig. 4-12). Becuase the 80+5 (5 μm) coating contained the highest amount of CeO_2 among the CeO_2-dispsered Ni_3Al coatings, excessive CeO_2 particles seemed to enhance scale growth. The void-free Al_2O_3 scale with columnar grains is clearly visible in Fig. 4-19 (b). The outer $NiAl_2O_4$ spinel scale is featured with a blocky morphology.

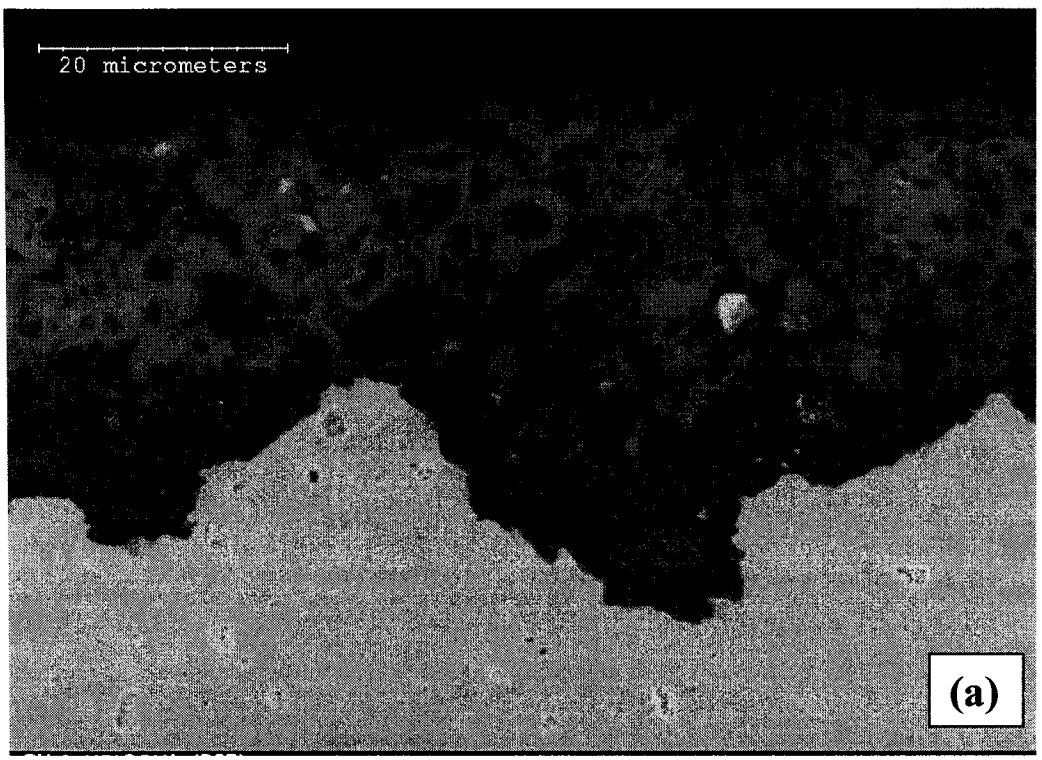

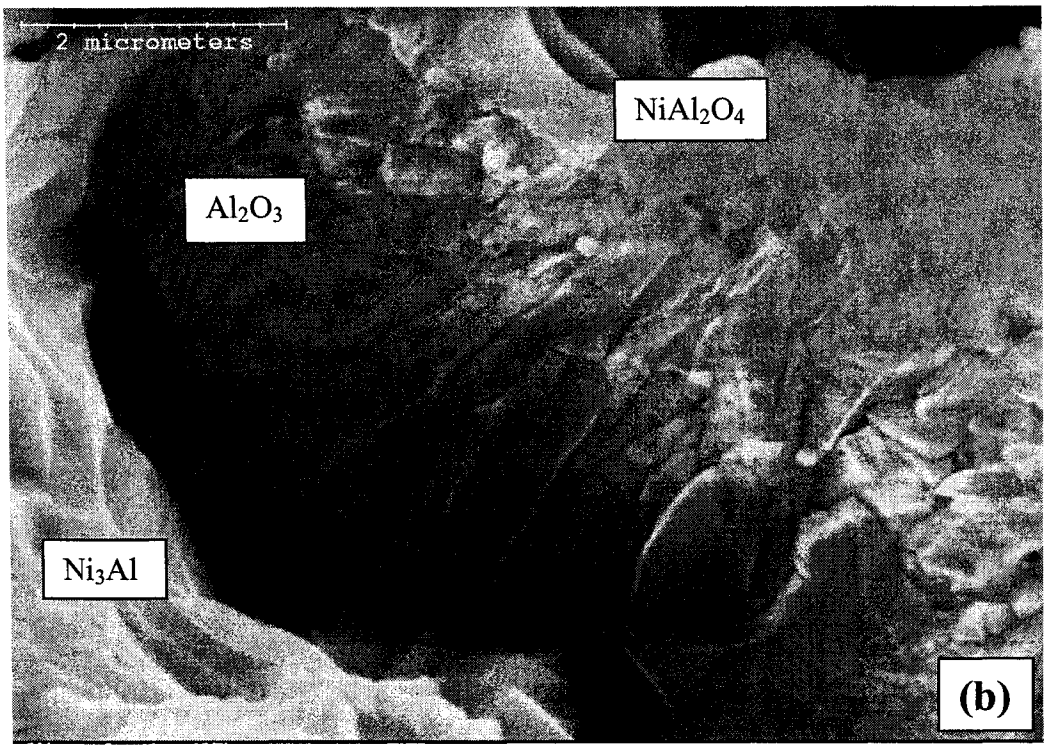

Figure 4-19. The morphology of Al_2O_3 scale on the 80+5 (5 μm) coatings after oxidation at 1050 °C for 500 hr: (a) the polished cross section; (b) the fracture surface.

4.5.3 CeO_2 Particles in Coatings and Oxide Scales

Fig. 4-20 (a) is a backscattered electron micrograph showing the distribution of micron CeO_2 particles in the 80+5 (5μm) coating, where CeO_2 particles (white phases) are homogeneously dispersed in the Ni_3Al coating matrix. Matrix material surrounding the white CeO_2 particles is always less dark on backscattered electron micrographs, which may be attributed to a lower Al content in those regions. This may explain the observation of prevailing Ni-rich oxides formed in CeO_2-rich regions in the early stage of oxidation (as seen in Fig. 4-16 (b)). Although a direct observation of nano CeO_2 particles is impossible from the polished cross-section of the coating due to the limitation of SEM, the plain view can provide an indirect indication of the location of nano CeO_2 particles. The several dark regions (less than 800 nm) pointed to by white solid arrows (Fig. 4-20 (b)) were identified to be rich in Ce by EDS analysis. These Ce-rich regions are normally located at a convergence of Ni-Al grain boundaries.

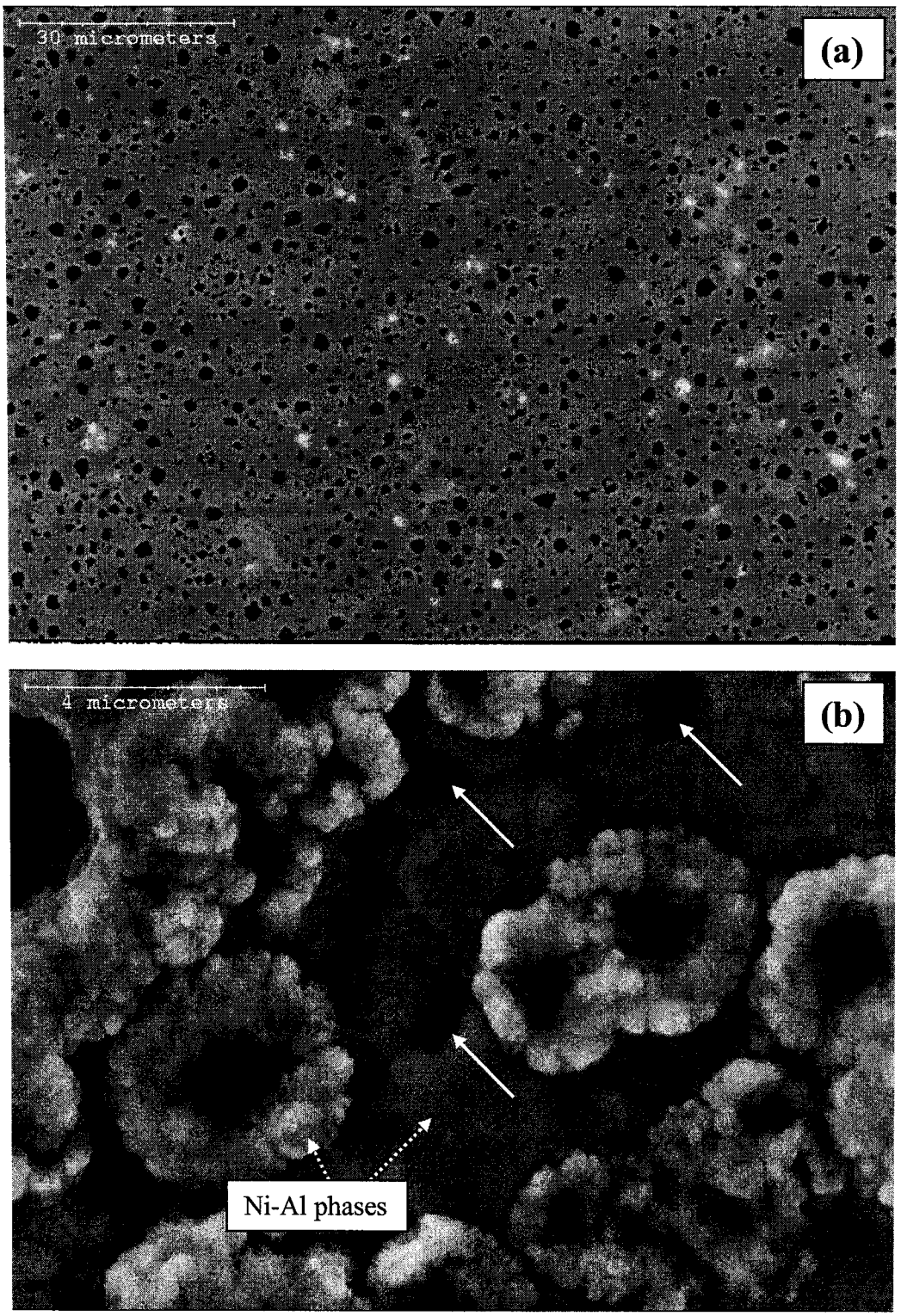

Figure 4-20. The distribution of CeO_2 particles: (a) in 80+5 (5 μm) coating (cross-sectional view) (BSE); (b) in 80+5 (9-15 nm) coating (plain view) (SE).

The distribution of CeO_2 particles in the coatings after long-term oxidation is shown in Fig. 4-21 (a). In the figure, some nano-size particles (less than 200nm) were found to locate at Ni-Al grain boundaries of the 80+5 (9-15nm) coating after 500hr exposure. An AES spectrum from the largest nano particle in Fig. 4-21 (a) is shown in Fig. 4-21 (b), clearly demonstrating the presence of Ce and O.

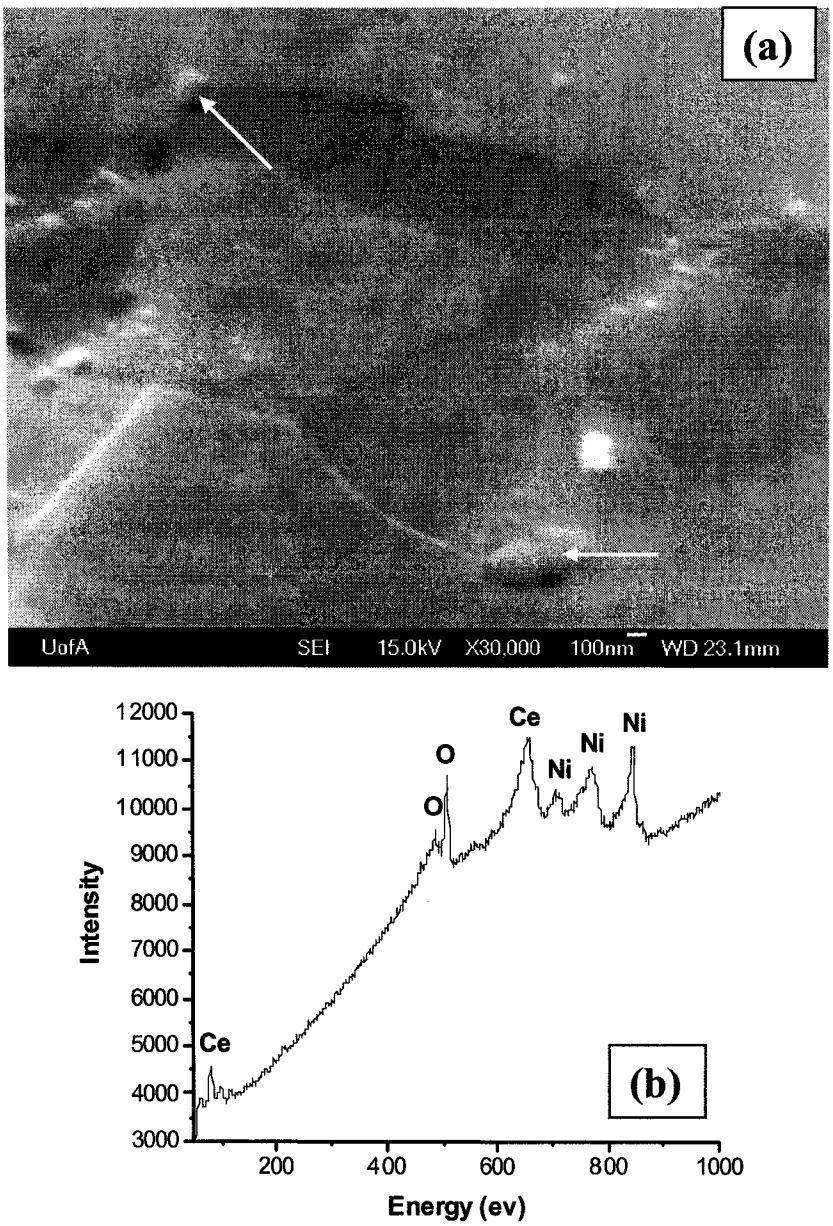

Figure 4-21. Nano CeO_2 particles in the 80+5 (9-15 nm) coating after oxidation at 1050 °C for 500 hr: (a) Secondary electron image; (b) AES spectrum.

Detection of CeO_2 in Al_2O_3 scale was very difficult, because of the extremely low doping concentration of CeO_2 and the detection limit of analyzing techniques, except for the 80+5 (5μm) coating with higher CeO_2 content. Fig. 4-22 (a) is a cross-section micrograph of the oxide scales on the 80+5 (5 μm) coating after 500 hr oxidation. Some Ce-rich particles in the $NiAl_2O_4$ spinel layer were identified using EDS analysis. Doychak et al. [31] also observed Zr-rich precipitates throughout the $NiAl_2O_4$ layer formed on the Zr-doped Ni_3Al alloy after oxidation at 1200 °C for 25 hr. With the aid of the JAMP-9500F Field Emission Auger Microprobe, CeO_2 was also detected in α-Al_2O_3 (Fig. 4-22 (b)). AES spectrums from both Area 1 and Area 2 in Fig. 4-22 (b) are compared in Fig. 4-22 (c). There was a weak peak of Ce in Area 1, whereas the spectrum of area 2 indicated the exclusive Al_2O_3 scale. Fig. 4-22 (d) provides the line scan of area 1 in Fig. 4-22 (b). There were at least three Ce-rich regions along the scanned line (Fig. 4-22 (d)). The Ce-rich regions were less than 100 nm, and the interspacing between these regions was about several hundred nanometers. As the solubility of CeO_2 in α-Al_2O_3 was negligible, the Ce-rich precipitates found in Fig. 4-22 (d) might be present at the grain boundaries of α-Al_2O_3. Other researchers have also found the presence of reactive-element-rich phases at the grain boundaries of the oxide scale, such as NiO [25, 56], Cr_2O_3 [57, 58], and Al_2O_3 [31, 59].

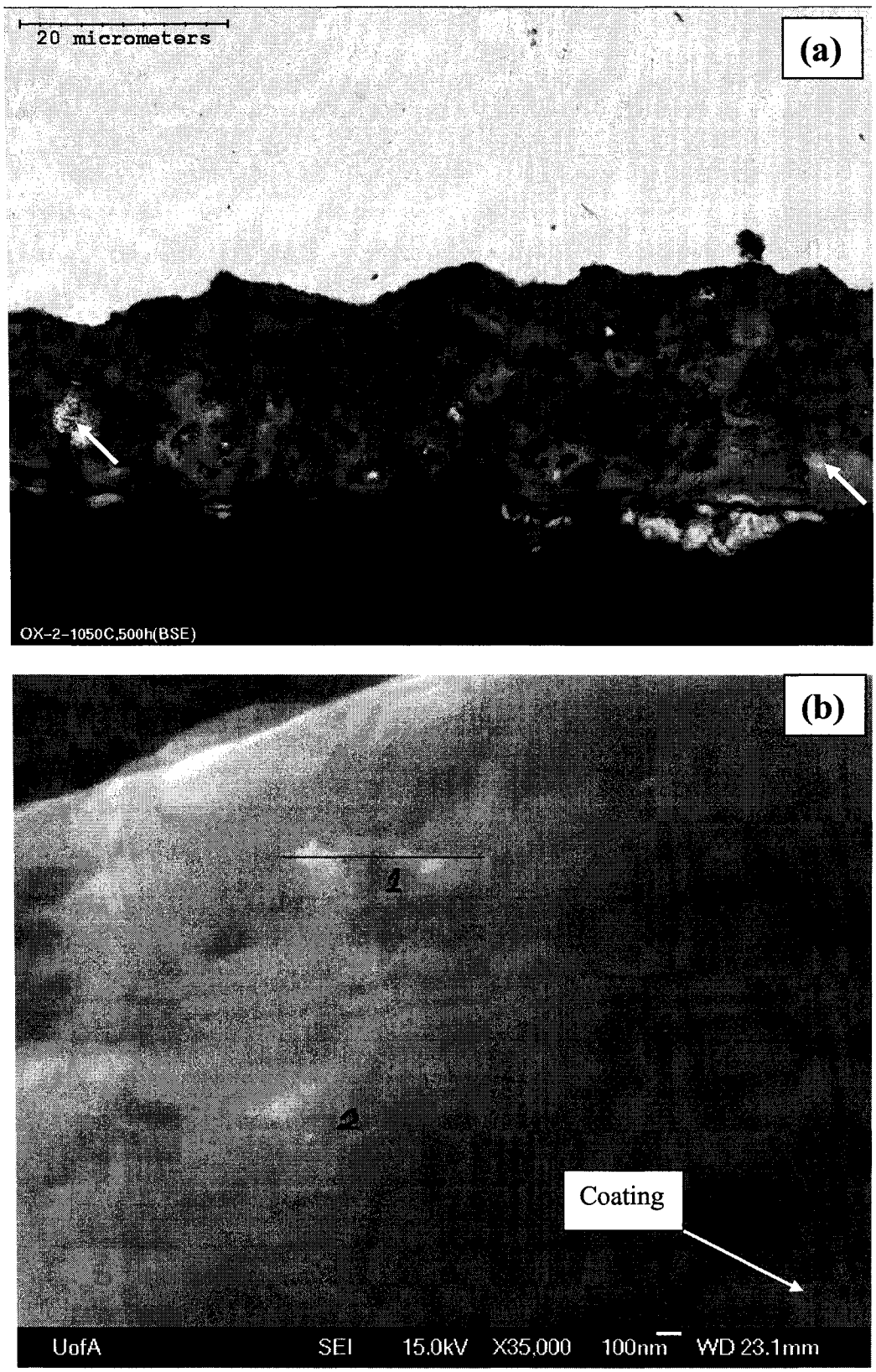

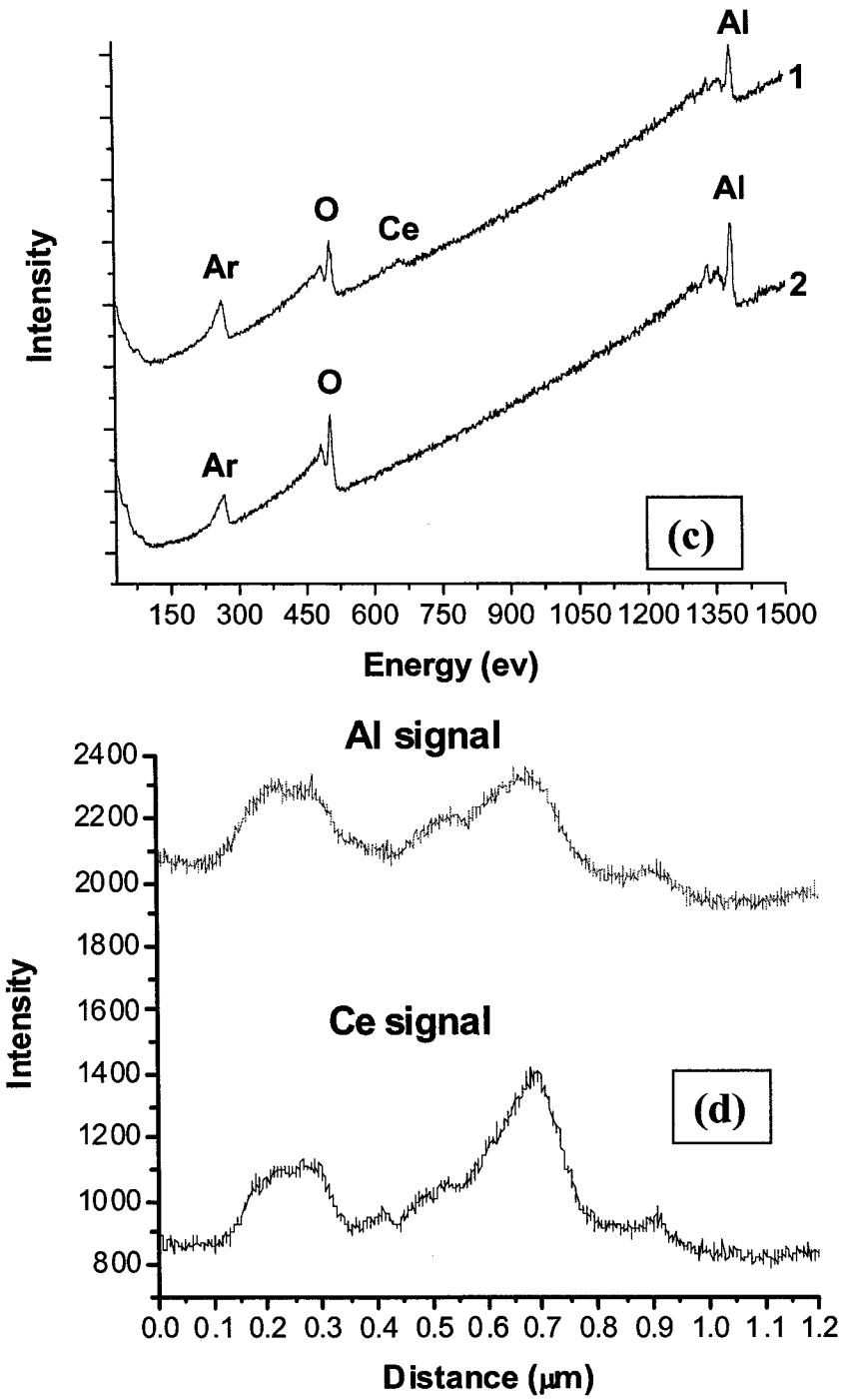

Figure 4-22. The distribution of CeO_2 particles in the oxide scales on the 80+5 (5 μm) coating after oxidation at 1050 °C for 500 hr: (a) in the $NiAl_2O_4$ spinel scale; (b) in the α-Al_2O_3 scale; (c) the AES spectrums of area 1 and area 2 in Fig. 4-22 (b); (d) the AES spectrums of line scan along area 1 in Fig. 4-22 (b).

4.5.4 Cross-sections of Oxidized Coatings

Cross-sections of the pure Ni_3Al coatings after oxidation for 10 hr, 20 hr and 500 hr are illustrated in Figs. 4-23 (a), (b) and (c) respectively.

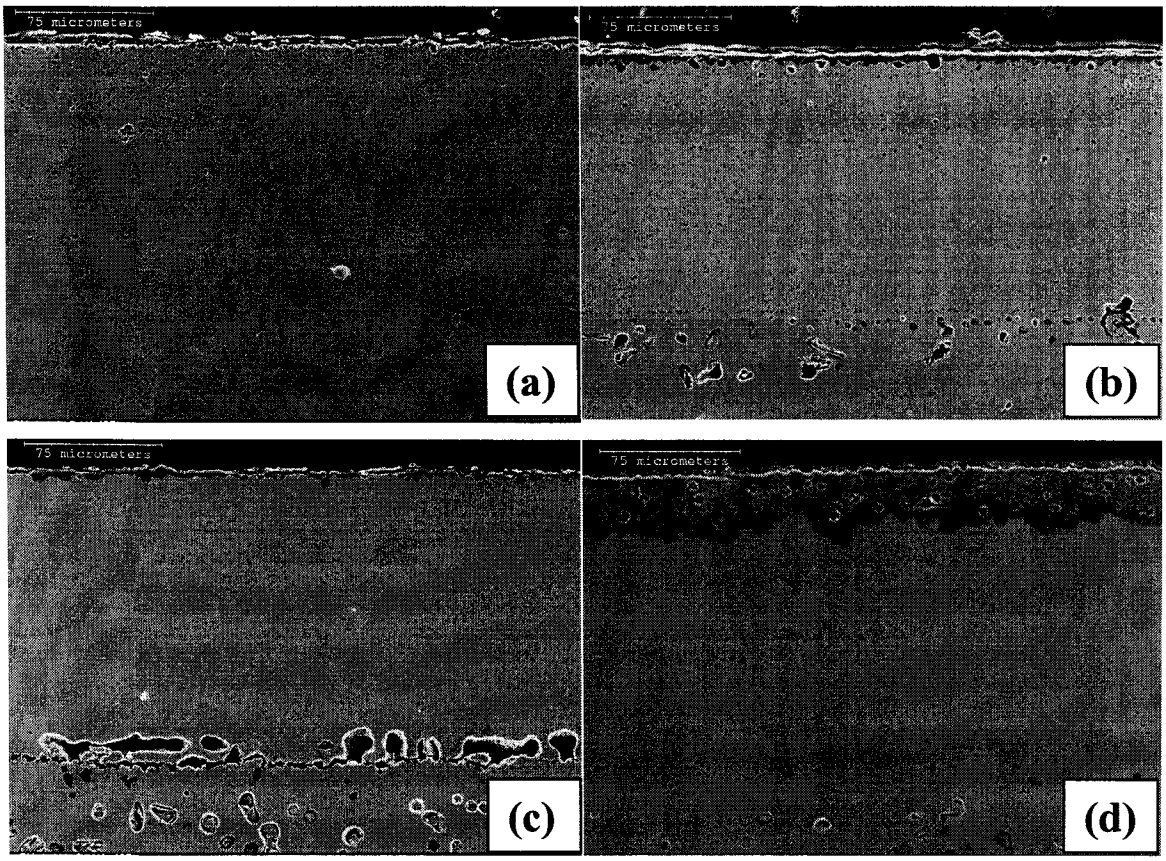

Figure 4-23. The cross-section morphologies of Ni_3Al base coatings after being cyclically oxidized at 1050 °C: (a) the pure Ni_3Al coating after 10 hr; (b) the pure Ni_3Al coating after 20 hr; (c) the pure Ni_3Al coating after 500 hr; (d) the 80+5 (5 μm) coating after 500 hr.

Two layers—a top high-porosity layer and a pore-free layer next to the coating/alloy interface—were seen in the pure Ni_3Al coating after oxidation for 10 hr (Fig. 4-23 (a)). Because all coatings before testing contained large amounts of pores that are homogeneously distributed in the coatings (Figs. 4-1 (a) and (b)), it is clear that a large fraction of pores has been healed in the first 10hr-run cycle. Most pores were eliminated after as little as 20 hr (Fig. 4-23 (b)). By 500 hr, the whole coating was free of pores (Fig. 4-23 (c)). All CeO_2-dispersed Ni_3Al coatings showed a pore-healing behavior

similar to the pure Ni_3Al coating during oxidation at 1050 °C. A typical cross-section of the 80+5 (5 μm) coating after oxidation for 500 hr is shown in Fig. 4-23 (d). The healing of pores started near the coating/alloy substrate, and then extended to top of the coating. Interdiffusion between the coating and the substrate is the main reason for the healing of pores. However, pores in those coatings oxidized at 850 °C cannot be healed completely even after 1000 hr. Internal oxides and the Kirdendall pores along the coating/substrate interface were observed in the pure Ni_3Al coating (Fig. 4-23 (c)). EDS analysis showed that these internal oxides were mixtures of O, Al, Ni, Cr, and Fe. Because the four edge surfaces of the rectangular coupon were not coated, oxygen might have diffused inward along the exposed coating/substrate interface to cause internal precipitation of oxides. The internal oxidation, however, occurred to a very minor extent in the four CeO_2-dispersed Ni_3Al coatings, as typically shown in Fig. 4-23 (d).

Fig. 4-24 provides the normalized composition profiles of Al in the pure Ni_3Al coating, the 80+1 (5 μm) coating, and the 80+1 (9-15 nm) coating after 500 hr exposure.

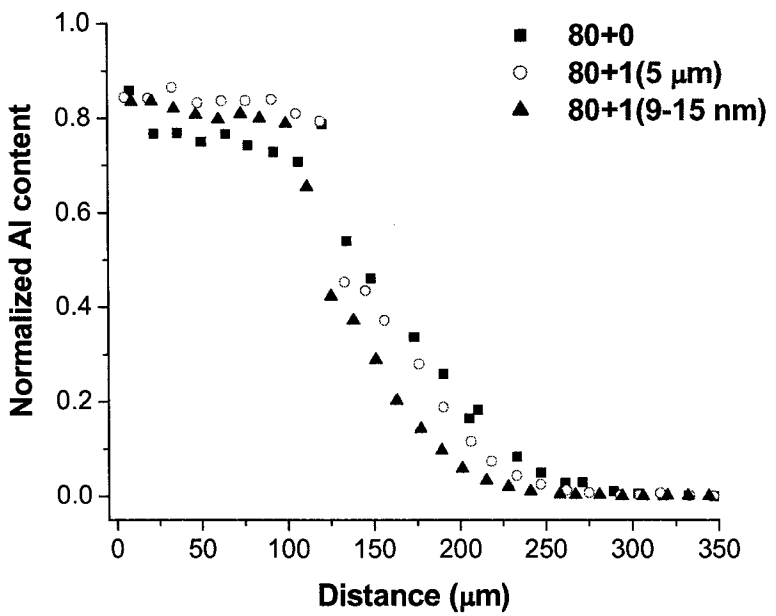

Figure 4-24. The composition profile of Al in the pure Ni_3Al coating, the 80+1 (5 μm) coating, and the 80+1 (9-15 nm) coating after being cyclically oxidized at 1050 °C for 500 hr.

According to Fig. 4-24, Al in all the three coatings has diffused inward to the substrate alloy after 500hr. All three coatings experienced a loss of Al, and the pure Ni_3Al coating had the highest loss of Al—more than 20% of Al after 500hr. The EPMA analysis also showed that all Ni_3Al-based coatings contained about 6.0-6.5 at% Fe, 4.0-4.5at% Cr, 1.0-1.5at% Si, and minor Mn and Nb from the substrate after 500 hr exposure.

4.5.5 Discussion

4.5.5.1 Effect of Porosity

The pure and CeO_2-dispersed Ni_3Al coatings obtained in this study have a high volume fraction of porosity (more than 10vol%). The detrimental effects of porosity on the long-term cyclic oxidation resistance of the coatings at 850 °C were discussed in Section 4.4. In view of the fact that the porosity dominates the cyclic oxidation of Ni_3Al base coatings, the effect of CeO_2 on the oxidation at 850 °C can't be well defined. At 1050 °C, because all the coatings become dense within 20 hr, the effect of porosity will be limited only in the first a few cycles. The beneficial effects of CeO_2 particles on suppressing the spallation of oxide scales on Ni_3Al coatings during long-term cyclic oxidation at 1050 °C are evident from the experimental results.

4.5.5.2 Failure of Al_2O_3 Scale on Pure Ni_3Al

Scale failure on pure alumina-forming alloys, including Ni_3Al alloys, during high temperature oxidation has been studied extensively. It is generally believed that the failure of oxide scale is related to internal compressive stresses resulting from the growth stress, the thermal stress, and the interfacial stress [20, 36, 37, 48, 60]. Based on the assumption that scale failure at a wavy scale/matrix interface was caused only by the internal compressive stresses, Rahmel et al. [20] proposed a fracture-mechanics equation to elucidate the failure of the oxide scale:

$$-\varepsilon_c = \frac{K_{IC}}{f\sqrt{\pi \bullet c}} \frac{1+r/d}{m} \tag{4-5}$$

$$m = \frac{E_{ox}}{1+\upsilon_{ox}} \tag{4-6}$$

where ε_c is the critical strain parallel to the scale/matrix interface for the failure of the oxide scale; K_{IC} is the fracture toughness of the scale; f is the geometrical factor, which is equal to 1; c is the half length of a physical defect at the site of the maximum interfacial strain; r is the depth of the oxide intrusion into the matrix; d is the scale thickness; E_{ox} is the Young's modulus for the oxide scale, and υ_{ox} is the Poisson ration of the scale. Although the applicability of Equation (4-5) is not yet verified, it provides a good theoretical basis to qualitatively account for the various factors affecting the failure of oxide scale, and thus the possible beneficial effects of rare earth elements or oxides [20, 48].

The marginal oxidation resistance of the pure Ni_3Al coating at 1050 °C can be attributed to the presence of compressive thermal stress in the scale upon cooling due to the mismatch of thermal expansion coefficients between the alumina scale and the Ni_3Al matrix. Thermal stress in the scale can be estimated using Equation (4-3). By assuming that only an α-Al_2O_3 scale with a thickness of 1 μm is formed on both surfaces of the substrate of about 2.3 mm thick after 10hr oxidation at 1050 °C, and adopting the data from Table 4-3, the compressive thermal stress in the scale can be estimated to be as high as 1.95 GPa, which is close to the ultimate compressive strength limit of bulk α-Al_2O_3, about 2.07 GPa [61]. Scale failure caused by mechanical forces becomes even more likely when the growth stress and the interfacial stress are also considered.

The formation of interfacial and/or internal voids in the oxide scale (Fig. 4-15 (c) and (d)) is another critical factor in scale failure. These voids are commonly observed in the alumina-forming alloys or coatings such as pure NiAl and Ni_3Al during high temperature oxidation [48, 62]. They often result from a condensation of excessive vacancies at the grain boundaries and/or the scale/coating interface. The vacancy flux may be induced either by dominant outward diffusion of Al cations through the scale, or by faster inward diffusion of Ni in the Al-depleted matrix adjacent to the scale due to a selective oxidation of Al [24, 48, 63]. Some large voids of several microns were observed in the Al_2O_3 scale during the cyclic oxidation (Fig. 4-15 (a), 4-18 (a) and 4-19 (a)). It is unlikely that voids of this size are formed by vacancy condensation. Recently, Pint [62]

had proposed a ridge-growth model to explain their formation. As the inward diffusion of oxygen anions and the outward diffusion of Al cations occurred simultaneously along the scale grain boundaries during the formation of Al_2O_3, corresponding inward and outward growth of the oxide ridges would occur and eventually seal off to form big internal voids. The voids at the scale/matrix interface can be further stabilized and enhanced by impurities (e.g., sulfur) segregated at the scale/matrix interface [63-65]. The existence of voids can significantly deteriorate the K_{IC} of the oxide scale. According to Equation (4-5), large voids (c) combined with a low K_{IC} value give a very low critical strain ε_c for spallation. The high thermal stress upon cooling, as well as other residual stresses (as discussed earlier), could induce scale cracking or decohesion around these voids.

Severe spallation of Al_2O_3 scale requires continuous consumption of Al in the pure Ni_3Al coating to regenerate Al_2O_3 scale. This, as well as the inward diffusion of Al to the substrate, results in a rapid decrease of Al content in the coating matrix (Fig. 4-24), which, in turn, deteriorates the coating performances and limits the lifetime of coating.

4.5.5.3 Effect of CeO_2 Particles

As in the case of the pure Ni_3Al coating, large internal voids were found in Al_2O_3 scale and the spinel layer on the CeO_2-dispersed Ni_3Al coatings. However, these voids don't lead to severe spallation, and a certain fraction of the porous spinel oxides formed in the early stage of oxidation is retained on the coating surface. The addition of nano and micron CeO_2 particles evidently enhances the adherence of the scale to the coating matrix and increases the threshold value of the scale for cracking or spalling. The so-called "reactive-element effect" (REE) has been extensively studied and reported for more than half a century, and well-reviewed in the literature [20, 24, 48, 66]. The possible beneficial effects of CeO_2 found in this investigation can be cataloged as follows based on the:

- CeO_2 particles suppress the formation of interfacial or internal voids [20, 24, 32, 61]. REOs such as CeO_2 particles are good vacancy sinks, and they provide alternative sites for vacancy condensation. Consequently, vacancy condensation at the scale grain boundaries or the scale / coating interface is

mitigated, which is confirmed by the observation of a dense Al_2O_3 scale on the CeO_2-dispersed Ni_3Al coatings (Fig. 4-18 (b) and 4-19 (b)). This will decrease the defect size (c) and increase the K_{IC} value of the oxide scale. As a result, a high critical strain, ε_c, for spallation can be expected according to Equation (4-5).

- CeO_2 particles alter the growth mechanism and the morphology of Al_2O_3 scale [32, 35, 50, 56, 67, 68]. As discussed earlier, the addition of CeO_2 particles changes the dominant outward diffusion of Al through the undoped Al_2O_3 scale (Fig. 4-15 (b)) to the dominant inward diffusion of oxygen via the doped Al_2O_3 scale (Fig. 4-18 (b) and Fig. 4-19 (b)). Because inward diffusion of oxygen is much slower than outward diffusion of Al, the growth of the doped scale can be retarded (for example, thinner Al_2O_3 scale on the 80+1 (9-15nm) coating, as shown in Fig. 4-18 (b)). According to Equation (4-5), thinner Al_2O_3 scale can offer higher spallation resistance.
- CeO_2 particles reduce the harmful effect of impurities such as sulfur [24, 63-65]. REEs or REOs prefer to react with sulfur and form stable sulfides in the alloy or coating matrix, which reduces its segregation at the scale/matrix interface and in turn improves the bonding of the scale to the matrix. Although this research did not detect any sulfur at the scale/coating interface of the pure Ni_3Al coating and the sulfides in CeO_2-dispersed Ni_3Al coatings, previous studies [24, 64] have reported that desulfidation treatment could significantly improve the adhesion of Al_2O_3 scale. Recently, yttrium sulfides have been directly detected in NiAl [65] and FeCrAl [69].

Although, REE has been consistently verified in various doped alloys or coatings, the underlying mechanisms are not yet been completely understood. Many models consider the segregation of the ions of REEs (e.g., La^{3+}, Ce^{4+}) [25, 49, 50] or the REO-rich particles (e.g., $YAlO_3$, $Y_3Al_5O_{12}$) [59, 70] at the scale-grain boundaries or the scale/matrix interface. In this investigation, we also observed the distribution of Ce-rich particles in the spinel scale and Al_2O_3 scale (Figs. 4-22 (a)-(d)). Based on previous theoretical studies and the experimental results presented herein, Pint [71] recently

proposed a dynamic-segregation model to explain the role of REs or REOs doped in the alloy matrix. According to his model, REs or REOs would not take effect until a complete Al_2O_3 scale is formed. Upon the formation of the scale, REs or REOs begin to segregate at the scale/matrix interface and diffuse outward through the scale via the scale-grain boundaries. Finally, they reach to the gas/scale interface. Due to a much lower diffusivity of RE ions along the scale grain boundaries than that of Al cations, the outward diffusion of Al cations will be suppressed and the slow inward diffusion of oxygen will become dominant. A lower growth rate of the scale can be then achieved. Furthermore, RE oxide precipitates will form if a critical doping concentration of RE ions along the grain boundary is exceeded. Due to the solute-drag effect by RE ions or the precipitates, the scale grain boundaries will be pinned, and fine-grained scales can be retained. REs or REOs also play a crucial role in reducing void formation and the segregation of sulfur at the scale/matrix interface. According to this investigation, Pint's model is also valid for the electrodeposited CeO_2-dispersed Ni_3Al coatings cyclically oxidized in air at 1050 °C. An optimum doping concentration exists for REs or REOs to achieve the REE, and excessive doping may cause more rapid oxidation, as shown in Fig. 4-19 (a) for the 80+5 (5μm) coating with the highest CeO_2 content.

4.5.5.4 Effect of Interdiffusion

Interdiffusion between the coating and the substrate alloy has both positive and negative effects on the cyclic oxidation behaviors of the current Ni_3Al base coatings. A positive effect of interdiffusion at 1050 °C is a quick healing of the pores in the coating leading to a dense coating. The latter eliminates harmful effects of high porosity such as the formation of deep internal oxidized channels observed during the oxidation at 850 °C.

As for the negative effects, interdiffusion firstly results in a loss of Al in the coatings, which decreases the ability of the coatings to regenerate Al_2O_3 scale. Susan et al. [72] has recently investigated the interdiffusion in Ni-15at%Al coating / Ni matrix system during isothermal oxidation. They found that the γ-Ni + γ'-Ni_3Al two-phase zone in the coating was quickly depleted to γ-Ni when oxidized at 1000 °C for 100 hr or 1100 °C for only 50 hr. They concluded that the rapid consumption of Al owing to

interdiffusion was the reason for the marginal isothermal oxidation resistance of electrodeposited Ni-15at%Al coating at 1000 °C [15]. It should be noted that although the inward diffusion of Al was also observed in our Ni_3Al-based coatings (Fig. 4-24), the Ni_3Al matrix had not been transformed into Ni-Al alloy after cyclic oxidation at 1050 °C for 500 hr. This deviation might have resulted from the different substrates used and much higher Al content present in the current coating matrix.

Another negative effect of interdiffusion may be the existence of substrate elements such as Fe, Cr, Si, and Mn in the Ni_3Al-based coatings. Fe and Cr can occupy either the Ni sites or the Al sites, whereas Si and Mn substitute only on the Al sites [39, 73]. Cr was found to decrease the cyclic oxidation resistance of Ni_3Al alloys because Cr_2O_3 would convert to volatile CrO_3 above 1050 °C [74, 75], which caused pitting in the scale or void formation at the scale/matrix interface [23]. Finally, the Kirkendall pores due to interdiffusion (Fig. 4-23 (c) and (d)) would significantly reduce the bonding strength between the coating and the substrate.

4.5.6 Conclusions

Electrodeposited pure and CeO_2-dispersed Ni_3Al intermetallic coatings were cyclically oxidized in flowing dry air at 1050 °C for periods up to 500 hr. Several conclusions can be summarized as follows:

1. The pure Ni_3Al coatings had a marginal resistance to cyclic oxidation at 1050 °C, and suffered severe spallation during the testing. The high residual compressive stresses, the rapid scale-growth rate, and the formation of internal or interfacial pores were the main reasons for the rapid failure of α-Al_2O_3 scale.
2. The CeO_2-dispersed Ni_3Al coatings were characterized by much better cyclic-oxidation resistance than the pure Ni_3Al coatings. The oxide scale on all the CeO_2-dispersed Ni_3Al coatings had a good adhesion to the coating matrix. A duplex-scale structure with the outer $NiAl_2O_4$/inner α-Al_2O_3 was observed even after 500 hr. It was found that Ce^{4+} ions in the coatings diffused into the scale and segregated at the scale-grain boundaries. The beneficial effects,

might include changing the growth mechanism of the α-Al_2O_3 scale, reducing the growth rate of the scale, improving mechanical properties of the scale, and reducing void formation at the scale/coating interface or at the scale-grain boundaries.

3. Interdiffusion was observed in the pure and CeO_2-dispsersed Ni_3Al coatings during cyclic oxidation. Interdiffusion was more rapid at 1050 °C than at 850 °C, which led to quicker pore healing in all coatings at 1050 °C. Rapid interdiffusion also caused a loss of Al and the diffusion of substrate elements into Ni_3Al base coatings, and the formation of the Kirkendall pores at the coating/matrix interface.

4.6 Concluding Remarks

It is clear that porosity of the electrodeposited Ni_3Al-based intermetallic coatings has reduced their oxidation resistance at low temperatures. Excellent resistance of the CeO_2-dispersed Ni_3Al coatings to cyclic oxidation at 1050 °C results from both the beneficial effects of CeO_2 particles and a rapid elimination of pores in the early stage of oxidation. Consequently, in order to achieve satisfactory long-term resistance to cyclic oxidation across the full temperature range, it is necessary to reduce porosity in these coatings. Chapter 5 will focus on the reduction of pores in the coatings and alternate ways to improve cyclic oxidation at low temperatures.

4.7 Bibliography

1. Izaki, M., M. Fukusumi, H. Dnomoto, T. Omi, and Y. Nakayama, Journal of The Japan Institute of Metals, 1993. **57**(2): p. 182-189.

2. Susan, D.F., K. Barmak, and A.R. Marder, Thin Solid Films, 1997. **307**: p. 133-140.

3. Susan, D.F., W.Z. Misiolek, and A.R. Marder, Metallurgical and Materials Transactions A., 2001. **32A**: p. 379-391.

4. Zhou, Y., X. Peng, and F. Wang, Scripta Materialia, 2004. **50**: p. 1429-1433.

5. Napłoszek-Bilnik, I., A. Budiok, and E. Łągiewka, Journal of Alloys and Compounds, 2004. **382**: p. 54-60.

6. Napłoszek-Bilnik, I., A. Budiok, B. Łosiewicz, L. Pająk, and E. Łągiewka, Thin Solid Films, 2005. **474**: p. 146-153.

7. Liu, H.F. and W.X. Chen, Surface and Coatings Technology, 2005. **191**: p. 341-350.

8. Liu, H.F. and W.X. Chen, Intermetallics, 2005. **13**: p. 805-817.

9. Bazzard, R. and P.J. Boden, Transactions of The Institute of Metal Finishing, 1972. **50**: p. 63-69.

10. Zhang, Y., X. Peng, and F. Wang, Materials Letters, 2004. **58**: p. 1134-1138.

11. Foster, J., B.P. Cameron, and J.A. Carew, Transactions of The Institute of Metal Finishing, 1985. **63**: p. 115-119.

12. Honey, F.J., E.C. Kedward, and V. Wride, Journal of Vacuum Science and Technology A., 1986. **4**(6): p. 2593-2597.

13. Saremi, M. and M. Bahraini, Transactions of The Institute of Metal Finishing, 2003. **81**(1): p. 24-27.

14. Susan, D.F. and A.R. Marder, Oxidation of Metals, 2002. **57**(1-2): p. 131-157.

15. Susan, D.F. and A.R. Marder, Oxidation of Metals, 2002. **57**(1-2): p. 159-180.

16. Brill, U., Materials and Corrosion, 1990. **41**(12): p. 682-688.

17. Klöwer, J., U. Brill, and U. Heubner, Intermetallics, 1999. **7**: p. 1183-1194.

18. Sidhu, B.S. and S. Prakash, Surface and Coatings Technology, 2003. **166**: p. 89-100.

19. Jung, H.G. and K.Y. Kim, Oxidation of Metals, 1996. **46**(1-2): p. 147-167.

20. Rahmel, A. and M. Schütze, Oxidation of Metals, 1992. **38**(3-4): p. 255-266.

21. Pint, B.A., Oxidation of Metals, 1998. **49**(5-6): p. 531-559.

22. Pint, B.A., K.L. More, and I.G. Wright, Materials at High Temperatures, 2003. **20**(3): p. 375-386.

23. Choi, S.C., H.J. Cho, and D.B. Lee, Oxidation of Metals, 1996. **46**(1-2): p. 109-127.

24. Grabke, H.J., Intermetallics, 1999. **7**: p. 1153-1158.

25. Peng, X., T.F. Li, and W.T. Wu, Oxidation of Metals, 1999. **51**(3-4): p. 291-315.

26. Peng, X., Z. Tang, T.F. Li, and W.T. Wu, Oxidation of Metals, 1999. **51**(3-4): p. 317-331.

27. Veleva, L., L. Diaz_Ballote, and D. Wipf, Journal of The Electrochemical Society, 2003. **150**(1): p. C1-C6.

28. Barmak, K., S.W. Banovic, C.M. Petronis, D.F. Susan, and A.R. Marder, Journal of Microscopy, 1997. **185**(2): p. 265-274.

29. Pérez, P., J.L. González-Carrasco, and P. Adeva, Oxidation of Metals, 1997. **48**(1-2): p. 143-170.

30. Pérez, P., J.L. González-Carrasco, and P. Adeva, Oxidation of Metals, 1998. **49**(5-6): p. 485-507.

31. Doychak, J. and M. Rühle, Oxidation of Metals, 1989. **31**(5-6): p. 431-452.

32. Prescott, R. and M.J. Graham, Oxidation of Metals, 1992. **38**(3-4): p. 233-254.

33. Yang, J.C., E. Schumann, I. Levin, and M. Rühle, Acta Materialia, 1998. **46**(6): p. 2195-2201.

34. Evans, H.E. and R.C. Lobb, Corrosion Science, 1984. **24**(3): p. 209-222.

35. Jung, H.G. and K.Y. Kim, Oxidation of Metals, 1998. **49**(5-6): p. 403-430.

36. Hancock, P. and J.R. Nicholls, Materials at High Temperatures, 1994. **12**(2-3): p. 209-217.

37. Bull, S.J., Oxidation of Metals, 1998. **49**(1-2): p. 1-17.

38. Meier, G.H., Materials and Corrosion, 1996. **47**: p. 595-618.

39. Dey, G.K., Sādhanā, 2003. **28**(1-2): p. 247-262.

40. Jeurgens, L.P.H., W.G. Sloof, F.D. Tichelaar, and E.J. Mitterneijer, Physic Review B., 2002. **62**(7): p. 4707-4718.

41. Taymaz, I., A. Mimaroglu, E. Avcl, V. Ucar, and M. Gur, Surface and Coatings Technology, 1999. **116-119**: p. 690-693.

42. Fujimura, T. and S.I. Tanaka, Acta Materialia, 1997. **45**(12): p. 4917-4921.

43. Barsoum, M.W., *Fundamentals of Ceramics*. 1997, McGraw-Hill Companies, Inc.: New York. p. 393-395.

44. Taub, A.I., S.C. Huang, and K.M. Chang, Metallurgical Transactions A., 1984. **15A**: p. 399-402.

45. Brumm, M.W., H.J. Grabke, and B. Wagemann, Corrosion Science, 1994. **36**(1): p. 37-53.

46. Katsman, A.V., H.J. Grabke, and L. Levin, Oxidation of Metals, 1996. **46**(3-4): p. 313-331.

47. Katsman, A.V., H.J. Grabke, L. Levin, and T. Werber, materials Science Forum, 1996. **Part 2, 207**: p. 737-740.

48. Stott, F.H., G.C. Wood, and J. Stringer, Oxidation of Metals, 1995. **44**(1-2): p. 113-141.

49. Czerwinski, F. and J.A. Szpunar, Journal of Sol-Gel Science and Technology, 1997. **9**: p. 103-114.

50. Haugsrud, R., Corrosion Science, 2003. **45**: p. 1289-1311.

51. Barsoum, M.W., *Fundamentals of Ceramics*. 1997, New York: McGraw-Hill Companies, Inc., p. 355-358.

52. Haanappel, V.A.C., P. Pérez, J.L. González-Carrasco, and M.F. Stroosnijder, Intermetallics, 1998. **6**: p. 347-356.

53. Pérez, P., J.L. González-Carrasco, and P. Adeva, Oxidation of Metals, 1999. **51**(3-4): p. 273-289.

54. Peng, X., T.F. Li, and W.P. Pan, Scripta Materialia, 2001. **44**: p. 1033-1038.

55. Choi, S.C., H.J. Cho, Y.J. Kim, and D.B. Lee, Oxidation of Metals, 1996. **46**(1-2): p. 51-72.

56. Czerwinski, F. and W.W. Smeltzer, Oxidation of Metals, 1993. **40**(5-6): p. 503-527.

57. Chevalier, S., G. Bonnet, K. Przybylski, J.C. Colson, and J.P. Larpin, Oxidation of Metals, 2000. **54**(5-6): p. 527-547.

58. Graham, M.J. and R.J. Hussey, Oxidation of Metals, 1995. **44**(1-2): p. 339-374.

59. Kim, K.Y., S.H. Kim, K.W. Kwon, and L.H. Kim, Oxidation of Metals, 1994. **41**(3-4): p. 179-201.

60. Christensen, R.J., D.M. Lipkin, and D.R. Clarke, Acta Materialia, 1996. **44**(9): p. 3813-3821.

61. Kuenzly, J.D. and D.L. Douglass, Oxidation of Metals, 1974. **8**: p. 139-178.

62. Pint, B.A., Oxidation of Metals, 1997. **48**(3-4): p. 303-328.

63. Grabke, H.J., Surface and Interface Analysis, 2000. **30**: p. 112-119.

64. Meier, G.H., F.S. Pettit, and J.L. Smialek, Materials and Corrosion, 1995. **46**: p. 232-240.

65. Schumann, E., J.C. Yang, and M.J. Graham, Scripta Materialia, 1996. **34**(9): p. 1365-1370.

66. Jedliński, J., Corrosion Science, 1993. **35**(5-8): p. 863-869.

67. Chevalier, S. and J.P. Larpin, Acta Materialia, 2002. **50**: p. 3105-3114.

68. Pint, B.A., Materials Science Forum, 1997. **251-254**: p. 397-404.

69. Schmutzler, H.J., H. Viefhaus, and H.J. Grabke, Surface and Interface Analysis, 1992. **18**: p. 581-584.

70. Wright, I.G., B.A. Pint, and P.F. Tortorelli, Oxidation of Metals, 2001. **55**(3-4): p. 333-357.

71. Pint, B.A., Oxidation of Metals, 1996. **45**(1-2): p. 1-37.

72. Susan, D.F. and A.R. Marder, Acta Materialia, 2001. **49**: p. 1153-1163.

73. Stoloff, N.S., International Materials Reviews, 1989. **34**(4): p. 153-183.

74. Stringer, J., Materials Science and Engineering, 1987. **87**: p. 1-10.

75. Yamauchi, A., K. Kurokawa, and H. Takahashi, Oxidation of Metals, 2003. **59**(5-6): p. 517-527.

Chapter 5

On The Improvement of Cyclic-oxidation Resistance of Electrodeposited Ni-Al-Based Intermetallic Coatings at 850 °C

5.1 Introduction

In this study, annealing of Ni-Al composite coatings at 800 °C produced a large fraction of closed pores in the Ni-Al base coatings (see Chapters 2-4). Fully-annealed Ni-Al composite coatings with 20 vol% Al and 33.5vol% Al had about 8 vol% [1] and 10.6vol% of porosity respectively, as reported in Chapter 4. Izaki et al. [2] indicated that the porosity in Ni-Al coatings with more than 16at% Al has no effect on the short-term resistance of coatings to isothermal and cyclic oxidation at temperatures ranging from 900 °C to 1100 °C. Susan et al. [3] reported that 8vol% of pores had no detrimental effect on the isothermal oxidation of Ni-Al coatings at 800 °C for 2000 hr. However, in Chapter 4, we observed that high porosity (about 10vol%) significantly decreased the long-term resistance of electrodeposited pure and CeO_2-dispersed Ni_3Al base coatings to cyclic oxidation at 850 °C by forming interconnected oxidizing channels among neighboring pores. At 1050 °C, the pores in coatings were quickly healed after as little as 20 hr due to rapid interdiffusion between the coating and the alloy substrate. Hence, the detrimental effect of the porosity in the coatings was negligible.

In order to achieve better oxidation resistance in the low temperature regime, it is of great importance to reduce the porosity in the electrodeposited Ni_3Al base coatings we produced. The pores and cracks open to the surface of the coating can be sealed by electroplating of Ni [4], or by applying ceramic base sealants [5] and phosphate base sealants [6]. To reduce closed pores inside coatings, laser remelting has proven to be effective [7]. The presence of hydrostatic pressure during annealing treatment of the as-plated composite coatings was also found to be helpful [1]. Because pores in our Ni_3Al-based coatings are mostly closed, laser modification or sintering under hydrostatic pressure would be suitable for their densification. This, however, may substantially increase the cost of coating.

This part of the study will explore alternative methods for pore-control and their effects on cyclic-oxidation resistance of Ni-Al base intermetallic coatings at 850 °C. The following approaches will be investigated:

1) Reduce the diffusion reaction rate using a slow ramping and cooling rate during annealing;
2) Modify the pure Ni-Al coating by doping reactive oxides to achieve better cyclic-oxidation resistance at 850 °C; and
3) Electro-deposit alternative films on the pure Ni-Al coating to achieve an enhanced oxidation resistance. The work reported in Chapter 4 demonstrated that the pores in Ni-Al-based coatings healed slowly during oxidation at 850 °C for 1000hr. If the top layer were able to provide good protection before pores are healed, an improved coating performance can be expected.

5.2 Experimental

5.2.1 Sample Preparation

Pure Ni-Al, Ni-Al-nano CeO_2, and Ni-Al-Y_2O_3 composite coatings were electroplated onto Fe-Ni-Cr HP alloy coupons of dimensions 20 mm×10 mm×2 mm from a Watt's nickel bath containing suspended Al particles, or both Al particles and Y_2O_3, or CeO_2 particles via sediment co-deposition. The coating process was described in Chapters 2 and 3. The centrifugally cast HP alloy contained 0.4wt% C, 35wt% Ni, 25wt% Cr, <1.5wt% Si, <1.5wt% Mn, <1.5wt% Nb, and the balance Fe. Al powders, purchased from Valimet Inc. (Stockton, CA, USA), had an average size of 3 μm. CeO_2 particles with an average size of 9-15 nm and Y_2O_3 particles less than 1 μm respectively, were obtained from Alfa Aesar (USA). A layer of coating, with an average thickness of about 150 μm, was deposited on both 20 mm×10 mm surfaces. All coatings were deposited with a constant Al bath loading of 80 g/l, but with various oxide particle loadings.

As presented in Chapter 4, the Ni-Al-nano CeO_2 coatings exhibited better oxidation resistance at 850 °C than did the pure Ni-Al coating. Moreover, the Ni-Al-nano CeO_2 coating with 5 g/l CeO_2 particle loading was more resistant to long-term oxidation than that with 1 g/l CeO_2 particle loading. As a result, the Ni-Al-nano CeO_2 coating with

a higher CeO_2 particle loading of 10 g/l, 80+10-nano, was produced. Ni-Al-Y_2O_3 coatings with 5 g/l Y_2O_3 (80+5-Y_2O_3), were also prepared and studied.

To deposit the 80+10-nano CeO_2 film and the 80+5-Y_2O_3 film, the as-plated pure Ni-Al coating (80+0) coupon was quickly transferred to a Ni-Al-nano CeO_2 (10 g/l) bath or a Ni-Al-Y_2O_3 (5 g/l) bath until a film of about 10 μm was deposited. All the coated coupons were then annealed in a vacuum furnace at 800 °C for 3hr to allow the formation of Ni-Al intermetallic coatings. Annealing treatment of the pure Ni-Al composite coating, 80+0-LA, was also performed by slowly heating the sample to 800 °C in 48 hr and then cooling the sample to room temperature in 48hr.

5.2.2 Cyclic Oxidation

Cyclic oxidation was conducted in a tube furnace. The uncoated HP alloy coupon was used as a reference. Before the test, all the coupons were polished with 600-grit SiC grinding paper, cleaned using acetone, and then air-dried. Test coupons were held in high-purity (99.8%) alumina boats with one coupon per boat (Vesuvius McDanel, PA, USA). Dry air was passed through the tube at a fixed rate of 60ml/min. The test cycle consisted of heating at 5 °C/min, holding at 850 °C for the required time, and cooling at 1.5 °C/min. After each cycle, the boats were removed from the furnace for mass gain measurement. Each coupon was weighed together with the boat and any spalled oxide from the coupon. Because each coated coupon has four edge surfaces uncoated, a correction was made to the measured mass gains on the assumption that the uncoated surfaces would have the same mass change per unit area as the coupon of bare HP alloy. After measurement, sample boats were returned to the furnace for the next run cycle.

5.2.3 Characterization

The microstructures, compositions and morphologies of oxidized samples were examined on a S-2700 Scanning Electron Microscope (SEM) attached with an Energy-Dispersive X-Ray Spectrometer (EDS). The oxidation products were analyzed using Rigaku Geigerflex 2173 X-ray diffractometer (XRD) with the Co K_α incident radiation generated at 40kV and 30mA. A 2θ range of 2 to 120 degrees was used to collect X-rays.

5.3 Results

5.3.1 Coating Microstructures

The following coatings were produced and tested: pure Ni-Al coating, 80+0, and pure Ni-Al coating with an extended annealing time, 80+0-LA; three Ni-Al-nano CeO_2 coatings, 80+1-nano, 80+5-nano and 80+10-nano; one Ni-Al-Y_2O_3 coating, 80+5-Y_2O_3; two pure Ni-Al coatings with a thin film, 80+10-nano/80+0 and 80+5-Y_2O_3/80+0. The compositions and phase characteristics of these coatings after annealing are summarized in Table 5-1.

Table 5-1. Ni_3Al base coatings used in the investigation.

Sample code*	Deposition condition	Al content (vol%)	Phases by XRD
80+0	no oxide particle	33.50±0.64	Ni_3Al (s)
80+0-LA	no oxide particle	33.50±0.64	Ni_3Al (s)
80+1-nano	1 g/l CeO_2 (9-15 nm)	30.98±0.60	Ni_3Al (s)
80+5-nano	5 g/l CeO_2 (9-15 nm)	29.83±1.81	Ni_3Al (s)
80+10-nano	10 g/l CeO_2 (9-15 nm)	27.07±1.86	Ni_3Al (s), Ni (m)
80+5-Y_2O_3	5 g/l Y_2O_3 (<1 μm)	18.69±0.55%	Ni_3Al (s), Ni (s), Y_2O_3 (m)

*: The Al particle loading of 80 g/l is constant for all coatings.

s: strong; m: moderate.

As shown in Fig. 5-1 (a), pores of several microns were homogenously distributed in the gray γ'-Ni_3Al matrix of the 80+0 coating. In contrast, the 80+0-LA coating contained smaller irregular pores rather than large round ones, along with some second phases as indicated by white solid arrows (Fig. 5-1 (b)).

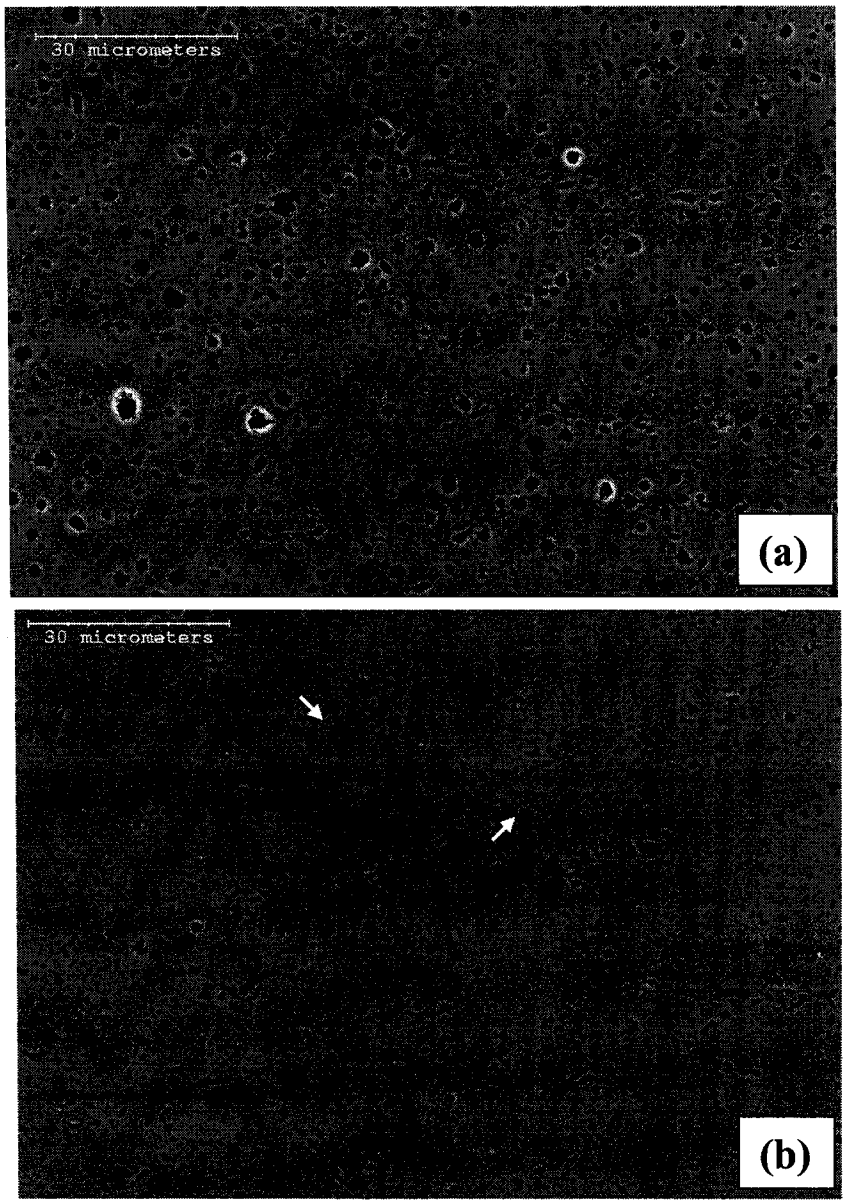

Figure 5-1. The cross-sectional morphologies of pure Ni-Al coatings: (a) 80+0; (b) 80+0-LA.

Figs. 5-2 (a)-(c) are the micrographs of the Ni-Al-nano CeO_2 coatings and the Ni-Al-Y_2O_3 coating. Fig. 5-2 (a) showed a uniform gray γ'-Ni_3Al matrix of the 80+1-nano coating with high porosity. The 80+10-nano coating shown in Fig. 5-2 (b), however, had a multiple-phase structure due to lower Al content (Table 5-1), which resulted from the interference of CeO_2 with Al particles as detailed in Chapter 3. The XRD and EDS analyses suggested that the matrix consisted of γ'-Ni_3Al phase (dark region), and Al-

saturated γ-Ni (light region). The porosity in the 80+10-nano coating (Fig. 5-2 (b)) was evidently lower than that in the 80+1-nano coating (Fig. 5-2 (a)). The 80+5-Y_2O_3 coating had a much lower Al content than the 80+10-nano coating (Table 5-1). The former contained mainly γ'-Ni_3Al (dark phase), γ-Ni-Al (light region), and a high amount of Y_2O_3 (needle-like phase) (Fig. 5-2 (c) and Table 5-1).

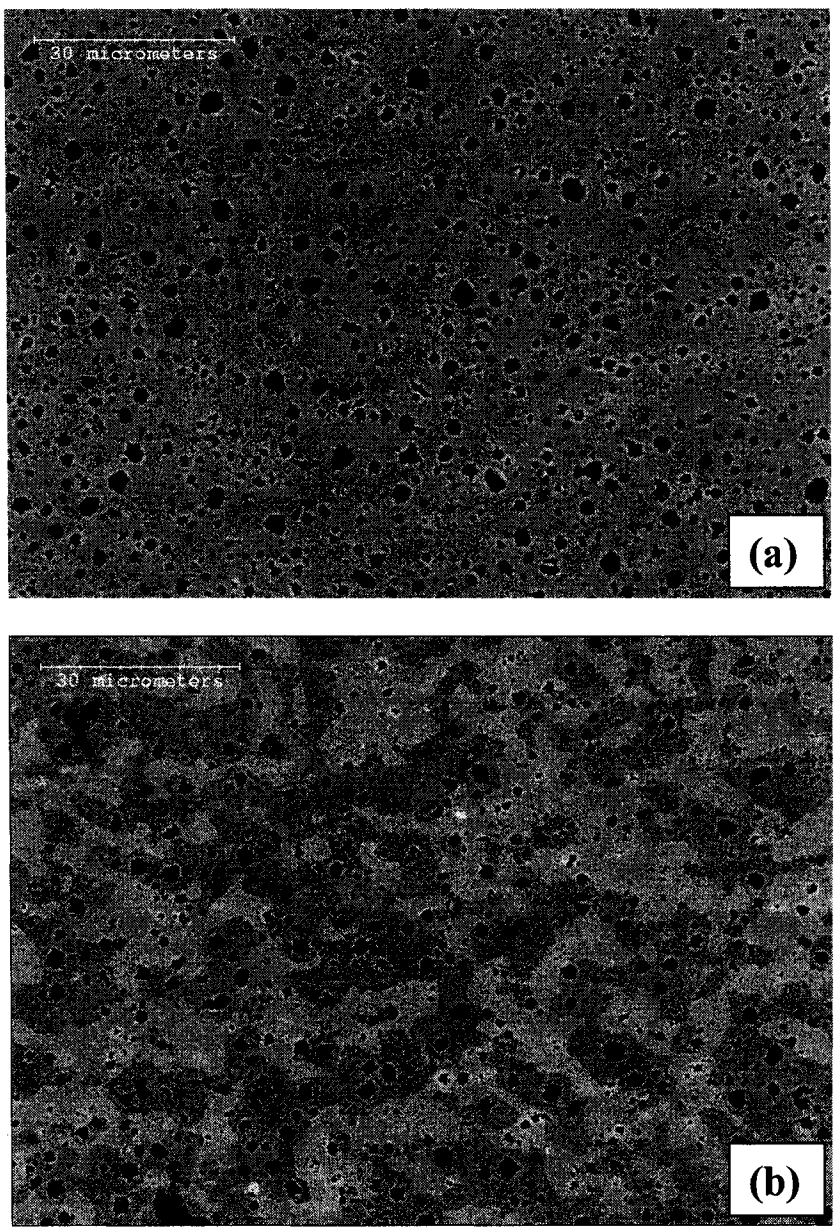

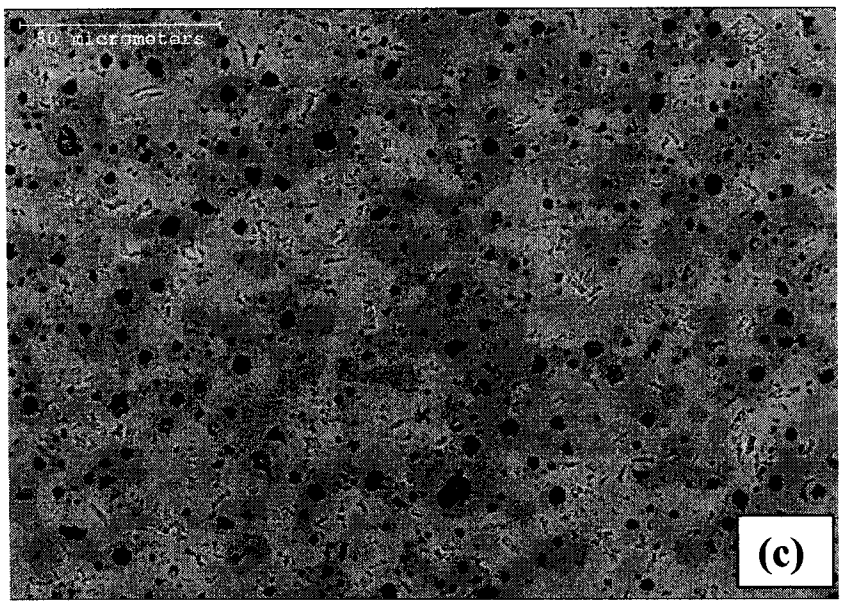

Figure 5-2. The cross-sectional morphologies of Ni-Al-oxide particle coatings: (a) 80+1-nano; (b) 80+10-nano; (c) 80+5-Y_2O_3.

5.3.2 Oxidation Kinetics

Figs. 5-3 provide the mass changes of all the Ni-Al-based coatings prepared during cyclic oxidation at 850 °C for periods of up to 1000 hr. The data for the uncoated Fe-Ni-Cr alloy, the 80+0 coating, the 80+1-nano coating and the 80+5-nano coating were from Fig. 4-2 in Chapter 4. The uncoated Fe-Ni-Cr alloy showed a very slow mass increase and a parabolic oxidation behavior during the whole testing period (Fig. 5-3 (a)), while the 80+0 coating (Fig. 5-3 (a)), the 80+1-nano coating and the 80+5-nano coating (Fig. 5-3 (b)) had a slow mass increase in the early stage and then experienced an accelerated pickup of oxygen with further oxidation, an indication of the onset of the breakaway stage. The 80+0-LA coating showed a slower mass increase than the 80+0 coating until 200 hr (Fig. 5-3 (a)). After 200 hr, although its mass increase was still much lower than that of the 80+0 coating, the breakaway stage was evident. The 80+10-nano coating, however, showed a parabolic oxidation in the entire testing period, which is comparable to the uncoated Fe-Ni-Cr (Fig. 5-3 (b)). The mass gain of the 80+10-nano coating after 1000 hr oxidation was as little as 0.6 mg/cm^2. Similar to the 80+10-nano coating, the 80+5-Y_2O_3 coating with a much lower Al content also exhibited excellent resistance to the cyclic oxidation at 850 °C (Fig. 5-3 (b)). The two pure Ni-Al coatings

with a thin film on the top, the 80+10-nano/80+0 coating and the 80+5-Y_2O_3/80+0 coating, also had a parabolic oxidation within the initial 200 hr, after which the breakaway oxidation prevailed (Fig. 5-3 (c)). These results suggest that, although the special annealing and the thin-film approach delayed the onset of breakaway stage, it failed to improve the long-term resistance to cyclic oxidation.

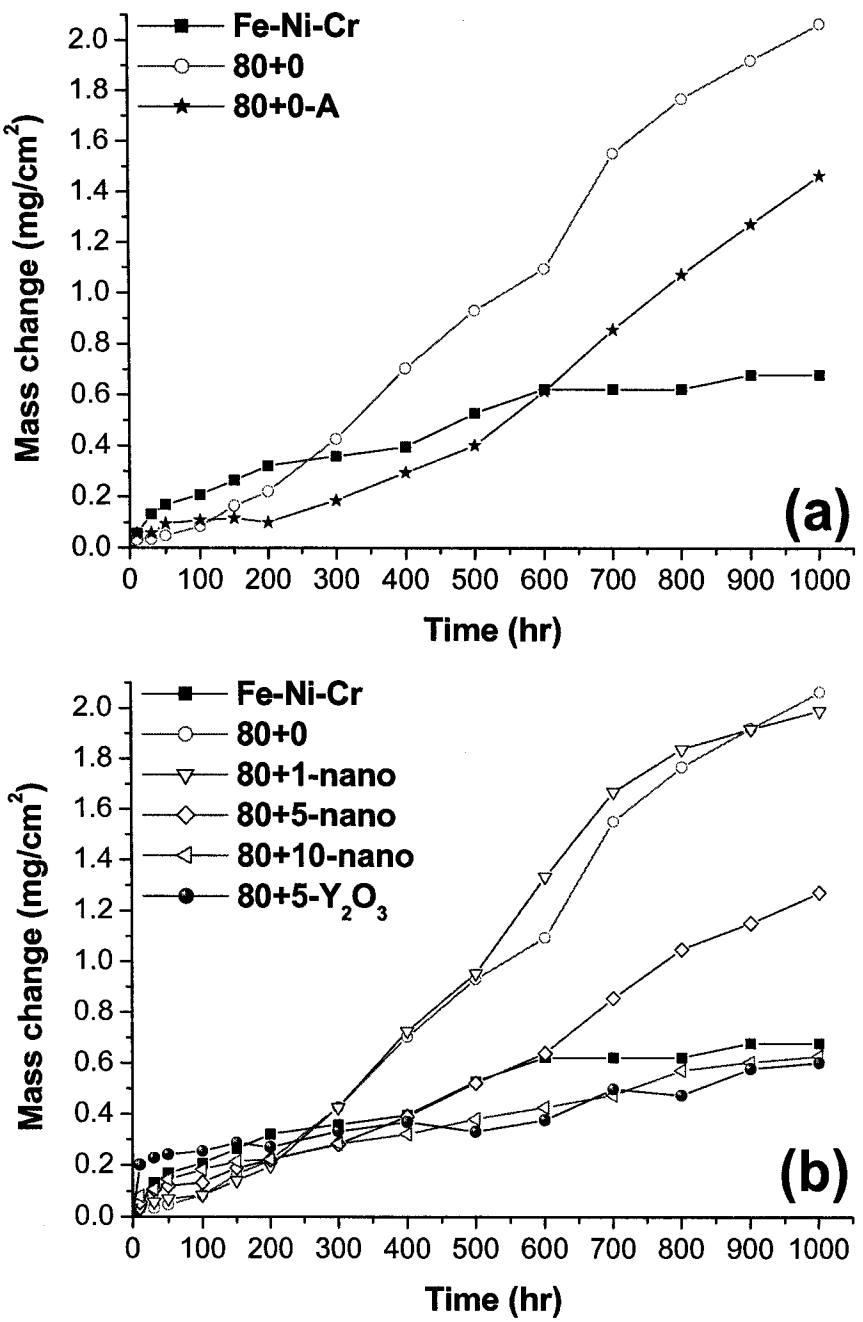

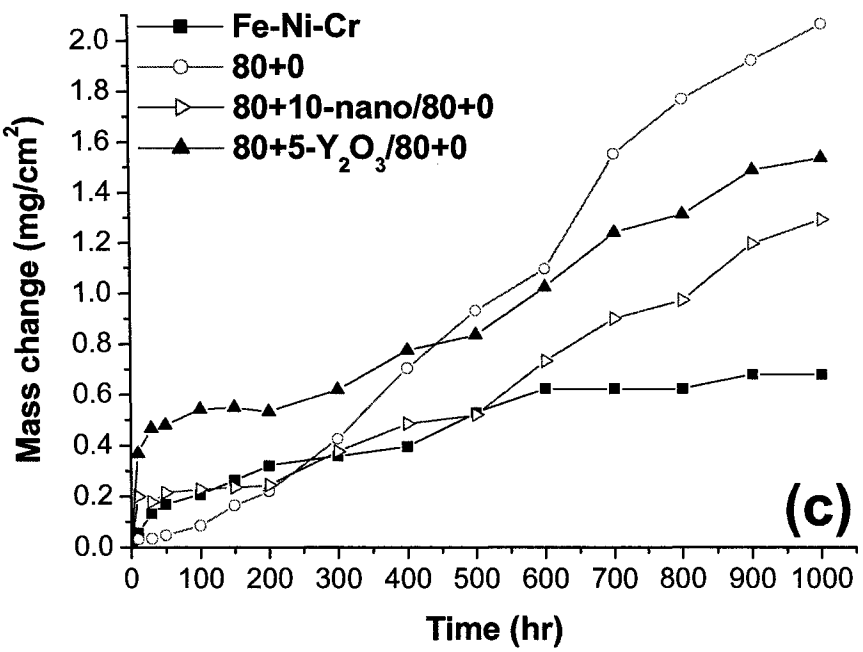

Figure 5-3. The cyclic-oxidation behaviors of various Ni-Al-based coatings at 850 °C for periods of up to 1000 hr: (a) slowly annealed; (b) doped with reactive oxides; (c) with additional electroplated thin film.

5.3.3 Cross-sections of Oxide Scales

Figs. 5-4 (a)-(c) provide the cross-sectional morphologies of the 80+0-LA coating after oxidation at 850 °C for periods of up to 1000 hr. For a short exposure period of 100hr, a thin oxide scale, along with pores and second phases below the scale, was seen on the 80+0-LA coating (Fig. 5-4 (b)). By 500 hr, a wide zone—containing a mixture of pores, separated coatings, and various oxides such as Al_2O_3, NiO, and $NiAl_2O_4$—had developed on the 80+0-LA coating (Fig. 5-4 (b)). At 1000 hr, the oxidation zone had expanded (Fig. 5-4 (c)) to a level similar to that seen on the 80+0 coating (Fig. 5-4 (d)). These observations are consistent with the mass increase of the 80+0-LA coating shown in Fig. 5-3.

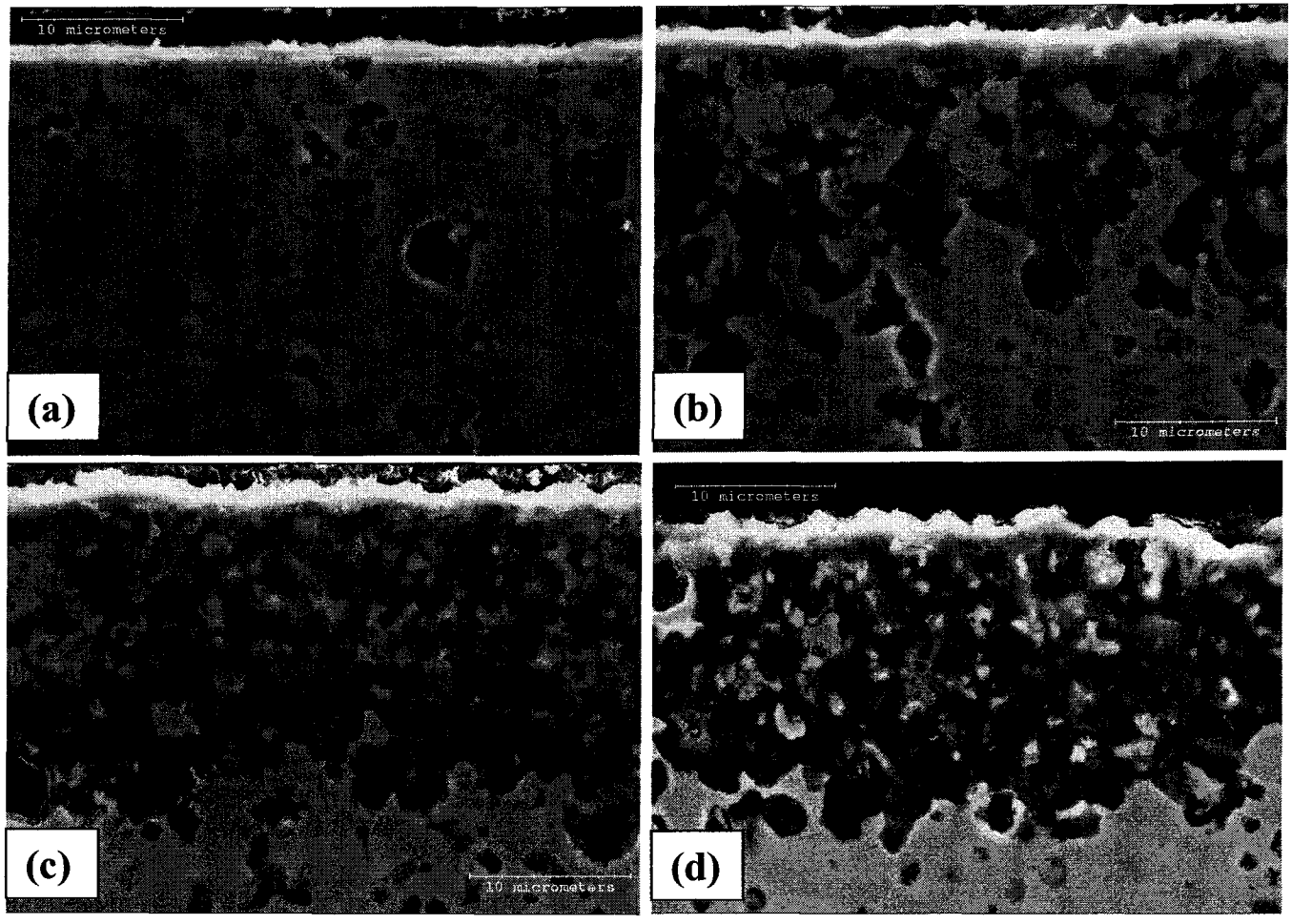

Figure 5-4. The cross-sectional morphologies of the 80+0-LA coating after cyclic oxidation at 850 °C: (a) for 100 hr; (b) for 500 hr; (c) for 1000 hr; (d) the 80+0 coating for 1000 hr.

In contrast, a thin Al_2O_3 scale was observed on the 80+10-nano coating throughout the testing period. The thin Al_2O_3 scale was well adhered to the coating matrix even after 1000 hr (Fig. 5-5 (a)). A similar situation was found on the 80+5-Y_2O_3 coating (Fig. 5-5 (b)), although the Al_2O_3 scale on the 80+5-Y_2O_3 coating was a bit thicker than that on the 80+10-nano coating (Fig. 5-5 (a)).

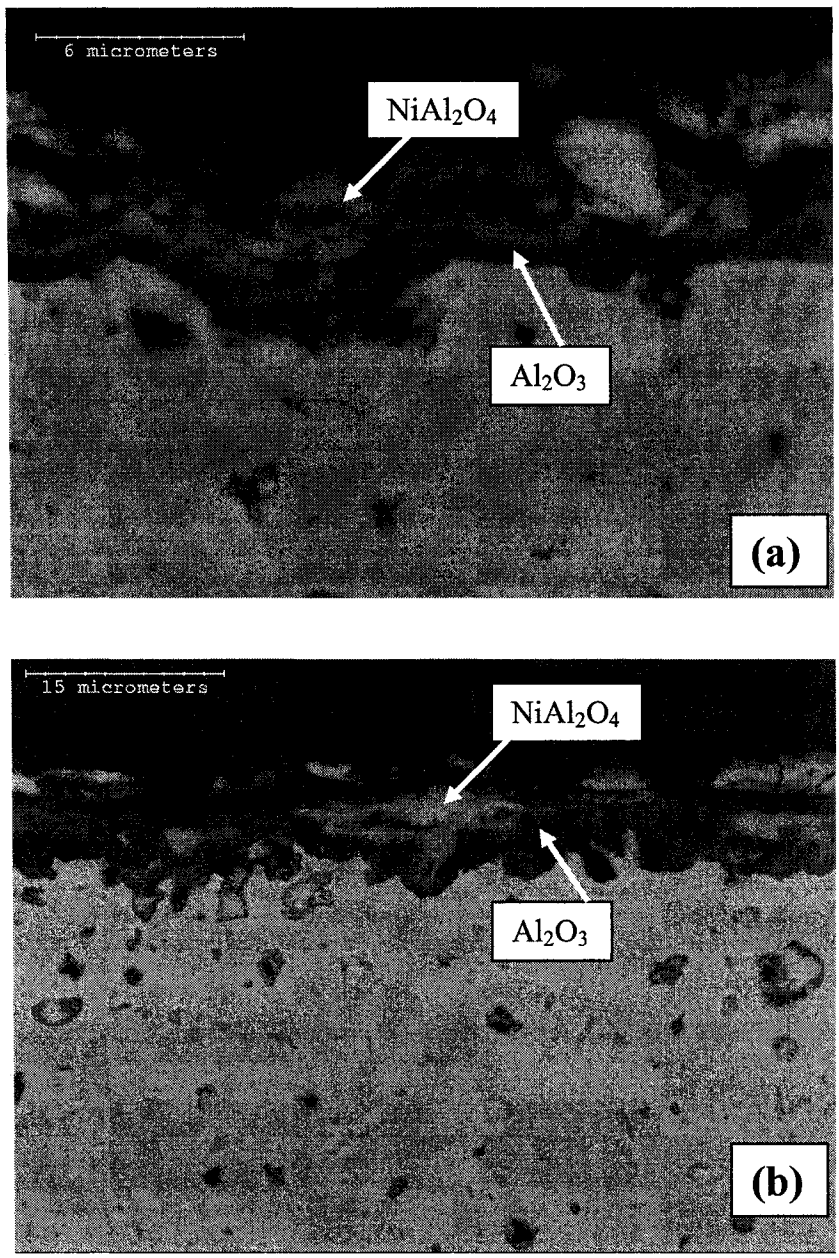

Figure 5-5. The cross-sectional morphologies of coatings after cyclic oxidation at 850 °C for 1000 hr: (a) the 80+10-nano coating; (b) the 80+5-Y_2O_3 coating.

The microstructures of the 80+10-nano/80+0 coating and the 80+5-Y_2O_3/80+0 coating during the cyclic oxidation were similar. Their typical cross-sectional morphologies are shown in Figs. 5-6 (a) and (b).

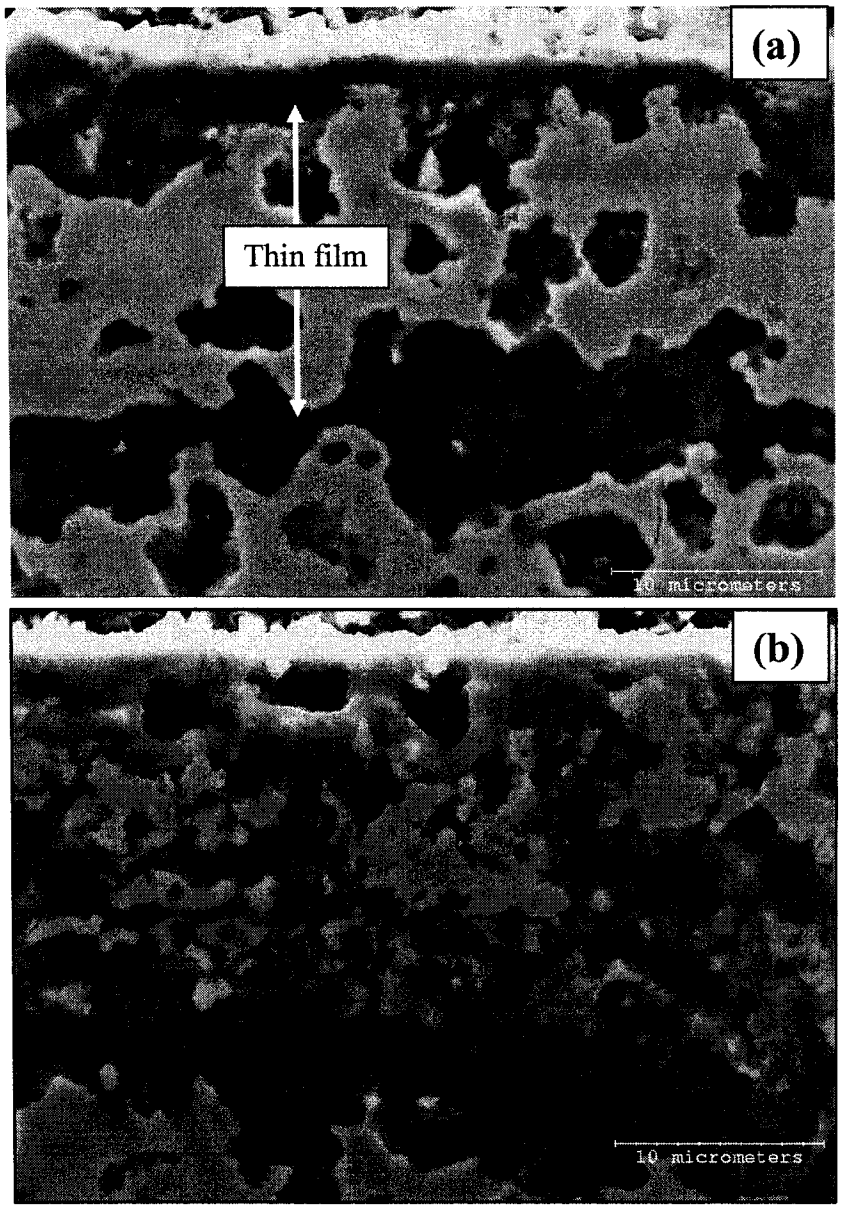

Figure 5-6. The cross-sectional morphology of the 80+10-nano/80+0 coating after cyclic oxidation at 850 °C for 1000 hr.

In the early stage of oxidation (up to 100 hr), a very thin oxide scale was induced on the thin layer deposited. However, by 500 hr, oxidation was seen to occur within the thin layer and along the thin layer/coating interface (Fig. 5-6 (a)), suggesting a rapid

inward diffusion of oxygen via the interface has occurred. Both the thin film and the coating matrix suffered severe oxidation by 1000 hr (Fig. 5-6 (b)). The morphology of the oxidation zone was the same as that in the 80+0 coating after 1000hr exposure. The two thin films failed to provide a long-term protection to pure Ni_3Al coatings with a large fraction of porosity.

5.4 Discussion

5.4.1 Special Annealing

The temperature- and time-dependent phase formation in Ni-Al composite coatings during annealing has been well studied [1, 2]. Susan [1] summarized the situation by stating that most Al particles in Ni-Al coatings remain unreacted during short-term annealing performed at low annealing temperatures (400-450 °C). If annealing time is increased, some Al-rich intermetallic phases such as $NiAl_3$, Ni_2Al_3, and NiAl may be formed. In the temperature range of 500-530 °C, formation of a NiAl phase would be dominant. Above 600 °C, the diffusion reaction is accelerated. The final phase structure after full annealing is controlled by the Al content in the Ni-Al coatings [2]. The long-term annealing performed in the present study was aimed at controlling the diffusion reaction between the Al particle and the Ni matrix. A slow ramping rate allows maximum formation of refractory intermetallic phases before the temperature approaches the melting point of Al (about 660 °C), and thus reduces the amount of melting Al particles during annealing at temperatures above 660 °C. Another benefit from the slow diffusion reaction is a reduction of the Kirkendall pores in the coating owing to rapid diffusion of Al.

Although it can reduce the amount of porosity, slow annealing cannot completely eliminate it. This is the case because its formation is mainly due to local densification in the absence of pressure, as proposed by Susan [1]. The cyclic oxidation of the 80+0-LA would then follow the same mechanism as reported for the 80+0 coating in Chapter 4, where interconnected oxidized channels are formed among the neighboring pores or second phases, thereby accelerating the inward oxygen attack and leading to the

disintegration of the coating matrix (Figs. 5-4). We may conclude that, although slow annealing reduces pore density in the pure Ni-Al coatings to some extent, it is not a solution to the poor cyclic oxidation resistance at 850 °C.

5.4.2 Modified Ni-Al Coatings and Thin Films

Unlike the 80+0 coating, the 80+10-nano coating and the 80+5-Y_2O_3 coating exhibit excellent long-term resistance to the cyclic oxidation at 850 °C for periods of up to 1000hr. This may be attributed firstly to the presence of nano CeO_2 or Y_2O_3 particles. As discussed in Chapters 4 and 6, these reactive oxide particles in Ni-Al coatings can significantly improve the mechanical properties of Al_2O_3 scale and enhance the adhesion of the scale to the coating matrix, which, in turn, greatly reduces the spalling or cracking of the scale during thermal cycling. However, we believe that the most crucial factor for the improved oxidation resistance of the 80+10-nano coating and the 80+5-Y_2O_3 coating is their lower porosity. As indicated in Table 5-1 and Figs. 5-2, the 80+1-nano coating and the 80+5-nano coating have higher Al content than the two-phase (γ-Ni+γ'-Ni_3Al) 80+10-nano coating, and they possess better cyclic oxidation resistance. In fact, the oxidation resistance of these two coatings was inferior (Fig. 5-3 (b)). The results in Chapter 4 demonstrated that the degradation mechanisms in the 80+1-nano coating and the 80+5-nano coating were similar to that in the 80+0 coating, due to the fact that they all contain high porosity. The 80+10-nano coating and the 80+5-Y_2O_3 coating are much denser than the 80+0 coating, the 80+1-nano coating and the 80+5-nano coating. Despite of their low Al content, especially in the case of the 80+5-Y_2O_3 coating, a thin Al_2O_3 scale was formed without spallation throughout the testing. The latter can be attributed to low porosity.

When the 80+10-nano coating and the 80+5-Y_2O_3 coating are deposited as a thin film onto the 80+0 coating, it is expected that the thin film will provide the protection until the porosity in the 80+0 coating becomes fully healed. However, this did not happen. In addition to the rapid oxidation of the thin film, the inward oxygen via the film/coating interface causes severe oxidation of the coating and the film, which plays a critical role in deteriorating the coating. As reported in Chapter 4, the overall oxidation

behavior is similar to that in the single 80+0 coating. During oxidation at 850 °C, interdiffusion will occur between the thin film and the 80+0 coating due to the chemical gradient. The resultant Kirkendall pores will segregate at the film/coating interface, which provides easy paths for the inward diffusion of oxygen. As discussed in Chapter 4 and Ref [8], pores in the coating will be healed by a process of self-sintering—a rapid atom flux to the pores, and vacancy flux away from the pores to vacancy sinks such as grain boundaries, interfaces and free surfaces. As both the thin film and the 80+0 coating have high porosity, vacancy flux will be noticeably high at the film/coating interface, which further contributes to the rapid inward diffusion of oxygen.

5.5 Concluding Remarks

Several attempts were made to improve the cyclic-oxidation resistance of porous electrodeposited Ni-Al base intermetallic coatings at 850 °C. Slow annealing failed to completely eliminate pores in the coating due to local densification, although it can reduce its presence to some extent. The 80+0-LA coating showed an oxidation behavior similar to that of the 80+0 coating during long-term oxidation at 850 °C. The 80+10-nano coating and the 80+5-Y_2O_3 coating with low porosity offered excellent long-term resistance to cyclic oxidation at 850 °C. However, the low Al content would limit their applications at temperatures above 1000 °C. The 80+10-nano and the 80+5-Y_2O_3 thin films were not enough to provide long-term protection for the 80+0 coating due to rapid oxidation along the film/coating interface.

5.6 Bibliography

1. Susan, D.F., Misiolek, W.Z., and Marder, A.R., Metallurgical and Materials Transactions A., 2001. **32A**: p. 379-391.

2. Izaki, M., Fukusumi, M., Dnomoto, H., Omi, T., and Nakayama, Y., Journal of The Japan Institute of Metals, 1993. **57**(2): p. 182-189.

3. Susan, D.F. and Marder, A.R., Oxidation of Metals, 2002. **57**(1-2): p. 131-157.

4. Westergård, R. and Hogmark, S., Wear, 2004. **256**: p. 1153-1162.

5. Sugama, T., Surface and Coatings Technology, 1998. **106**: p. 106-116.

6. Ahmaniemi, S., Tuominen, J., Vuoristo, P., and Mantyla, T., Journal of Thermal Spray Technology, 2002. **11**(3): p. 320-332.

7. Sidhu, B.S., Puri, D., and Prakash, S., Materials Science and Engineering A., 2004. **368**: p. 149-158.

8. Barsoum, M.W., *Fundamentals of Ceramics*. 1997, McGraw-Hill Companies, Inc.: New York. p. 393-395.

Chapter 6

Carburization of Electrodeposited Ni_3Al-CeO_2-Based coatings in 2%CH_4-H_2 Reducing Atmospheres*

* A version of this chapter has been submitted for publication. Liu, H.F. and Chen, W.X., submitted to **Journal of The Electrochemical Society**, 2005.

6.1 Introduction

Carburization is a common problem for Fe-based and Ni-based heat resistant alloys used in chemical, petrochemical, and energy conversion industries. It refers to the ingress of carbon and the precipitation of carbides when the alloys are served at 800-1100 °C in the carburizing atmospheres with low carbon activities ($a_c \leq 1$) [1-6]. Excessive carbides in alloys cause volume increase and significant internal stresses, which may induce premature failure of the alloys [2]. Brittle carbides also deteriorate the room-temperature ductility of alloys. Klöwer et al. [7] reported that alloy 800H and AC66 Fe-Ni-Cr alloys lose nearly 100% of Charpy impact energy after carburization in CH_4-H_2 at 1000 °C for 1008 hr.

Fe-based and Ni-based heat resistant alloys generally contain high Cr, which can form a protective Cr_2O_3 scale at high temperatures. However, Cr_2O_3 is inherently unstable above 1050 °C due to its conversion to chromium carbides [1, 2, 4] or volatile CrO_3 [8, 9]. Another disadvantage is that protective Cr_2O_3 cannot be formed in highly reducing carburizing atmospheres, such as CH_4-H_2. Novel Fe-base or Ni-base alloys are often alloyed with Al or Si [10-12]. The addition of Al or Si can form thermodynamically more stable Al_2O_3 or SiO_2 scale beneath the Cr_2O_3 scale to further block the inward diffusion of carbon. Recently, Klöwer et al. [7] reported that 602CA Ni-Cr-2.3wt%Al alloy showed extremely low carbon uptake at 1100 °C for 1000 hr in CH_4-H_2. Unfortunately, an addition of Al or Si more than 2wt% undermines the ductility and weldability of the alloys [11], while a minimum 4wt% of Al or Si is required to form an external scale [1, 3, 10]. Other alloying elements such as Mo, Mg, Nb, Ti, and reactive elements are reported to improve the carburization resistance of alloys to some extent [7, 11-14].

Surface-engineered coating is a feasible solution to the carburization problem. The most successful coating systems developed to date are the Cr-Si, Al-Si, and Al-Cr-Si metallic coatings [11, 15-18], which have reached commercial application. Diffusion Al-Cr-Si coatings have shown excellent carburization resistance up to 1149 °C during a test in an ethylene furnace for 27 months [15, 16].

The current trend is to develop Ni_3Al or NiAl as novel carburization-resistant alloys or coatings. Brill [19] reported superior carburization resistance of Ni_3Al base alloys in CH_4-H_2 ($a_c = 0.8$) to alloy 800H and alloy 617 at temperatures up to 1000 °C. Commercial Ni_3Al-based trays have been successfully adopted in industrial carburizing furnaces to replace those made of stainless steels, which often fail after six-month in-field use. Ni_3Al trays, however, didn't experience failure even after 39 months of service [20]. Wang et al. [21] recently reported that no carbon ingress was observed in NiAl-coated Fe-Ni-Cr alloys after exposure to in CH_4-H_2 at 1100 °C for 100 hr.

In Chapters 2 and 3, we successfully electrodeposited pure and CeO_2-dispersed Ni_3Al intermetallic coatings on Fe-Ni-Cr tube alloys. This chapter deals mainly with the cyclic carburization behaviors of these electrodeposited Ni_3Al-based coatings in 2%CH_4-H_2 reducing atmospheres at 850 °C and 1050 °C. Due to a lack of detailed studies on the carburization behaviors of Ni_3Al alloys and coatings, the current investigation focused on the carburization mechanisms and the microstructure changes of Ni_3Al base coatings, as well as on the role of CeO_2 particles in coatings when exposed to the reducing carbon environments.

6.2 Experimental Procedures

6.2.1 Sample Preparation

Ni-Al-based composite coatings were electroplated onto the Fe-Ni-Cr coupons with dimensions of 20 mm×10 mm×2 mm from a Watt's nickel bath containing Al particles or both Al particles and CeO_2 particles via sediment co-deposition (details of the coating process can be found in Chapters 2 and 3). The centrifugally-cast HP alloy contained 0.4wt% C, 35wt% Ni, 25wt% Cr, <1.5wt% Si, <1.5wt% Mn, <1.5wt% Nb, and the balance Fe. The Al powder had an average size of 3 μm. Two types of CeO_2 particles, 5 μm and 9-15 nm, were chosen. The following coatings were deposited on the Fe-Ni-Cr coupons and tested: pure Ni-Al coating, 80+0; two Ni-Al-5 μm CeO_2 coatings, 80+1 (5 μm) and 80+5 (5 μm); and two Ni-Al-9-15 nm CeO_2 coatings, 80+1 (9-15 nm) and 80+5 (9-15 nm). The thickness of all the coatings was controlled to be around 150 μm. Prior to

carburization testing, all the as-plated samples were annealed at 800 °C for 3 hr in a vacuum furnace pumped down to about 0.8 mtorr to achieve a uniform single-phase γ'-Ni_3Al in the coating. The compositions and phase characteristics of these five coatings after annealing are summarized in Table 6-1.

Table 6-1. Ni_3Al base coatings used in the investigation.

Sample code	Deposition condition	Al content (vol%)	Phases by XRD
80+0	0 g/l CeO_2	33.50±0.64	Ni_3Al (s)
80+1 (5 μm)	1 g/l CeO_2 (5 μm)	30.58±0.52	Ni_3Al (s); CeO_2 (vw)
80+5 (5 μm)	5 g/l CeO_2 (5 μm)	31.03±0.40	Ni_3Al (s); CeO_2 (w)
80+1 (9-15 nm)	1 g/l CeO_2 (9-15 nm)	30.98±0.60	Ni_3Al (s)
80+5 (9-15 nm)	5 g/l CeO_2 (9-15 nm)	29.83±1.81	Ni_3Al (s)

s: strong; w: weak; vw: very weak

6.2.2 Cyclic-carburization Test

The cyclic-carburization test was performed in a tube furnace. Uncoated Fe-Ni-Cr alloy coupons were used as a reference. Before the test, all the coupons were polished with 600-grit SiC grinding paper, cleaned using acetone, and then air-dried. Test coupons were held in high-purity (99.8%) alumina boats with one coupon per boat (Vesuvius McDanel, PA, USA). 2%CH_4-H_2 was used to simulate the reducing carburizing atmosphere, and its carbon activity and oxygen partial pressure could be obtained by [2, 6]:

$$CH_4 = 2H_2 + C \tag{6-1}$$

$$a_c = K\ \frac{p_{CH_4}}{(p_{H_2})^2}, \log K = \frac{4791}{T} - 5.789 \tag{6-2}$$

$$H_2O = H_2 + \frac{1}{2}O_2 \tag{6-3}$$

$$p_{O_2} = K'\left(\frac{p_{H_2O}}{p_{H_2}}\right)^2 \tag{6-4}$$

where a_c is the carbon activity; K and K' are the reaction constant; and T is the absolute reaction temperature.

The 2%CH_4-H_2 gas mixture, dried with phosphorus pentoxide, was flowed through the tube at a fixed rate of 60ml/min. The test cycle consisted of heating at 5 °C/min, holding at the specific test temperature for the required time, and cooling at 1.5 °C/min. After each cycle, the boats were removed from the furnace for mass-gain measurement. Each coupon was weighed together with the boat and any spalled products from the coupon. Because each coated coupon had four edge surfaces uncoated, a correction was made to the measured weight gains on the assumption that the uncoated surfaces would have the same mass change per unit area as the coupon of bare HP alloy. After measurement, sample boats were returned to the furnace for this next run cycle. In this study, carburization temperatures of 850 °C and 1050 °C were chosen. The corresponding carbon activity of 2%CH_4-H_2 at the two temperatures is about 0.73 and 3.21 respectively.

6.2.3 Materials Characterization

The microstructures and the morphologies of carburized samples were examined using a S-2700 Scanning Electron Microscope (SEM) with an Energy-Dispersive X-Ray Spectrometer (EDS) attachment. The carburization products were analyzed using a Rigaku Geigerflex 2173 X-ray diffractometer (XRD) with Co K_α incident radiation generated at 40kV and 30mA. A 2θ range of 2 to 120 degrees was adopted for collection of X-rays.

6.3 Results

6.3.1 Carburization Kinetics

Figs. 6-1 (a) and (b) show the mass changes of the uncoated Fe-Ni-Cr alloy and the Ni_3Al base coatings after carburization for periods of up to 500hr at 850 °C and 1050 °C respectively.

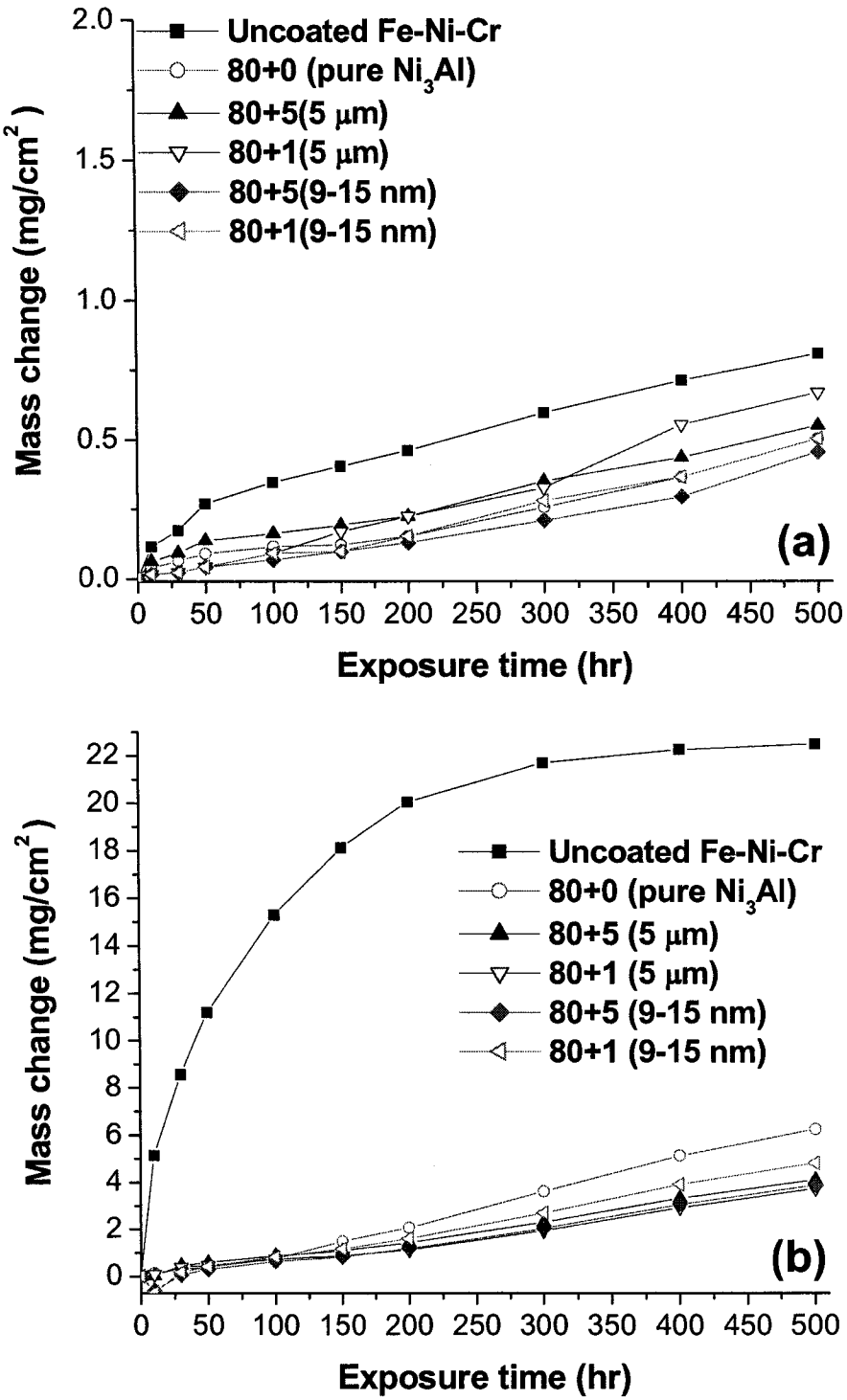

Figure 6-1. The cyclic-carburization results of the Fe-Ni-Cr alloy and the Ni-Al-based coatings for periods up to 500 hr: (a) at 850 °C; (b) at 1050 °C.

All the samples showed very low mass changes at 850 °C (Fig. 6-1(a). The Fe-Ni-Cr alloy had the highest mass change during carburization. The mass change after 500hr was more than 0.8mg/cm^2. For all the coatings, the mass increase was below 0.5mg/cm^2 after 500hr except that for the 80+1 (5μm) coating, which had a mass gain of 0.66mg/cm^2. At 1050 °C, the cyclic-carburization result of the uncoated Fe-Ni-Cr alloy was clearly distinct from those of Ni_3Al base coatings (Fig. 6-1 (b)). The uncoated base alloy suffered severe attack by the carbon, and showed the highest mass increase: more than 22 mg/cm^2 after 500 hr. Its mass-change curve quickly leveled off after about 300 hr, which, as will discussed later, might be due to the saturation of carbon in the alloy. All the coating coupons, however, showed much lower mass increases. The pure Ni_3Al coating showed higher mass gain than the four CeO_2-dispersed Ni_3Al coatings (Fig. 6-1 (b)). In contrast, the difference in mass changes among the four CeO_2-dispersed Ni_3Al coatings was minor. It should be noted that the mass gain of all the coated samples, calculated on the basis of the measured mass increase subtracting the mass gains of four side surfaces of coated specimen, can be overestimated. This is due to the fact that the four side surfaces of the coated samples may experience carburization at a higher rate than the uncoated Fe-Ni-Cr coupon in the latter stage of carburization because of the saturation of carbon in the uncoated alloy coupon.

6.3.2 Morphologies of The Uncoated Fe-Ni-Cr Alloy

Figs. 6-2 (a) and (b) show the cross-sections of the uncoated Fe-Ni-Cr alloys after cyclic carburization for 500 hr at 850 °C and 1050 °C respectively. The ingress of carbon to the uncoated Fe-Ni-Cr alloy was relatively slow at 850 °C (Fig. 6-2 (a)). A zone of precipitated carbides at the surface is narrow even after 500hr, and the other region of the alloy is free of secondary carbides except the primary carbides at the grain boundaries. This observation is consistent with the low mass change shown in Fig. 6-1 (a). The carburization zone in the Fe-Ni-Cr alloy generally consisted of the outer Cr_7C_3 and the inner $Cr_{23}C_6$ (Table 6-2), which is consistent with other investigations [1, 5, 22]. In contrast, carburization was much more rapid at 1050 °C. As shown in Fig. 6-2 (b), the 2 mm thick Fe-Ni-Cr coupon had been completely carburized after 500 hr. The XRD results listed in Table 6-3 clearly showed the predominant Cr_7C_3 phase and the graphite

after exposure for as short as 10 hr. This observation, plus the rapid decrease of the mass-increase rate for the uncoated Fe-Ni-Cr alloy after 300 hr (Fig. 6-1 (b)), suggests that the alloy matrix might have been saturated with carbon before 500 hr exposure.

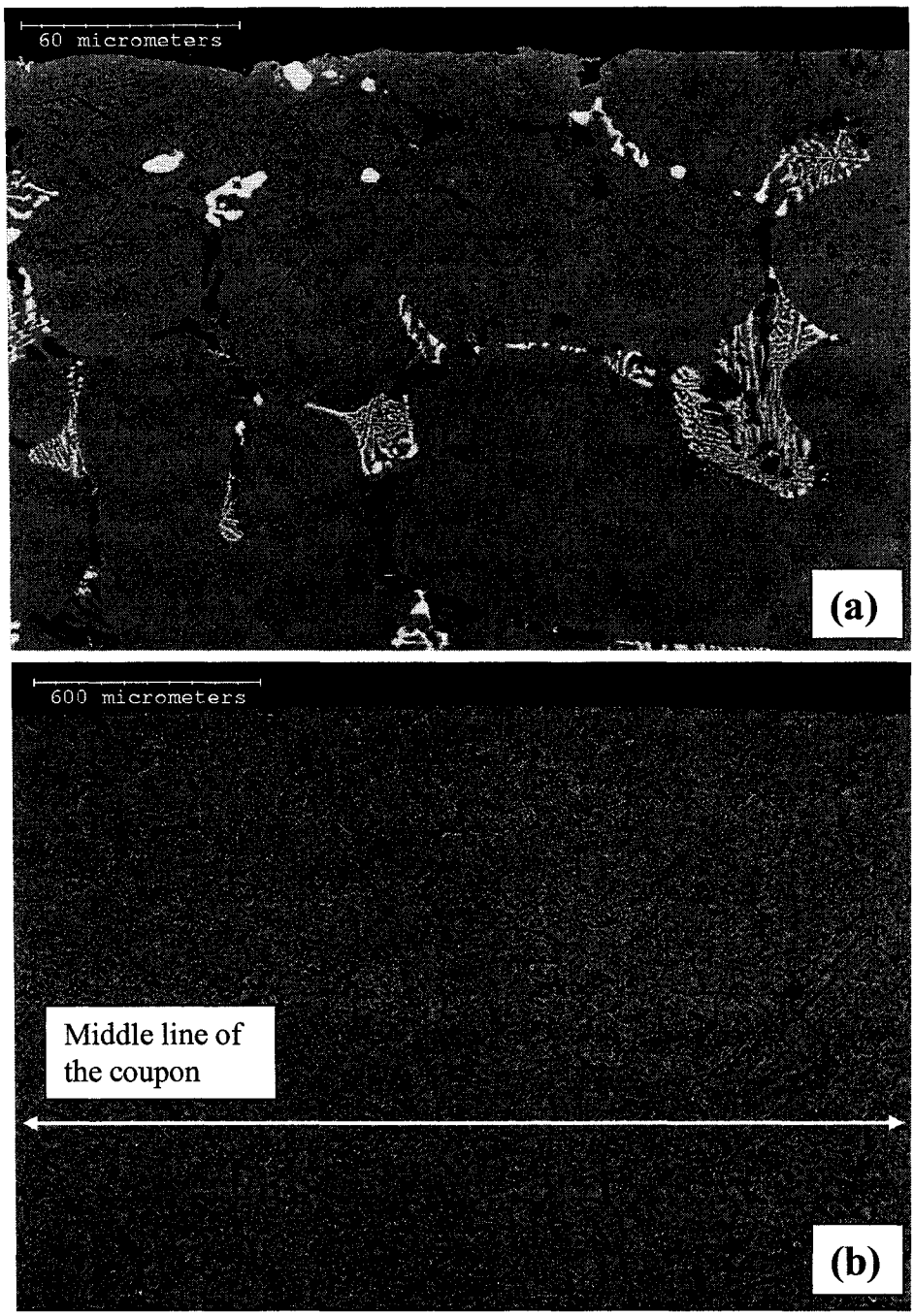

Figure 6-2. The cross-sectional morphology of the uncoated Fe-Ni-Cr alloy after carburization for 500 hr: (a) at 850 °C; (b) at 1050 °C.

Table 6-2. The XRD analysis of the carburization products at 850 °C.

Sample	10 hr	100 hr	500 hr
Fe-Ni-Cr	$Cr_{23}C_6$ (m), Cr_7C_3 (m)	Cr_7C_3 (m)	Cr_7C_3 (s)
80+0			γ-Al_2O_3 (w)
80+5 (5 μm)			γ-Al_2O_3 (w)
80+1 (5 μm)			γ-Al_2O_3 (w)
80+5 (9-15 nm)			γ-Al_2O_3 (w)
80+1 (9-15 nm)			γ-Al_2O_3 (w)

s: strong; m: medium; w: weak; vw: very weak.

Table 6-3. The XRD analysis of the carburization products at 1050 °C.

Sample	10 hr	100 hr	500 hr
Fe-Ni-Cr	Cr_7C_3 (s), C (m), NbC (w)	C (s), Cr_7C_3 (m), NbC (w)	C (s), $(Fe,Cr)_7C_3$ (m), NbC (w)
80+0	α-Al_2O_3 (w)	α-Al_2O_3 (w), C (vw)	α-Al_2O_3 (w), C (vw)
80+5 (5 μm)	α-Al_2O_3 (w), $CeAlO_3$ (w)	α-Al_2O_3 (w), $CeAlO_3$ (w), C (vw)	α-Al_2O_3 (w), $CeAlO_3$ (w), C (vw)
80+1 (5 μm)	α-Al_2O_3 (w), $CeAlO_3$ (w)	α-Al_2O_3 (w), $CeAlO_3$ (vw), C (vw)	α-Al_2O_3 (w), $CeAlO_3$ (vw), C (vw)
80+5 (9-15 nm)	α-Al_2O_3 (w), $CeAlO_3$ (vw)	α-Al_2O_3 (w), $CeAlO_3$ (vw), C (vw)	α-Al_2O_3 (w), $CeAlO_3$ (vw), C (vw)
80+1 (9-15 nm)	α-Al_2O_3 (w), $CeAlO_3$ (vw)	α-Al_2O_3 (w), $CeAlO_3$ (vw), C (vw)	α-Al_2O_3 (w), $CeAlO_3$ (vw), C (vw)

C detected in all samples is identified to be graphite.

s: strong; m: medium; w: weak; vw: very weak.

6.3.3 Morphologies of The Pure Ni_3Al Coating

(a) At 850 °C

Figs. 6-3 (a) and (b) depict the surface morphologies of the pure Ni_3Al coating after 10hr and 500hr exposure respectively.

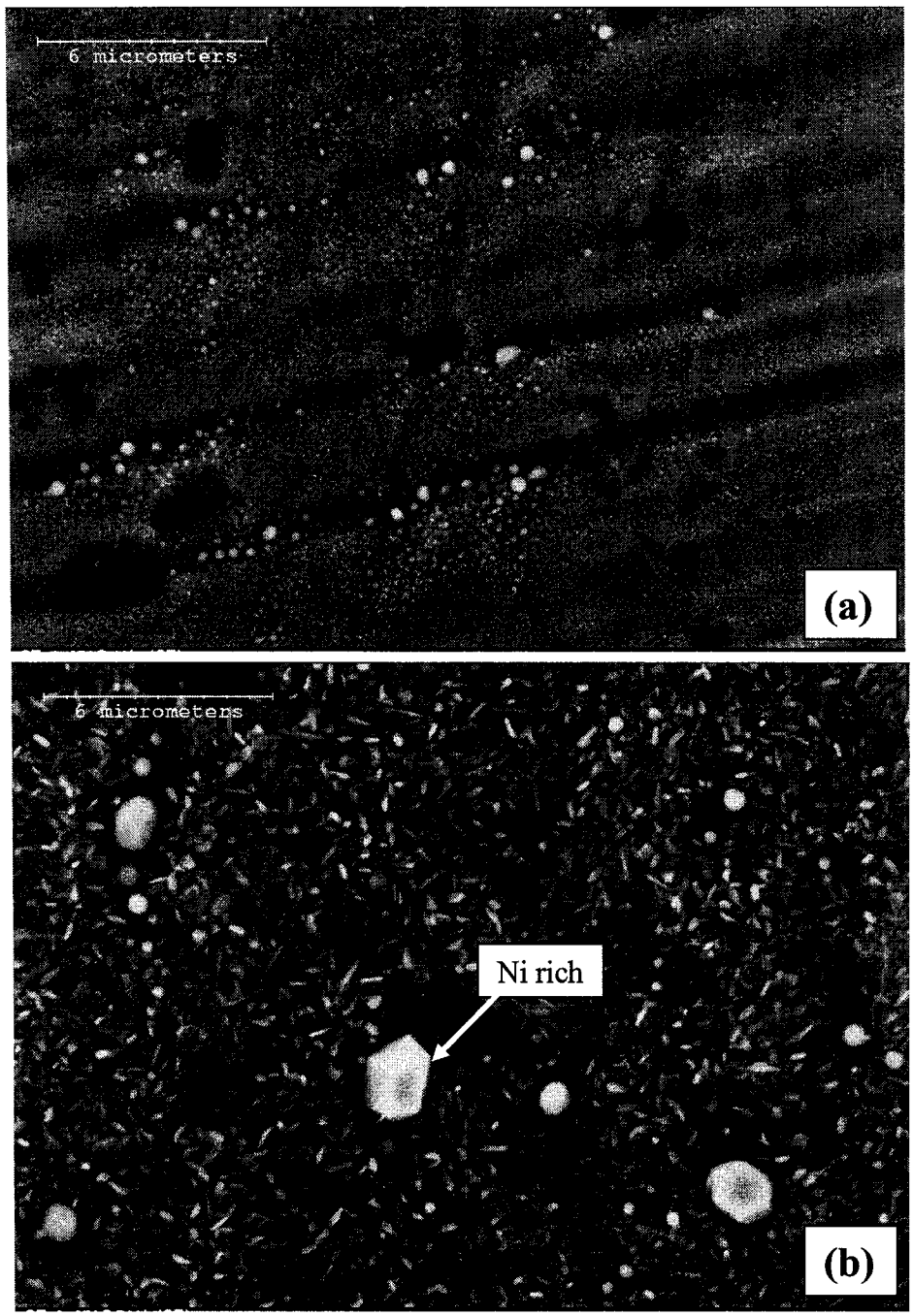

Figure 6-3. The surface morphology of the pure Ni_3Al coating after carburization at 850 °C for: (a) 10 hr; (b) 500 hr.

Fig. 6-3 (a) shows the coating surface after carburization for 10hr. Many small particles are visible on the surface. EDS analysis indicated that the surface was rich in Ni, Al and O. After 500 hr, the platelet Al-rich oxides dominated the coating surface. According to XRD analysis (Table 6-2), this oxide scale was γ-Al_2O_3, a transition alumina before the formation of thermodynamically stable α-Al_2O_3. It forms favorably at temperatures below 900 °C, and is featured with a blade- or plate-like shape due to the dominant outward diffusion of Al cations through the oxide scale [23-25]. It can be also seen in Table 6-2 that no other oxides or carbides were detected on the pure Ni_3Al coating, except for several big Ni-rich particles (Fig. 6-3 (b)).

The cross-section of the pure-Ni_3Al coated coupon after carburization at 850 °C for 500 hr is shown in Figs. 6-4 (a) and (c). It is seen in Fig. 6-4 (a) that the coating is characterized by a dual-layer structure consisting of a porous layer on top and a dense layer above the coating/substrate interface (Fig. 6-4 (a)). This structure was also observed in the CeO_2-dispersed Ni_3Al. After initial annealing treatment, all Ni_3Al coatings contained high-density homogenously distributed micro-pores. These pores could be healed by interdiffusion (the Kirkendall effect) during high-temperature exposure, which has been described in Chapter 4. No carbon attack in the form of carbide formation in the Fe-Ni-Cr substrate occurred (Fig. 6-4 (b)). Fig. 6-4 (c) shows that a thin γ-Al_2O_3 scale, indicated by the white arrow, was formed on the pure Ni_3Al coating after 500 hr.

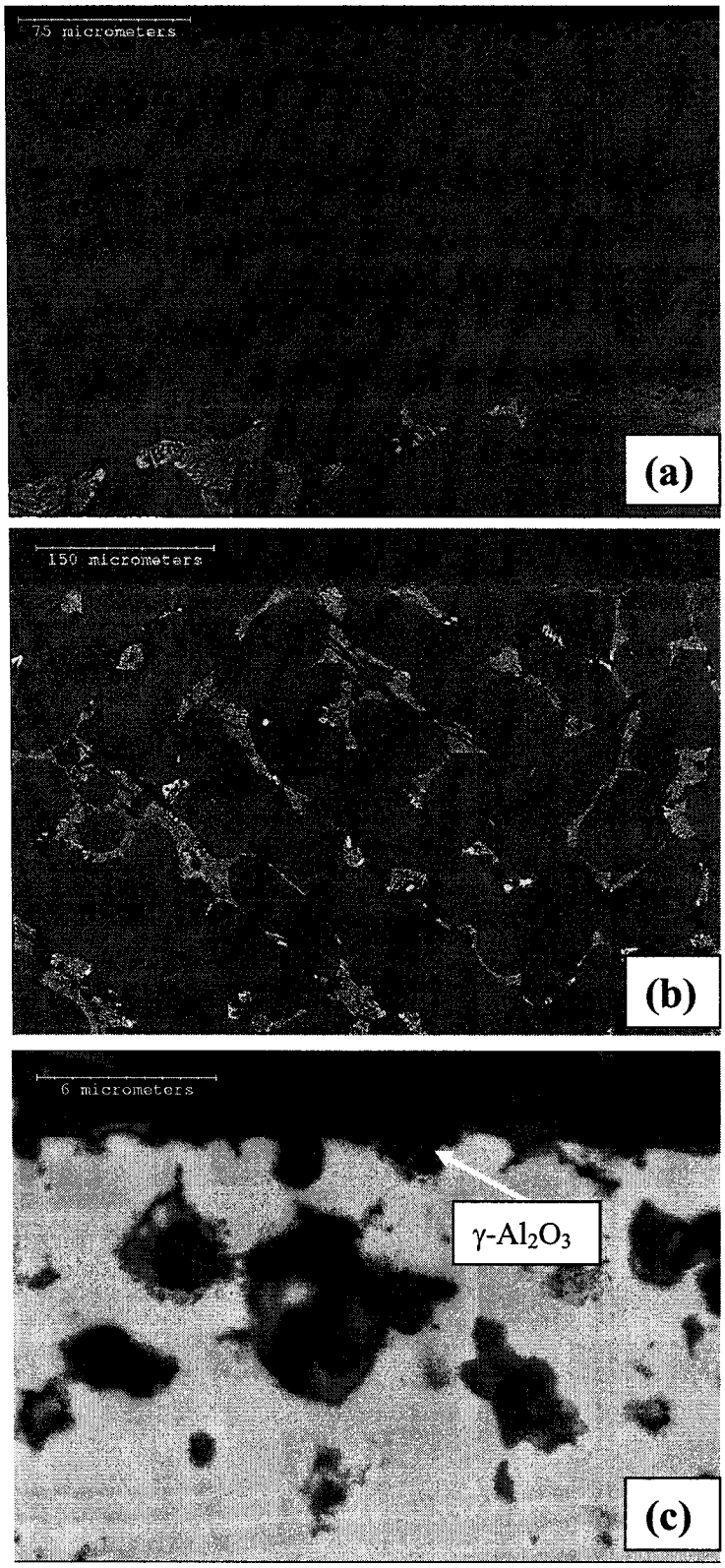

Figure 6-4. The cross-sectional morphology of the pure Ni_3Al coating after carburization at 850 °C for 500 hr: (a) the coating section; (b) the coating/substrate; interface; (c) the Al_2O_3 scale.

(b) At 1050 °C

The surface morphologies of the pure Ni_3Al coating after carburization at 1050 °C for 10 hr and 100 hr are presented in Fig. 6-5 (a) and Fig. 6-5 (b) respectively.

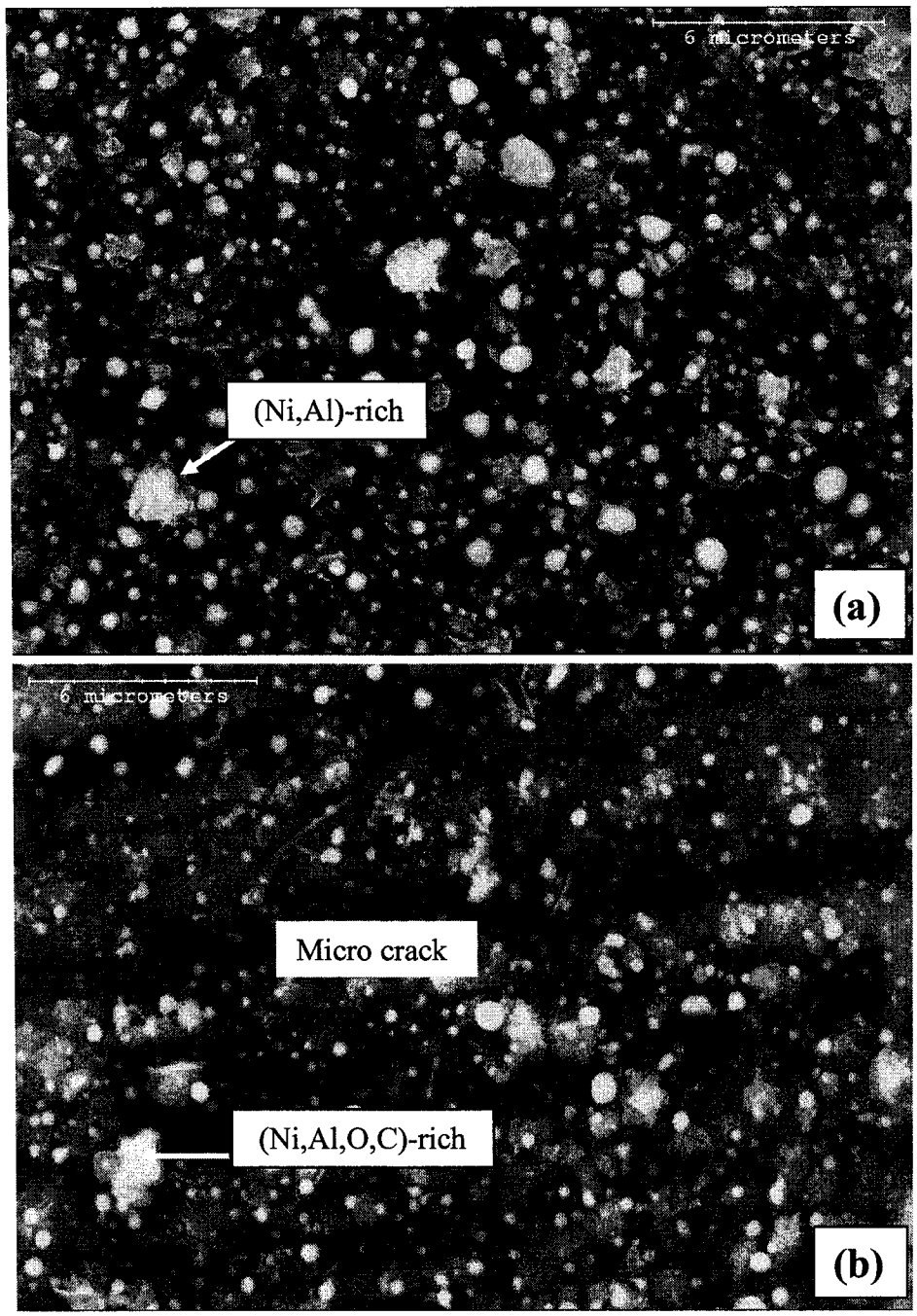

Figure 6-5. The surface morphologies of the pure Ni_3Al coating after carburization at 1050 °C for: (a) 10 hr; (b) 100 hr.

The coating surface after 10 hr featured the dominant Al-rich oxides and many fine particles containing mainly Ni, Al, and/or O (Fig. 6-5 (a)). Based on the XRD analysis in Table 6-3, the Al-rich oxides were identified to be α-Al_2O_3. The coating surface after 100 hr on which micro cracks were constantly observed is shown in Fig. 6-5 (b). This observation indicates the failure of Al_2O_3 scale. After 100 hr exposure, the nickel-rich particles found earlier remained on the pure Ni_3Al coating. However, their compositions appear more complicated: additional elements such as Al, O, C, as well as small amounts of substrate constituents such as Fe, Cr, Si and Mn, were also detected. The carbon proved to be graphite (Table 6-3). Carbon deposition on the surface increased at 500 hr exposure (Fig. 6-6 (a)). Noteworthy carbon filaments on the surface and carbon aggregates located at those nickel-rich crystals have also been found (Fig. 6-6 (b)). It is obvious that coke had formed on the pure Ni_3Al coating.

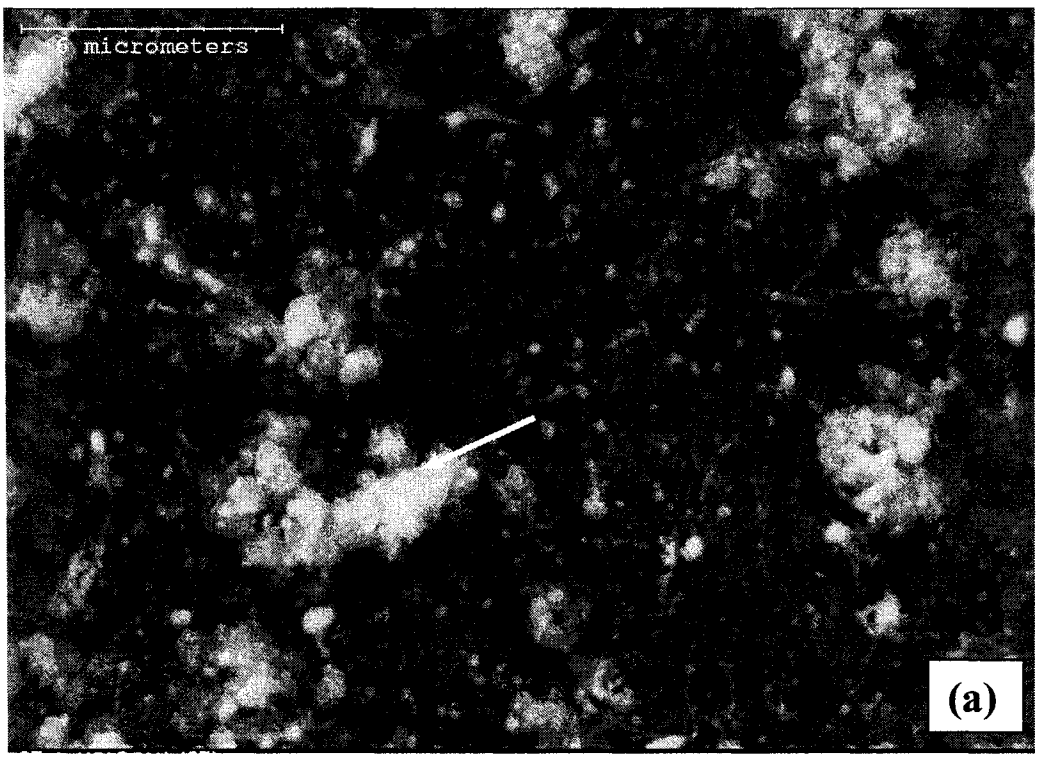

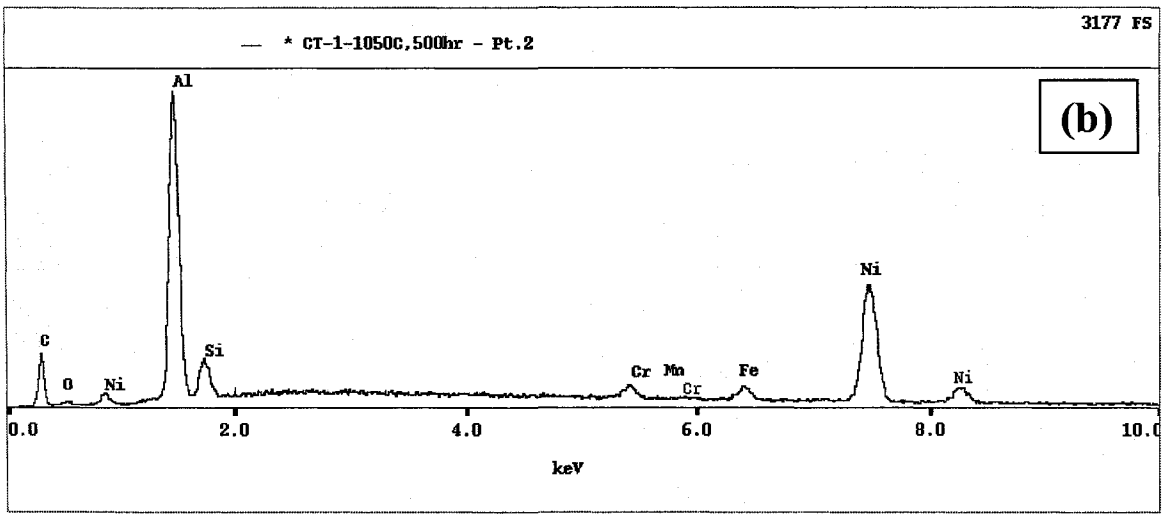

Figure 6-6. The surface morphology of the pure Ni_3Al coating after carburization at 1050 °C for 500 hr: (a) the plain view; (b) EDS analysis of the phase indicated by the arrow in (a).

Figs. 6-7 show the cross-sections of the pure Ni_3Al coating after 500 hr.

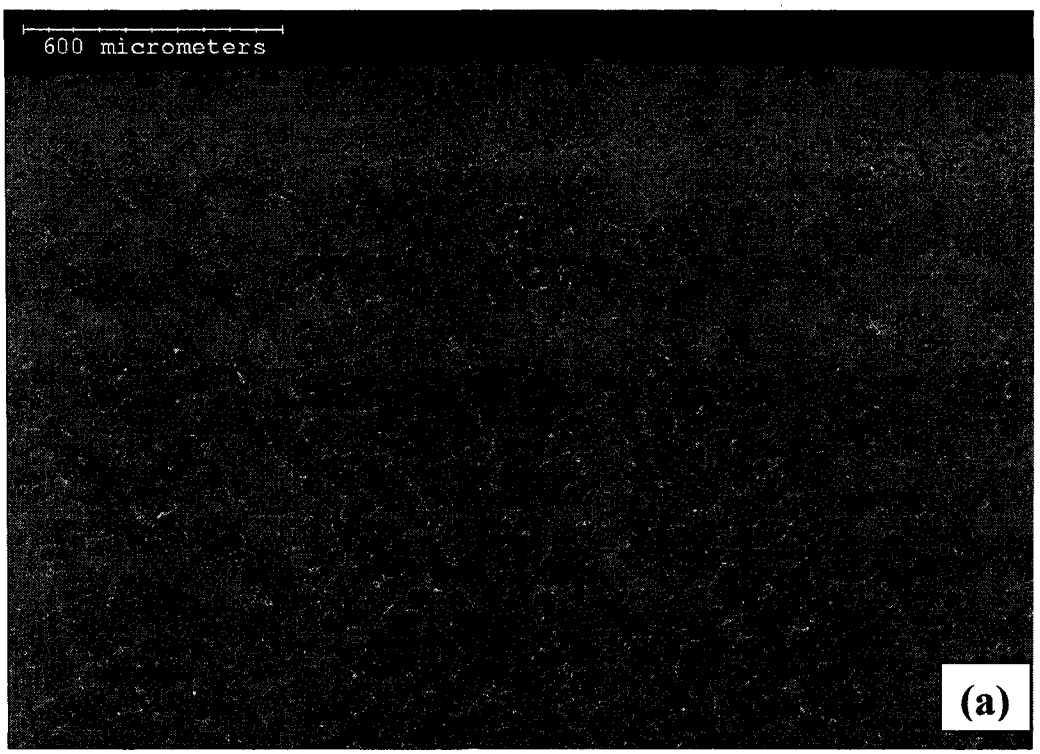

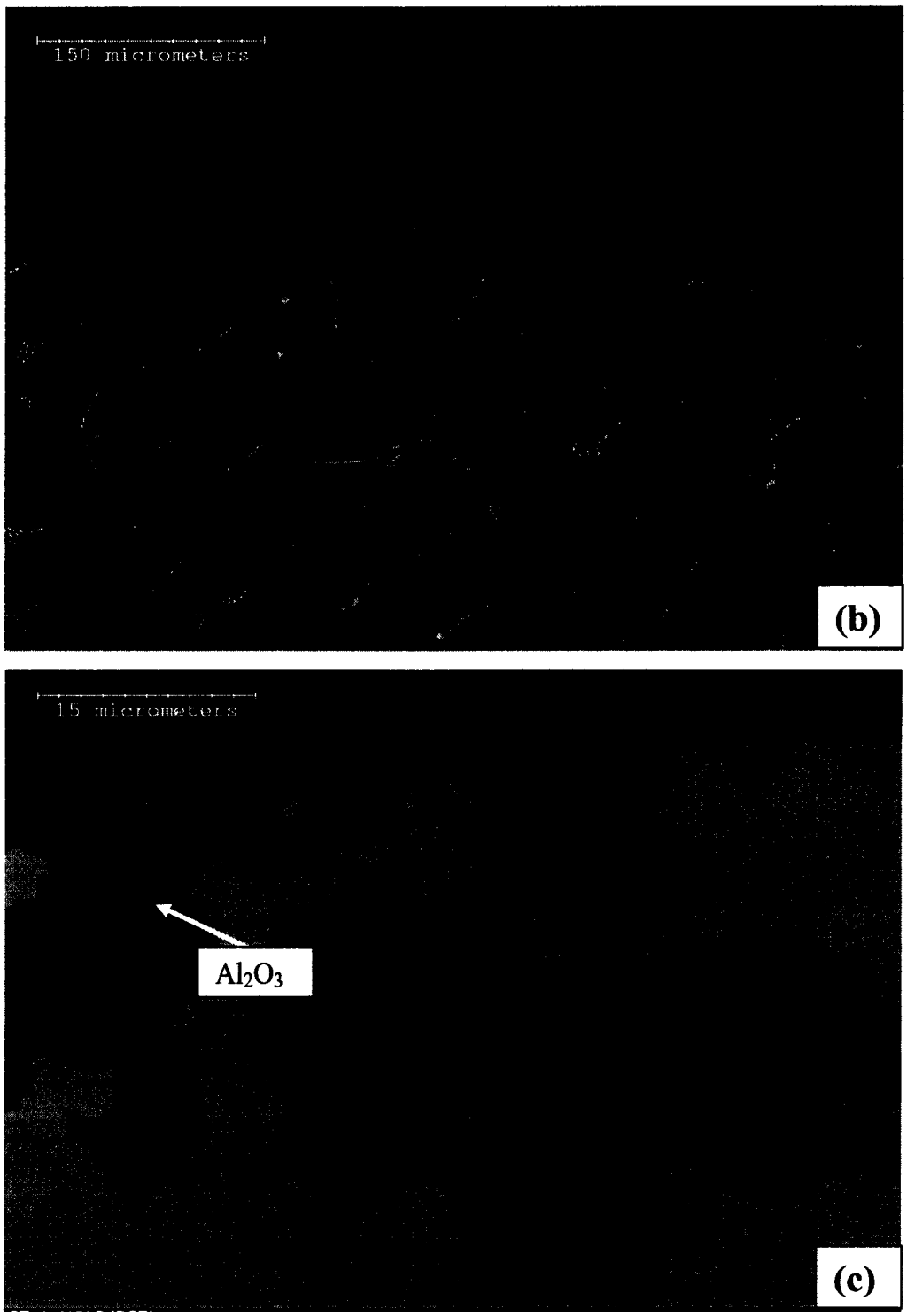

Figure 6-7. The cross section of the pure Ni_3Al coating after carburization at 1050 °C for 500 hr: (a) a low-magnification view; (b) the coating/substrate interface; (c) the severe oxidation zone.

From Figs. 6-7 (a) and (b), the coated Fe-Ni-Cr substrate was invulnerable to carburization. The XRD data in Table 6-3 and the micrograph shown in Fig. 6-7 (c) suggest that a thin α-Al_2O_3 scale had been developed on the pure Ni_3Al coating. The coating cross-section is also characterized by many dark protrusions that originated from the surface (Figs. 6-7 (a) and (c). The EDS analysis showed that the protrusions were exclusively Al_2O_3, indicating severe internal oxidation beneath the alumina scale. The internal oxidation could occur through micro-cracks in the Al_2O_3 scale (Fig. 6-5 (a)).

6.3.4 Morphologies of The CeO_2-dispersed Ni_3Al Coatings

(a) At 850 °C

The surface and the cross-sectional morphologies of the four CeO_2-dispersed Ni_3Al coatings during carburization at 850 °C were generally similar to those of the pure Ni_3Al coating. No carburization was found in the coated Fe-Ni-Cr substrates. Figs. 6-8 (a) and (b) show typical morphologies of the 80+1 (5μm) coating after 500 hr.

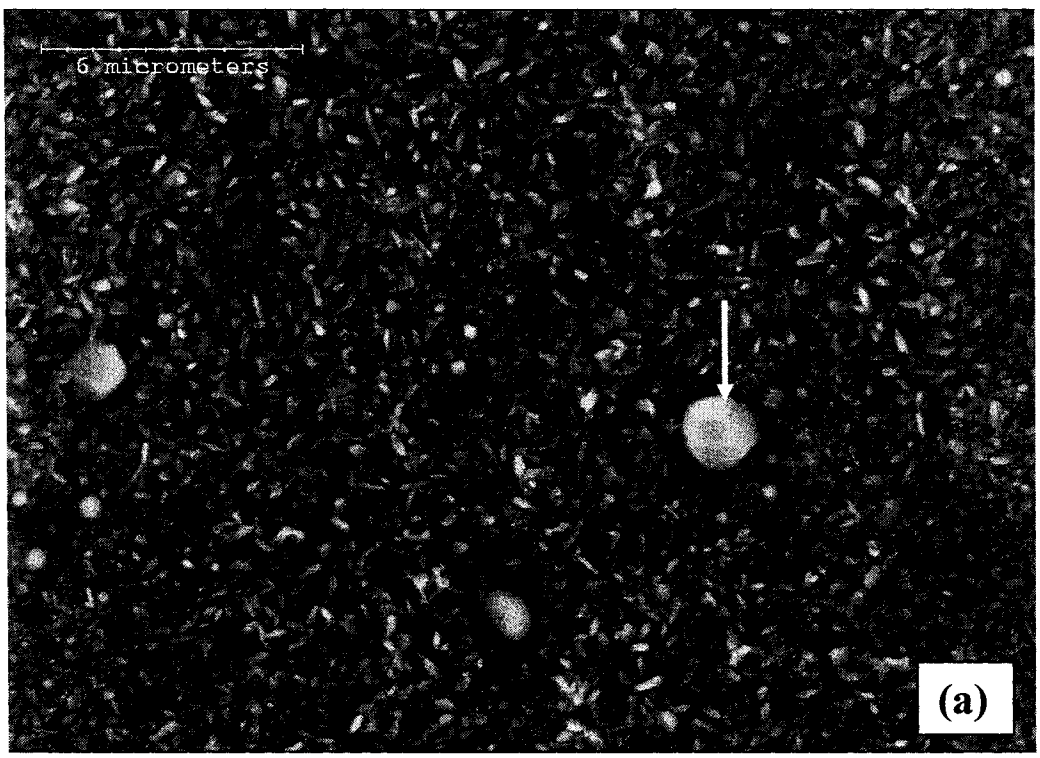

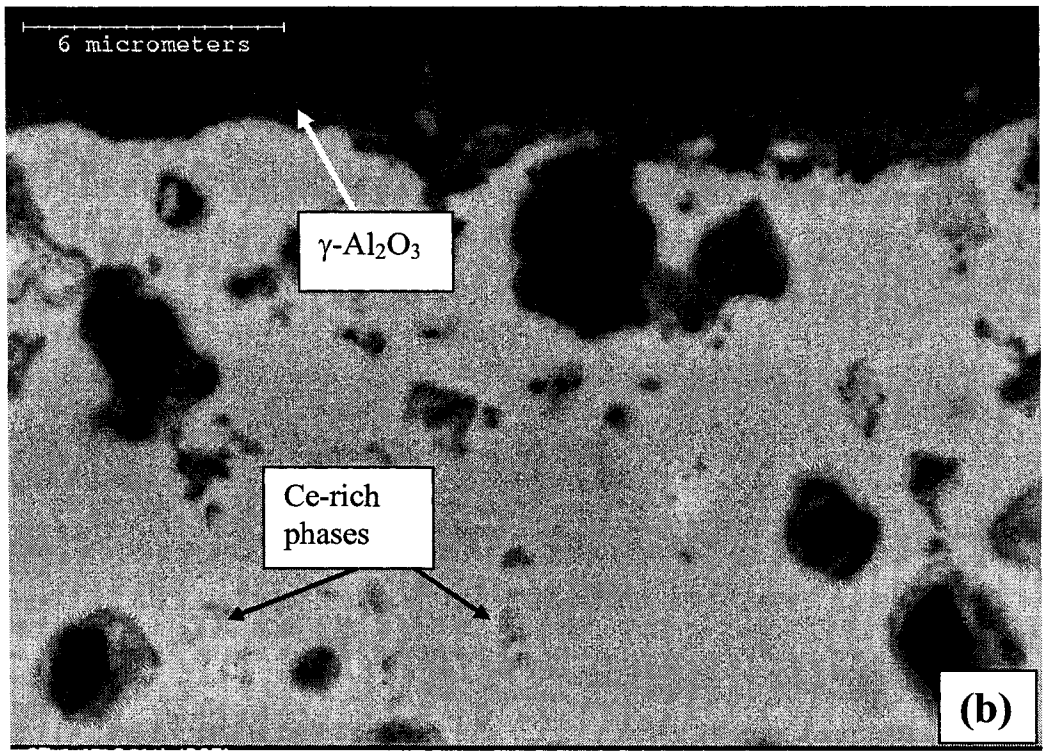

Figure 6-8. The typical morphology of the 80+1 (5 mm) coating after carburization at 850 °C for 500 hr: (a) the plain view; (b) the cross sectional view.

According to Fig. 6-8 (a) and Table 6-2, the surface oxides on the 80+1 (5 μm) coating were dominantly plate-like γ-Al_2O_3. Some Ni-rich crystals (arrow) were also found in Fig. 6-8 (a). The γ-Al_2O_3 scale was seen to be dense and thin from Fig. 6-8 (b), and some Ce-rich oxide phases were also observed in the coating.

(b) At 1050 °C

All the CeO_2-dispersed Ni_3Al coatings were able to block carbon ingress at 1050 °C for periods of up to at least 500 hr. Surface examination didn't reveal any micro-cracks on CeO_2-dispersed Ni_3Al coatings during carburization. This suggests that α-Al_2O_3 scale on the CeO_2-dispersed Ni_3Al coatings had much better mechanical integrity than that on the pure Ni_3Al coating during cyclic testing. Fig. 6-9 shows the surface morphologies of the 80+1 (5 μm) coating after cyclic carburization, which differ little from those of the pure Ni_3Al coating. Many Ni-rich particles were found on the α-Al_2O_3 scale on the 80+1 (5 μm) coating after 10 hr at 1050 °C (Fig. 6-9 (a)). Similar to the pure

Ni_3Al coating, filamentous coke containing various elements was observed on the surface of the 80+1 (5 μm) coating after 100 hr and 500 hr (Figs. 6-9 (b) and (c) respectively). $CeAlO_3$ phases were formed in all CeO_2-dispersed coatings (Table 6-3).

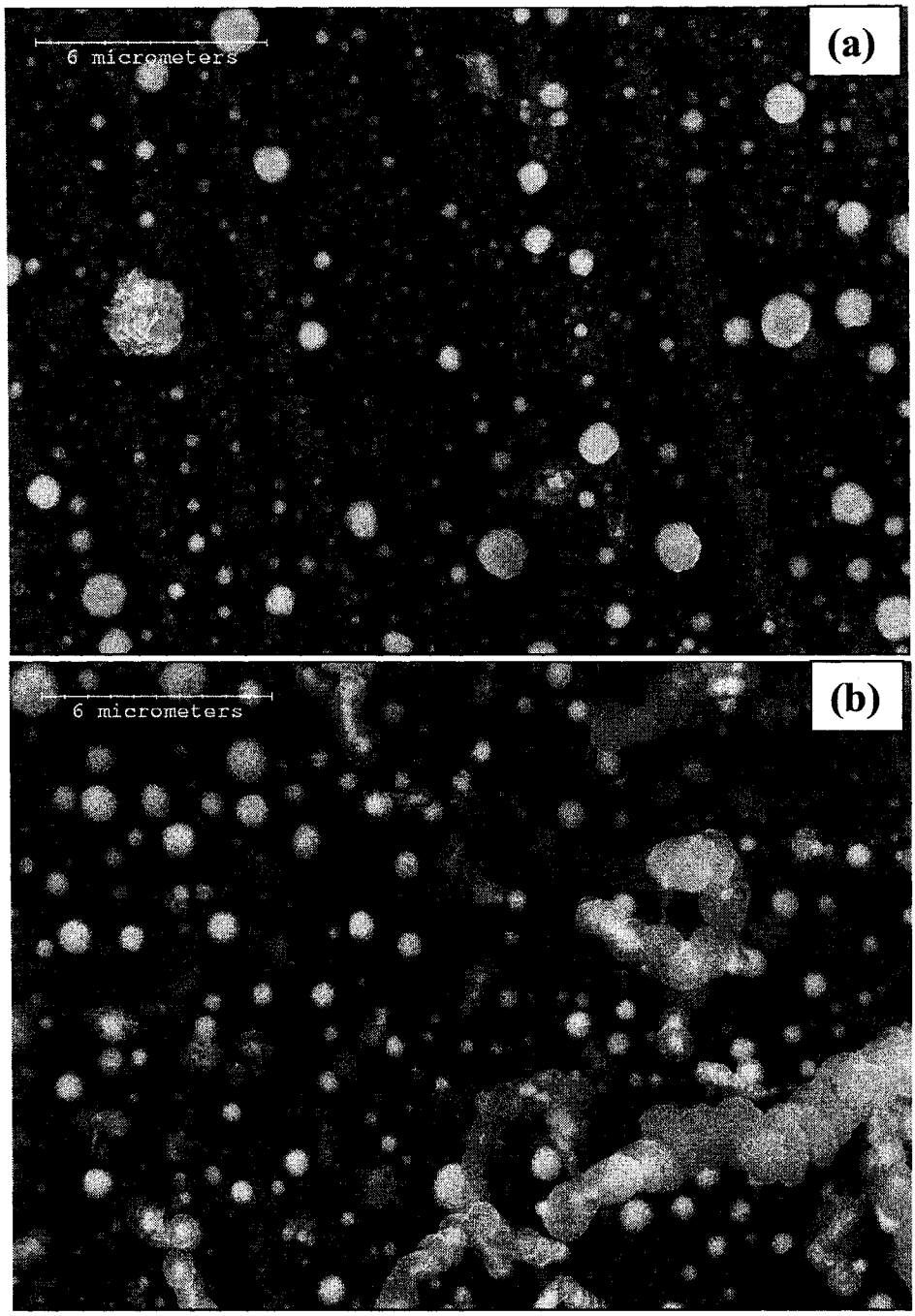

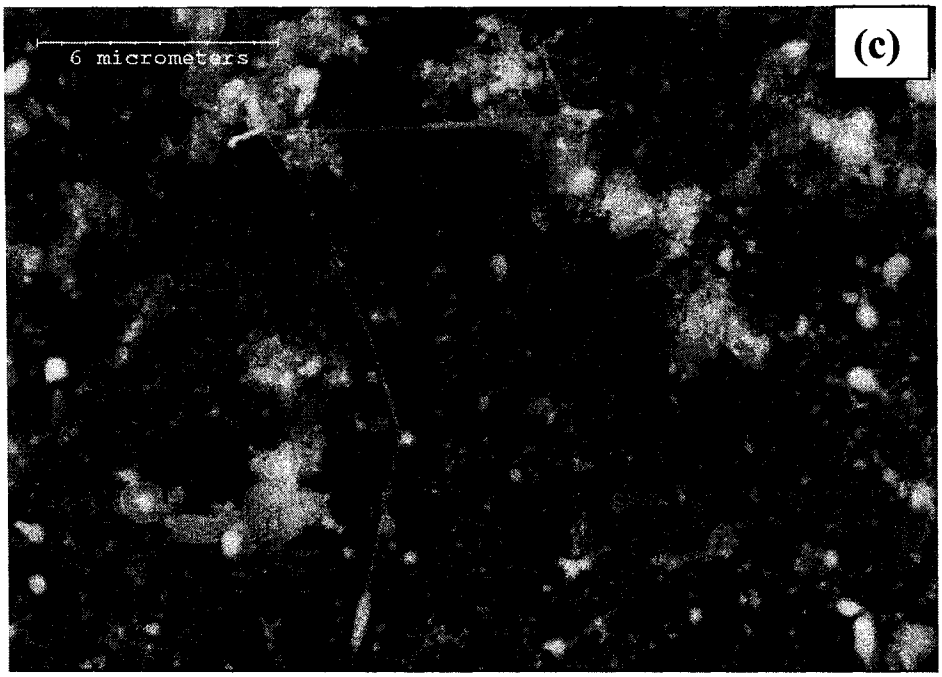

Figure 6-9. The surface morphology of the 80+1 (5 μm) coating after carburization at 1050 °C for: (a) 10 hr; (b) 100 hr; (c) 500 hr.

A typical cross-section of the 80+1 (5 μm) coating after 500 hr is shown in Fig. 6-10. Pores in the coating produced during annealing treatment had been healed completely (Fig. 6-10 (a)). A thin oxide layer, which was α-Al_2O_3 according to the XRD analysis in Table 6-3, adhered to the coating matrix (Fig. 6-10 (b)). No internal oxidation was observed on the 80+1 (5 μm) coating or other CeO_2-dispersed coatings.

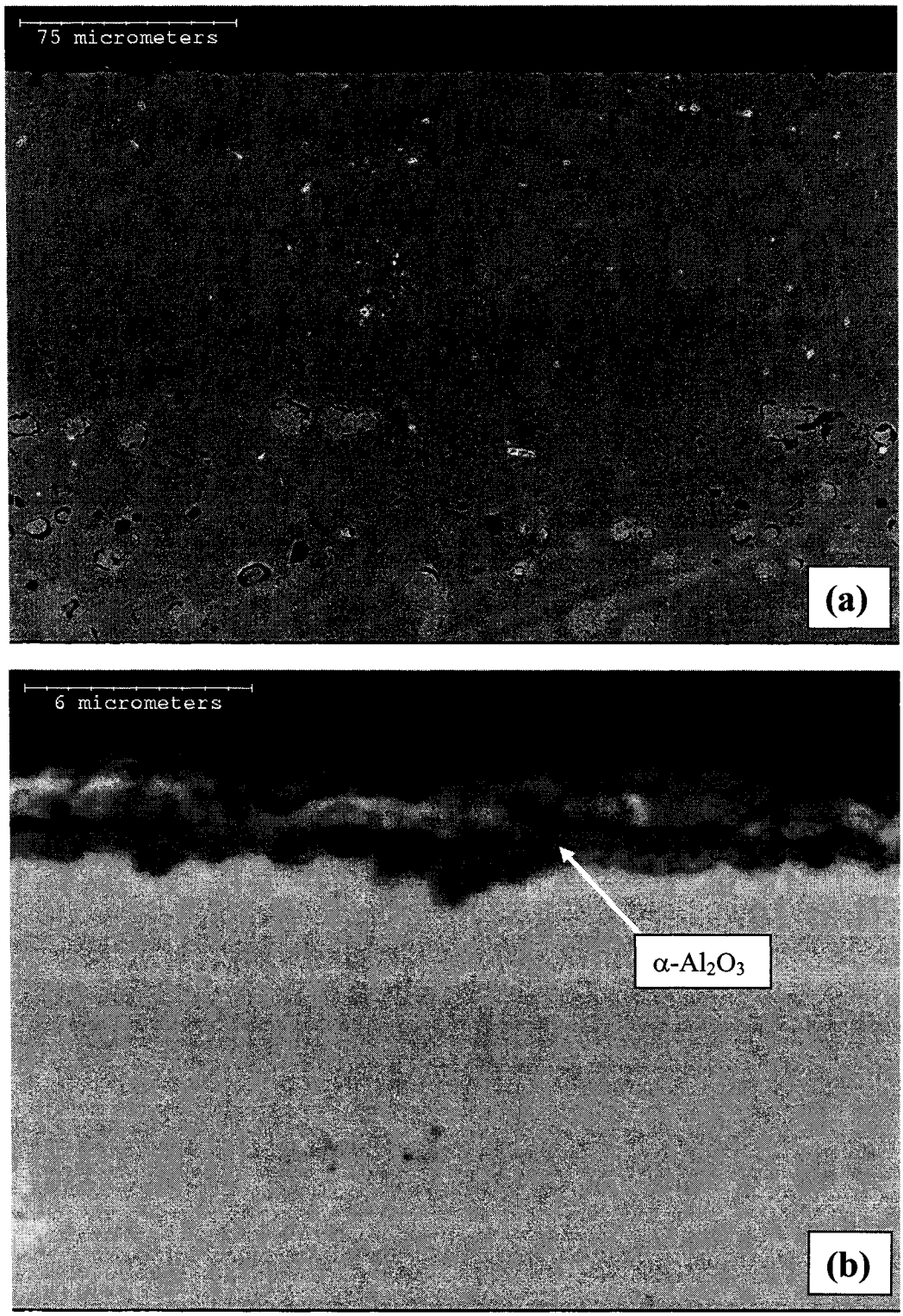

Figure 6-10. The cross-section of the 80+1 (5 μm) coating after carburization at 1050 °C for 500 hr: (a) a low-magnification view; (b) a high-magnification view.

6.4 Discussion

6.4.1 Carburization in 2%CH_4-H_2

The CH_4-H_2 gas mixture is often employed to simulate reducing carburization under extremely low oxygen partial pressures. Carburization resistance of the alloys in the oxygen-deficient CH_4-H_2 depends strongly on the ability to form a protective scale. If formation of oxide scale is impossible, carburization of Fe-based or Ni-based alloys is controlled by the direct inward diffusion of carbon, and excessive precipitation of carbides can occur in the alloys [1-6]. However, if the alloy establishes a protective scale, carburization will be controlled by the transportation of carbon through the oxide scale. As the solubility of carbon in oxides such as Cr_2O_3, Al_2O_3 and SiO_2 is negligible [1, 4], the ingress of carbon can be completely blocked if a highly dense and compact scale is present. It has been reported that carbon accumulation in the scale is expected only in a range of 100 to 1000 ppm after many years of exposure [2].

The development of oxide scale on the alloys in highly reducing environments is directly associated with the dissociation pressure of the oxide. Table 6-4 provides the calculated dissociation pressure of Cr_2O_3 and Al_2O_3 at different temperatures by using thermodynamic data from the literature [26].

Table 6-4. The dissociation pressures of Cr_2O_3 and Al_2O_3.

Temperature (°C)	The dissociation pressure of Cr_2O_3, (atm)	The dissociation pressure of Al_2O_3, (atm)
850	1.5×10^{-26}	1.1×10^{-41}
1050	2.4×10^{-21}	9.0×10^{-34}

From Table 6-4, it is obvious that Al_2O_3 will be much more stable than Cr_2O_3 in the reducing 2%CH_4-H_2 atmosphere. Yin [27, 28] reported that the commercial grade 2% CH_4-H_2 gas inevitably contained some oxygen impurities of less than 100 ppm, such as

in the form of moisture. This was equivalent to an oxygen partial pressure of about 10^{-26}-10^{-21} atm at temperatures ranging from 800 to 1100 °C. Yin [27] also proposed that 1000 °C was a critical temperature, below which 2%CH_4-H_2 was a carburizing/oxidizing atmosphere for the Fe-Ni-Cr alloys and the formation of chromia scale could be possible. Above 1000 °C, the gas mixture became fully reducing for the Fe-Ni-Cr alloys. Consequently, 310SS alloys showed a low carburization rate at temperatures below 1000 °C due to the formation of Cr-rich oxides, but had no resistance to carburization above 1000 °C. The uncoated Fe-Ni-Cr alloys used in our study showed similar carburization behaviors. However, no Cr-rich oxides or other oxides were found on the uncoated Fe-Ni-Cr alloy samples during carburization at 850 °C (the results aren't presented). This could be due to the fact that the amount of oxide products was too low to be detected by EDS and XRD. More importantly, the 2%CH_4-H_2 gas used in this study was dried prior to flowing through the furnace. Consequently, the actual moisture level in the gas could be significantly lower than that necessary for the formation of Cr-rich oxides reported by Yin. Because our research focused on the carburization of Ni_3Al base coatings, a discussion of carburization behavior of Fe-Ni-Cr alloys is not included herein. Details concerning the carburization of Fe-Ni-Cr alloys in reducing carburizing environments have been well documented [13, 22, 27-31].

According to our experimental results, pure and CeO_2-dispersed Ni_3Al coatings exhibit excellent carburization resistance at 850 °C and 1050 °C. Unlike uncoated Fe-Ni-Cr alloys, all the Ni_3Al coatings developed a protective oxide scale, Al_2O_3, in the 2%CH_4-H_2 gas mixture at both temperatures. This indicates that the oxygen partial pressure used is favorable to the formation of Al_2O_3, which may be the main reason for the observation of superior carburization resistance of our Ni_3Al-based coatings. This also suggests that Al_2O_3-forming alloys such as nickel aluminides and iron aluminides are superior to the conventional Cr_2O_3-forming alloys in the reducing carburizing environments, especially at temperatures above 1000 °C.

The mass changes of Ni_3Al base coatings shown in Figs. 1 (a) and (b) result from a combination of coke formation, carburization and oxidation rather than carburization

alone. Carburization occurs by dissolution of carbon in the Ni_3Al matrix. It has been reported that the solubility of carbon in the stoichimetric Ni_3Al is about 6at% [32]. At 850°C, coke formation was prevented by a dense and compact γ-Al_2O_3 scale that developed on all coatings. Therefore, the mass increase must be caused mainly by the growth of γ-Al_2O_3, particularly in the last stage of carburization. At 1050 °C, coke formation contributes significantly to the increase of mass, particularly after Al_2O_3 scale is fully developed. For the pure Ni_3Al coating, internal oxidation and carburization due to the cracking of Al_2O_3 may add to mass gains.

6.4.2 Oxidation of Ni_3Al-Based Coatings in 2%CH_4-H_2

The oxidation behavior of Ni_3Al in the environments with a high oxygen partial pressure, such as air and pure oxygen, has been thoroughly investigated. Ni_3Al alloys or coatings are usually covered by multi-layer oxide scales, e.g., outer NiO/$NiAl_2O_4$/inner Al_2O_3 [33-35]. Similar behaviors were observed in our Ni_3Al-based coatings when they were oxidized in dry air at 850 °C and 1050 °C, as described in Chapter 4. However, in our oxygen-deficient 2%CH_4-H_2, all Ni_3Al coatings nonetheless suffered oxidation with γ-Al_2O_3 scale formed at 850 °C and α-Al_2O_3 scale at 1050 °C. Ni-rich metal particles and some (Ni, Al)-rich oxide particles were also observed on all the coatings at both the temperatures.

This oxidation behavior is consistent with the results reported by other researchers [36-38]. Schumann et al. [36] observed that only γ-Al_2O_3 formed on the single-crystal Ni_3Al in the initial stage of oxidation at 950 °C under $p_{O_2} = 4.0\times10^{-19}\,atm$. The outward diffusion of Ni through Al_2O_3 scale was also found. Yi et al. [37] performed the oxidation of Ni_3Al alloys at 800 °C for up to 25 hr in oxygen-deficient environments. Only Al_2O_3 was identified at $p_{O_2} = 1.2\times10^{-19}\,atm$. Recent work by Gao et al. [38] identified two different oxidation behaviors of Ni_3Al alloys within $10^{-15}\,atm \le p_{O_2} \le 10^{-22}\,atm$. At $10^{-15}\,atm \le p_{O_2} < 10^{-18}\,atm$, pure Ni particles were initially observed. Later, Al_2O_3 slowly formed. In contrast, only Al_2O_3 could be found at $p_{O_2} = 10^{-22}\,atm$.

As the oxygen partial pressure in 2%CH_4-H_2 is extremely low, it would appear that a selective oxidation of Ni in Ni_3Al is impossible and that only Al element can be oxidized. According to Wagner's internal-oxidation theory [39], the critical concentration of Al required to form external Al_2O_3 scale depends on oxygen partial pressure. Consequently, a decrease of oxygen partial pressure can reduce the critical concentration of Al, and thereby enhance the transition of the internal oxidation to the external oxidation. The occurrence of selective oxidation of Ni_3Al at the low oxygen partial pressure can be given by:

$$Ni_3Al + O_2 \rightarrow Al_2O_3 + Ni \qquad (6\text{-}5)$$

In the initial stage of oxidation, an internal-oxidation zone containing Al_2O_3 and Ni is formed. With time, an external Al_2O_3 scale can be developed. It has been reported that the reaction in Equation (6-5) induced a 28% volume expansion, which led to very high compressive stresses [36]. This, as proposed by Schumann [36], may cause an outward diffusion of Ni along the oxide/matrix interface to relieve the stresses. However, Yi et al. [37] argued that Ni diffused out via the lattices or dislocation pipes of the alloy matrix. The outward diffusion of Ni usually ceases when a dense and compact Al_2O_3 scale is formed. Those Ni particles, according to our experimental results, will stay on the Al_2O_3 scale during further testing.

6.4.3 Coke Formation on Ni_3Al Base Coatings

Coke formation often occurs on Fe base or Ni base alloys during exposure in a carburizing atmosphere with $a_c > 1$. Two types of coke, namely catalytic coke and thermal coke, have been identified [11, 40-43]. Catalytic coke always results from the heterogeneous reaction of hydrocarbon feedstock on some metals such as Fe and Ni, which are excellent catalysts for carbon deposition [40]. The sources of catalysts also include transiently-formed FeO, NiO or (Fe,Ni,Cr)-spinel, which can be reduced to Fe, Ni, or Fe-Ni particles [29, 40, 42]. Catalytic coke contains crystalline graphite and some metal, carbide or oxide particles, and has a filamentous and porous morphology. Thermal coke is related to the thermal cracking of hydrocarbon, from which a dense and

amorphous coke layer will deposit on the tube surface [41]. This coke layer is characterized by a columnar, radial and axial structure.

Because the carbon activity at 850 °C in the current 2%CH_4-H_2, is less than one ($a_c = 0.73$), coke formation should be quite difficult. This was confirmed by our experimental results. However, coke formation is evidently observed on all the Ni_3Al base coatings during carburization in 2%CH_4-H_2 at 1050 °C with $a_c = 3.21$. The coke deposited has a filamentous morphology and a complex composition consisting mainly of graphite, suggesting its catalytic nature. As alumina scale is formed on all Ni_3Al base coatings during carburization, the formation of catalytic coke should be impossible on the inert Al_2O_3 scale. However, as discussed ealier, Al_2O_3 scale is formed with the outward diffusion of Ni and the aggregation of its particles plus (Ni, Al)-rich oxides. These are are excellent catalysts for coke formation. Consequently, catalytic coke grows on all the Ni_3Al base coatings despite of the existence of inert alumina scale.

6.4.4 Effect of CeO_2 Particles

Excellent carburization and oxidation resistance of Ni_3Al is obtained when Al_2O_3 scale with good mechanical integrity is formed during exposure. A dense and compact scale effectively blocks the inward diffusion of corrosive species, e.g., O or C. However, Al_2O_3 scale on the undoped Ni-Al alloys is inherently susceptible to mechanical failure under cyclic thermal conditions. The failure of Al_2O_3 scale often results from several factors. The presence of compressive residual stresses, including thermal stress and growth stress in the scale, is one major reason. Thermal stress is induced by the large mismatch of the thermal expansion coefficient between Al_2O_3 and Ni_3Al upon cooling, while growth stress is owing to volume expansion during the formation of Al_2O_3 [44-46]. Internal or interfacial voids in Al_2O_3 scale and/or at the scale/matrix interface are also important contributors to scale failure [45, 47]. The segregation of impurity, e.g., sulfur, at the scale/matrix significantly deteriorates the bonding strength of Al_2O_3 scale [48, 49]. These factors, acting independently or jointly, lead to failures of Al_2O_3 scale such as spalling, cracking or buckling [44, 45, 50]. Cracks and pores in the scale provide short-circuit paths for the transportation of corrosive species, which causes internal oxidation

or carburization. This has been observed in the cyclic carburization of the pure Ni_3Al coating at 1050 °C (Figs. 6-1 (b), 6-5 (b) and 6-7 (c)). In contrast, all the CeO_2-dispersed Ni_3Al coatings were packed with a thin and compact Al_2O_3 scale and suffered a lower mass increase. It is evident that CeO_2 particles can enhance the resistance of alumina scale to mechanical failure during thermal cycling. Scale failure is more common at higher temperatures. At a relatively lower temperature, 850 °C, no obvious damage of Al_2O_3 was found on the pure and the CeO_2-dispersed Ni_3Al coatings. All the coatings exhibit excellent carburization resistance, and the difference in carburization resistance among the coatings is negligible.

It is well known that small amounts of reactive elements or their oxides can effectively improve the failure resistance of Al_2O_3 scale. The so-called reactive-element effect (REE) has been extensively reviewed in several papers [44, 45, 51, 52]. The major roles of the reactive elements or oxides include mitigating growth stress, improving the mechanical properties of the scale, enhancing the adherence of the scale to the matrix by reducing void formation, and scavenging detrimental sulfur by forming stable sulfides in the matrix. As presented in Chapter 4, the dispersion of Ce^{4+} ions or Ce-rich oxide particles resulted in a thin and void-free alumina scale with excellent adherence to the coatings, especially at 1050 °C. In contrast, the pure Ni_3Al coating experienced excessive spallation during cyclic oxidation at 1050 °C.

6.5 Concluding Remarks

Cyclic carburization of electrodeposited pure and CeO_2-dispersed Ni_3Al intermetallic coatings was investigated in 2%CH_4-H_2 at 850 °C and 1050 °C for periods of up to 500 hr. The following are some concluding remarks, which are also schematically illustrated in Fig. 6-11 and Fig. 6-12 for the purpose of clarification.

1. At the relatively low temperature of 850 °C, all the Ni_3Al base coatings exhibited low mass increases for a period of up to 500 hr. The uncoated Fe-Ni-Cr coupon experienced slow carburization. In contrast, no carburization was observed in coated Fe-Ni-Cr alloys after 500 hr. Al in the Ni_3Al coatings was selectively oxidized to form γ-Al_2O_3 in the initial stage of carburization in

$2\%CH_4$-H_2 with an extremely low oxygen partial pressure (Step I) (Fig. 6-11). With time, a thin and compact γ-Al_2O_3 scale gradually formed (Step II), which effectively blocked the ingress of carbon. Ni was also observed to diffuse outward to relieve the residual compressive stress owing to the formation of γ-Al_2O_3, and to form Ni-rich metal particles on γ-Al_2O_3 scale.

2. At 1050 °C, the 2 mm-thick uncoated Fe-Ni-Cr coupon suffered severe carburization and was saturated with carbon after about 300hr exposure. All coated Fe-Ni-Cr alloys were immune to attack by carbon because of α-Al_2O_3 scale formed on Ni_3Al base coatings, as indicated in Fig. 6-12 (Step I). As in the case of carburization at 850 °C, Ni-rich metal particles were observed on the scale. With continuing cyclic carburization, the pure Ni_3Al coating exhibited a behavior different from that of the CeO_2-dispersed Ni_3Al coatings. Al_2O_3 scale on the pure Ni_3Al coating cracked during thermal cycling. Corrosive species then quickly migrated through the scale via these cracks, and resulted in severe internal oxidation and carburization (Step II). In contrast, the addition of CeO_2 particles in Ni_3Al coatings reduced scale failure (Step III). No visible internal oxidation and carburization was observed for any CeO_2-dispersed Ni_3Al coatings. Due to the high carbon activity of $2\%CH_4$-H_2 ($a_c = 3.21$) at 1050 °C and the existence of Ni-rich metal particles, catalytic coke was induced on all Ni_3Al base coatings.

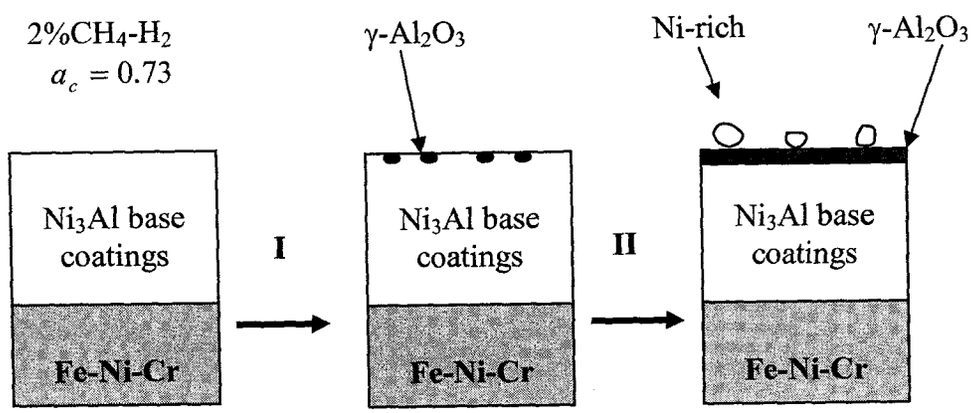

Figure 6-11. A schematic summary of the cyclic carburization of electrodeposited Ni_3Al base coatings in 2%CH_4-H_2 at 850 °C for periods of up to 500 hr.

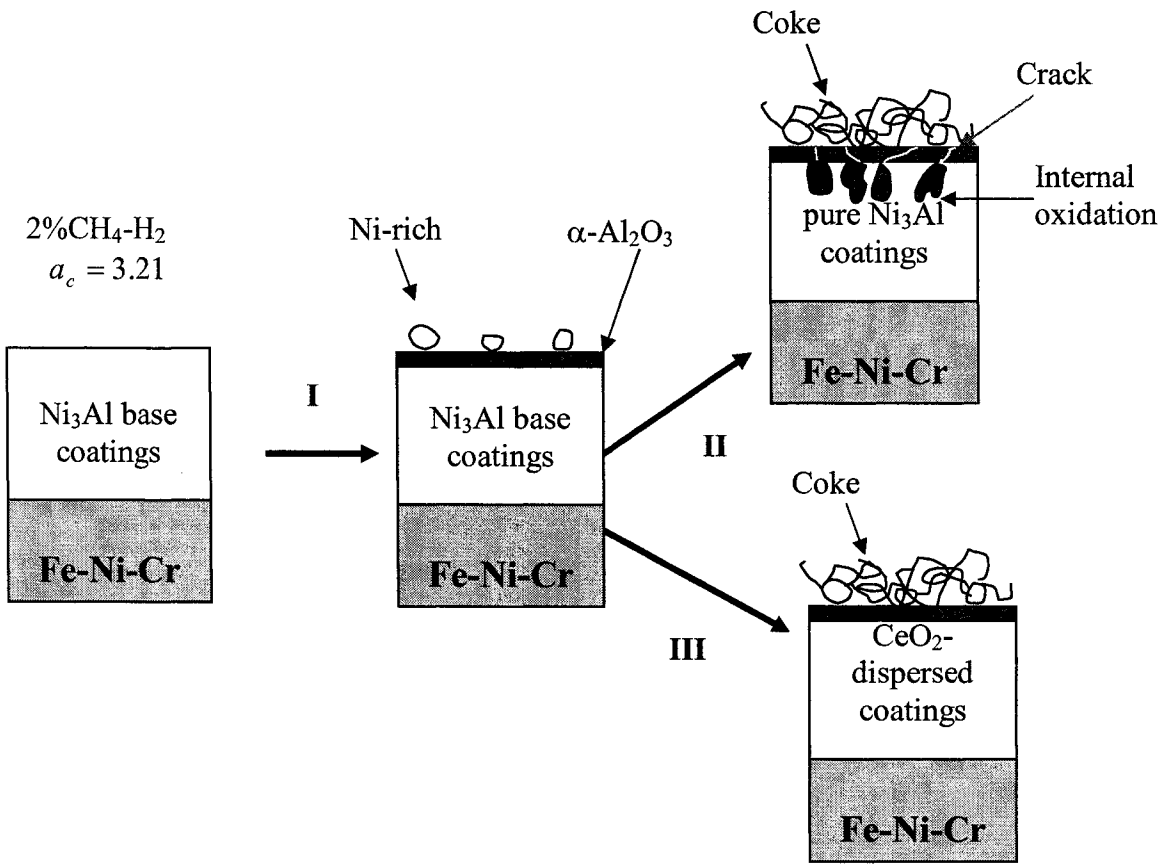

Figure 6-12. A schematic summary of the cyclic carburization of electrodeposited Ni_3Al base coatings in $2\%CH_4$-H_2 at 1050 °C for periods of up to 500 hr.

6.6 Bibliography

1. Grabke, H.J. and Wolf, I., Materials Science and Engineering, 1987. **87**: p. 23-33.

2. Grabke, H.J., *Carburization: A High Temperature Corrosion Phenomenon.* 1998, St.Louis, MO, USA: MTI.

3. Grabke, H.J., Materials Science Forum, 2001. **369-372**: p. 101-108.

4. Grabke, H.J., Corrosion, 2000. **56**(8): p. 801-808.

5. Ramanarayanan, T.A., Chun, C.M., and Mumford, J.D., Materials Science Forum, 2001. **369-372**: p. 55-76.

6. Grabke, H.J., Materials and Corrosion, 2003. **54**(10): p. 736-746.

7. Klöwer, J. and Heubner, U., Materials and Corrosion, 1998. **49**: p. 237-245.

8. Stringer, J., Materials Science and Engineering, 1987. **87**: p. 1-10.

9. Yamauchi, A., Kurokawa, K., and Takahashi, H., Oxidation of Metals, 2003. **59**(5-6): p. 517-527.

10. Lai, G.Y., Materials at High Temperatures, 1993. **11**(1-4): p. 143-150.

11. Wysiekierski, A.G., Fisher, G., and Schillmoller, C.M., Hydrocarbon Processing (International Edition), 1999. **78**(1): p. 97-100.

12. Baker, B.A., Hartmann, V.M., Shoemaker, L.E., McCoy, S.A., and Rajendran, S., Transactions of The Indian Institute of Metals, 2003. **56**(3): p. 327-333.

13. Mitchell, D.R.G., Young, D.J., and Kleemann, W., Materials and Corrosion, 1998. **49**: p. 231-236.

14. Piekarski, B., Corrosion Review, 2001. **19**(5-6): p. 453-465.

15. Wynns, K.A. and Bayler, G.T., *Diffusion Coated Ethylene Furnace Tubes, U.S. Patent 5,873,951.* 1999: USA.

16. Kurlekar, A. and Bayler, G.T., Hydrocarbon Processing (International Edition), 2001. **80**(1): p. 80-84.

17. Radmond, T. and Bergeron, M.P., Oil and Gas Journal, 1999. **97**(19): p. 39-42.

18. Wang, K.L., Chen, F.S., and Leu, G.S., Materials and Engineering A., 2003. **357**: p. 27-38.

19. Brill, U., Materials and Corrosion, 1990. **41**(12): p. 682-688.

20. Wessel, J.K. and Long, W.G., Advanced Materials and Processes, 2003. **161**(6): p. 55-57.

21. Wang, Y. and Chen, W.X., Surface and Coatings Technology, 2004. **183**: p. 18-28.

22. Hall, D.J., Hossain, M.K., and Atkinson, R.F., High Temperatures-High Pressures, 1982. **14**: p. 527-539.

23. Prescott, R. and Graham, M.J., Oxidation of Metals, 1992. **38**(3-4): p. 73-87.

24. Prescott, R. and Graham, M.J., Oxidation of Metals, 1992. **38**(3-4): p. 233-254.

25. Yang, J.C., Schumann, E., Levin, I., and Rühle, M., Acta Materialia, 1998. **46**(6): p. 2195-2201.

26. Gaskell, D.R., *Introduction to the thermodynamics of materials*. 3rd ed. 1995, Washington, D.C.: Taylor & Francis.

27. Yin, R.C., Corrosion Science, 2005. **47**: p. 1896-1910.

28. Yin, R.C., Allam, I.M., and Al-Farayedhi, A., Oxidation of Metals, 2003. **2003**(3-4): p. 315-333.

29. Steurbaut, C., Grabke, H.J., Stobbe, D., Van Buren, F.R., Korf, S.J., and Defrancq, J., Materials and Corrosion, 1998. **49**: p. 352-359.

30. Yin, R.C., Materials Science and Engineering A., 2004. **380**: p. 281-289.

31. Yin, R.C., Materials Science and Engineering A., 2005. **391**: p. 19-28.

32. Zhang, Y.G., Han, Y.F., Chen, G.L., Guo, J.T., Wan, X.J., and Feng, D., *Structural intermetallics*. 2001, Beijing, China: National Defense Industry Press.

33. Doychak, J. and Rühle, M., Oxidation of Metals, 1989. **31**(5-6): p. 431-452.

34. Schumann, E. and Rühle, M., Acta Metallurgica ET Materialla, 1994. **42**(4): p. 1481-1487.

35. Pérez, P., González-Carrasco, J.L., and Adeva, P., Oxidation of Metals, 1997. **48**(1-2): p. 143-170.

36. Schumann, E., Schnotz, G., Trumble, K.P., and Rühle, M., Acta Metallurgica ET Materialla, 1992. **40**(6): p. 1311-1319.

37. Yi, H.C., Smeltzer, W.W., and Petrix, A., Oxidation of Metals, 1996. **45**(3-4): p. 281-299.

38. Gao, W., Li, Z.W., Wu, Z., Li, S., and He, Y.D., Intermetallics, 2002. **10**: p. 263-270.

39. Wagner, C., Z. Electrochem., 1959. **63**: p. 772-782.

40. Tokura, S., Otsuka, N., and Kudo, T., Corrosion, 1993. **49**(7): p. 561-568.

41. Bennett, M.J., Materials and Corrosion, 1998. **49**: p. 345-351.

42. Figueiredo, J.L., Materials and Corrosion, 1998. **49**: p. 373-377.

43. Ganser, B., Wynns, K.A., and Kurlekar, A., Materials and Corrosion, 1999. **50**: p. 700-705.

44. Rahmel, A. and Schütze, M., Oxidation of Metals, 1992. **38**(3-4): p. 255-266.

45. Stott, F.H., Wood, G.C., and Stringer, J., Oxidation of Metals, 1995. **44**(1-2): p. 113-141.

46. Christensen, R.J., Lipkin, D.M., and Clarke, D.R., Acta Materialia, 1996. **44**(9): p. 3813-3821.

47. Pint, B.A., Oxidation of Metals, 1997. **48**(3-4): p. 303-328.

48. Meier, G.H., Pettit, F.S., and Smialek, J.L., Materials and Corrosion, 1995. **46**: p. 232-240.

49. Grabke, H.J., Surface and Interface Analysis, 2000. **30**: p. 112-119.

50. Bull, S.J., Oxidation of Metals, 1998. **49**(1-2): p. 1-17.

51. Jedliński, J., Corrosion Science, 1993. **35**(5-8): p. 863-869.

52. Grabke, H.J., Intermetallics, 1999. **7**: p. 1153-1158.

Chapter 7

Coke Formation and Metal Dusting of Electroplated Ni_3Al-CeO_2-Based Coatings in CO-H_2-H_2O

7.1 Introduction

Metal dusting is a carbon-induced form of corrosion that occurs in Fe-based and Ni-based alloys when they are served at 400~800 °C in carbonaceous atmospheres with carbon activities a_c>1 [1-5]. It is a process of disintegration of the alloy matrix into dusts containing fine metallic particles (Fe or Ni), graphite carbon, and sometimes carbides or oxides. Fine Fe or Ni particles in the dust can accelerate the deposition of catalytic coke from carburizing atmospheres [6]. Metal dusting on Fe base alloys starts with a formation of a Fe_3C layer, followed by the decomposition of Fe_3C into fine Fe particles and graphite [1, 4, 7]. Ni-based alloys, however, are characterized by direct formation and inward growth of graphite during metal dusting [1, 4, 8]. In the case of Fe-based and Ni-based alloys with high Cr content, metal dusting may be suppressed or may occur locally via defects in the scale if a Cr-rich oxide scale is formed [1, 4]. Metal dusting can cause severe wear and erosion problems due to the particulate nature of the dust and the wastage of metal components, while the buildup of thick coke significantly decreases heat-transfer efficiency of the alloy matrix and leads to excessive precipitation of carbides in the matrix.

Many efforts have been made to control metal dusting in Fe base or Ni base alloys. Grabke et al. [2, 4, 9] reported that H_2S addition up to 10 ppm retarded the metal-dusting rate of pure iron, 2.25Cr-Mo steel, alloy 800, and Fe-25Cr-20Ni. It was believed that surface-active S can preferentially react with Fe or Ni to form Fe-S or Ni-S compounds, which quickly deactivates the catalytic surface [6, 10, 11]. Ni base alloys are more resistant to metal dusting than Fe base alloys [4, 12, 13]. Klöwer et al. [12] reported that Fe base alloys generally showed unacceptable metal wastage rate at 650 °C only after 190 hr in CO-H_2-H_2O. Ni-based alloys, however, exhibited extremely low metal-dusting rate even after 10000 hr exposure. Any method that could enhance the formation of Cr_2O_3, or maintain a compact and adherent Cr_2O_3 scale, on chromia-forming alloys can result in better metal dusting resistance. Ferritic structure was more favorable than austentic structure because Cr diffused more rapidly in ferrite than in austenite [2, 4, 14]. Grabke et al. [15, 16] found that surface finish and cold working on Fe-or Ni-based alloys can reduce metal dusting because the resultant surface defects provide short-circuit paths

for the outward transport of Cr to establish Cr_2O_3. Fine grains also facilitated the formation of Cr_2O_3 scale owing to a quick diffusion of Cr via a large fraction of grain boundaries [15]. Strauß et al. [17] recently reported that alloying elements such as Ti, Zr, Nb, Mo, and W retarded metal dusting of alloy 800. Surprisingly, only 0.05% Ce in alloy 800 was found to deteriorate resistance to metal dusting. Small amount of Si or Al is beneficial, as they can form additional SiO_2 or Al_2O_3 scale below Cr_2O_3 during long-term exposure [13, 17].

Nickel aluminides (e.g., NiAl, Ni_3Al) and iron aluminides (e.g., FeAl and Fe_3Al) represent novel intermetallic compounds with superior resistance to high-temperature corrosion, and can be applied as protective coatings on Fe- or Ni-based alloys. NiAl and Ni_3Al were reported to exhibit excellent carburization resistance in reducing carburizing atmospheres [18-21]. However, coke formation and metal dusting behaviors of NiAl and Ni_3Al have not yet been studied in detail. Limited research on short-term metal dusting of Fe-Al and Ni-Al intermetallics were reported by Strauß et al. [22] and Schneider et al. [23, 24]. They found that Fe_3Al was very susceptible to metal dusting and coke formation, but that Ni_3Al was surprisingly invulnerable to metal dusting [22].

This study was initiated to understand coke formation and metal dusting of Ni_3Al base coatings, along with the effect of pre-oxidation treatment and CeO_2 addition on their performances in an environment prone to coke formation and metal dusting.

7.2 Experimental Procedures

7.2.1 Sample Preparation

Ni-Al-based composite coatings were electroplated via sediment co-deposition onto Fe-Ni-Cr coupons of dimensions 20 mm×10 mm×2 mm from a Watt's nickel bath containing Al particles or both Al particles and CeO_2 particles. The detailed coating process was described in Chapters 2 and 3. The centrifugally cast HP alloy contained 0.4wt% C, 35wt% Ni, 25wt% Cr, <1.5wt% Si, <1.5wt% Mn, <1.5wt% Nb, and the balance Fe. Al powder had an average size of 3 μm. Two types of CeO_2 particles, 5 μm and 9-15 nm, were used for coating deposition. The following coatings were deposited on

the Fe-Ni-Cr coupons and tested: pure Ni-Al coating, 80+0; two Ni-Al-5 μm CeO_2 coatings, 80+1 (5 μm) and 80+5 (5 μm); and two Ni-Al-9-15 nm CeO_2 coatings, 80+1 (9-15 nm) and 80+5 (9-15 nm). The thickness of all coatings was controlled to be around 150 μm. Prior to metal-dusting testing, all the as-plated samples were annealed at 800 °C for 3 hr in a vacuum furnace pumped down to about 0.8 mtorr to achieve a uniform single-phase γ'-Ni_3Al in the coatings. The compositions and phase characteristics of those five coatings after annealing are summarized in Table 7-1. All coatings after annealing had high porosity, which derived from the annealing treatment of the as-plated Ni matrix/Al particles composite coatings according to Chapter 2-3 and Ref [25].

Table 7-1. Ni_3Al base coatings used in the investigation.

Sample code	Deposition condition	Al content (vol%)	Phases by XRD
80+0	0 g/l CeO_2	33.50±0.64	Ni_3Al (s)
80+1 (5 μm)	1 g/l CeO_2 (5 μm)	30.58±0.52	Ni_3Al (s); CeO_2 (vw)
80+5 (5 μm)	5 g/l CeO_2 (5 μm)	31.03±0.40	Ni_3Al (s); CeO_2 (w)
80+1 (9-15 nm)	1 g/l CeO_2 (9-15 nm)	30.98±0.60	Ni_3Al (s)
80+5 (9-15 nm)	5 g/l CeO_2 (9-15 nm)	29.83±1.81	Ni_3Al (s)

s: strong; w: weak; vw: very weak

7.2.2 Metal-dusting Test

The metal-dusting test was performed in a tube furnace. Uncoated Fe-Ni-Cr alloy coupons were used as a reference. Before the test, all the coupons were polished with 600-grit SiC grinding paper, cleaned using acetone, and then air-dried. Test coupons were held in high-purity (99.8%) alumina boats with one coupon per boat (Vesuvius McDanel, PA, USA). The CO-H_2-H_2O gas mixture was used to simulate the metal dusting atmosphere. The carbon activity and the oxygen partial pressure was determined by [4, 26, 27]:

$$CO + H_2 = H_2O + C \tag{7-1}$$

$$a_c = K\ \frac{p_{CO} \bullet p_{H_2}}{p_{H_2O}}, \log K = \frac{7100}{T} - 7.496 \tag{7-2}$$

$$H_2O = H_2 + \frac{1}{2}O_2 \tag{7-3}$$

$$p_{O_2} = K'\left(\frac{p_{H_2O}}{p_{H_2}}\right)^2, \log K' = -\frac{12935}{T} + 2.919 \tag{7-4}$$

where a_c is the carbon activity; K and K' the reaction constants; and T the absolute reaction temperature. The 24.4%CO-73.3%H_2-2.3%H_2O gas mixture, which yields a carbon activity of $a_c = 12.2$ and an oxygen partial pressure of $p_{O_2} = 6.35 \times 10^{-26} atm$ at 650 °C, was flowed through the tube at a fixed rate of 60 ml/min. The test cycle consisted of heating at 5 °C/min with argon gas, holding in the CO-H_2-H_2O gas mixture at 650 °C for a specified period, and cooling at 1.5 °C/min with argon gas. After each cycle, the boats were removed from the furnace for mass gain measurement. Each coupon was weighed together with the boat and spalled products from the coupon (if any). Because each coated coupon has four edge surfaces uncoated, a correction was made to the measured weight gains on the assumption that the uncoated surfaces would have the same mass change per unit area as the coupon of bare HP alloy. After measurement, sample boats were returned to the furnace for the next run cycle.

Ni_3Al is not a good alumina-former at temperatures below 1200 °C [28]. The testing temperature, 650 °C, is too low to form Al_2O_3 scale on our Ni_3Al base coatings. In addition, formation of Al_2O_3 is often accompanied by non-protective Ni-rich oxide scales on the coatings [29-31], which may reduce the resistance of coatings to coke formation and metal dusting. Pretreatment of Ni_3Al in a weak oxidizing atmosphere is often used to induce an exclusive Al_2O_3 scale. To study the effect of pre-oxidation treatment, the uncoated Fe-Ni-Cr and the five Ni_3Al base coatings were pre-oxidized at 1100 °C for 24 hr in the H_2-0.6%H_2O gas mixture at a fixed flow rate of 60 ml/min. The corresponding ramping rate and the cooling rate were 5 °C/min and 1.5 °C/min respectively. The oxygen partial pressure during the pre-oxidation treatment, and the dissociation pressures of NiO, Cr_2O_3, and Al_2O_3 at 1100 °C were calculated using thermodynamic data from Ref [27]. The results are presented in Table 7-2. As reported in a later section, this pre-oxidation processing could induce an exclusive α-Al_2O_3 oxide layer 1-2 μm thick on all coatings.

The pre-oxidized samples were also tested in the 24.4%CO-73.3%H_2-2.3%H_2O gas mixture at 650 °C to determine their resistance to coke formation and metal dusting.

Table 7-2. The oxygen partial pressures in H_2-0.6%H_2O and the dissociation pressures of NiO, Cr_2O_3, and Al_2O_3 at 650 °C and 1100 °C.

	650 °C	1100 °C
The oxygen partial pressure	2.35×10^{-27} atm	3.61×10^{-18} atm
The dissociation pressure of NiO	2.04×10^{-18} atm	1.13×10^{-9} atm
The dissociation pressure of Cr_2O_3	5.16×10^{-34} atm	2.79×10^{-20} atm
The dissociation pressure of Al_2O_3	4.99×10^{-53} atm	3.73×10^{-32} atm

7.2.3 Materials Characterization

The microstructures and the morphologies of tested samples were examined using a S-2700 Scanning Electron Microscope (SEM) with an Energy-Dispersive X-Ray Spectrometer (EDS) attachment. It was noted that our EDS detector had a reduced ability to collect oxygen signals from the samples. Corrosion products were analyzed using an X-ray Imaging Photoelectron Spectrometer (XPS) Axis Ultra (Kratos Analytical), and a Rigaku Geigerflex 2173 X-ray diffractometer (XRD) with Co K_α incident radiation generated at 40kV and 30mA, where a 2θ range of 2 to 120 degrees was adopted for collection of X-rays.

7.3 Results

7.3.1 Metal-dusting Kinetics

(a) Without Pre-oxidation

Fig. 7-1 (a) depicts the mass changes of the uncoated Fe-Ni-Cr alloy and the five Ni_3Al base coatings for periods of up to 500hr.

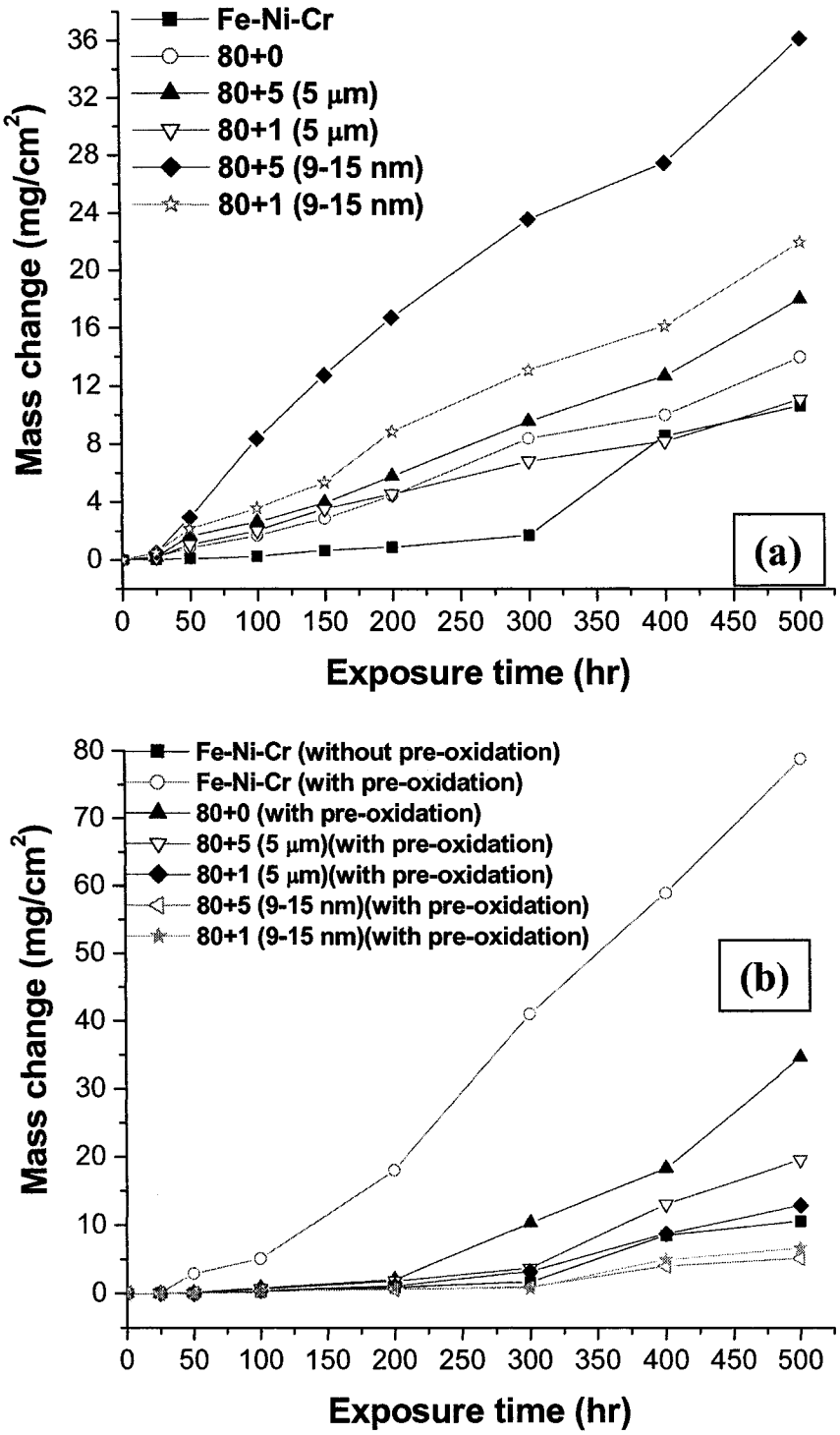

Figure 7-1. Cyclic metal dusting behavior of the Fe-Ni-Cr alloys and Ni_3Al-based coatings at 650 °C for periods of up to 500 hr: (a) without pre-oxidation; (b) with pre-oxidation.

The uncoated Fe-Ni-Cr alloy had a very slow mass increase up to 300 hr. Although it experienced a sudden mass increase after 300 hr, its final mass gain was, nonetheless, the lowest. All coating samples experienced continuous mass increase during metal dusting (Fig. 7-1 (a)). The mass increase of the pure Ni_3Al coating (80+0) was slower than that of the two nano CeO_2-dispersed coatings and the 80+5 (5 μm) coating, but slightly higher than that of the uncoated Fe-Ni-Cr alloy and the 80+1 (5 μm) coating. The two nano CeO_2-dispersed Ni_3Al coatings (especially the 80+5 (9-15nm) coating) showed much higher mass increase than the pure Ni_3Al coating and the two 5 μm CeO_2-dispersed Ni_3Al coatings. The 80+5 (9-15 nm) coating recorded the highest mass gain after 500 hr (about 36 mg/cm^2). CeO_2-dispersed Ni_3Al coatings with higher CeO_2 content generally had a higher mass gain than those with less CeO_2 content (Fig. 7-1 (a)). Coke was observed on all samples tested after 500 hr, but the two nano CeO_2-dispersed Ni_3Al coatings had the highest coke formation. The above results suggest that all Ni_3Al coatings were more susceptible to metal dusting than the Fe-Ni-Cr substrate alloy, and that the addition of nano CeO_2 particles in the coatings impaired their resistance to coke formation and metal dusting.

(b) With Pre-oxidation

The mass changes of the pre-oxidized uncoated Fe-Ni-Cr alloy and the five Ni_3Al base coatings during metal dusting are showed in Fig. 7-1 (b). The pre-oxidized uncoated Fe-Ni-Cr alloy had a rapid mass increase during metal dusting (as high as 78.83 mg/cm^2 after 500 hr). Excessive coke was seen on the alloy surface. The pre-oxidized pure and CeO_2-dispersed Ni_3Al coatings all showed low mass changes until 200 hr, but exhibited distinct behaviors with further exposure. The pre-oxidized pure Ni_3Al coating experienced an abrupt mass increase after 200 hr, and showed the highest mass increase among all coating samples after 500 hr exposure. It was higher than that of the pure Ni_3Al coating without pre-oxidation (Fig. 7-1 (a)). The two pre-oxidized 5 μm CeO_2-dispersed Ni_3Al coatings showed rapid mass changes after 200 hr as well. The pre-oxidized 80+5 (5 μm) coating had the second-highest mass increase among the five coating samples, while the pre-oxidized 80+1 (5 μm) coating showed a mass increase comparable to that of the uncoated Fe-Ni-Cr alloy without pre-oxidation. According to

Figs. 7-1 (a) and (b), the mass changes of both pre-oxidized 5 μm CeO_2-dispersed Ni_3Al coatings after 200 hr were similar to those without pre-oxidation, suggesting that the pre-oxidation treatment suppressed coke formation on both the 5 μm CeO_2-dispersed Ni_3Al coatings only before 200 hr. It is noteworthy that the two nano CeO_2-dispersed Ni_3Al coatings after pre-treatment, which were most susceptible to coke formation and metal dusting when they were not pre-oxidized (Fig. 7-1 (a)), surprisingly showed the lowest mass gains even after 500 hr exposure (Fig. 7-1 (b)). This highlights the benefit of pre-oxidation. The mass increase of the pre-oxidized 80+1 (9-15 nm) coating with lower CeO_2 content was slightly higher than that of the pre-oxidized 80+5 (9-15 nm) coating.

7.3.2 Coating Morphologies

7.3.2.1 Un-pre-oxidized Coatings

(a) Pure Ni_3Al Coating (80+0)

Fig. 7-2 (a) shows the surface morphologies of the pure Ni_3Al coating (80+0) after metal dusting for 50 hr. Some filaments of nano size were found on the coating surface. These filaments were rich in C, Ni, Al, and O according to the EDS analysis in Fig. 7-2 (b), indicating coke formation. The coating surface free of filamentous coke consisted mainly of Ni, Al, and O based on the EDS spectrum in Fig. 7-2 (c), suggesting the occurrence of oxidation. More coke was seen on the pure Ni_3Al coating after 200 hr (Fig. 7-3 (a)). Coke formation continued with time, as more filamentous coke was found after 200 hr (Fig. 7-3 (b)). By 500 hr, the coke, in the form of small clusters, covered the entire coating surface (Fig. 7-4 (a)). The filamentous morphology of coke is clear at higher magnification (Fig. 7-4 (b)). Coke on the coating surface was scraped and analyzed with the aid of XRD. As reported in Table 7-3, the coke was comprised predominantly of graphite carbon and Ni. It is noteworthy that coke filaments formed at different stages of exposure always had a particle at their tip, as indicated by the white arrows in Figs. 7-2 (a), 7-3 (b), and 7-4 (b). These particles proved to be Ni-rich according to EDS analysis, which is consistent with the detection of Ni in the scraped coke. The filamentous morphology, plus the detection of significant Ni-rich

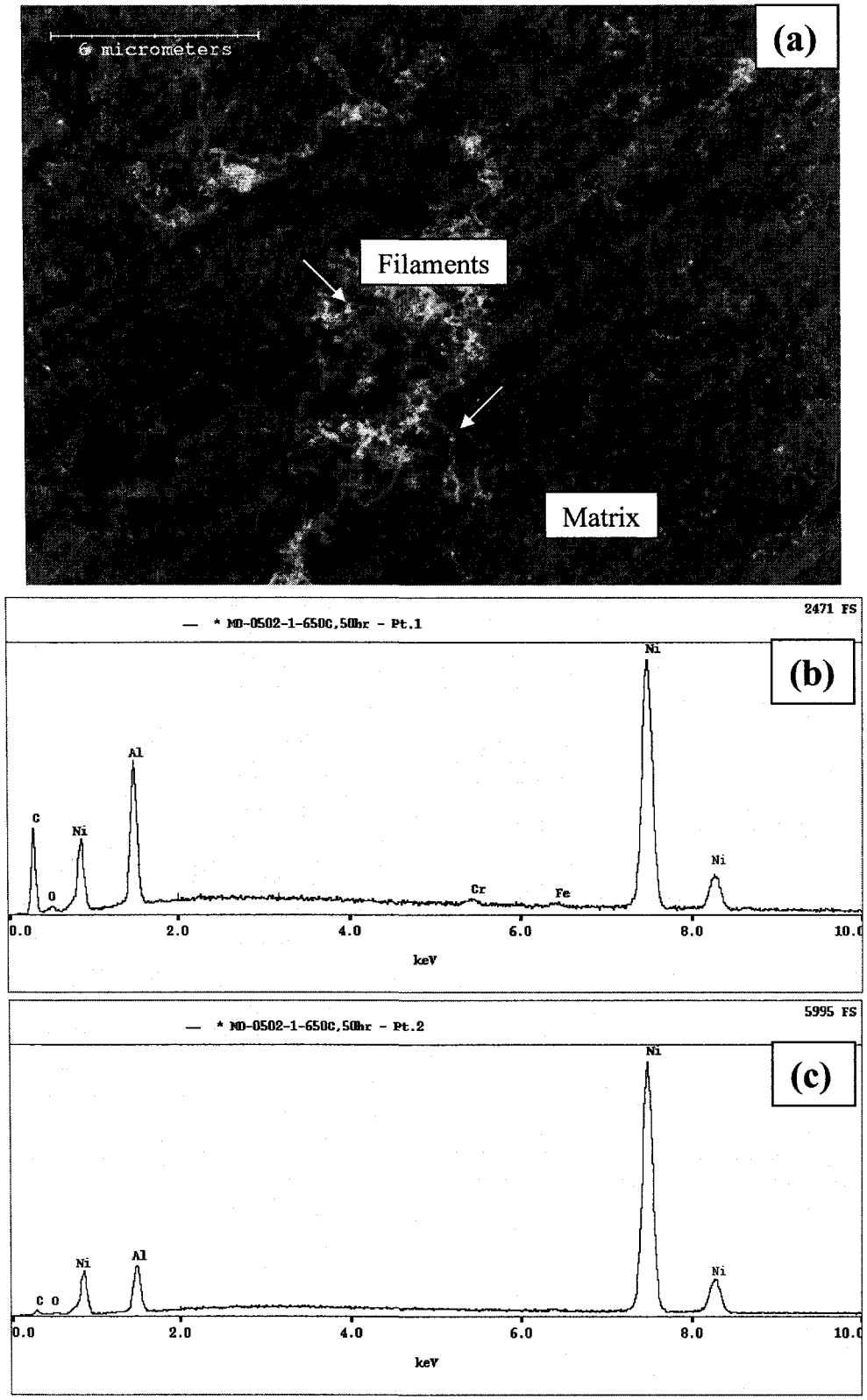

Figure 7-2. The pure Ni_3Al coating (80+0) after metal dusting for 50 hr: (a) the coating surface; (b) EDS analysis of the filaments cluster in (a); (b) EDS analysis of the coating matrix in (a).

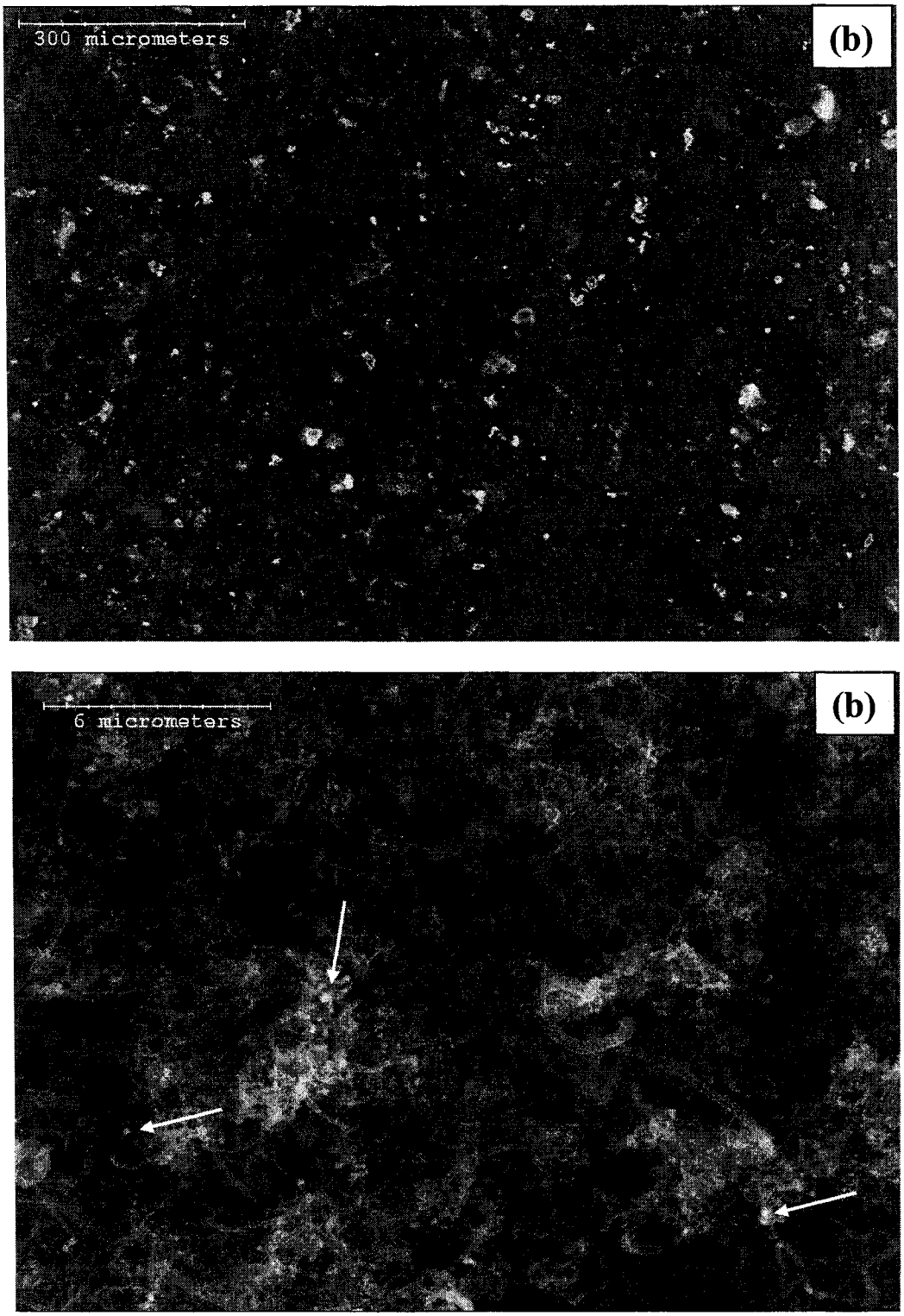

Figure 7-3. The surface morphology of the pure Ni_3Al coating (80+0) after metal dusting for 200 hr: (a) at low magnification; (b) at high magnification.

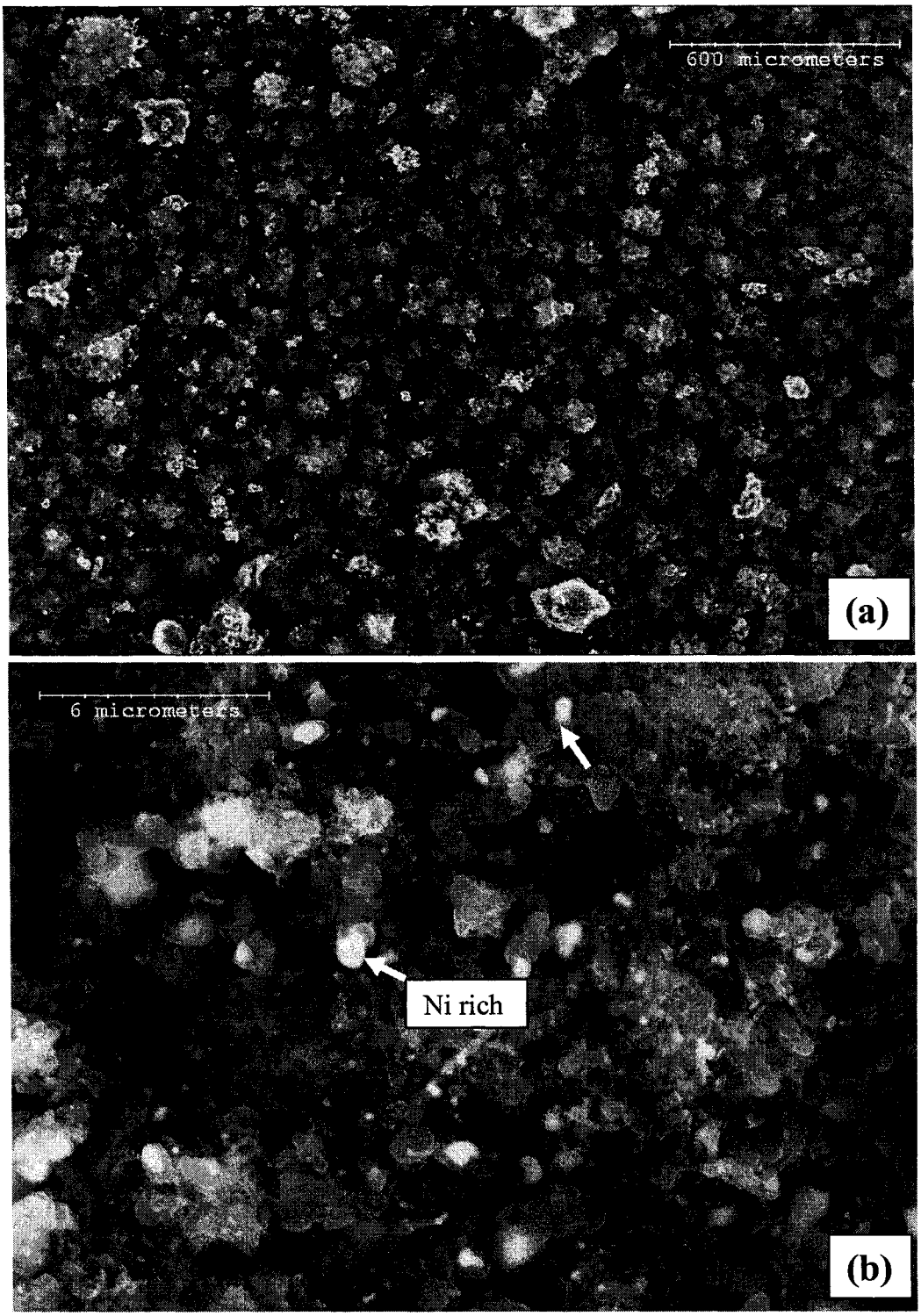

Figure 7-4. The surface morphology of pure Ni_3Al coating (80+0) after metal dusting for 500 hr: (a) the coating surface before the removing of coke; (b) at high magnification; (c) pits on the coating surface after the removing of coke; (d) EDS analysis of the pit area in (c).

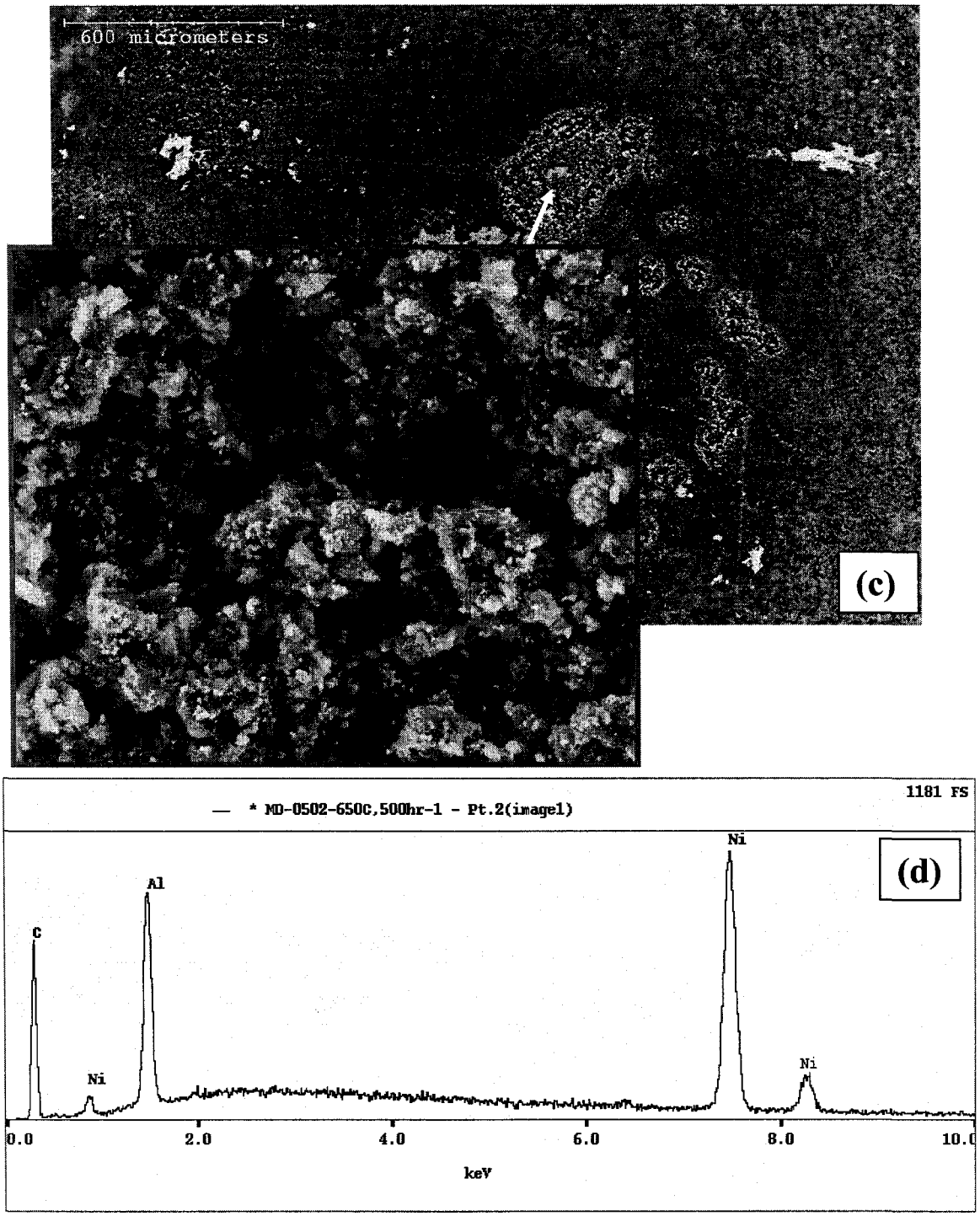

Fig. 7-4 (continued)

Particles, highlights the catalytic nature of coke, which has been well described by previous studies [10, 32-34]. The coating surface after removal of coke is presented in Fig. 7-4 (c). Clusters of pits full of disintegrated materials were observed (Fig. 7-4 (c)).

According to the EDS analysis in Fig. 7-4 (d), the pitted area contained mainly graphite, Ni, Al, and possibly O.

A cross-section of the pure Ni_3Al coating after metal dusting for 200 hr is shown in Fig. 7-5 (a). Some small pits were observed on the coating surface, and coke rich in C, Al, Ni and O was found in the pits. In each pit, the graphite coke penetrated into the coating matrix and disintegrated the matrix, as indicated by the white dashed arrows in Fig. 7-5 (a). By 500 hr, more pits with a size of several microns were formed along the coating surface (Fig. 7-5 (b)). Fig. 7-5 (c) provides a high-magnification view of a typical pit shown in Fig. 7-5 (b). The EDS analysis in Figs. 7-5 (d) and (e) revealed that the pit was comprised mainly of C and Ni. It had much higher Al in the inner portion (Fig. 7-5 (d)), but much less in the outer (Fig. 7-5 (e)). These observations are consistent with the EDS analysis in Fig. 7-4 (d) of bare pitting areas after a removal of coke from the surface (Fig. 7-4 (c)), and the XRD results of the coke scraped from the surface as listed in Table 7-3. The difference in compositions between the outer and the inner portion of the pit indicates that Ni might be transported outward, while Al stayed in the inner layer as Ni-Al particles or possibly Al_2O_3 at 650 °C. No Al-rich oxide scale was observed on the coating surface even after 500hr exposure (Figs. 7-5 (a)-(c)).

Table 7-3. The XRD analysis of coke formed on the samples after 500hr exposure.

Without Pre-oxidation	Phase Information
80+0	Graphite (s), Ni (s)
80+1 (5 μm)	Graphite (m), Ni (s)
80+5 (5 μm)	Graphite (m), Ni (s)
80+1 (9-15 nm)	Graphite (m), Ni (s)
80+5 (9-15 nm)	Graphite (m), Ni (s)
With Pre-oxidation	
80+0	Graphite (m), Ni (s)
80+1 (5 μm)	Graphite (m), Ni (s)
80+5 (5 μm)	Graphite (s), Ni (s)
80+1 (9-15 nm)	Graphite (s), Ni (s)
80+5 (9-15 nm)	Graphite (s), Ni (s)

s: strong; m: medium; w: weak.

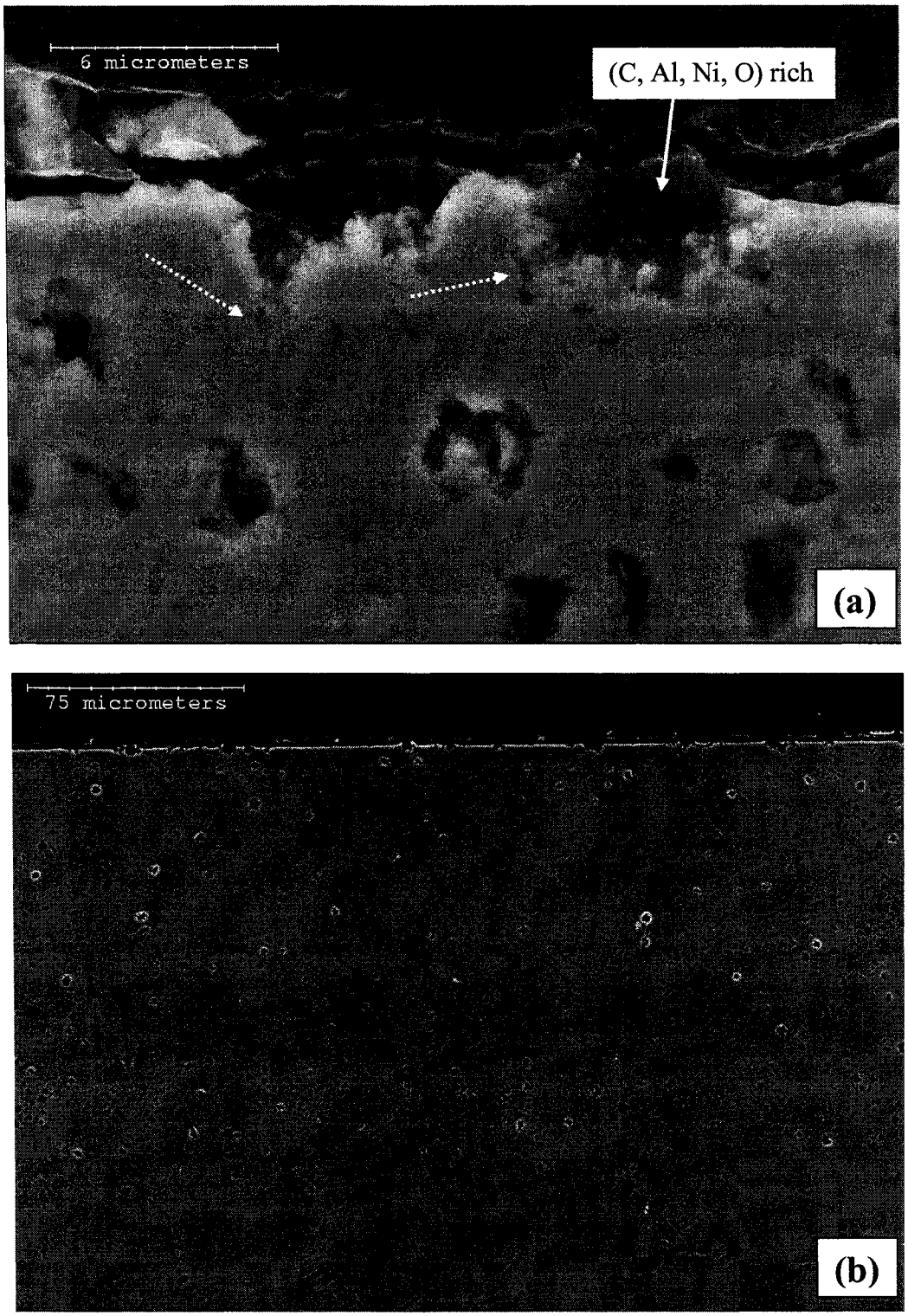

Figure 7-5. The cross section of the pure Ni_3Al coating after metal dusting: (a) for 200 hr; (b) for 500 hr; (c) a high-magnification view of the pits in (b); (d) EDS analysis of area 1 in (c); (e) EDS analysis of area 3 in (c).

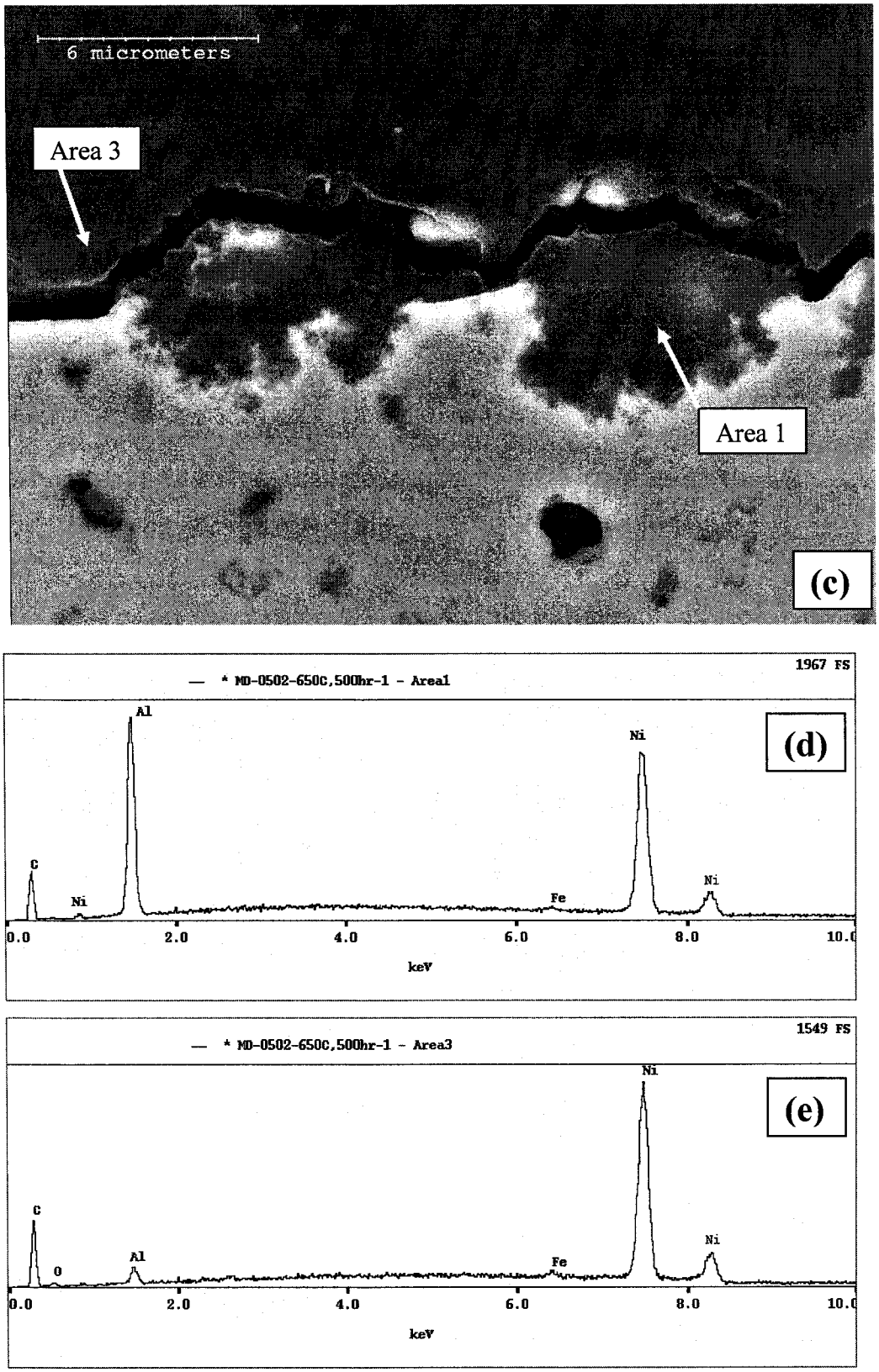

Figure 7-5 (continued)

(b) 5 μm CeO_2-dispersed Ni_3Al Coatings

Coke formation on the two 5 μm CeO_2-dispersed Ni_3Al coatings was generally similar to that on the pure Ni_3Al coating (80+0). The coke on the 5 μm CeO_2-dispersed Ni_3Al coatings was preferentially deposited in regions high in Ce. A typical surface of the 80+5 (5 μm) coating after 50 hr exposure is shown in Fig. 7-6 (a). As shown in Fig. 7-6 (b), strong peaks of carbon and Ce were detected in those regions marked by white arrows in Fig. 7-6 (a). By 500 hr, a thick layer of coke was formed on the 80+5 (5 μm) coating (Fig. 7-7 (a)). The coke exhibited a tangled filamentous morphology (Fig. 7-7 (b)), a characteristic of catalytic coke. The surface coke also consisted mainly of Ni phases and graphite crystals (Table 7-3). Fig. 7-8 (a) showed severe pitting attack on the surface of the 80+5 (5 μm) coating after metal dusting for 500 hr. These pits had morphologies similar to those on the pure Ni_3Al coating (Fig. 7-4 (c)). Ce, together with C, Ni, Al, and O, was detected in these pitting areas by EDS analysis. Compared to the pure Ni_3Al coating, the 80+5 (5 μm) coating is more severe after 500 hr of exposure in terms of coke formation and pitting attack (Figs. 7-4 (a) and (c), Fig. 7-7 (a) and Fig. 7-8 (a)). As indicated in Fig. 7-8 (b), the 80+1 (5 μm) coating with lower CeO_2 content after 500 hr exposure exhibited much less pitting than the 80+5 (5 μm) coating. Moreover, the 80+1 (5 μm) coating had lower mass increase than the 80+5 (5 μm) coating (Fig. 7-1 (a)).

The cross-sectional morphologies of the 5 μm CeO_2-dispersed Ni_3Al coatings during metal dusting were comparable to those of the pure Ni_3Al coating. Fig. 7-9 (a) depicts a typical distribution of pits on the 5 μm CeO_2-dispersed Ni_3Al coatings after metal dusting for 500 hr. Many fine Ni-rich particles dispersed in the outer coke layer, while the inner coke layer was mixed with graphite and isolated fragments of coating materials (Fig. 7-9 (b)). CeO_2 particles were observed in the pitting area. Some CeO_2 particles had been separated from the coating matrix and disintegrated into many smaller pieces (Fig. 7-9 (b)). This is consistent with the detection of Ce in the pitting area (Fig. 7-8 (a)). As was the case with the pure Ni_3Al coating, no Al-rich oxide scale formed on the 5 μm CeO_2-dispersed Ni_3Al coatings during metal dusting.

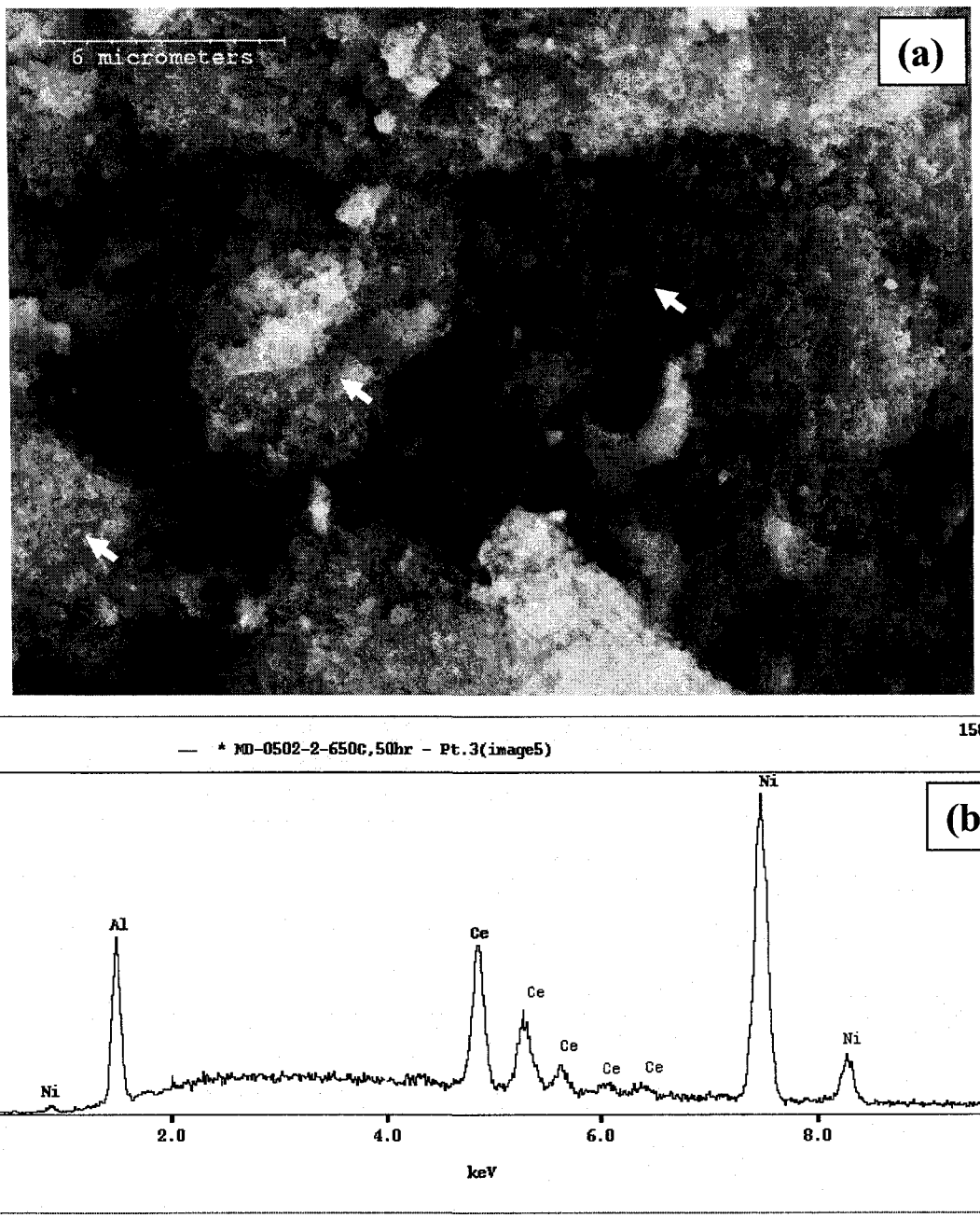

Figure 7-6. The surface morphology of the 80+5 (5 μm) coating after metal dusting for 50 hr: (a) a typical coking region; (b) EDS analysis of the area indicated in (b).

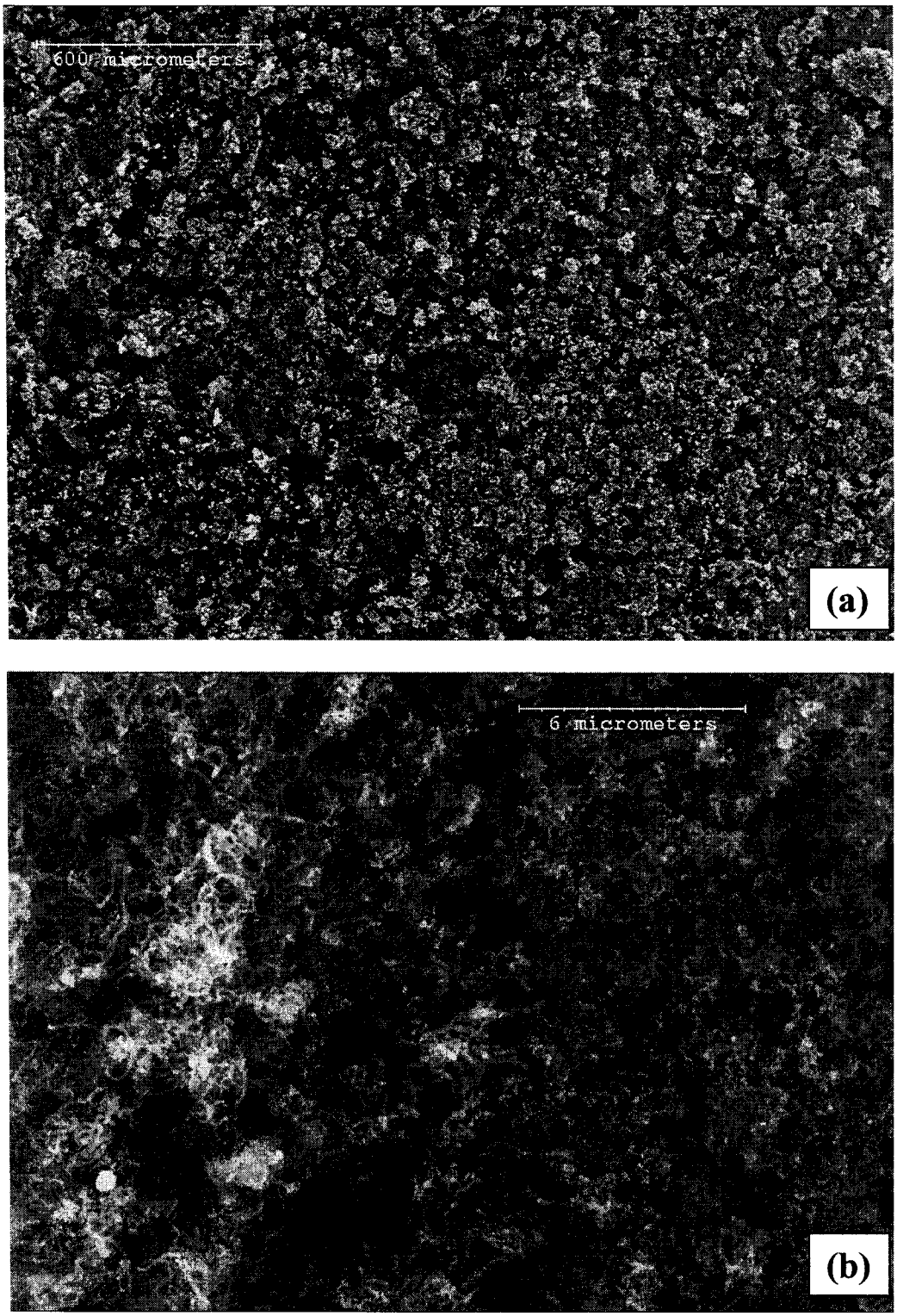

Figure 7-7. The surface morphology of the 80+5 (5 μm) coating after metal dusting for 500 hr: (a) a low-magnification view; (b) a high-magnification view.

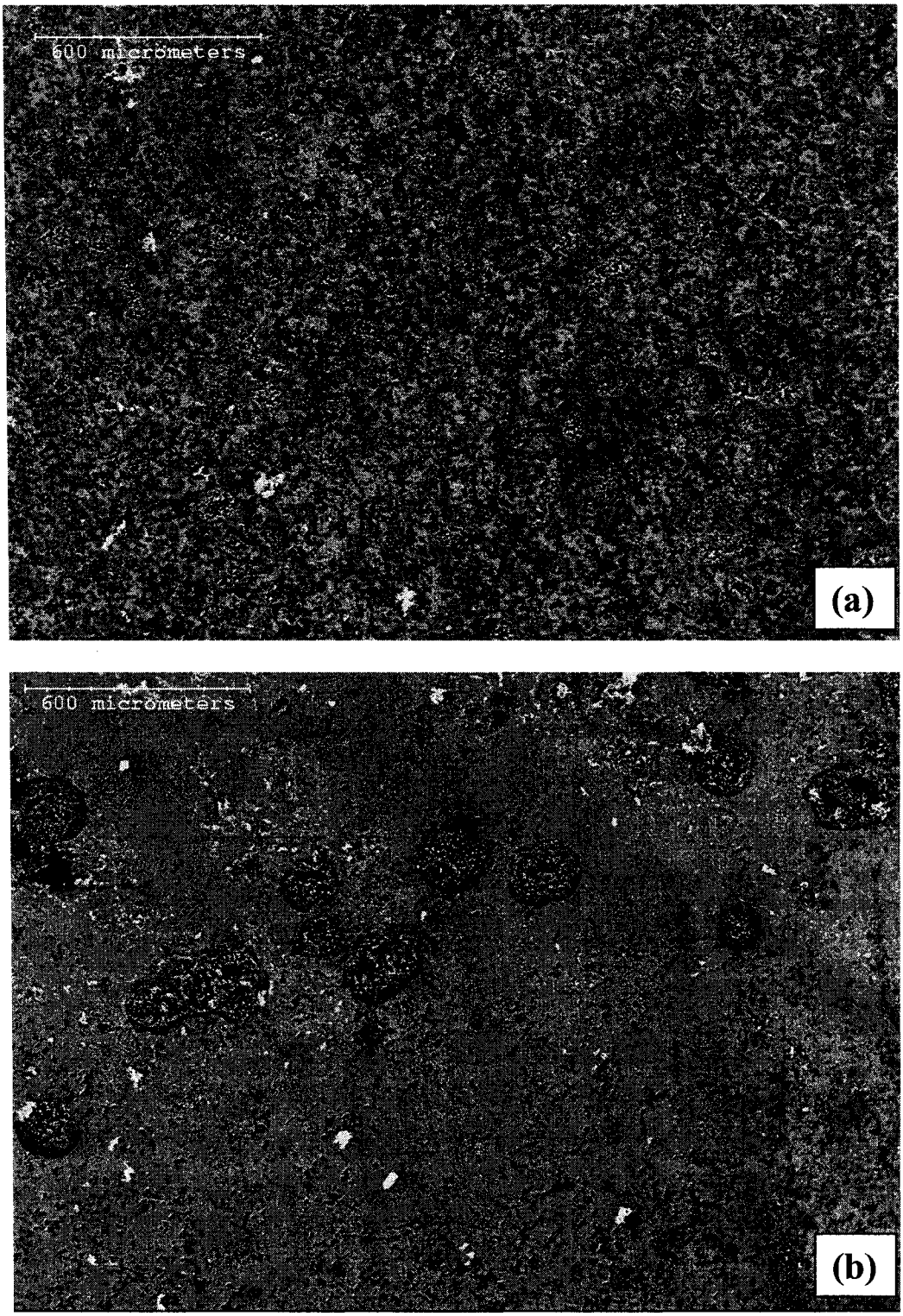

Figure 7-8. The surface morphologies (after the removing of coke) of the two 5 μm CeO_2-dispersed Ni_3Al coatings after metal dusting for 500 hr: (a) the 80+5 (5 μm) coating; (b) the 80+1 (5 μm) coating.

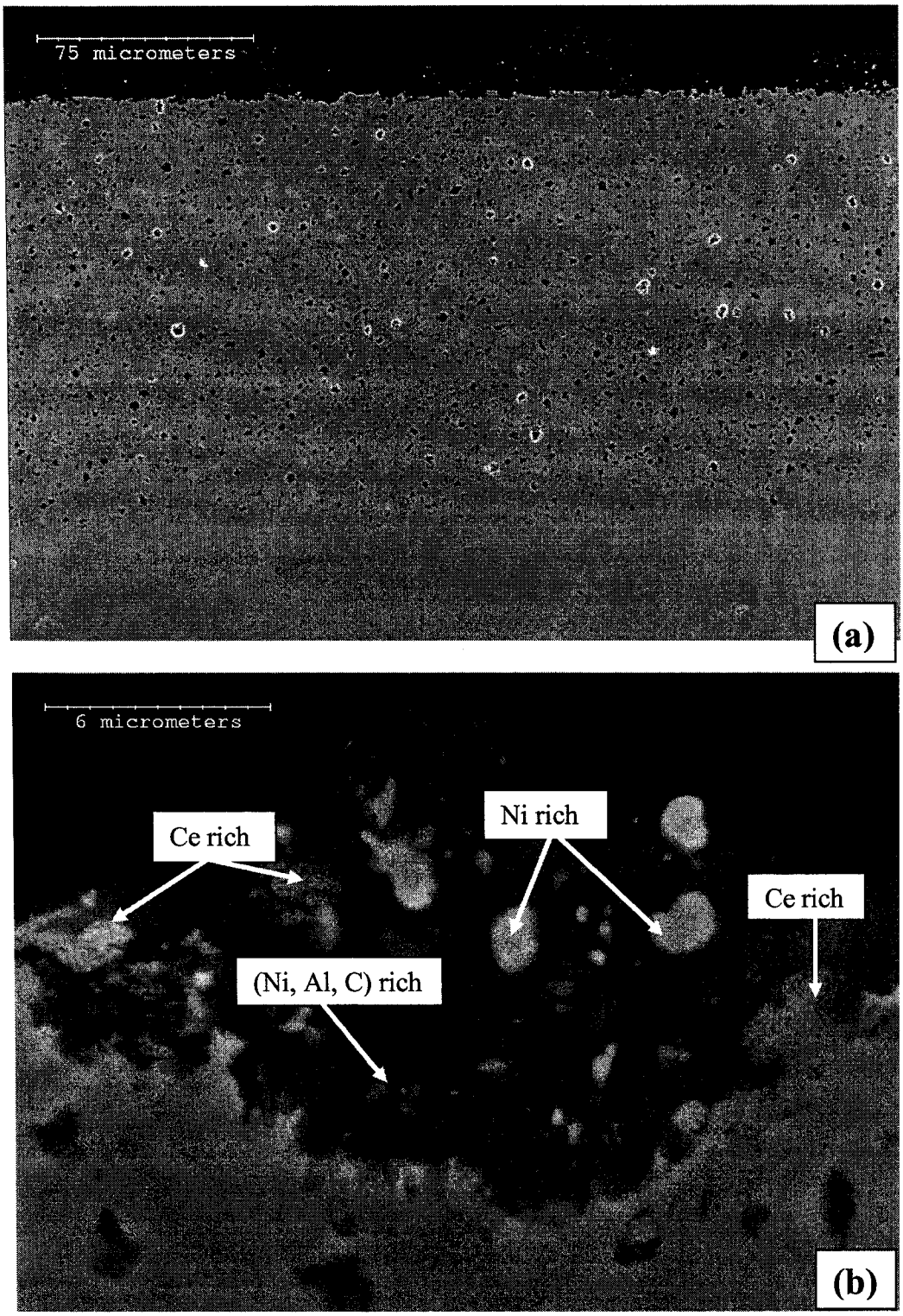

Figure 7-9. The cross section of the 80+5 (5 μm) coating after metal dusting for 500 hr: (a) at low magnification; (b) at high magnification.

(c) Nano CeO_2-dispersed Ni_3Al Coatings

Figs. 7-10 (a) and (b) present the surface morphologies of the 80+5 (9-15 nm) coating after metal dusting for 50hr. The 80+5 (9-15 nm) coating had a much larger fraction of surface areas covered with coke than the pure Ni_3Al coating and the 80+5 (5 μm) coating. By 200 hr, excessive filamentous coke had already built up on the 80+5 (9-15 nm) coating (Figs. 7-10 (c) and (d)). The coke was thick and coarse on the coating surface after 500 hr (Fig. 7-11 (a)), indicating increased carbon deposition. Scraping coke deposits from the surface revealed pitting attack in the coating matrix (Fig. 7-11 (b)). According to the XRD results in Table 7-3, the coke contained Ni and C. Similar surface morphologies were observed on the 80+1 (9-15 nm) coating after metal dusting.

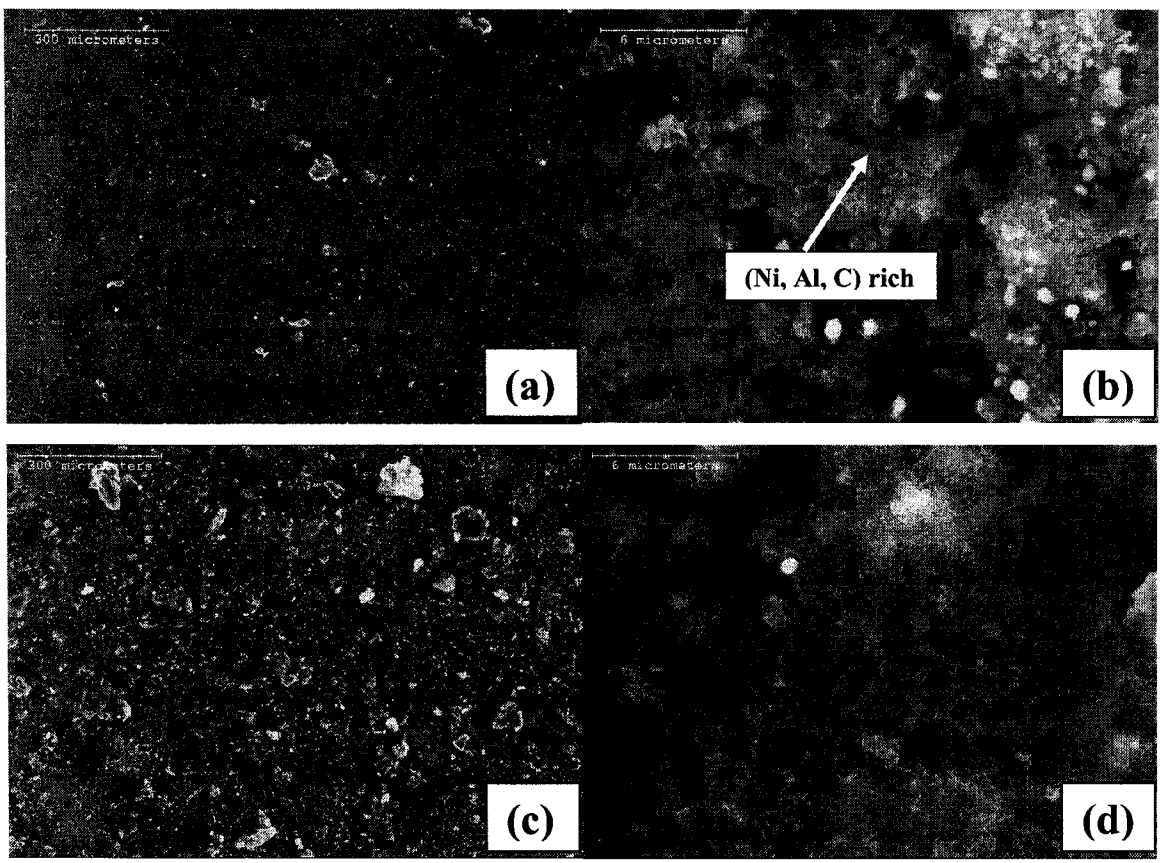

Figure 7-10. The surface morphology of the 80+5 (9-15 nm) coating after metal dusting: (a) a low-magnification view after 50 hr; (b) a high-magnification view after 50 hr; (c) a low-magnification view after 200 hr; (b) a high-magnification view after 200 hr.

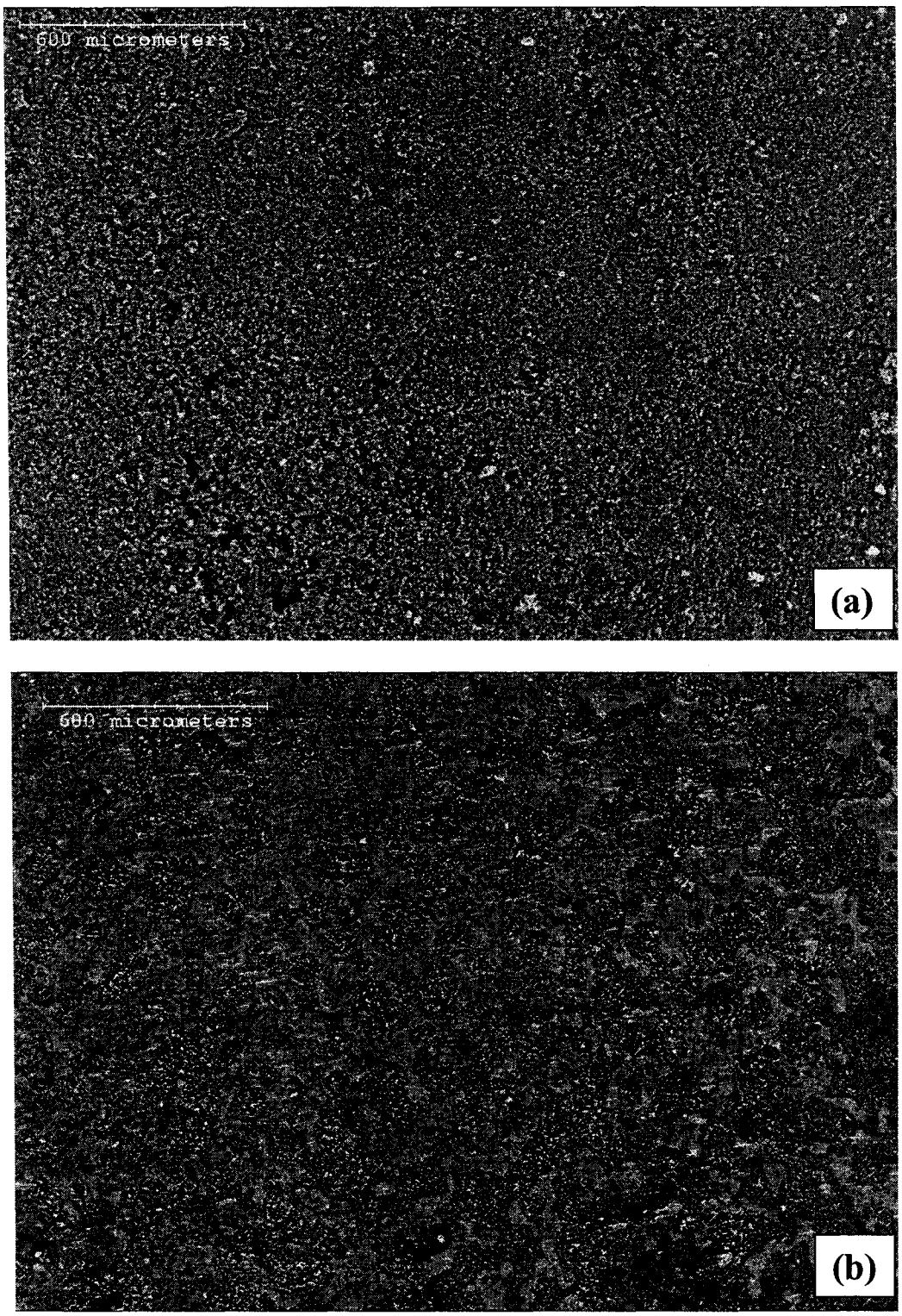

Figure 7-11. The surface morphology of the 80+5 (5 μm) coating after metal dusting for 500 hr: (a) before the scraping of coke; (b) after the scraping of coke.

The two nano CeO_2-dispersed Ni_3Al coatings were found to have much more severe pitting attack on the coating surface during metal dusting. Figs. 7-12 (a) and (b) show a typical cross-section of the 80+5 (9-15 nm) coating after metal dusting for 200 hr. Pitting on the coating was much more intense than that on the pure Ni_3Al coating and the 5 μm CeO_2-dispersed Ni_3Al coatings after metal dusting for 200hr. Pits on the 80+5 (9-15 nm) coating by 500 hr became much larger and deeper than those on the pure and 5 μm CeO_2-dispersed Ni_3Al coatings tested for the same length of time (Fig. 7-13 (a)). Fig. 7-13 (b) is an enlarged micrograph showing the cross-section of a pit formed after 500 hr of exposure.

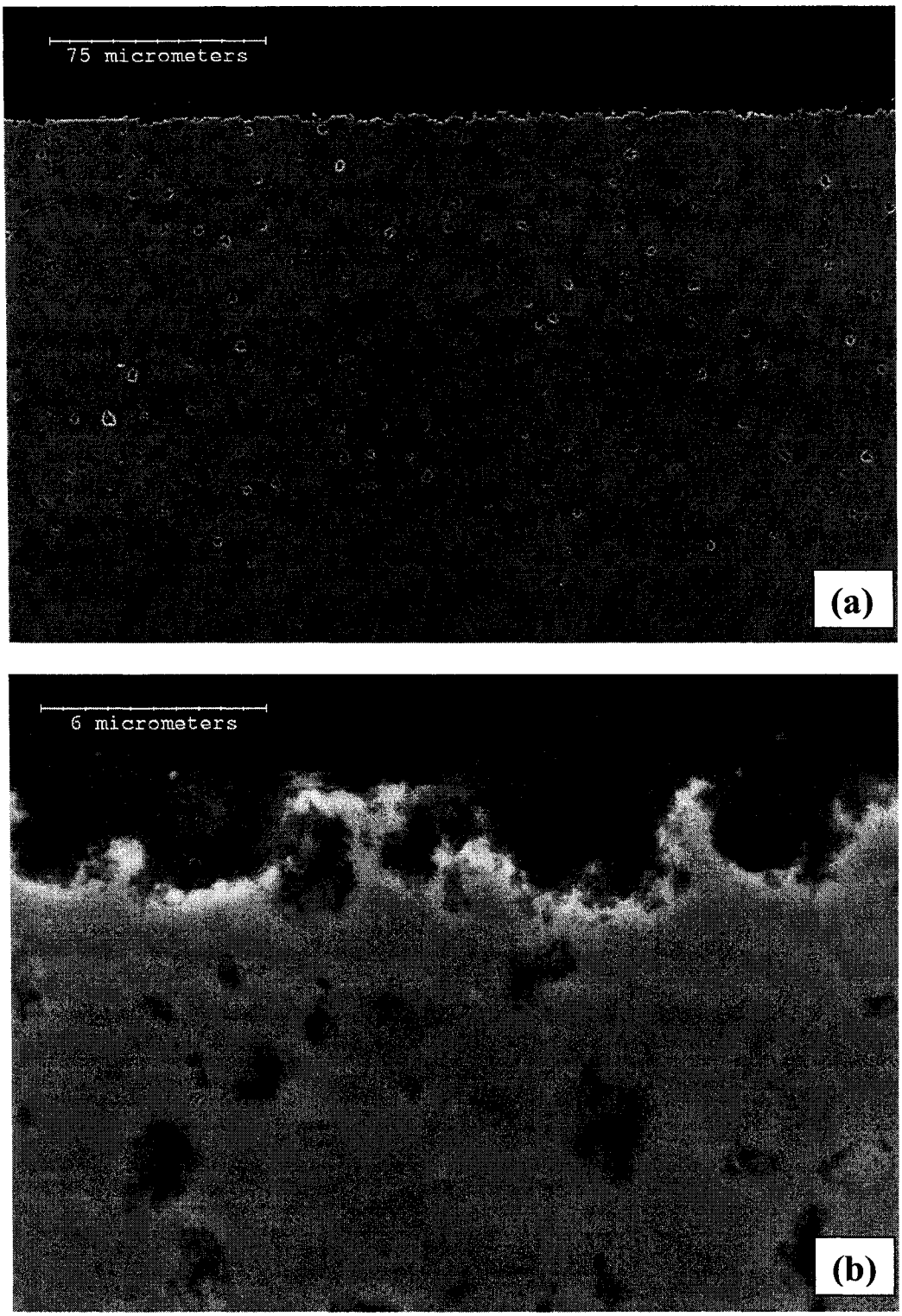

Figure 7-12. The cross section of the 80+5 (9-15 nm) coating after metal dusting for 200 hr: (a) a low-magnification view; (b) a high-magnification view.

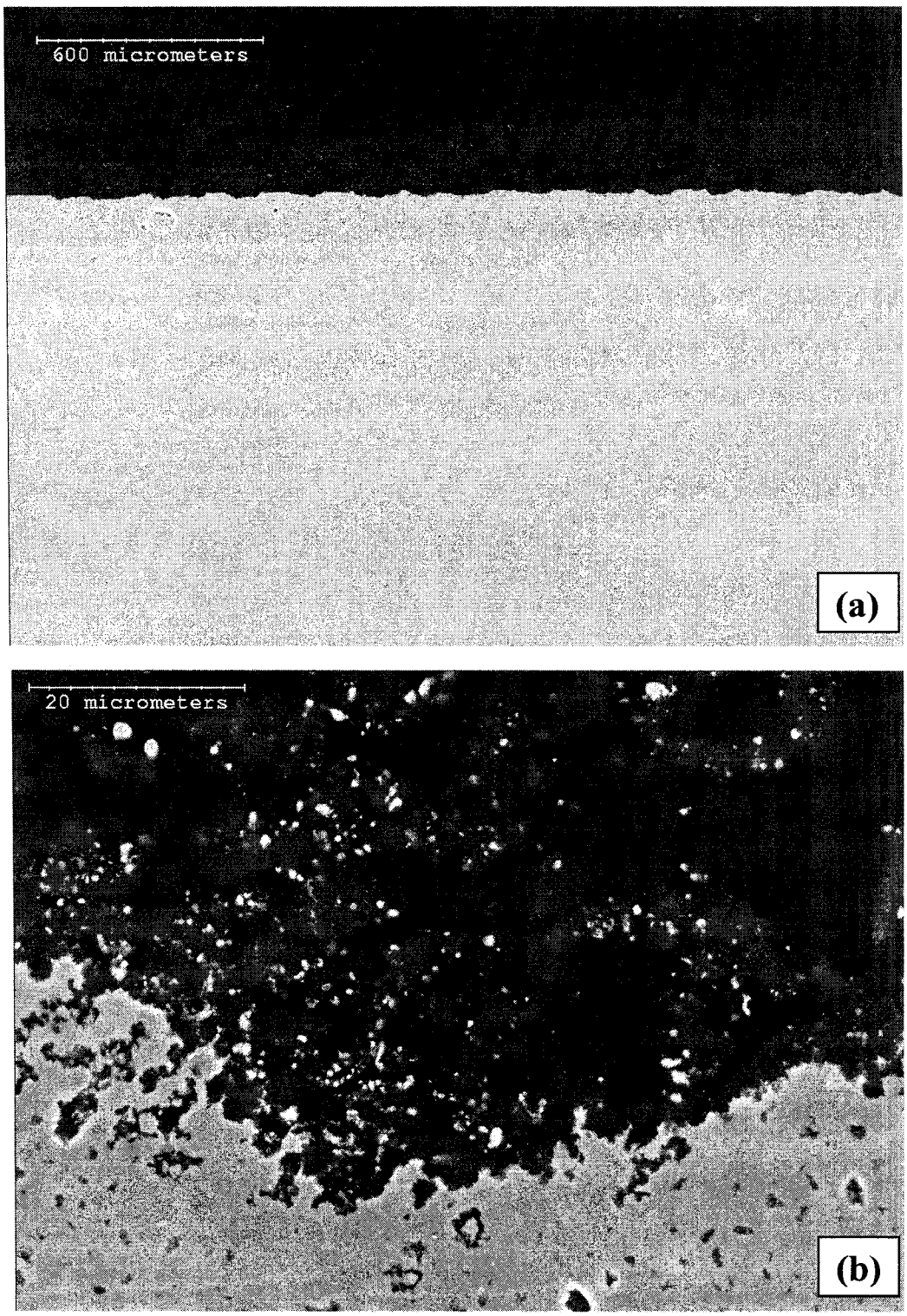

Figure 7-13. The cross section of the 80+5 (9-15 nm) coating after metal dusting for 500 hr: (a) a low-magnification view; (b) a high-magnification view.

7.3.2.2 Pre-oxidized Coatings

(a) Pre-oxidation Treatment

Figs. 7-14 (a)-(f) show the surface morphologies of the Ni_3Al base coatings after pre-oxidation in H_2-0.6%H_2O at 1100 °C for 24 hr.

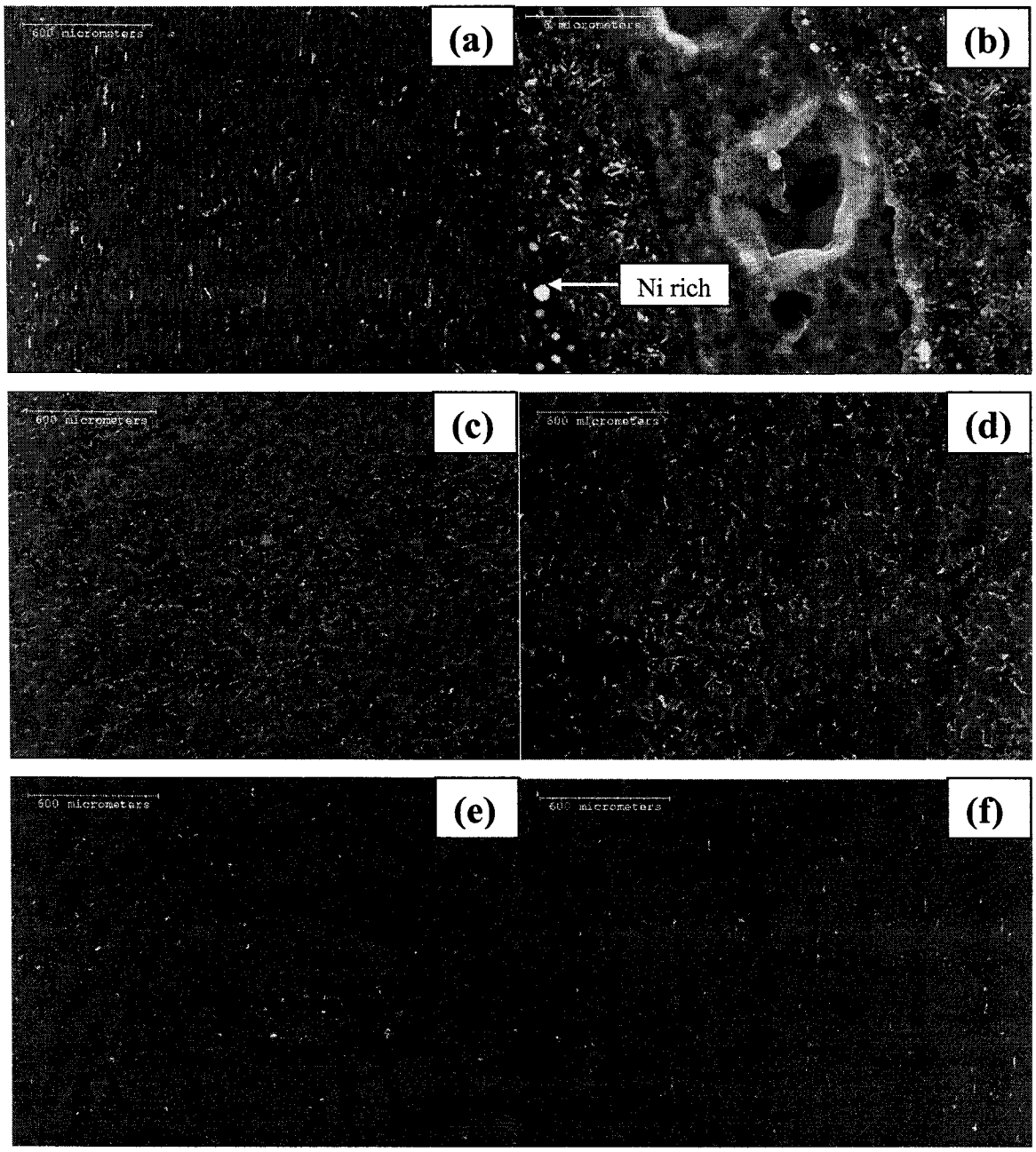

Figure 7-14. Surface morphologies of Ni_3Al-based coatings after pre-oxidation in H_2-0.6%H_2O at 1100 °C for 24 hr: (a) pure Ni_3Al coating; (b) a high-magnification view of the spalled area in (a); (c) the 80+5 (5 μm) coating; (d) the 80+1 (5 μm) coating; (e) the 80+5 (9-15 nm) coating; (f) the 80+1 (9-15 nm) coating.

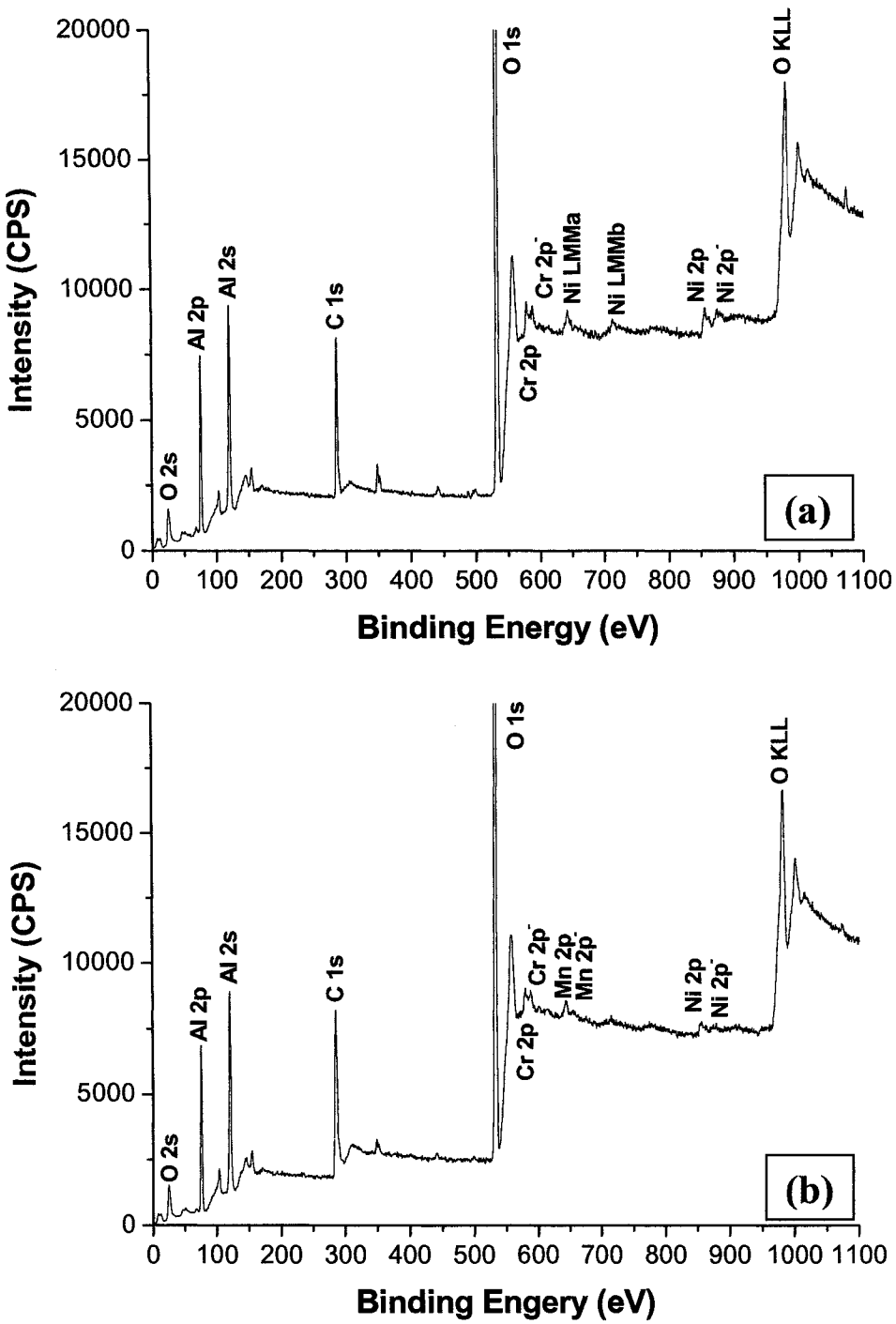

Figure 7-15. The XPS analysis of the surfaces of pure Ni_3Al coatings: (a) after pre-oxidation; (b) after metal dusting for 50 hr. (The strong peak of O 1s isn't fully showed in both the figures, and some minor impurities, such as Ca, Na, and Si, are not labeled in both the figures.)

An Al-rich oxide layer had been formed on the pre-oxidized pure Ni_3Al coating (Figs. 7-14 (a) and (b)). Fig. 7-15 (a) provides a XPS analysis of the pre-oxidized pure Ni_3Al coating. It was found that the surface contained mainly Al and O, plus minor quantities of Ni and Cr. Cr in the coating might derive from the substrate owing to rapid interdiffusion between the coating and the substrate at high temperatures, and had been observed during high-temperature oxidation as was presented in Chapter 4 and Chapter 6. The high-resolution XPS detected impurities on the surface, including C, Na, Ca, and Si (not labeled) (Fig. 7-15 (a)). XPS examination on all the CeO_2-dispersed Ni_3Al coatings after pre-oxidation yielded similar results, and are therefore not presented here. XRD analysis further identified the oxide layer formed on all the pre-oxidized Ni_3Al base coatings to be α-Al_2O_3. Some nickel-rich particles were observed on the surface of the pre-oxidized pure Ni_3Al coating (indicated by a white arrow in Fig. 7-14 (b)), which were consistently observed on all the pre-oxidized CeO_2-dispersed Ni_3Al coatings. It should be noted that excessive scale spallation was observed on the pre-oxidized pure and the two pre-oxidized 5 μm CeO_2-dispersed Ni_3Al coatings. The spallation was most severe on the pre-oxidized pure Ni_3Al coating and the pre-oxidized 80+5 (5 μm) coating, but less on the pre-oxidized 80+1 (5 μm), as shown in Figs. 7-14 (a)-(d). Grains of coating matrix are visible at spalled sites. However, two pre-oxidized nano CeO_2-dispersed Ni_3Al coatings exhibited excellent resistance to spallation (Figs. 7-14 (e) and (f)), with only a few spalled areas scattered on the surface .

Figs. 7-16 (a) and (b) Present typical cross-sectional micrographs of the pre-oxidized Ni_3Al base coatings. The entire coating was free of original pores (Fig. 7-16 (a)) owing to the annealing treatment described in Chapters 2 and 3. It was found that pores in the coatings could be healed during high temperature exposure by self-sintering, inter-diffusion and the Kirdendall effect, and that the healing rate strongly depended on temperature (Chapters 4 and 6). Fig. 7-16 (b) shows that α-Al_2O_3 scale on the coating is very thin (1-2 μm thick).

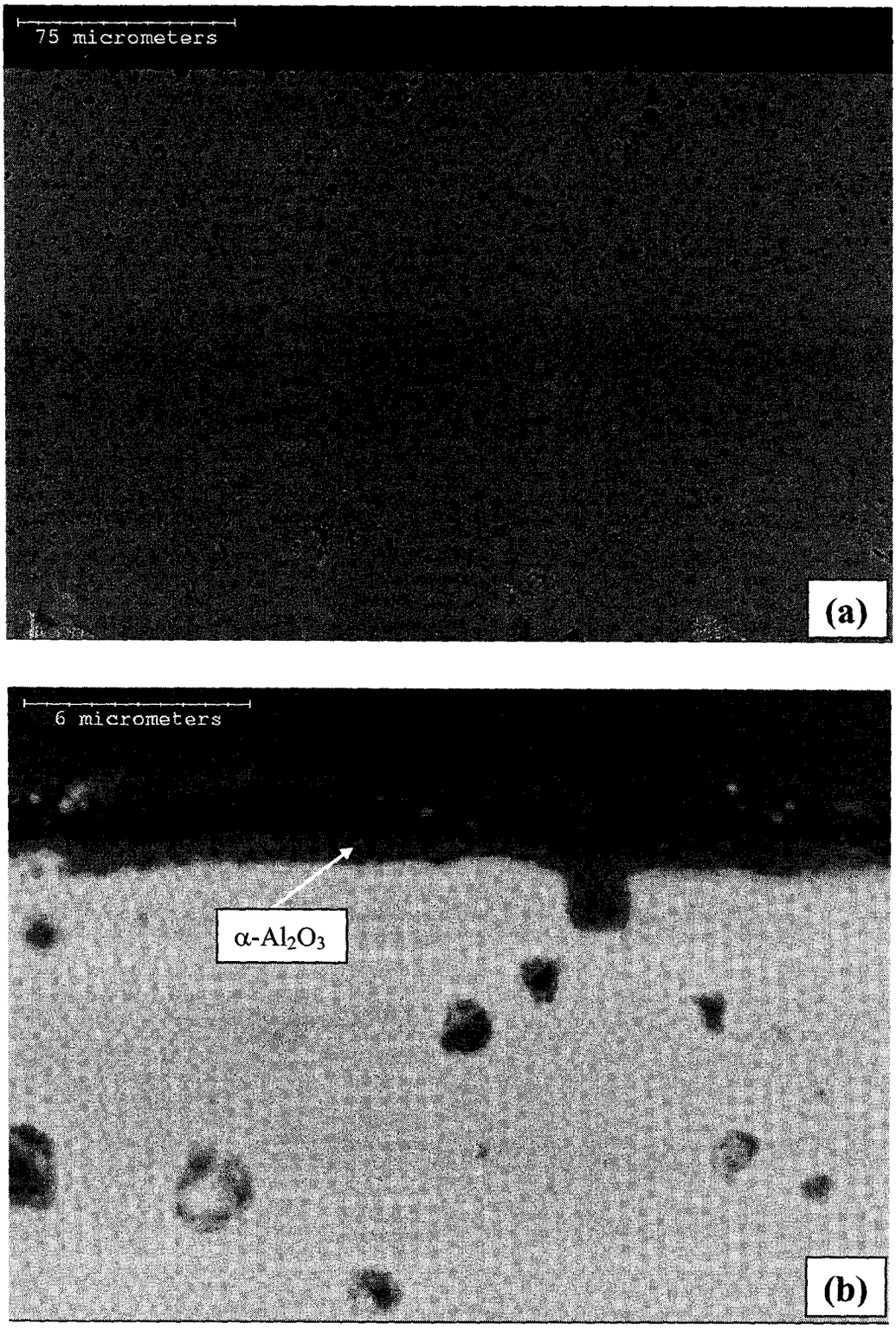

Figure 7-16. The cross-section view of the pure Ni_3Al coating after pre-oxidation at 1100 °C in H_2-0.6%H_2O for 24 hr: (a) the cross section of coating, (b) the oxide layer induced by the pretreatment.

(b) Pre-oxidized Pure Ni_3Al Coating (80+0)

Figs. 7-17 depict the surface morphologies of the pre-oxidized pure Ni_3Al coating after metal dusting for 50 hr.

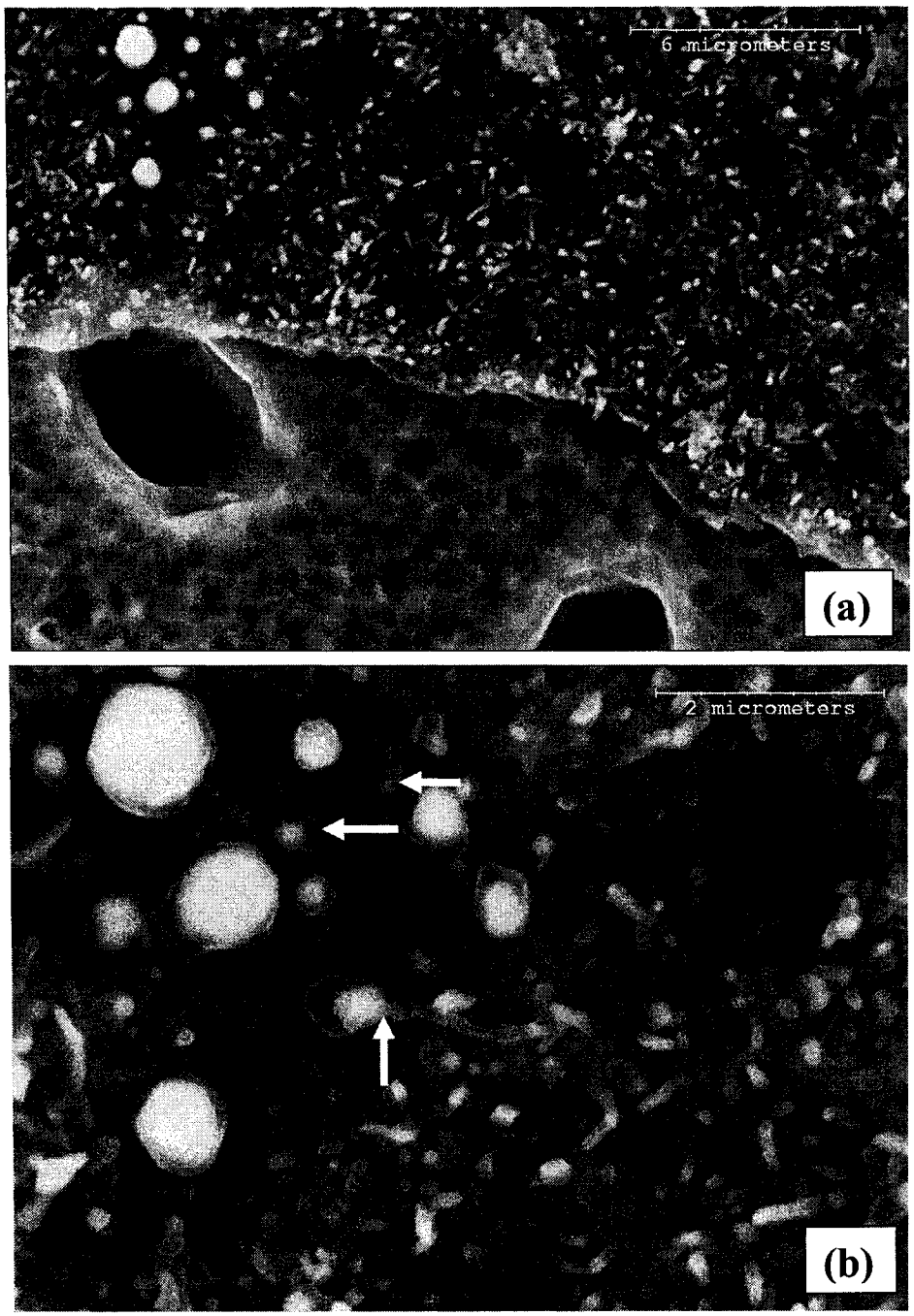

Figure 7-17. The surface morphology of the pre-oxidized pure Ni_3Al coating after metal dusting for 50 hr: (a) the low-magnification view; (b) the high-magnification view showing the formation of catalytic coke.

As shown in Fig. 7-17 (a), the coating surface after metal dusting differed little from that just after pre-oxidation in Fig. 7-14 (b). No noticeable coke was seen on the coating surface, except that several fine catalytic coke filaments were nucleated at Ni-rich particles (indicated by white arrows in Fig. 7-17 (b)). The XPS spectrum of the coating surface after metal dusting for 50 hr is similar to that of the as-pre-treated. The intensity of C peaks in the two spectrums also differs little, indicating negligible coke formation from testing. With time, the coating surface suffered from accelerated coke deposition. The micrograph of the coating surface, which is covered with numerous coke clusters after 200 hr, is shown in Fig. 7-18 (a). The spalled areas were no longer visible after pre-oxidation, probably because they were covered by coke. The coke clusters are highly filamentous at high magnification (Fig. 7-18 (b)). By 500 hr, coke clusters on the pre-oxidized pure Ni_3Al coating have been intensified (Fig. 7-19 (a)). The catalytic filamentous coke with Ni-rich particles at filament tips was predominant (Fig. 7-19 (b)). Coke scraped from the coating surface was analyzed by XRD to be mainly graphite and Ni (Table 7-3). The coating surface morphology after removal of coke is presented in Fig. 7-20 (a). Significant pitting attack, an indication of severe metal dusting, is clearly observed. According to the EDS spectrum in Fig. 7-20 (b), the pitting area was mixed with high quantities of C, Al, O, and Ni along with certain substrate elements including Cr, Mn, Fe, and Si.

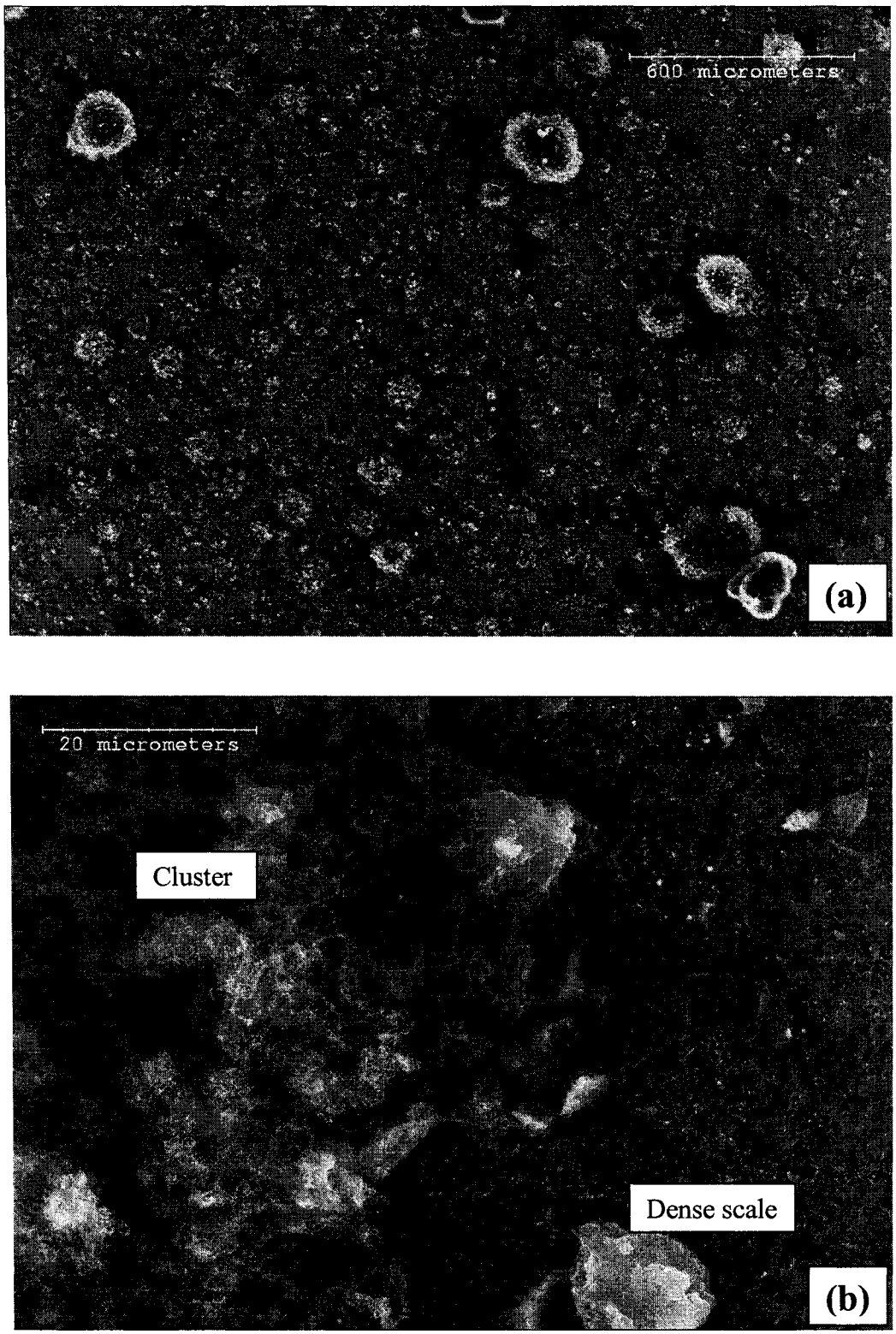

Figure 7-18. The coke on the pre-oxidized pure Ni_3Al coating after metal dusting for 200 hr: (a) the low-magnification view; (b) the high-magnification view.

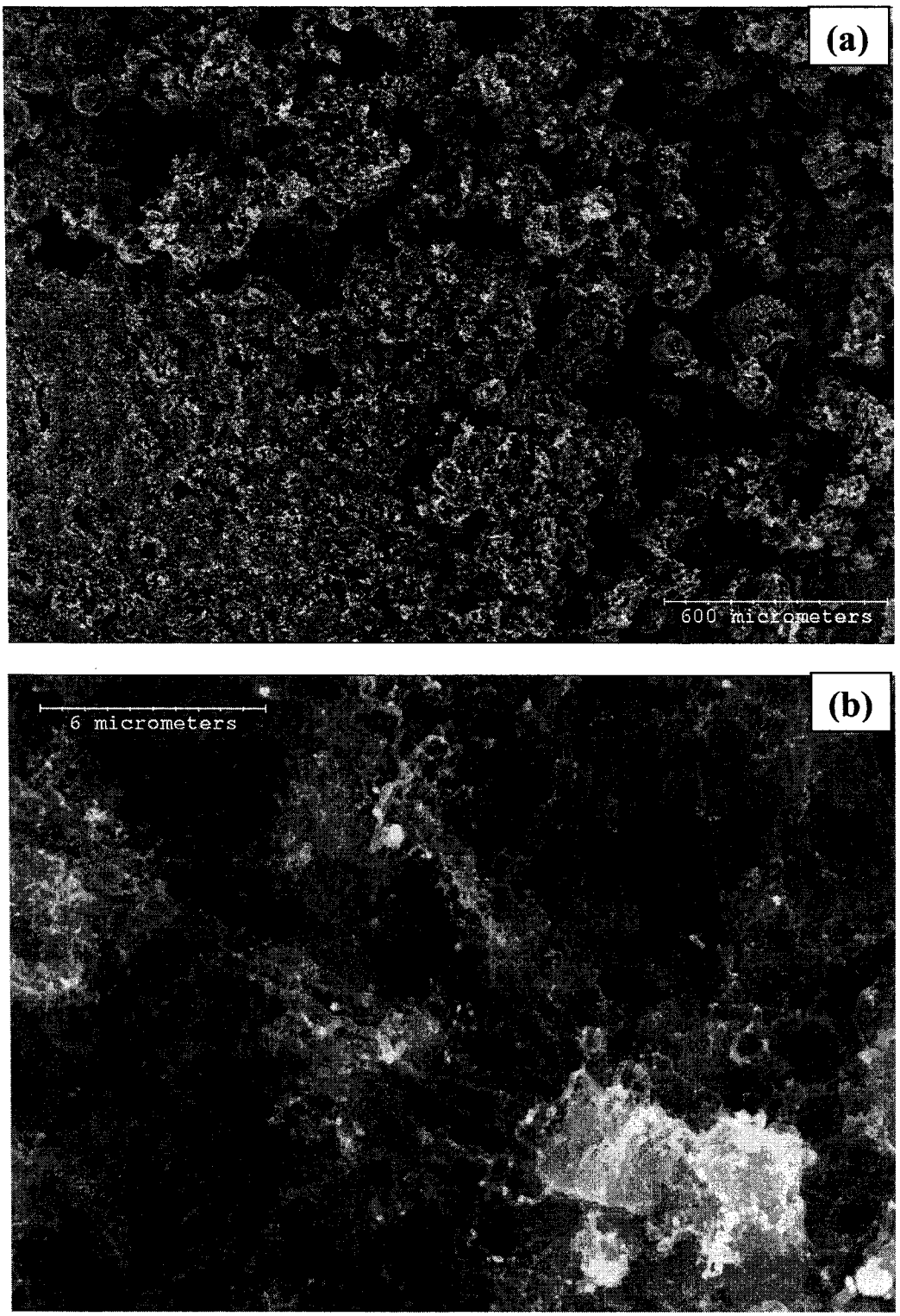

Figure 7-19. The surface morphology of the pre-oxidized pure Ni_3Al coating after metal dusting for 500 hr: (a) the massive coke on the coating surface; (b) the high-magnification view of the coke.

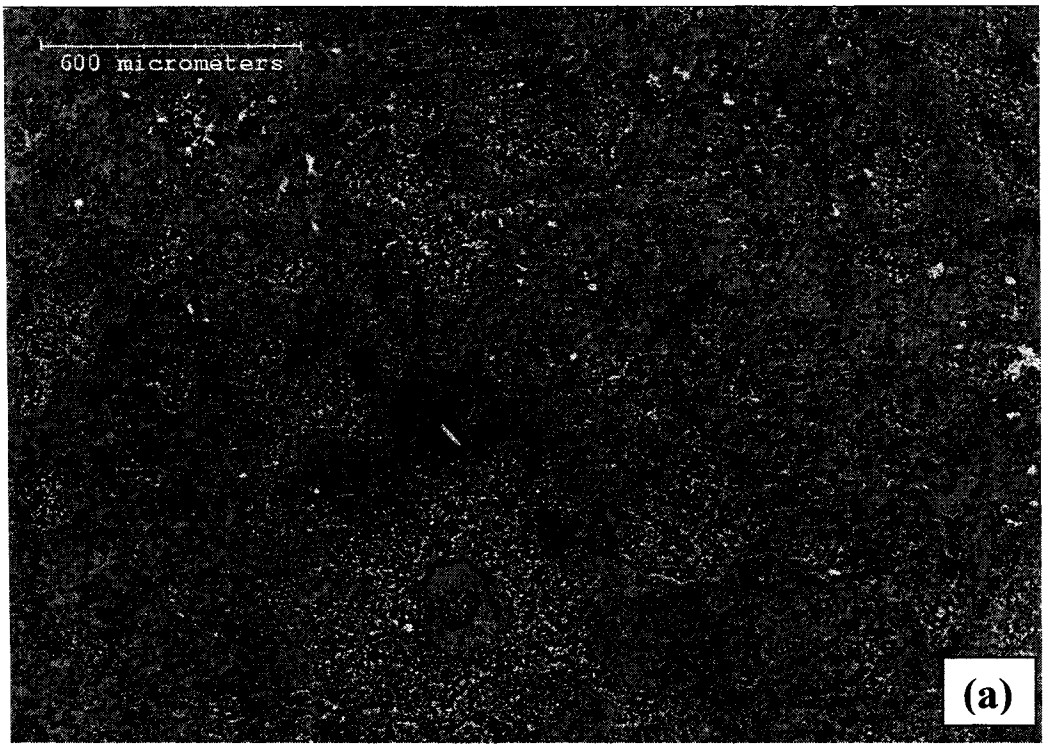

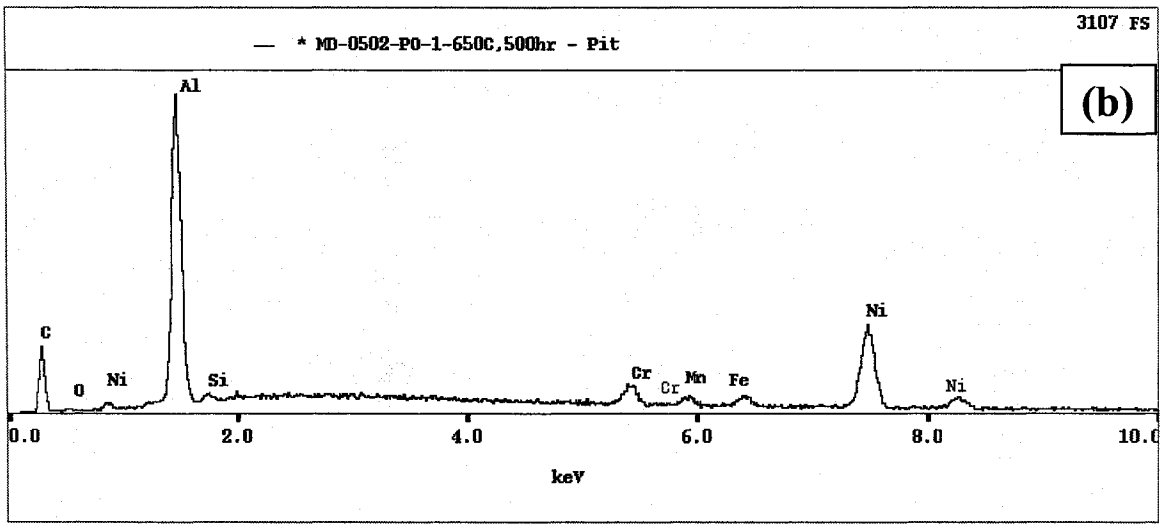

Figure 7-20. The surface morphology of the pre-oxidized pure Ni_3Al coating after metal dusting for 500 hr (after the scraping of coke): (a) the severe pitting on the coating surface; (b) the EDS analysis of the pitting area.

Figs. 7-21 (a) and (b) show the cross-sections of the pre-oxidized pure Ni_3Al coating after metal dusting for 200 hr. According to Fig. 7-21 (a), some pits had been nucleated by 200hr. They are located under the thick coke protrusions. Ni-rich particles were dispersed within the coke protrusions (Fig. 7-21 (b)). A Ni-rich band existed along the coating surface within the pit (Fig. 7-21 (b)). By 500 hr, pits became bigger and attached to each other at some locations (Fig. 7-22 (a)). Coke protrusions on the pits had also grown to larger dimensions. These observations are comparable to those of the un-pre-oxidized 80+5 (9-15 nm) coating after metal dusting for 500 hr (Fig. 13 (a)). The coke protrusions in Fig. 7-22 (b) had a stratified structure, which was typical of other coating samples. This structure might result from a cyclic deposition of coke. The morphology of the pit / the coating interface is shown in Fig. 7-22 (c). The coke within the pits above the coating matrix was rich in Ni, Al, O, and C, with minor amount of Fe, Cr, and Mn. The coating matrix contained mainly Ni and Al, plus small amount of Fe and Cr. There is a narrow Al-depleted zone on top of the coating matrix (Fig. 7-21 (b)). In contrast, the coating surfaces free of carbon attack were always covered with a compact Al_2O_3 scale, as shown in Fig. 7-22 (d).

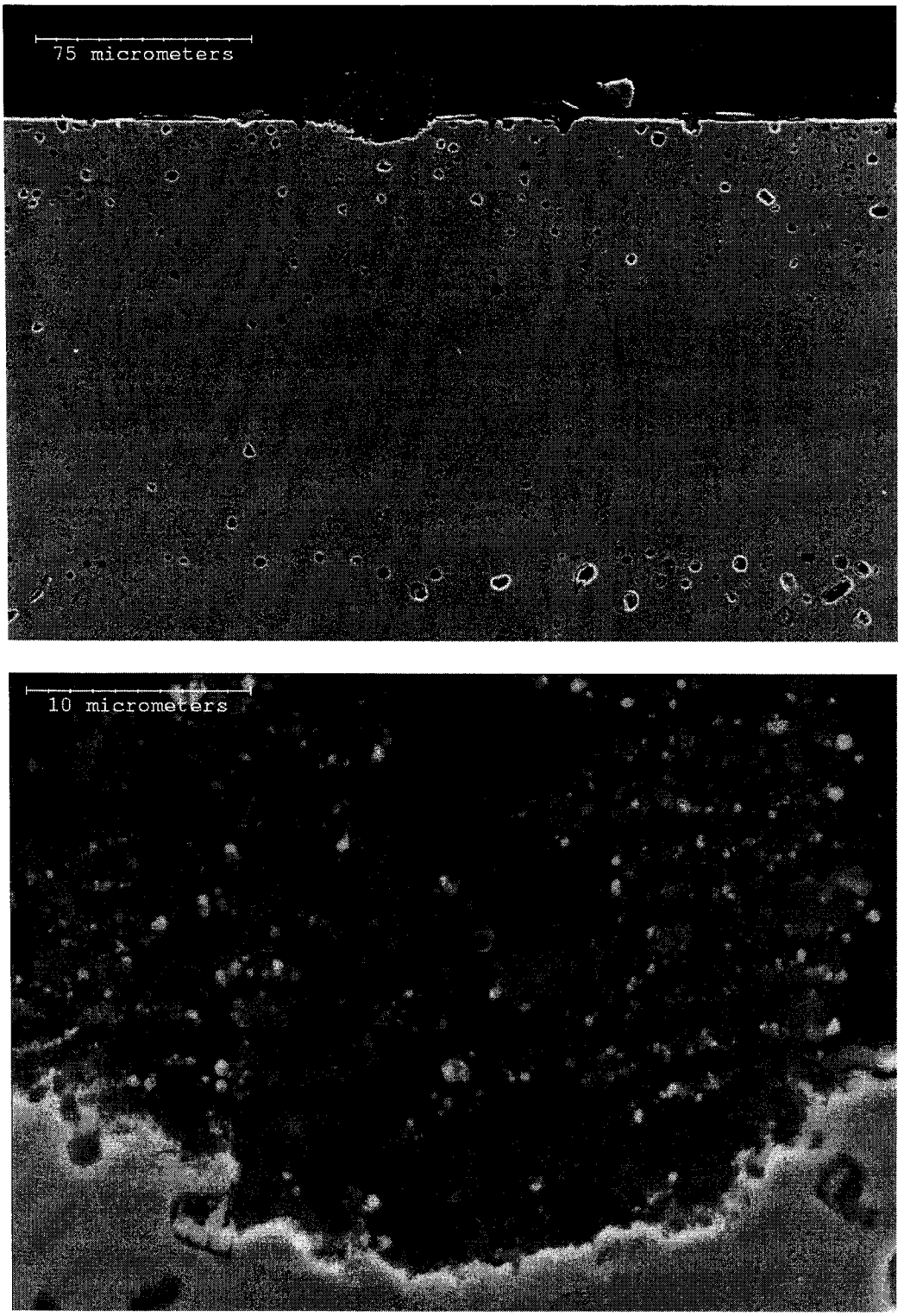

Figure 7-21. The cross section of the pre-oxidized pure Ni_3Al coating after metal dusting for 200 hr: (a) the low-magnification view; (b) the high-magnification view of a typical pit.

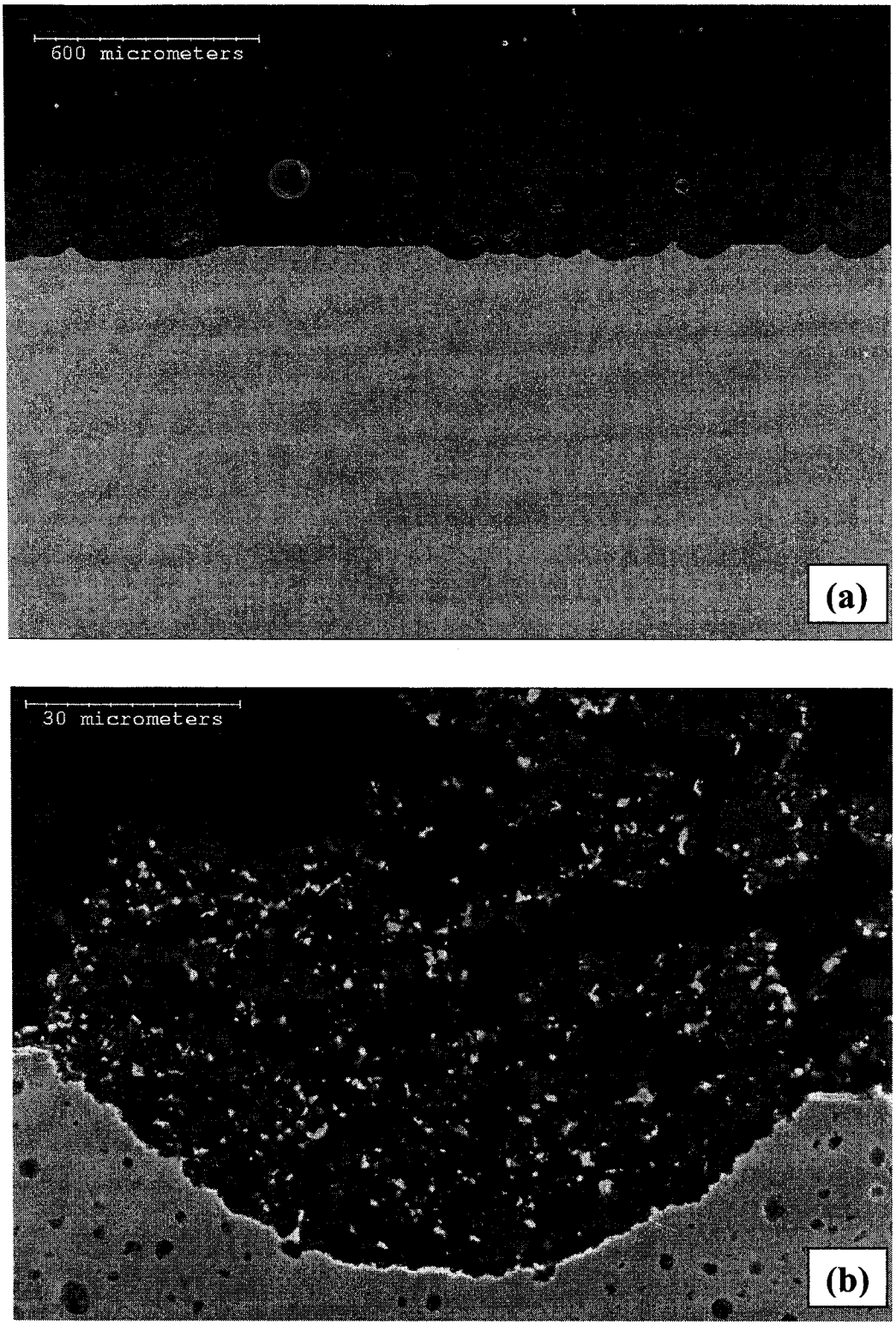

Figure 7-22. The cross section of the pre-oxidized pure Ni_3Al coating after metal dusting for 500 hr: (a) the low-magnification view; (b) the high-magnification view of a typical pit; (c) the pit / the coating matrix interface in (b); (d) the view of the area without pitting.

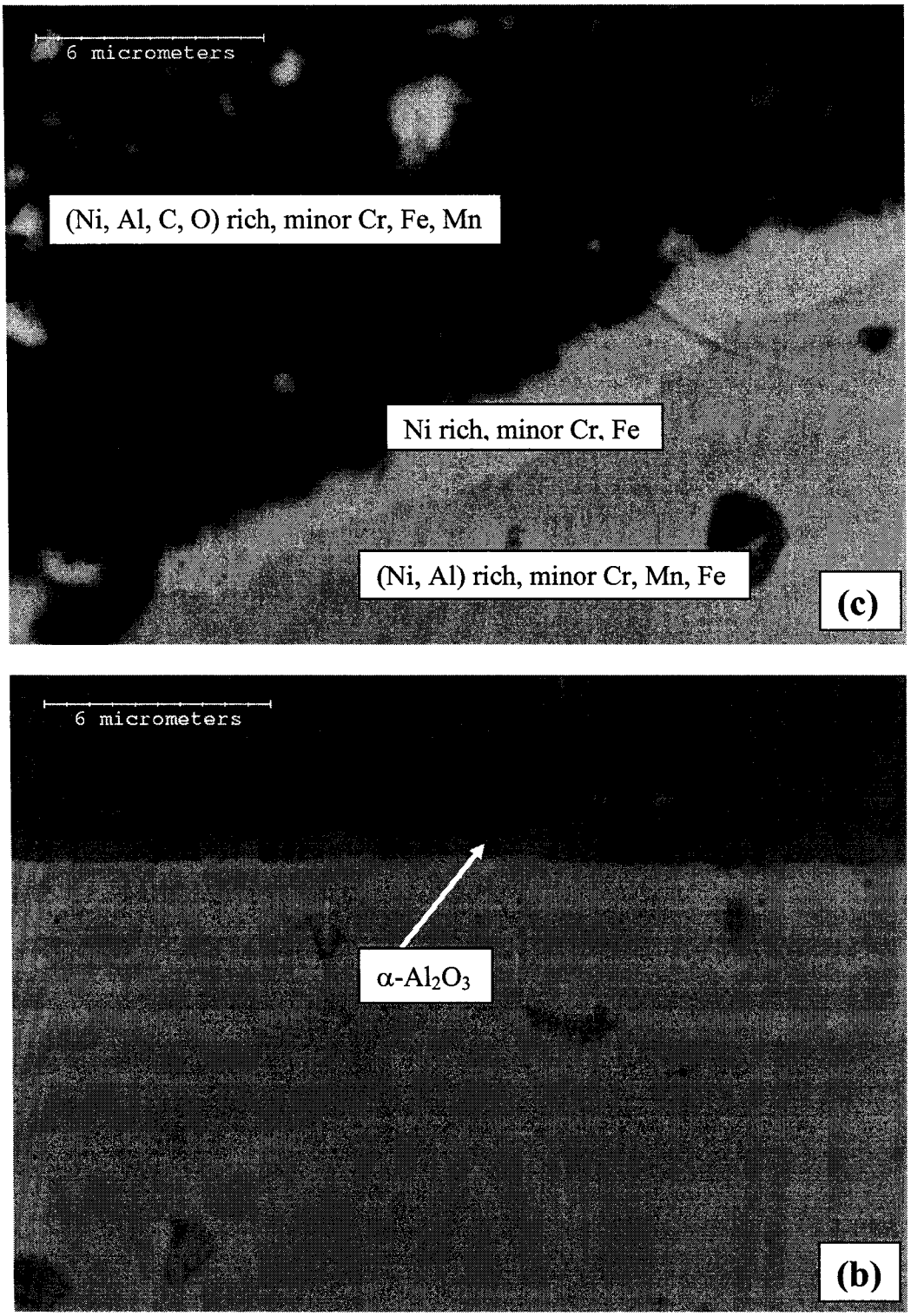

Figure 7-22 (continued).

(c) Pre-oxidized 5 μm CeO_2-dispersed Ni_3Al Coatings

The two pre-oxidized 5 μm CeO_2-dispersed Ni_3Al coatings exhibited a metal-dusting behavior similar to that of the pre-oxidized pure Ni_3Al coating. Coke formation was slow in the early stage of metal dusting, but accelerated after 200 hr. Figs. 7-23 (a)-(d) provide the surface morphologies of the two coatings after 500 hr.

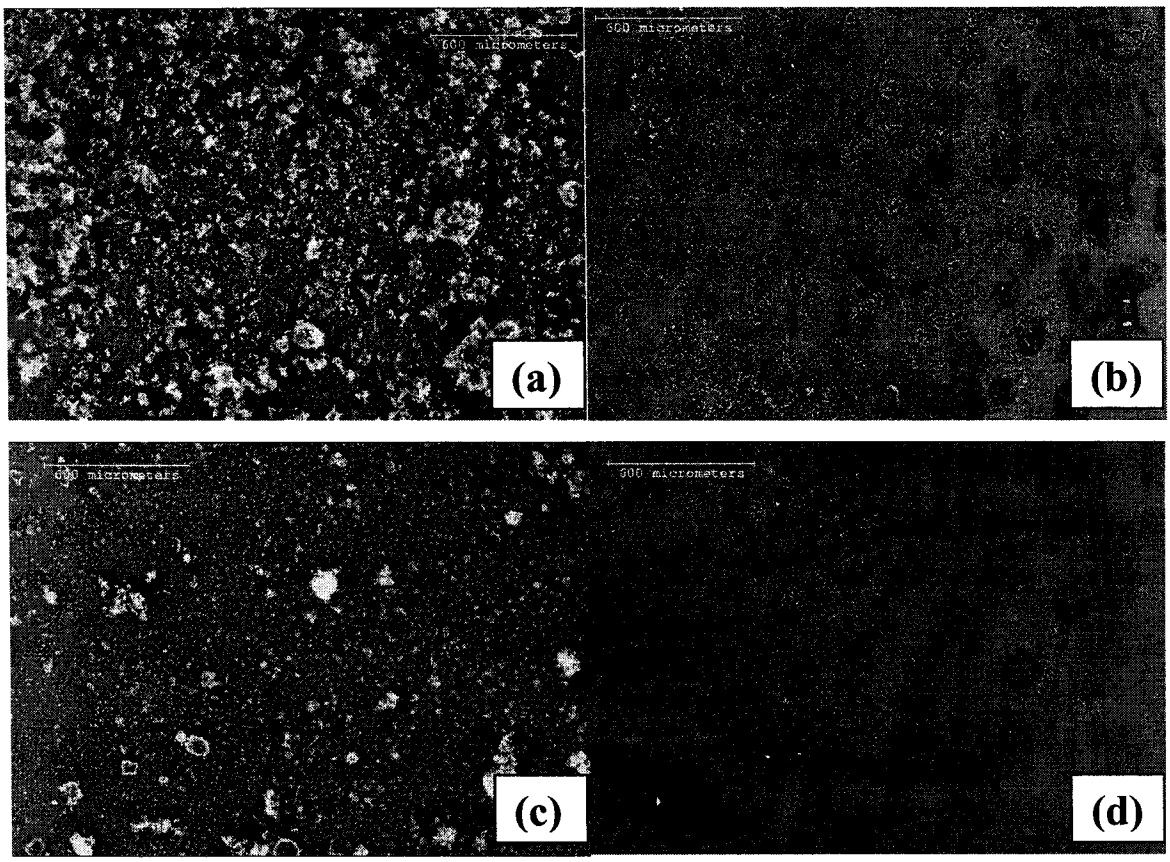

Figure 7-23. The surface morphologies of the pre-oxidized 5μm CeO_2-dispersed Ni_3Al coatings after metal dusting for 500 hr: (a) the 80+5 (5 μm) coating; (b) the 80+5 (5 μm) coating after the removing of coke; (c) the 80+1 (5 μm) coating; (d) the 80+1 (5 μm) coating after the coke deposits were removed.

Although coke formation on the pre-oxidized 80+5 (5μm) coating (Fig. 7-23 (a)) was minor compared with that on the pure Ni_3Al coating (Fig. 19 (a)), many coarse coke clusters were nonetheless visible on the surface. Coke composition on the pre-oxidized 80+5 (5 μm) coating was determined to be graphite and Ni (Table 7-3), which was

similar to the pre-oxidized pure Ni_3Al coating after metal dusting for 500 hr. The coating surface after removal of the coke deposit showed significant pitting attack (Fig. 7-23 (b)). The severity of pitting, however, appeared less than that on the pre-oxidized pure Ni_3Al coating (Fig. 20 (a)). The pre-oxidized 80+1 (5 μm) coating after 500 hr of metal dusting exhibited much less coke formation and pitting attack than the pre-oxidized 80+5 (5 μm) coating and the pre-oxidized pure Ni_3Al coating (Figs. 7-23 (c) and (d) respectively). Coke clusters on the pre-oxidized 80+1 (5 μm) coating (Fig. 7-23 (c)) were much finer than those on the pre-oxidized 80+5 (5 μm) coating (Fig. 7-23 (a)). Pitting attack was found only at some local areas, and the coating surface remained mostly undamaged (Fig. 7-23 (b)).

The evolution of cross-sectional morphologies of the pre-oxidized 5 μm CeO_2-dispersed Ni_3Al coatings with time was similar to that of the pre-oxidized pure Ni_3Al coating. Some small pits were seen on the coating at 200 hr. With increasing time, pitting expanded laterally and in depth, and coke protrusions began to build up as well. Typical morphologies of the pre-oxidized 80+5 (5 μm) coating upon 500 hr exposure are shown in Figs. 24 (a) and (b). Surface areas with pitting attack on the pre-oxidized 5 μm CeO_2-dispersed Ni_3Al coatings (Fig. 24 (a)) were found significantly less than those on the pre-oxidized pure Ni_3Al coating (Fig. 7-22 (a)). A zone rich in Ni was also observed on the coating matrix within a pit (Fig. 7-24 (b)). Pitting attack did not occur on surfaces with intact protective scale.

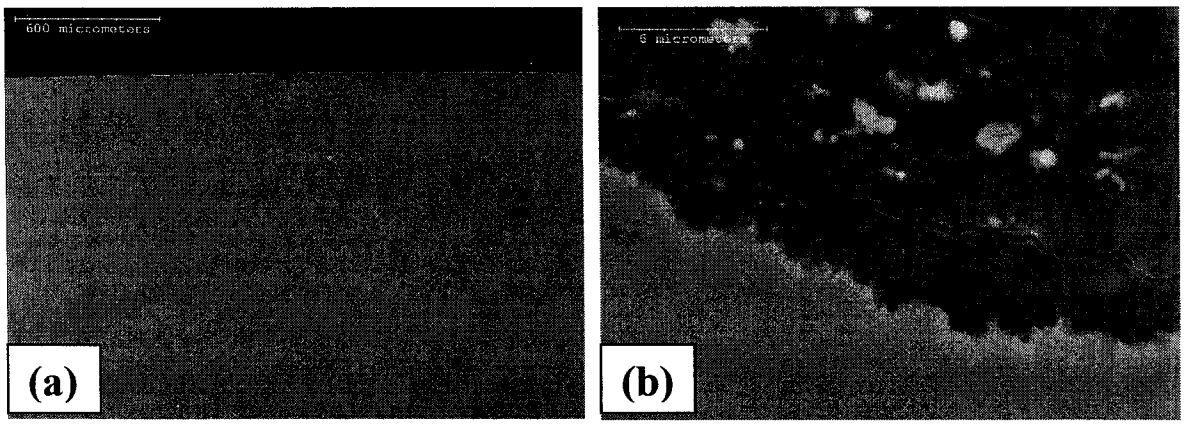

Figure 7-24. The cross section of the pre-oxidized 80+5 (5 μm) coating after metal dusting for 500 hr: (a) at low magnification; (b) at high magnification.

(d) Pre-oxidized Nano CeO_2-dispersed Ni_3Al Coatings

The surface morphologies of the two pre-oxidized nano CeO_2-dispersed Ni_3Al coatings after 200hr exposure are shown in Fig. 7-25. There were much fewer coke clusters on these coatings compared to those of the pre-oxidized pure and 5 μm CeO_2-dispersed Ni_3Al coatings. The high-magnification micrograph in Fig. 7-25 (b) revealed only scattered coke filaments at some Ni-rich catalytic sites. Fig. 7-26 shows the morphologies after 500 hr of exposure. According to Figs. 7-26 (a) and (b), coke clusters at 500 hr were comparable to those at 200 hr of exposure. Pitting attack on both coating surfaces was negligible, although it appeared even lesser on the 80+5 (9-15 nm) coating (Fig. 7-26 (c) and (d)). No pitting attach was observed on the cross-section of coatings after 500 hr (Fig. 7-27 (a)). This could be related to the presence of a close-packed thin layer of α-Al_2O_3 on the surface (Fig. 7-27 (b)).

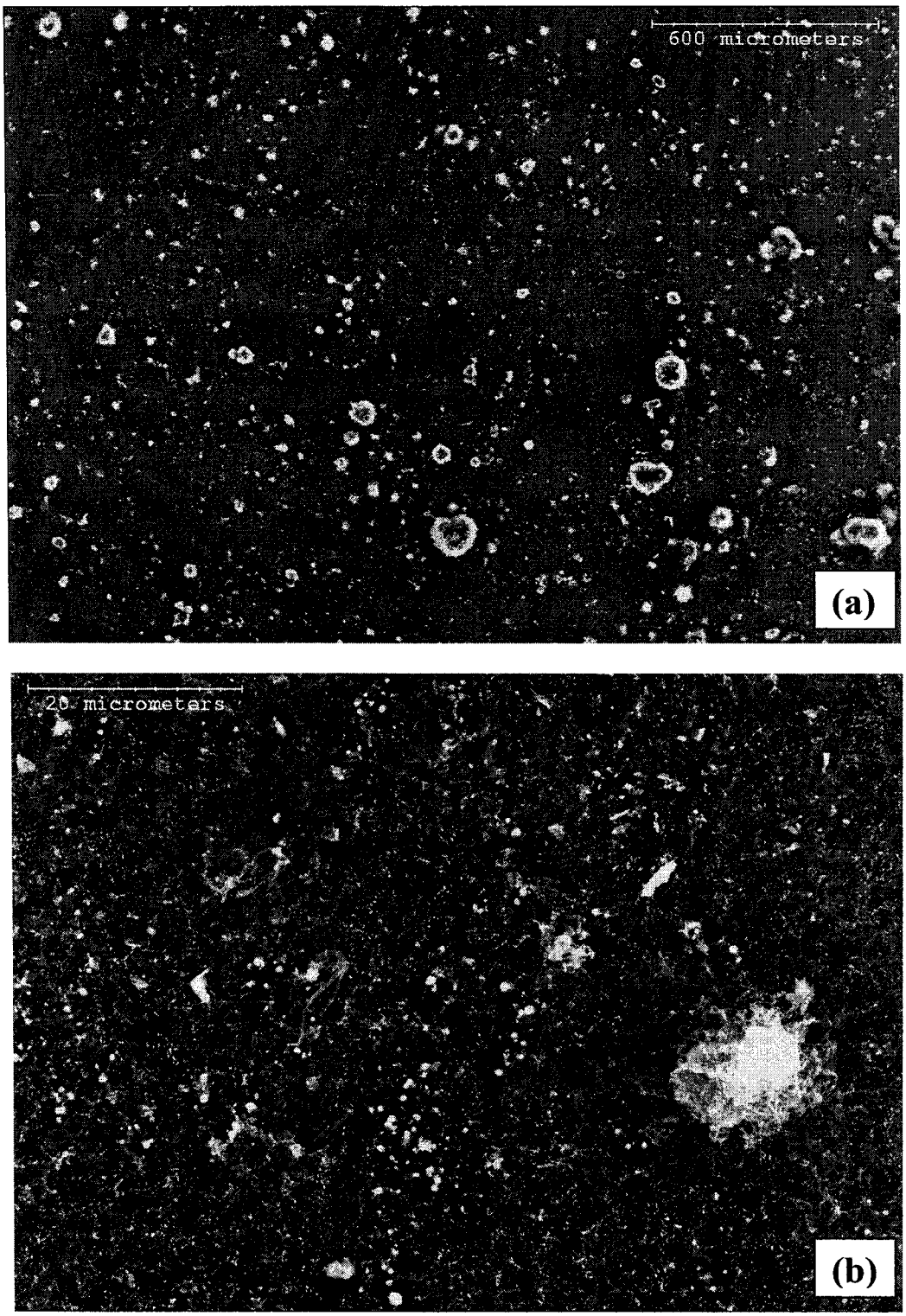

Figure 7-25. The surface morphology of the pre-oxidized 80+5 (9-15 nm) coating after metal dusting for 200 hr: (a) at low magnification; (b) at high magnification.

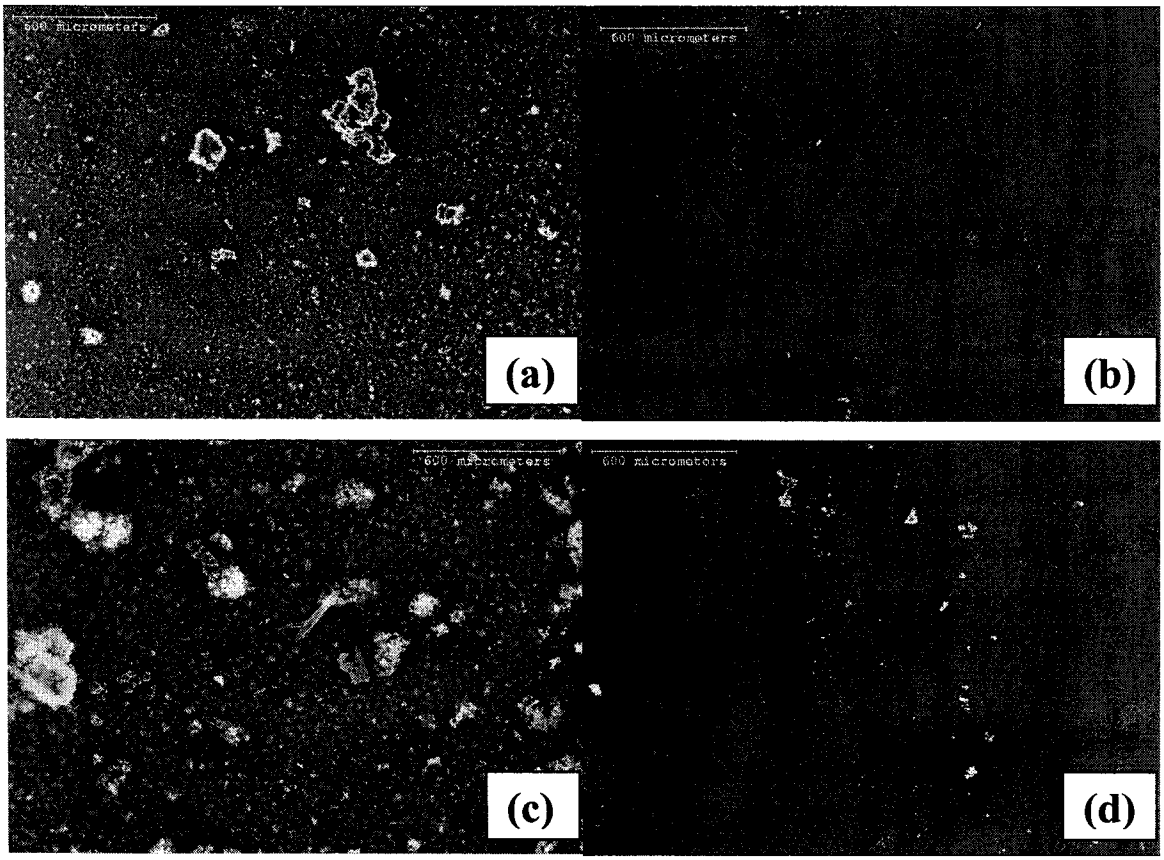

Figure 7-26. The surface morphologies of pre-oxidized nano CeO_2-dispersed Ni_3Al coatings after metal dusting for 500 hr: (a) the 80+5 (9-15 nm) coating; (b) the 80+5 (9-15 nm) coating after the removing of coke; (c) the 80+1 (9-15 nm) coating; (d) the 80+1 (9-15 nm) coating after the removing of coke.

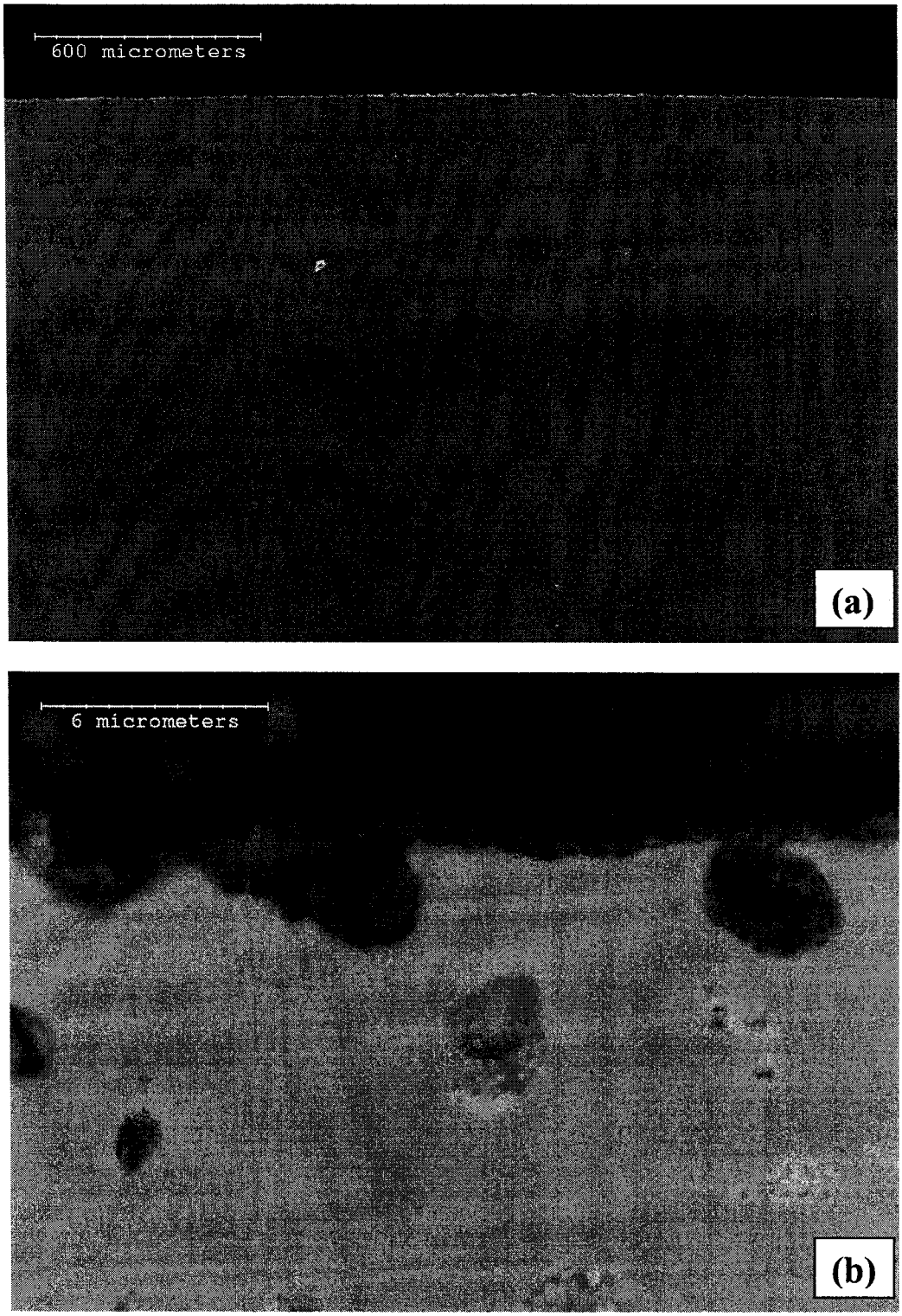

Figure 7-27. The cross section of the pre-oxidized 80+5 (9-15 nm) coating after metal dusting for 500 hr: (a) at low magnification; (b) at high magnification.

7.4 Discussion

7.4.1 Un-pre-oxidized Coatings

(a) General Characteristics

In this study, un-pre-oxidized Ni_3Al-based coatings were observed to be susceptible to metal dusting as well as coke formation when exposed to 24.4%CO-73.3%H_2-2.3%H_2O gas mixtures at 650 °C. Metal dusting and coke formation appear to be more severe on the two nano CeO_2-dispersed Ni_3Al coatings. In the early stage of metal dusting, only catalytic coke filaments were nucleated on all the coating surfaces. Catalytic coke continued to build up with time, and the coating surface began to suffer from local pitting attack by graphite carbon. The coating matrix was then delaminated into fine particles by the inward growth of graphite. The catalytic coke derives a heterogeneous reaction of hydrocarbon feedstock with metals such as Fe and Ni, which are excellent catalysts for carbon deposition [6]. Recent studies [6, 33, 35] found that sources of catalysts included transiently-formed FeO, NiO or (Fe,Ni,Cr)-spinel, which would be reduced to Fe, Ni, or Fe-Ni particles by reducing atmospheres. Formation of filamentous coke in the early stage of metal dusting on the current Ni_3Al base coatings (e.g., Fig. 7-2(a)) suggests that the surfaces of Ni_3Al base coatings contain abundant catalytic sources, primarily Ni particles, according to EDS and XRD analysis of the coke. No evidence of Al-rich oxide scale was found on coating surfaces even after 500 hr, nor were carbides observed either in the coke layer or in the coating matrix during metal dusting. The metal-dusting behavior of the current Ni_3Al base coatings is very similar to that of Ni and Ni base alloys free of Cr, which is characterized by (a) direct inward growth of graphite into the matrix, (b) catalytic coke formation at Ni particles [1, 4, 8], and (c) disintegration of metal matrix at the end. The short-term metal dusting behavior of the pure Ni_3Al coating in our study contradicts that reported by Strauß et al. [22], who observed severe metal dusting only in Fe_3Al base alloys and Fe-containing Ni_3Al base alloys, but little metal dusting in the pure Ni_3Al alloy when exposed to CO-H_2-H_2O with $a_c = 41.5$ at 650 °C for 48 hr.

(b) Oxidation of Ni_3Al-Based Coatings

The formation of protective Al_2O_3 on Ni_3Al alloys is complicated. It is strongly affected by composition (the Al content), temperature, oxygen partial pressure, and alloying elements. According to the Wagner's internal-oxidation theory [36], Al_2O_3 particles precipitated in an internal-oxidation zone (IOZ) shall exceed a critical concentration to become an external Al_2O_3 scale. High Al content, high temperature, and low oxygen partial pressure promote the transition from internal oxidation to external oxidation. Oxidation of Ni_3Al alloys at low temperatures ranging from 500-730 °C and high oxygen partial pressures has been studied by Pérez et al. [29, 30] and Haerig et al. [31]. They found that an internal-oxidation zone (IOZ), mixed with a Ni matrix and selectively oxidized Al_2O_3 particles, formed first, followed by the intermediate Ni layer and finally the outer NiO layer. A thin Al_2O_3 scale formed only after a considerable period of time. At 635 °C, a close-packed Al_2O_3 scale would not form until 200 hr [30]. Haerig et al. [31] also observed a 2-3 nm thick native oxide layer, consisting of NiO and amorphous Al_2O_3, which always formed on the pure Ni_3Al alloy during exposure at room temperature in air. At low oxygen partial pressure, $p_{O_2} < 10^{-8} atm$, and low temperature (below 800 °C), Al_2O_3 scale, or possibly Ni particles on the surface, would be exclusive [31, 37-40]. Venezia et al. [39] reported that only γ-Al_2O_3 was formed initially on the pure Ni_3Al alloy above 700 °C, whereas two types of Al_2O_3, an amorphous Al_2O_3 and an intermediate oxide with weaker Al-O bonds, were observed below 700 °C.

The CO-H_2-H_2O in this study has a theoretical oxygen partial pressure of $p_{O_2} = 6.35 \times 10^{-26} atm$ at 650 °C, as mentioned earlier. Ni_3Al base coatings will experience oxidation in such an oxygen-deficient atmosphere. Consequently, the formation of NiO on our Ni_3Al base coatings seems impossible, whereas the formation of Al_2O_3 is favored (Table 7-2). Al_2O_3 scale is inert to catalytic coke and well resistant to carbon attack. The work in Chapter 6 also revealed that our Ni_3Al-based coatings exhibited superior carburization resistance at 850 °C and 1050 °C in the highly reducing 2%CH_4-H_2 atmospheres. This was due to slowly-formed Al_2O_3 scale. As a result, it is expected that our Ni_3Al base coatings should exhibit resistance to metal dusting, which

contradicts the experimental observations. Strauß et al. [22] and Schneider et al. [23] also reported a lack of Al_2O_3 scale on the pure Fe_3Al alloy during metal dusting at 650 °C in CO-H_2-H_2O. Our Ni_3Al base coatings did suffer oxidation during metal dusting at 650 °C by forming Ni-Al-O clusters, which were detected on the coating surface after 50 hr exposure (Fig. 7-2 (a) and (c)). In this study, pitting attacks had occurred only at a few locations on the surface during the early stage of metal dusting. This suggests that an Al-rich oxide scale might have been present on our Ni_3Al-based coatings prior to or during metal dusting. The growth rate of scale at a temperature of 650 °C is very slow, and the scale is too thin to be detected. As proposed by Venezia et al. [39], below 700 °C the growth of Al_2O_3 on the pure Ni_3Al alloy was controlled by the slow diffusion of oxygen through amorphous Al_2O_3 scale. Rapid pitting attack on the Ni_3Al-based coatings during metal dusting is another crucial factor for the absence of a healing Al_2O_3 scale, a matter that will be further discussed later.

(c) Mechanisms of Coke Formation and Metal Dusting

Many catalytic coke filaments containing Ni or Ni-rich particles were formed on all the Ni_3Al base coatings in the early stage of metal dusting. According to the above discussion, these catalytic Ni or Ni-rich sources could derive from NiO oxides in the native oxide layer, or Ni particles formed during selective oxidation of Al_2O_3, or regions of Ni-Al matrices free of Al_2O_3 scale. At these catalytic sites, CO gas molecules are adsorbed and dissociated to C atoms and O atoms [3, 4, 10, 33, 41]. C atoms diffuse into the Ni matrix, where a saturation of C atoms can cause a nucleation of graphite, especially at grain boundaries. Graphite grows as more C atoms diffuse inward through the Ni matrix. At the same time, the matrix disintegrates, which in turn intensifies the above processes. If the catalytic particles on the coating surfaces or the metal particles from disintegration were of nano sizes, carbon atoms dissolved in the particle, may precipitate out on the particle surface rather than in the interior of the particle [3, 10, 41]. This forms the body of the carbon filament, while other carbon atoms migrating via the particle surface build up the outer skin of the filament. Consequently, the particle will be lifted up from the coating matrix as more carbon atoms are deposited at the particle/the graphite filament interface, resulting in an outward growth of the graphite filament. This

mechanism concerning the formation of nano carbon filaments may well explain the observation that a carbon filament on all the coating surfaces during metal dusting is always of nano size and contains a nano Ni-rich particle at its tip. This phenomenon was also commonly observed on Fe-based or Ni-based alloys or catalysts [3, 10, 33, 34, 42]. However, Schneider et al. [8] and Grabke [1, 4, 43] believe that compressive stresses deriving from the inward growth of graphite into the matrix cause outward diffusion of metal elements (Fe or Ni) via the graphite filaments, and nano metal particles form due to the subsequent agglomeration. The validity of this mechanism is still being debated [3].

Localized carbon attack on Ni_3Al-based coatings was observed during the early stage of metal dusting. This may result from a poor coverage of Al_2O_3 scale at some locations or the presence of defects in Al_2O_3 scale. In a disintegrated area, Ni-atoms will be transported outward, while Al atoms are oxidized and precipitated in the coke as Al_2O_3 particles. The latter may stay in the inner portion of the coke layer, as they are inert for carbon deposition. This can explain why the coke outside a pit contained a higher concentration of Ni, whereas the coke within a pit has a higher Al content. The degradation may become intensified at a given location, and may also take place at less vulnerable locations with time.

(d) Effect of CeO_2 Particles

It is believed that CeO_2 facilitates the formation of Cr_2O_3 or Al_2O_3 on Cr-or Al-containing alloys or coatings [44-47]. This effect shall offer our CeO_2-dispersed Ni_3Al coatings with much better resistance to metal dusting and coke formation than the pure Ni_3Al coating. However, this is contrary to our experimental results, in which the CeO_2-dispersed Ni_3Al coatings—especially the two nano CeO_2-dispersed coatings—had inferior resistance to metal dusting and coke formation. Strauß et al. [17] found that as little as 0.05wt% Ce reduced the resistance of Alloy 800 to metal dusting. However, no explanation was provided for this effect. It is well-known that the addition of CeO_2 can improve Ni catalysts for methane reforming [48-54]. The beneficial effects of CeO_2 include (a) maintaining high specific surface area of oxide supporters at high temperatures, (b) enhancing the dispersion of Ni particles, (c) interrupting the sintering of

Ni particles, and (d) mitigating carbon deposition on Ni particles. Hettige et al. [55] reported that carbon deposition on the Ce/Al_2O_3 catalyst during the oxidation of cyclohexane was as low as that on the pure Al_2O_3 catalyst. Consequently, CeO_2 itself cannot be responsible for the severe carbon deposition and metal dusting observed on Ni_3Al-based coatings in this study.

CeO_2-modified Ni catalysts always have a low Ni loading, less than 10wt% [48-50, 52, 53, 56]. Ni loadings above 10wt% can cause a loss of full dispersion of fine Ni particles due to sintering, which, in turn, reduces the conversion efficiency of Ni catalysts and lead to an accelerated carbon deposition [53]. Our CeO_2-Ni_3Al-based coatings are bulk materials with high Ni content, more than 85wt%, which are distinct from CeO_2-modified Ni catalyst systems. Carbon deposition and pitting attack were observed to take place preferentially in Ce-rich regions (e.g., Figs. 7-6 (a) and (b), and Fig. 7-9 (b)). This suggests that those areas might be highly catalytic, and that CeO_2 particles may have enhanced the formation of catalytic sources such as Ni and NiO particles.

Figs. 7-28 (a)-(d) depict the cross-sections of CeO_2-dispersed Ni_3Al coatings prior to metal dusting. According to these figures, the 80+5 (5 μm) coating (Fig. 7-28 (a)) contained more CeO_2 particles (white phases) than the 80+1 (5 μm) coating (Fig. 7-28 (b)). Matrix material surrounding white CeO_2 particles has invariably shown less darkness on backscattered electron micrograph, probably as a result of a lower Al content in those regions. This can be seen also in the 80+5 (9-15 nm) coating, although individual nano particles are not discernible. It is natural that more Ni-rich phases can be expected in the coatings with higher CeO_2 content. According to Chapter 3, an increase of the CeO_2 concentration in the plating bath increases CeO_2 particle content but decreases Al particle content in the Ni matrix. Consequently, some Ni phases with low Al content will be formed if the volume fraction of Al in the coating is lower than 30vol%, for example, the 80+5 (9-15nm) coating in Fig. 7-28 (d), which contains 29.83vol% of Al particles according to Table 7-1.

Previous work by Pettit [28] indicated that the lower the Al content in Ni-Al alloys and the temperature, the easier the formation of NiO during oxidation. Chapter 4 had also observed that Ni-rich oxide crystals were formed preferentially over CeO_2 particles during oxidation at 850 °C and 1050 °C in dry air. NiO seems unlikely to be formed in the current oxygen-deficient environment, $p_{O_2} = 6.35 \times 10^{-26} atm$. The recent works by Hultquist, et al. [57-61], however, found that noble metals such as Pt and reactive oxides such as Y_2O_3 and CeO_2 could significantly enhance the dissociation of O_2, and thus the effective oxygen activity at the gas/scale interface. Less stable As_2O_5 in GaAs [58] and NiO in NiAl [61] were found to be more dominant at the outmost oxide scale rich in Pt than that without Pt during oxidation under $p_{O_2} = 1.97 \times 10^{-6} atm$ at 500 °C and at 1050 °C, respectively. It is reasonable to assume that the presence of CeO_2 particles in the current Ni_3Al base coatings also promotes the dissociation of oxygen at the CeO_2-rich regions and increases the actual oxygen activity to such a level that the formation of NiO would be possible. NiO can be easily reduced to Ni under the current test conditions. The latter is directly related to the carbon deposition and subsequent metal dusting and pitting attack observed.

As for the worst performances of nano CeO_2-dispersed Ni_3Al coatings, the size of CeO_2 particles played a crucial role. Firstly, nano CeO_2 may be more potent than 5 μm CeO_2 for the dissociation of O_2. Secondly, the existence of CeO_2 can further enhance the formation of NiO owing to the reactive-element effect (REE) [62-64]. Czerwinski, et al. [62, 65] reported that the effectiveness of CeO_2 particles, in terms of the ability to supply Ce^{4+} ions, strongly depended on particle size, and CeO_2 particles above 10 nm could not serve as effective sources of Ce^{+4} ions, especially at low temperatures. As a result, nano CeO_2 will be more favorable to the formation of NiO than 5 μm CeO_2, and thus cause more coke formation and metal dusting. The 80+5 (9-15 nm) coating, since contained the largest fraction of Ni-rich phases, had the poorest resistance to metal dusting and coke formation.

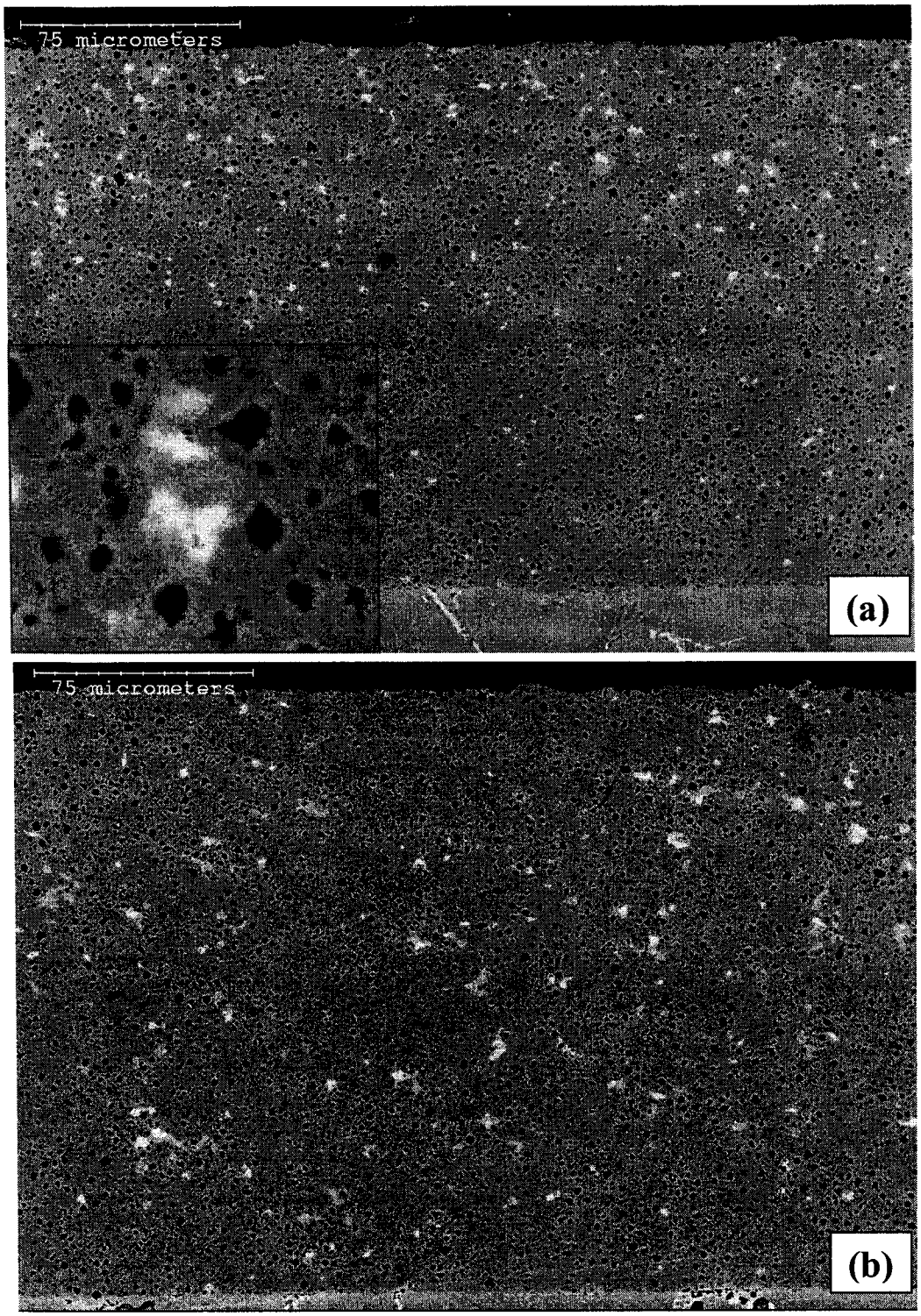

Figure 7-28. Backscattered Electron Micrographs showing the cross-sectional morphologies of the CeO_2-dispersed Ni_3Al coatings: (a) the 80+1 (5 μm) coating; (b) the 80+5 (5 μm) coating. (c) the 80+1 (9-15 nm) coating; (d) the 80+5 (9-15 nm) coating.

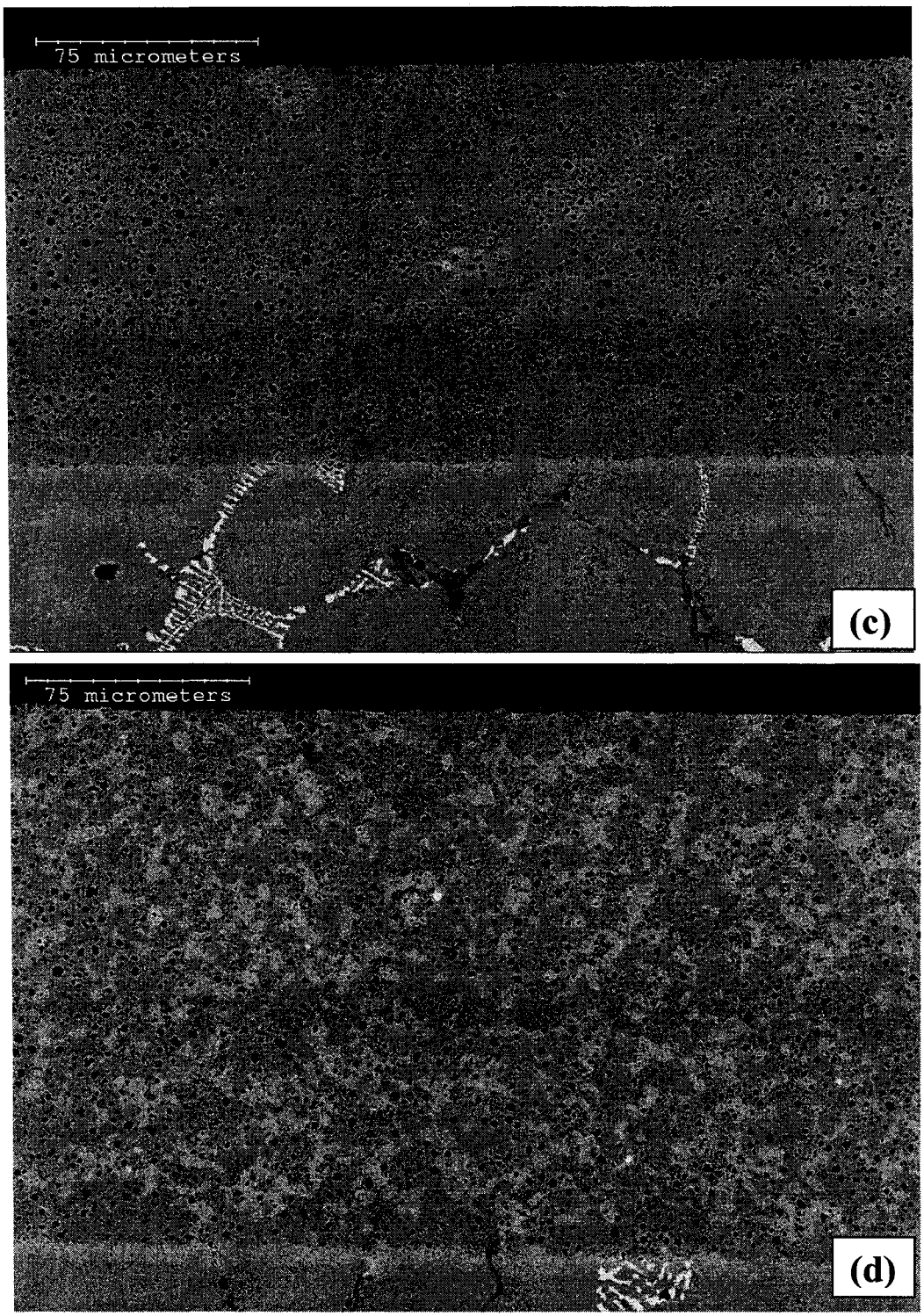

Figure 7-28. (Continued)

7.4.2 Pre-oxidized Coatings

(a) General Characteristics

According to our experimental results, the pre-oxidation treatment can improve the resistance of the pure and the CeO_2-dispersed Ni_3Al coatings to coke formation and metal dusting. All pre-oxidized coatings showed much less catalytic coke formation and pitting attacks than corresponding coatings without pre-oxidation during metal dusting up to 200 hr. This improvement can be attributed to the presence of a thin α-Al_2O_3 scale on the coatings formed during the pre-oxidation treatment. As the solubility of carbon in the oxides such as Cr_2O_3, Al_2O_3, and SiO_2 is negligible [43, 66], the ingress of carbon can be completely blocked if the oxide scale is fully dense and compact. It takes many years for carbon to accumulate to level of 100 to 1000 ppm in the oxide scale [26]. Furthermore, because Al_2O_3 scale is fully inert, the deposition of catalytic coke can then be greatly suppressed. The experimental results also showed that coke formation and metal dusting behaviors of the Ni_3Al base coatings were significantly affected by the integrity of α-Al_2O_3 scale. The pre-oxidized pure Ni_3Al coating experienced the most severe spallation after pre-oxidation, and also exhibited the least resistance to coke formation and pitting attack, which was comparable to the un-pre-treated 80+5 (9-15 nm) coating. The two pre-oxidized 5 μm CeO_2-dispersed Ni_3Al coatings had also suffered severe coke formation and metal dusting due to poor resistance to spallation during pre-treatment.

The two pre-oxidized nano CeO_2-dispersed Ni_3Al coatings had formed an ample coverage of α-Al_2O_3 scale by pre-treatment, and showed almost no metal dusting and much less coke formation. Al_2O_3 spallation leads to a direct exposure of the bare coating matrix to CO-H_2-H_2O during metal dusting, and regeneration of Al_2O_3 scale on the spalled areas is also impossible due to low testing temperature of 650 °C. Coke formation and metal dusting are probably initiated in the spalled regions. The underlying mechanisms of coke formation and metal dusting in the spalled area are similar to those occurring on the Ni_3Al base coatings without pre-oxidation. More importantly, the formation of Al_2O_3 scale during pre-oxidation at high temperatures always leads to an Al-depleted zone (Ni solid solution) in the matrix below the scale due to the consumption of Al [29, 67-69]. Ni-Al solid solution is more susceptible to coke formation and metal

dusting than the Ni_3Al matrix. Consequently, this Al_2O_3-free Ni-Al matrix would be more vulnerable to carbon attack than the Ni_3Al matrix. This explains why the pre-oxidized pure Ni_3Al coating was inferior to the un-treated pure Ni_3Al coating in terms of coke formation and metal dusting during extended exposure.

(b) Spallation and Effect of CeO_2

The pure Ni_3Al coating in this study experiences severe spallation of Al_2O_3 scale after pre-oxidation at 1100 °C for 24 hr (Figs.7-14 (a) and (b)). The spallation of Al_2O_3 has commonly been observed on the pure Ni-Al base alloys or coatings during cyclic oxidation at high temperatures. Work presented in Chapters 4 and 6 showed excessive spallation of the pure Ni_3Al coating during cyclic oxidation and carburization at 1050 °C, and the spallation during cyclic oxidation occurred at as soon as 10 hr. It is generally believed that the failure of the oxide scale is mainly related to the internal compressive stresses, that result from scale growth, thermal cycling, and mismatch at the scale/substrate interface [44, 45, 70-72], and from the formation of interfacial and/or internal voids in the Al_2O_3 scale [44, 73].

The presence of CeO_2 particles in Ni-Al base alloys or coatings can effectively reduce the spallation of the protective scale owing to the REE: (a)suppressing the formation of interfacial or internal voids [45, 47, 67, 74]; (b)modifying the growth mechanisms of the scale; (c)enhancing the mechanical properties of the scale [47, 62, 64, 75-77]; and (d) eliminating the harmful effect owing to the segregation of impurities such as sulfur at the scale / coating interface [74, 78-80]. In Chapters 4 and 6, we had observed that CeO_2 improved the adherence of the oxide scale to Ni_3Al base coatings, and reduced the spalling and cracking of the scale during either cyclic oxidation in the flowing air or cyclic carburization in CH_4-H_2 at 1050 °C.

The CeO_2-dispersed Ni_3Al coatings under study exhibit a dependence of spallation resistance on the size of CeO_2 particles. Two nano CeO_2-dispersed Ni_3Al coatings showed almost no spallation after pre-oxidation, while 5 μm CeO_2-dispersed Ni_3Al coatings experience extensive scale damage. Previous studies had suggested that

the REE was linked to the segregation [64, 65, 81] or the precipitation [82, 83] of the ions of reactive elements (e.g., Y, La, Ce, Hf) at the scale-grain boundaries or the scale/matrix interface. As mentioned earlier, the ability of CeO_2 particles to supply Ce^{4+} ions is determined by their sizes, and CeO_2 particles larger than 10nm could not serve as effective sources of Ce^{4+} ions [62, 65]. Consequently, 9-15 nm CeO_2 particles have an advantage over 5 μm CeO_2 particles in providing Ce^{4+} ions for the improvement of the spallation resistance of Al_2O_3 scale. However, this beneficial effect is seen largely at low temperatures, at which the decomposition of CeO_2 particles is slow. At higher temperatures, e.g., 1100 °C, the decomposition of CeO_2 and the supply of Ce^{4+} become sufficiently rapid, and the particle-size effect if present may be limited only in the very early stage of oxidation. The two 5 μm CeO_2-dispersed Ni_3Al coatings have much higher CeO_2 content than the two nano CeO_2-dispersed Ni_3Al coatings (Table 7-1 and Figs. 7-28 (a)-(d)). During the pre-oxidation at 1100 °C, the two 5 μm CeO_2-dispersed Ni_3Al coatings would produce much more Ce^{4+} ions than the two nano CeO_2-dispersed Ni_3Al coatings. An optimum doping concentration for reactive elements or their oxides exists in the oxide scale to achieve the "reactive-element effect" [84, 85]. Excessive doping can deteriorate only the mechanical properties of the scale, while too low doping has no effect. From these observations, we believe that high CeO_2 content is the main reason why the two 5 μm CeO_2-dispersed Ni_3Al coatings were inferior to the two nano CeO_2-dispersed Ni_3Al coatings in terms of spallation resistance. This mechanism may also explain the difference in spallation resistance between the two pre-oxidized 5 μm CeO_2-dispersed Ni_3Al coatings with different amounts of CeO_2.

(c) Catalytic Coke on α-Al_2O_3 Scale

Although the two pre-oxidized nano CeO_2-dispersed Ni_3Al coatings had the best α-Al_2O_3 scale coverage and showed the highest resistance to carbon attack, some catalytic coke was nonetheless observed on the coating surface after metal dusting for 500 hr. This type of coke formation always derives from catalytic Ni-rich sources (Fig. 7-17 (b)), which are present on α-Al_2O_3 scale for all the Ni_3Al base coatings after pre-oxidation (Figs. 7-14 (b) and 7-15 (a)). The formation of Ni-rich particles on α-Al_2O_3 scale was also found on our Ni_3Al base coatings during carburization at 850 °C and 1050

°C in 2%CH_4-H_2 with an extremely low oxygen partial pressure as indicated in Chapter 6. This has been reported to be common for Ni_3Al base alloys during oxidation at low oxygen partial pressures [86-88]. The mechanism may be associated with selective oxidation of Ni_3Al in the oxygen-deficient atmosphere. Significant compressive stresses are often generated during selective oxidation of Ni_3Al at the low oxygen partial pressure as given by [86]

$$Ni_3Al + O_2 \rightarrow Al_2O_3 + Ni \qquad (7\text{-}3)$$

To reduce these stresses, Ni would diffuse outward either along the oxide/matrix interface [86] or via the lattices or dislocation pipes of the alloy matrix [87]. This process usually stops when a dense and compact Al_2O_3 scale is formed. Our experimental results indicate that Ni particles will remain on the Al_2O_3 scale to act as catalysts for the deposition of filamentous coke. The formation of Ni particles on α-Al_2O_3 scale may be suppressed or even eliminated if the oxygen partial pressures during pre-oxidation were controlled below $10^{-19} - 10^{-22}\,atm$ [87, 88].

7.5 Concluding Remarks

Coke formation and metal dusting of electrodeposited pure, nano CeO_2-dispersed, and 5 μm CeO_2-dispersed Ni_3Al coatings with and without pre-oxidation were investigated at 650 °C for periods of up to 500hr in a CO-H_2-H_2O gas mixture with $a_c = 12.2$. The following conclusions can be drawn:

1. All the Ni_3Al base coatings, especially the two nano CeO_2-dispersed Ni_3Al coatings, showed much lower resistance to metal dusting and coke formation than the uncoated Fe-Ni-Cr alloys. Excessive catalytic coke and severe pitting attacks were observed for the two nano CeO_2-dispersed Ni_3Al coatings and the 80+5 (5 μm) coatings.
2. It was proposed that the inferior resistance of the current Ni_3Al base coatings to coke formation and metal dusting was related to the testing temperature of 650 °C, which was too low to form a full coverage of Al_2O_3 scale on the Ni_3Al

base coatings during metal dusting. As a result, localized pitting attack took place at vulnerable sites of the coatings.

3. CeO_2 particles in the coatings promoted the formation of NiO, which, in turn, allowed more coke formation and pitting attacks. This explains the inferior resistance of the CeO_2-dispersed Ni_3Al coatings to coke formation and metal dusting as compared to the pure Ni_3Al coating. Because they were more effective in facilitating the formation of NiO than the 5 μm CeO_2 particles, nano CeO_2 particles had resulted in the worst resistance to coke formation and metal dusting.
4. Pre-oxidation treatment significantly improved the resistance of Ni_3Al base coatings to coke formation and metal dusting by pre-forming a thin Al_2O_3 scale on the coating surface. However, the effectiveness of pretreatment strongly depended on the mechanical integrity of the scale. The pure Ni_3Al coating and the two 5 μm CeO_2-dispersed Ni_3Al coatings suffered excessive spallation after pre-oxidation, and consequently had more severe coke formation and pitting attack during subsequent metal dusting testing. In contrast, the two nano CeO_2-dispersed Ni_3Al coatings acquire an excellent protective scale through pretreatment. They showed much less coke formation and were almost free of pitting attack. Coke deposition and carbon attack always began at spalled areas, where the underlying mechanisms would be similar to those in the case of Ni_3Al base coatings without pre-oxidation.
5. The two 5 μm CeO_2-dispersed Ni_3Al coatings contained much more CeO_2 than the two nano CeO_2-dispersed Ni_3Al coatings. Higher CeO_2 doping reduced the resistance of Al_2O_3 scale to spallation.
6. Ni-rich particles were formed concurrently with the Al_2O_3 scale during pre-oxidation at 1100 °C in H_2-0.6%H_2O with $p_{O_2} = 3.61 \times 10^{-18} atm$. These Ni-rich particles catalyzed coke formation, and were responsible for the mass increase of all the Ni_3Al base coatings during metal dusting.

7.6 Bibliography

1. Grabke, H.J., Materials and Corrosion, 1998. **49**: p. 303-308.

2. Grabke, H.J., Materials Science Forum, 2001. **369-372**: p. 101-108.

3. Szakálos, P., Materials and Corrosion, 2003. **54**(10): p. 752-762.

4. Grabke, H.J., Materials and Corrosion, 2003. **54**(10): p. 736-746.

5. Grabke, H.J. and Spiegel, M., Materials and Corrosion, 2003. **54**(10): p. 799-804.

6. Tokura, S., Otsuka, N., and Kudo, T., Corrosion, 1993. **49**(7): p. 561-568.

7. Pippel, E., Woltersdorf, J., Grabke, H.J., and straußß, S., Steel Research, 1995. **66**(5): p. 217-221.

8. Schneider, R., Pippel, E., Woltersdorf, J., Strauß, S., and Grabke, H.J., Steel Research, 1997. **68**(7): p. 326-332.

9. Schneider, R., Viefhaus, H., Inden, G., Grabke, H.J., and Müller-Lorenz, E.M., Materials and Corrosion, 1998. **49**: p. 336-339.

10. Bennett, M.J., Materials and Corrosion, 1998. **49**: p. 345-351.

11. Wysiekierski, A.G., Fisher, G., and Schillmoller, C.M., Hydrocarbon Processing (International Edition), 1999. **78**(1): p. 97-100.

12. Klöwer, J., Grabke, H.J., and Müller-Lorenz, E.M., Materials and Corrosion, 1998. **49**: p. 328-329.

13. Baker, B.A., Hartmann, V.M., Shoemaker, L.E., McCoy, S.A., and Rajendran, S., Transactions of The Indian Institute of Metals, 2003. **56**(3): p. 327-333.

14. Grabke, H.J. and Müller-Lorenz, E.M., Materials and Corrosion, 1998. **49**: p. 317-320.

15. Grabke, H.J., Müller-Lorenz, E.M., Strauss, S., Pippel, E., and Woltersdorf, J., Oxidation of Metals, 1998. **50**(3-4): p. 241-254.

16. Grabke, H.J., Müller-Lorenz, E.M., and Zinke, M., Materials and Corrosion, 2003. **54**(10): p. 785-792.

17. Strauß, S. and Grabke, H.J., Materials and Corrosion, 1998. **49**: p. 321-327.

18. Brill, U., Materials and Corrosion, 1990. **41**(12): p. 682-688.

19. Klöwer, J., Brill, U., and Heubner, U., Intermetallics, 1999. **7**: p. 1183-1194.

20. Wang, Y. and Chen, W.X., Surface and Coatings Technology, 2004. **183**: p. 18-28.

21. Lu, Y.X., Chen, W.X., and Eadie, R., Intermetallics, 2004. **12**: p. 1299-1304.

22. Strauß, S., Krajak, R., Palm, M., and Grabke, H.J., Materials and Corrosion, 1996. **47**(12): p. 701-702.

23. Schneider, A. and Zhang, J., Materials and Corrosion, 2003. **54**(10): p. 778-784.

24. Schneider, A., Zhang, J., and Inden, G., The Journal of Corrosion Science and Engineering, 2003. **6**: p. Paper H043.

25. Susan, D.F., Misiolek, W.Z., and Marder, A.R., Metallurgical and Materials Transactions A., 2001. **32A**: p. 379-391.

26. Grabke, H.J., *Carburization: A High Temperature Corrosion Phenomenon.* 1998, St.Louis, MO, USA: MTI.

27. Gaskell, D.R., *Introduction to the thermodynamics of materials.* 3rd ed. 1995, Washington, D.C.: Taylor & Francis.

28. Pettit, F.S., Transactions of TMS-AIME, 1967. **239**: p. 1296-1305.

29. Pérez, P., González-Carrasco, J.L., and Adeva, P., Oxidation of Metals, 1997. **48**(1-2): p. 143-170.

30. Pérez, P., González-Carrasco, J.L., and Adeva, P., Corrosion Science, 1998. **40**(4-5): p. 631-644.

31. Haerig, M. and Hofmann, S., Applied Surface Science, 1998. **125**: p. 99-114.

32. Alstrup, I., Tavares, M.T., Bernardo, C.A., Sorensen, O., and Rostrup-Nielsen, J.R., Materials and Corrosion, 1998. **49**: p. 367-372.

33. Figueiredo, J.L., Materials and Corrosion, 1998. **49**: p. 373-377.

34. Toh, C.H., Munroe, P.R., and Young, D.J., Oxidation of Metals, 2002. **58**(1-2): p. 1-21.

35. Steurbaut, C., Grabke, H.J., Stobbe, D., Van Buren, F.R., Korf, S.J., and Defrancq, J., Materials and Corrosion, 1998. **49**: p. 352-359.

36. Wagner, C., Z. Electrochem., 1959. **63**: p. 772-782.

37. Atrei, A., Bardi, U., and Rovida, G., Journal of Electron Spectroscopy and Related Phenomena, 1991. **57**: p. 99-102.

38. Venezia, A.M. and Loxton, C.M., Surface and Interface Analysis, 1988. **11**(6-7): p. 287-290.

39. Venezia, A.M. and Loxton, C.M., Surface Science, 1988. **194**: p. 136-148.

40. Venezia, A.M., Loxton, C.M., and Horton, J.A., Surface Science, 1990. **225**: p. 195-205.

41. Baker, R.T.K., Barber, M.A., Harris, P.S., Feates, F.S., and Waite, R.J., Journal of Catalysis, 1972. **26**: p. 51.

42. Park, C., Rodriguez, N.M., and Baker, R.T.K., Journal of Catalysis, 1997. **169**: p. 212-227.

43. Grabke, H.J., Corrosion, 2000. **56**(8): p. 801-808.

44. Stott, F.H., Wood, G.C., and Stringer, J., Oxidation of Metals, 1995. **44**(1-2): p. 113-141.

45. Rahmel, A. and Schütze, M., Oxidation of Metals, 1992. **38**(3-4): p. 255-266.

46. Prescott, R. and Graham, M.J., Oxidation of Metals, 1992. **38**(3-4): p. 73-87.

47. Prescott, R. and Graham, M.J., Oxidation of Metals, 1992. **38**(3-4): p. 233-254.

48. Ferreira-Aparicio, P., Benito, M., Kouachi, K., and Menadb, S., Journal of Catalysis, 2005. **231**: p. 331-343.

49. Flytzani-Stephanopoulos, M., Zhu, T.L., and Li, Y., Catalysis Today, 2000. **62**: p. 145-158.

50. Luo, J.Z., Yu, Z.L., Ng, C.F., and Au, C.T., Journal of Catalysis, 2000. **194**: p. 198-210.

51. Stagg-Williams, S.M., Noronha, F.B., Fendley, G., and Resasco, D.E., Journal of Catalysis, 2000. **194**: p. 240-249.

52. Yang, Y.L., Li, W.Z., and Xu, H.Y., Reaction Kinetics and Catalysis Letters, 2002. **77**(1): p. 155-162.

53. Zhu, T.L. and Flytzani-Stephanopoulos, M., Applied Catalysis A: General, 2001. **208**: p. 403-417.

54. Wang, W., Stagg-Williamsa, S.M., Noronha, F.B., Mattosb, L.V., and Passos, F.B., Catalysis Today, 2004. **98**: p. 553-563.

55. Hettige, C., Mahanama, K.R.R.R., and Dissanayake, D.P., Chemosphere, 2001. **43**: p. 1079-1083.

56. Shi, K.Y., Li, H.Y., Shang, Y.C., Xu, G.L., and Wei, Y.D., Reaction Kinetics and Catalysis Letters, 2000. **71**(1): p. 177-182.

57. Hultquist, G., Hörnlund, E., and Dong, Q., Corrosion Science, 2003. **45**: p. 2697-2703.

58. Hultquist, G., Sproule, G.I., Moisa, S., Graham, M.J., and Södervall, U., Journal of The Electrochemical Society, 2003. **150**(10): p. G617-G623.

59. Hultquist, G., Tveten, B., Hörnlund, E., Limbäck, M., and Haugsrud, R., Oxidation of Metals, 2001. **56**(3-4): p. 313-346.

60. Tveten, B., Hultquist, G., and Wallinder, D., Oxidation of Metals, 2001. **55**(3-4): p. 279-289.

61. Dong, Q., Hultquist, G., Graham, M.J., Anghel, C., and Sproule, G.I. *Paper No. 18-B-19.* in *The 16th International Corrosion Congress.* 2005. Beijing, China.

62. Czerwinski, F. and Smeltzer, W.W., Oxidation of Metals, 1993. **40**(5-6): p. 503-527.

63. Czerwinski, F., Szpunar, J.A., Macaulay_Newcombe, R.G., and Smeltzer, W.W., Oxidation of Metals, 1995. **43**(1-2): p. 25-57.

64. Haugsrud, R., Corrosion Science, 2003. **45**: p. 1289-1311.

65. Czerwinski, F. and Szpunar, J.A., Journal of Sol-Gel Science and Technology, 1997. **9**: p. 103-114.

66. Grabke, H.J. and Wolf, I., Materials Science and Engineering, 1987. **87**: p. 23-33.

67. Kuenzly, J.D. and Douglass, D.L., Oxidation of Metals, 1974. **8**: p. 139-178.

68. Doychak, J. and Rühle, M., Oxidation of Metals, 1989. **31**(5-6): p. 431-452.

69. Schumann, E. and Rühle, M., Acta Metallurgica ET Materialla, 1994. **42**(4): p. 1481-1487.

70. Hancock, P. and Nicholls, J.R., Materials at High Temperatures, 1994. **12**(2-3): p. 209-217.

71. Bull, S.J., Oxidation of Metals, 1998. **49**(1-2): p. 1-17.

72. Christensen, R.J., Lipkin, D.M., and Clarke, D.R., Acta Materialia, 1996. **44**(9): p. 3813-3821.

73. Pint, B.A., Oxidation of Metals, 1997. **48**(3-4): p. 303-328.

74. Grabke, H.J., Intermetallics, 1999. **7**: p. 1153-1158.

75. Jung, H.G. and Kim, K.Y., Oxidation of Metals, 1998. **49**(5-6): p. 403-430.

76. Chevalier, S. and Larpin, J.P., Acta Materialia, 2002. **50**: p. 3105-3114.

77. Pint, B.A., Materials Science Forum, 1997. **251-254**: p. 397-404.

78. Grabke, H.J., Surface and Interface Analysis, 2000. **30**: p. 112-119.

79. Meier, G.H., Pettit, F.S., and Smialek, J.L., Materials and Corrosion, 1995. **46**: p. 232-240.

80. Schumann, E., Yang, J.C., and Graham, M.J., Scripta Materialia, 1996. **34**(9): p. 1365-1370.

81. Peng, X., Li, T.F., and Wu, W.T., Oxidation of Metals, 1999. **51**(3-4): p. 291-315.

82. Kim, K.Y., Kim, S.H., Kwon, K.W., and Kim, L.H., Oxidation of Metals, 1994. **41**(3-4): p. 179-201.

83. Wright, I.G., Pint, B.A., and Tortorelli, P.F., Oxidation of Metals, 2001. **55**(3-4): p. 333-357.

84. Stott, F.H., Gleeson, B., and Castello, P., Materials at High Temperatures, 1999. **16**(1): p. 15-26.

85. Quadakkers, J. and Singheiser, L., Materials Science Forum, 2001. **369-3**(Part 1&2): p. 77-92.

86. Schumann, E., Schnotz, G., Trumble, K.P., and Rühle, M., Acta Metallurgica ET Materialla, 1992. **40**(6): p. 1311-1319.

87. Yi, H.C., Smeltzer, W.W., and Petrix, A., Oxidation of Metals, 1996. **45**(3-4): p. 281-299.

88. Gao, W., Li, Z.W., Wu, Z., Li, S., and He, Y.D., Intermetallics, 2002. **10**: p. 263-270.

Chapter 8

Concluding Remarks and Future Work

8.1 Concluding Remarks

The goal of this research project was to develop novel Ni_3Al base intermetallic coatings to protect Fe-Ni-Cr commercial tube alloys widely used in petrochemical, chemical, and energy conversion industries from high-temperature corrosion. The study consisted of two main aspects: the coating process and the coating evaluation. The coating process was covered in Chapter 2 and Chapter 3. The coating evaluation was reported in Chapters 4-7. The following are some concluding remarks concerning study.

8.1.1 The Coating Process

As a basis for the entire project, Chapter 2 focused on developing co-deposited Ni-Al binary composite coatings from a Watt's nickel bath via SCD. We produced Ni-Al composite coatings with 30-35vol% Al particles, which is required for the formation of single-phase γ'-Ni_3Al intermetallic coatings after annealing treatment. Al particle content in the coatings was found to be insensitive to the change of current density but sensitive to Al particle loading. The co-deposition of Al particles followed the Guglielmi two-step adsorption model, and was distinct from that of non-conducting particles.

Chapter 3 extended the cost-effective SCD technique to co-deposit Ni-Al-REO ternary composite coatings, which were *in situ* synthesized to form reactive oxide-dispersed Ni_3Al coatings. CeO_2, Y_2O_3, and Al_2O_3-dispersed Ni_3Al intermetallic coatings were produced. The interfering of the REO particles with the co-deposition of Al particles was observed. This interfering effect was related to the difference in surface charge state between REO particles and Al particle in the plating bath.

8.1.2 The Coating Evaluation

Based on the work in Chapter 2 and Chapter 3, the pure, two 5 μm CeO_2-dispersed, and two 9-15 nm CeO_2-dispersed Ni_3Al coatings were selected to assess their performances at high temperatures in various environments typically encountered during hydrocarbon cracking.

Chapter 4 dealt with the long-term resistance of our electrodeposited Ni_3Al coatings to cyclic oxidation in flowing dry air with high oxygen partial pressure, $p_{O_2} = 0.21atm$. All coatings were characterized by poor resistance to cyclic oxidation at 850 °C in the early stage due to high porosity in the coatings. Pore healing, caused by interdiffusion and self-sintering, significantly reduced the oxidation rate in the final stage of oxidation. At 1050 °C, the porosity effect was not observed due to a rapid densification of coatings. CeO_2 particles in the coatings evidently suppressed the spallation of Al_2O_3 scale, which was severe in the CeO_2-free Ni_3Al coating. A discussion of the oxidation behavior, the degradation mechanism and the beneficial effect of CeO_2 provided a theoretical basis for elucidation of the carburization, coke formation, and metal dusting behaviors of the Ni_3Al base coatings reported in Chapters 6 and 7.

The work in Chapter 5 focused on a number of ways to improve the long-term resistance of the current Ni_3Al base coatings to cyclic oxidation at 850 °C. The nano CeO_2 and micron Y_2O_3-dispersed two-phase, γ-Ni+γ'-Ni_3Al, Ni-Al coatings showed superior cyclic-oxidation resistance at 850 °C for periods of up to 1000 hr. However, the low Al content would limit their applications at higher temperatures. Long-term annealing and plating a very thin film proved to be ineffective.

Highly-reducing carburizing atmospheres are typical of Fe-Ni-Cr cracking tubes used in modern ethylene plants. Compared to the uncoated Fe-Ni-Cr alloy, all the Ni_3Al base coatings showed superior carburization resistance in 2%CH_4-H_2 at 850 °C and especially 1050 °C for periods of up to 500 hr. This was attributed to the strong ability of Ni_3Al base coatings to form a thin Al_2O_3 scale at extremely low oxygen partial pressure. CeO_2 improved the adherence of Al_2O_3 scale, and suppressed the cracking of Al_2O_3 scale on the pure Ni_3Al coating at 1050 °C. Another important finding was catalytic coke formation on the Ni_3Al base coatings during an exposure at 1050 °C, which was attributed to the presence of Ni-rich particles on Al_2O_3 scale during selective oxidation of Ni_3Al at the low oxygen partial pressure.

Coke formation and metal dusting are very problematic for Fe-Ni-Cr alloys used in ethylene production furnaces. Based on the work reported in Chapter 7, all the Ni_3Al base coatings exhibited inferior resistance to coke formation and metal dusting at 650 °C in 24.4%CO-73.3%H_2-2.3%H_2O compared to the uncoated Fe-Ni-Cr alloy. It was believed that the testing temperature was too low to form a full coverage of Al_2O_3 scale on the Ni_3Al base coatings. This was responsible for the marginal performances observed. CeO_2 particles in the Ni_3Al base coatings promoted the formation of NiO and reduced the resistance to coke formation and metal dusting.

Pre-oxidation treatment was used to pre-form a thin Al_2O_3 scale on the coatings. The pre-treated pure Ni_3Al coating suffered accelerated coke formation and metal dusting during long-term exposure owing to severe spallation during the pre-treatment. The two pre-treated nano CeO_2-dispersed Ni_3Al coatings showed much better performances than the uncoated Fe-Ni-Cr alloy due to excellent mechanical integrity of Al_2O_3 scale. It was also found that the oxygen partial pressure during pre-treatment might be too high to suppress the formation of Ni particles catalytic to coke formation on Al_2O_3 scale.

8.2 Future Work

8.2.1 Interfering Effect

In Chapter 2, the interfering effect of REO particles on the co-deposition of Al metal particle was identified. We had proposed that the REO particles might have more positive surface charge (zeta potential) than the Al particles in the Watt's nickel bath. IN such case, the REO particles would be preferentially adsorbed onto the cathode surface and entrapped in the Ni coating. To support this hypothesis, zeta potential of either the REO particle or the Al particle in the bath must be determined. However, the conventional zeta potential measurement gives only a value averaging the contribution of all the particles. Recently, Liu et al. [1, 2] reported a novel approach to measuring the distribution of zeta potential in a solution containing two or more kinds of particles. In such an approach, the motion of charged particles can be traced with the aid of a laser-illuminating and video-viewing system and captured by a charge-coupled-device (CCD) digital camera. The built-in image software can automatically process the images

obtained, and the corresponding electrophoresis mobility of each type of charging particles can be calculated and converted to the zeta potential distribution. If two types of particles have a distinct surface charge and are separated from each other in the solution, two different peaks corresponding to each type of particle can be expected in the zeta potential distribution. If this method can be applied in this research, it will make a solid contribution to the understanding of the interfering effect and the co-deposition mechanism.

8.2.2 Elimination of Pores

High porosity in the electrodeposited Ni_3Al base coatings exerted a profoundly detrimental effect on the long-term resistance of coatings to cyclic oxidation and carburization at low temperatures (e.g., 850 °C). Although preliminary work has been conducted, additional studies are required to ensure that the coatings will have adequate corrosion resistance over a wide range of temperatures.

8.2.3 Elimination of Ni Particles During Pre-oxidation

According to Chapter 7, pre-treatment significantly improved the resistance of Ni_3Al base coatings to coke formation and metal dusting at 650 °C by forming a thin Al_2O_3 scale. However, the formation of Ni particles on the Al_2O_3 scale during pre-treatment led to the deposition of catalytic coke. Other researchers have proposed that these Ni particles could be suppressed or eliminated by controlling oxygen partial pressure to a level below $10^{-19} - 10^{-22} atm$ [3, 4]. Consequently, the determination of an optimum oxygen partial pressure in pre-oxidizing atmospheres is crucial to improve the performances of electrodeposited Ni_3Al base coatings.

8.3 Bibliography

1. Liu, J., Xu, Z., and Masliyah, J., Langmuir, 2003. **19**: p. 3911-3920.

2. Liu, J., Zhou, Z., Xu, Z., and Masliyah, J., Journal of Colloid and Interface Science, 2002. **252**: p. 409-418.

3. Yi, H.C., Smeltzer, W.W., and Petrix, A., Oxidation of Metals, 1996. **45**(3-4): p. 281-299.

4. Gao, W., Li, Z.W., Wu, Z., Li, S., and He, Y.D., Intermetallics, 2002. **10**: p. 263-270.